



UNIVERSITÀ DEGLI STUDI DI PADOVA

**ISM in numerical simulations:
chemistry, energy feedbacks
and related issues - numerical
methods**

Author:
Tommaso GRASSI

Supervisor:
Prof. Cesare CHIOSI

January 28, 2011

Ai miei genitori

Abstract

The physics of the interstellar medium (ISM) and its processes play a key role in determining the formation and the evolution of the galaxies. The description of the ISM includes many interacting phenomena, namely the energy feedback, the chemical reactions between molecules and atoms, the physics of the dusts, the cooling, the heating and, finally, the interactions of the ISM with photons and with cosmic rays.

The most important issue for the star formation process is the amount of cooling given by the roto-vibrational lines of the molecules (H_2 , HD, CO) and by the fine-structure lines of the metals. Since all the aforementioned phenomena take part to the formation of such coolants, we need an accurate description of these processes.

In this framework we develop a model aimed at the study of the ISM. This model includes a large number of physical processes such as a detailed chemical network including hydrogen-based species (H , H^+ , H^- , H_2 , H_2^+), helium-based (He , He^+ , He^{++}), metals and their ions (C , C^+ , O , O^+ , Si , Si^+ , Fe , Fe^+), deuterium-based (D , D^+ , D^- , D_2 , HD, HD^+), and molecules containing carbon (CO , CH , CH^+ , CH_2 , CH_2^+ , CH_3 and CH_3^+). The cooling model adopted uses the metals (including ions) and the molecules, considering the analysis of the statistical equilibrium for the excitation levels (where necessary). Moreover, the interaction of the UV photons with the gas, which determines the heating and the ionization of the ISM. The last ingredient is the dust which interacts with all the previous components; The temperature of the grains is determined by the impinging UV radiation, they catalyze the formation of molecules (such as molecular hydrogen), and provide cooling and heating to the surrounding medium. We also include their evolution and the influence of their different sizes in all the interactions listed above.

All these processes of the ISM have their counterpart in the algorithms of a chemical/physical code called ROBO. The aim of this code is to study the ISM and the interplay of its phenomena.

The results of the code ROBO are than used to describe the evolution of the phases of the ISM in a NB-TSPH cosmological simulation to study the

star formation for different evolving galaxies. This class of simulation must take into account a wide range of chemical species to track the formation of the key-role molecules and atoms (H_2 , HD, CO and metals). In this sense, modeling the gas chemistry (and related processes) is crucial within this context.

However, too detailed a chemistry reduces the computational performances of the evolutionary code. This requires the development of a strategy to optimize the accuracy of the model with the computational speed. One way to approach to this problem is to create a database in advance, which feeds the data to the main NB-TSPH simulation during the execution of the code. The database is then embedded into the NB-TSPH code using the Artificial Neural Networks.

In this work we first discuss the physical phenomena of the ISM, than we introduce the code ROBO, which is the companion code of the ISM model, and finally we show how Artificial Neural Networks are included in such a scenario.

Abstract (Italian)

La fisica del mezzo interstellare (ISM) e i relativi processi giocano un ruolo decisivo nella formazione e nell'evoluzione delle galassie. La descrizione del mezzo interstellare include molti fenomeni che interagiscono tra di loro, quali i feedback, le reazioni chimiche che vedono coinvolti atomi e molecole, la fisica delle polveri, i processi di raffreddamento e di riscaldamento e le interazione del mezzo con i fotoni e i raggi cosmici.

Il processo che maggiormente influenza la star formation è il raffreddamento dovuto allo spettro rotovibrazionale delle molecole (H_2 , HD, CO) e allo spettro derivante dalla righe di struttura fine dei metalli. Dato che i processi precedentemente elencati prendono parte alla distruzione e alla formazione di tali molecole, è necessaria una descrizione accurata dei fenomeni presenti nel mezzo interstellare.

In questo contesto abbiamo sviluppato un modello per lo studio del mezzo interstellare. Questo modello comprende un'ampia varietà di fenomeni, come ad esempio un network chimico dettagliato che include le species idrogenoidi (H, H^+ , H^- , H_2 , H_2^+), l'elio e i suoi ioni (He, He^+ , He^{++}), i metalli con i relativi ioni (C, C^+ , O, O^+ , Si, Si^+ , Fe, Fe^+), le species che contengono il deuterio (D, D^+ , D^- , D_2 , HD, HD^+), ed infine le molecole che contengono il carbonio (CO, CH, CH^+ , CH_2 , CH_2^+ , CH_3 and CH_3^+).

Il modello di cooling adottato utilizza i metalli (e relativi ioni) e le molecole, considerando dove necessario un calcolo diretto dell'equilibrio statistico dei livelli atomici e molecolari. Inoltre le interazioni con la radiazione ultravioletta determinano il riscaldamento e la ionizzazione del gas. L'ultimo ingrediente sono le polveri che interagiscono con tutte le precedenti componenti, poiché la temperatura dei grani è determinata dalla radiazione che illumina il volume di gas considerato, inoltre le polveri catalizzano la formazione di molecole e contemporaneamente scaldano o raffreddano il mezzo a seconda delle condizioni in cui si trovano. Abbiamo anche introdotto la loro evoluzione considerando che grani di diverse dimensioni hanno una diversa influenza sui processi descritti.

Tutti questi processi hanno una loro controparte negli algoritmi di un

codice chiamato ROBO che è la rappresentazione numerica del modello proposto. Lo scopo principale di questo codice è quello di studiare il mezzo interstellare e l'interazione tra i fenomeni che lo caratterizzano.

I risultati prodotti dal codice ROBO vengono inoltre utilizzati per descrivere l'evoluzione delle diverse fasi del mezzo interstellare all'interno di un codice evolutivo NB-TSPH. Questo codice permette di studiare la formazione stellare nelle galassie durante la loro evoluzione su scala cosmologica. Inoltre le simulazioni di formazione ed evoluzione delle galassie su larga scala devono tenere conto di una varietà di specie chimiche che permettano la formazione delle molecole e degli atomi più importanti (H_2 , HD, CO e metalli).

Tuttavia una descrizione troppo dettagliata di questi fenomeni riduce le prestazioni del codice NB-TSPH a livello computazionale. Siamo quindi costretti a sviluppare una strategia per ottimizzare il bilancio tra precisione algoritmica e velocità di tali algoritmi. Un approccio possibile è quello di creare un database precedente alla fase di esecuzione del codice NB-TSPH con un apposito codice chimico-fisico, cioè ROBO. Il database diventa quindi accessibile dal codice evolutivo durante la sua esecuzione, e la metodologia usata per interfacciare database e codice NB-TSPH fa utilizzo delle Reti Neurali Artificiali.

In questa tesi discuteremo prima i vari fenomeni che agiscono all'interno del mezzo interstellare, poi introdurremo il codice chimico ROBO e infine mostreremo alcuni risultati prodotti con l'ausilio delle reti neurali all'interno del codice NB-TSPH.

Contents

1	Introductory outline	21
2	The Interstellar Medium	25
2.1	ISM: Introduction	25
2.1.1	Interstellar objects	26
2.1.2	ISM components	28
2.1.3	Energy sources	31
2.1.4	The ISM and the Milky Way	33
2.1.5	The ISM and the stars	35
2.2	ISM: Chemistry	37
2.2.1	The chemical network	37
2.2.2	Photoionization	39
2.2.3	Chemistry: numerical issues	41
2.3	ISM: Cooling	43
2.3.1	Atomic Cooling	45
2.3.2	Molecular Cooling	47
2.4	ISM: Heating	51
2.4.1	Heating by Cosmic Rays	52
2.4.2	Heating by Turbulence	53
2.5	ISM: Dust	54
2.5.1	Size distribution	55
2.5.2	Formation	57
2.5.3	Temperature	58
2.5.4	Destruction	60
2.5.5	Formation of molecules	69
2.5.6	Heating and cooling	72
2.6	ISM: Conclusions	74
3	ROBO	77
3.1	Introduction	77
3.2	ROBO: chemistry	80

3.2.1	Reaction by reaction: notes on a few cases	87
3.2.2	Minimal CO network	90
3.2.3	Photochemistry	92
3.3	ROBO: cooling	96
3.3.1	Which are the sources of cooling to consider?	96
3.3.2	H ₂ cooling.	97
3.3.3	HD cooling.	97
3.3.4	Cooling by the CO molecule	98
3.3.5	Cooling by the Metals	100
3.3.6	Total cooling	102
3.4	ROBO: heating	103
3.5	ROBO: dusts	103
3.5.1	Size distribution function of dust grains	105
3.5.2	Dust-driven H ₂ and HD formation	105
3.5.3	Grain formation	107
3.5.4	Grain destruction	109
3.5.5	Heating by photoelectric ejection of electrons from dust grains	113
3.6	ROBO: the code	116
3.6.1	Mass conservation	119
3.6.2	Time-step	119
3.6.3	Numerical Solver	119
3.6.4	Ranges of applicability	120
3.6.5	Free parameters	120
3.7	ROBO: tests	121
3.7.1	Dust-Free Models	121
3.7.2	Models with dust: parameter set up	132
4	Interfacing ROBO with Nbody/TreeSPH	141
4.1	Introduction	141
4.2	Interfacing ROBO with a NB-TSPH code	142
4.2.1	Classical methods	143
4.2.2	AI-based methods	145
4.3	Our choice: Artificial Neural Networks	148
4.3.1	The learning stage	151
4.4	Training and testing MaNN	156
4.4.1	Input data from ROBO	156
4.4.2	Compression of data?	158

<i>CONTENTS</i>	11
5 ANN and NB-TSPH	161
5.1 The NB-TSPH code: EvOL	161
5.2 ANN and EvOL	164
5.3 ROFO or: how I learned to stop worrying...	167
5.3.1 ROFO: an application to EvOL	170
5.4 Summary	171
6 Future developments	177
6.1 Including stellar feedback	178
6.2 Metallicity dependent cooling - a more accurate version	179
6.3 Markovian-like ISM evolution	180
6.3.1 A simple application	183
7 Conclusions	187
A Complete matrices for metal cooling	191

List of Figures

2.1	Some of the fine-structure lines included in our cooling model for the ions C^+ , O , Si^+ and Fe^+ . From [89].	48
2.2	Target-projectile interaction. If the mass of the projectile is lower than the half of the mass of the target, the target is partially damaged (left), else the target is totally destroyed (right). In this picture $\tilde{m} = m_{\text{target}}/2$. From [68].	64
2.3	The distribution of charge in different environments (PDR, WIM and diffuse ISM), and for different grain sizes (5, 15 and 100 Å). The solid lines represent spherical grains of a given radius, while the dashed lines are for planar particles of the same radius. The purpose of this picture is to illustrate the shape of the distribution of charge. From [5] (in the same paper are also given the physical properties of the environments considered - see their Table 2).	75
3.1	Top panel: charge transfer cross section for the reaction $H_2 + H^+ \rightarrow H_2^+ + H$. Bottom Panel: Rate coefficient $k(T)$ derived from the cross section in the top panel. The fits of $k(T)$ (dashed line) given by Eqn. (3.18) and Table 3.6 cannot be visually distinguished from $k(T)$	88
3.2	The cooling calculated for different rotational quantum numbers J with the method proposed in the Section 3.3.4. The Figure is for $T = 100$ K accounting for the collisions with ortho-molecular hydrogen. Each line represents the cooling at a different number density of H_2 . In particular we have $n_{H_2} = 10^5 \text{ cm}^{-3}$ for the upper line and $n_{H_2} = 10^{-3} \text{ cm}^{-3}$ for the lower line. Each step in density is logarithmic.	101
3.3	The sticking coefficient for the carbon molecules over a carbon lattice derived from [81]. The different lines indicate a different dust temperature: 3 K (solid), 100 K (dotted) and 200 K (dashed). T_g is the gas temperature in Kelvin.	110

- 3.4 Top Panel: heating by dusts (solid line), cooling (dotted line) and the difference between heating and cooling (dashed line) for different diameters of the dust particles. Bottom Panel: the probability of finding a grain with a certain charge Z as a function of the grain dimensions. 117
- 3.5 The structure of the code ROBO. *Dvode* is the solver for the ordinary differential equations, dn , dT and dg are the differential functions for the species, the temperature and the dust bins, *init* is the initialization of the parameters of the different models and *I/O* is the interface with the input/output devices. *Heat* represents the dust destruction by heating, *accr* is the dust accretion and *shock* represents the processes related to shocks. k are the rate coefficients, *FUV* is the impinging radiation, H_2 and *HD dust* are the contribution of molecules of the dust to the gas-phase. *Heating* and *cooling* are self-explanatory. The cooling is determined by metals (Z), molecular hydrogen cooling (H_2), *HD*, *CO*, *CEN* [27] and *SD* [122]. *CO* and Z need a linear system solver, namely *dgesv*, while *SD* needs a subroutine to interpolate (*interp*). The arrows are for illustrative purposes only, and do not represent the actual code data-flow. 118
- 3.6 Temperature evolution for different values of the initial H_2 densities. The lines represent the time evolution in the cases $H_2 = 10^{-10}$ (solid line), $H_2 = 10^{-6}$ (dotted line), $H_2 = 10^{-2}$ (dashed line), $H_2 = 10^{-1}$ (dashed-dotted line) and, finally, $H_2 = 10$ (three dots-dashed line). All the densities are in cm^{-3} . Top Panel: the models with $Z = 10^{-10}$. Bottom Panel: the same as in the top panel but for $Z = 1$. See the text for more details. 127
- 3.7 Top Panel: Temperature evolution for different metallicities Z and in presence of the UV radiation field. Bottom Panel: evolution of the number density of molecular hydrogen for the same set of parameters. We represent the cases $Z = 1$ (dot-dashed line), $Z = 10^{-1}$ (dashed line), $Z = 10^{-2}$ (dotted line) and, finally $Z = 10^{-10}$ (solid line). See the text for more details. 128
- 3.8 Top Panel: Temperature evolution for different metallicities Z but in absence of the UV radiation field. Bottom panel: evolution of the molecular hydrogen for the same set of parameters. We represent the following cases: $Z = 1$ (dot-dashed line), $Z = 10^{-1}$ (dashed line), $Z = 10^{-2}$ (dotted line) and, finally, $Z = 10^{-10}$ (solid line). See the text for more details. 129

- 3.9 Temporal evolution of the electrons number density for different metallicities Z and in presence of the UV radiation field (top panel, related to Fig. 3.7) or without the UV field (bottom panel, same model of Fig. 3.8). The metallicities are $Z = 1$ (dot-dashed line), $Z = 10^{-1}$ (dashed line), $Z = 10^{-2}$ (dotted line) and, finally $Z = 10^{-10}$ (solid line). See the text for more details. 130
- 3.10 Temperature evolution for different metallicities Z and with the cooling contribution by ionized or neutral metals alternatively switched off. Top Panel: no cooling by ionized metals. Bottom panel: no cooling by neutral metals. In both panels the meaning of the lines is as follows: the dot-dashed line is for $Z = 1$, the dashed line for $Z = 10^{-1}$, the dotted line for $Z = 10^{-2}$, and the solid line for $Z = 10^{-10}$. See the text for more details. 131
- 3.11 Temperature evolution with different metallicities Z and cooling options. The meaning of the lines is as follows: high Z and no cooling (solid line), low Z and no cooling (dotted line), high Z and cooling included (dashed line), low Z and cooling included (dashed-dotted). The dashed-dotted and dotted lines overlap. Top Panel: the H_2 cooling is enabled. Bottom Panel: the H_2 cooling is switched off. The cooling by Cen is switched off in both panels. 133
- 3.12 Evolution of the number density of molecular hydrogen for different initial metallicity Z and options for the cooling. The meaning of the lines is as follows: high Z and no cooling (solid line), low Z and no cooling (dotted line), high Z and cooling enabled (dashed line), low Z and cooling switched off (dashed-dotted line). The dashed-dotted and dotted lines overlap. The cooling by Cen is switched off in both panels. 134
- 3.13 Temperature evolution for different amounts of initial dust. Top Panel: low metallicity cases. Bottom Panel: high metallicity cases. In both panels the meaning of the lines is as follows: the solid line is for $n_{\text{dust}} = 10^{-3}$, dotted line is for $n_{\text{dust}} = 10^{-2}$ and, finally, the dashed line is for $n_{\text{dust}} = 10^{-1}$. See the text for more details. 136
- 3.14 Evolution of molecular hydrogen for different amounts of initial dust. Top Panel: low metallicity cases. Bottom Panel: high metallicity cases. In both panels the meaning of the lines is the same as in Fig. 3.13. See the text for more details. 137

- 3.15 Dust density evolution for different initial amounts of dust. Top panel: low metallicity cases. Bottom panel: high metallicity cases. The meaning of the lines is the same as in Fig. 3.13. See the text for more details. 138
- 3.16 Temperature evolution for different amounts of dust. Shock disruption is enabled. Top panel: low metallicity cases. Bottom panel: high metallicity cases. The meaning of the lines is the same as in Fig. 3.13. See the text for more details. 139
- 3.17 Dust density evolution for different dimension bins. Shock disruption is enabled. Lines represent the distribution of dust among the bins for different ages (from top to bottom, 10 , 10^2 , 10^3 and 10^4 years). See the text for more details. 140
- 4.1 The architecture of MaNN. Circles indicate neurons, lines are connections (i.e. weights). Input units are labeled with the symbol \bar{x} , hidden neurons with \bar{h} if they belong to the first layer, and \bar{g} if they belong to the second one; finally, output units are indicated with \bar{y} . The matrix W_{xh} represents the weights between input and the first hidden units, W_{hg} are the connections between the first hidden units and the second hidden layer and W_{gy} connects the second layer of hidden units and the output. A single output is shown. In this Figure the forward propagation is from lower neurons to the upper ones. Back-propagation is from \bar{y} to \bar{x} neurons. Here $n_x = 4$, $n_h = n_g = 2$ and $n_y = 1$ 152
- 4.2 The architecture of a double hidden layer ANN. Circles indicate neurons, while lines represent the connections between the layers (i.e. weights). The input units are labeled with the symbol \bar{x} , the hidden neurons with \bar{h} if they belong to the first layer, and with \bar{g} if they belong to the second one; finally, the output units are indicated with \bar{y} . The matrix W_{xh} represents the weights between the output and the first hidden units, W_{hg} are the connections between the first hidden units and the second one and W_{gy} connects the second layer of hidden units and the output. Multiple outputs are shown. In this Figure the forward propagation is from the lower neurons to the upper ones. The back-propagation is from \bar{y} to \bar{x} neurons. Here $n_x = 4$, $n_h = n_g = 2$ and $n_y = 3$ 155

- 4.3 Comparison between normalized data from MaNN (cross) and ROBO (square), for molecular hydrogen density (left panel) and free electrons (right panel). We show only 50 randomly picked models. Similar results for the other outputs. 160
- 5.1 Sedov-Taylor OB-wind test with chemical evolution. Left to right, top to bottom: radial profiles of H^+ and H_2 mass fractions, ρ , and T , at $t = 0.5$ Myr. Plotted are all particles within the central 200 pc. 163
- 5.2 Sedov-taylor OB-wind test without chemical evolution. Left to right: radial profiles of ρ and T , at $t = 0.5$ Myr. Plotted are all particles within the central 200 pc. 163
- 5.3 Sedov-taylor OB-wind test. Pressure field in a central slice of side $l = 500$ pc, with (left) and without (right) chemical evolution. 165
- 5.4 The result of the RFST. Top: hydrogen mass fraction. Bottom: ionized hydrogen mass fraction. The radius is arbitrary. Each point represents a gas particle in the NB-TSPH code. 172
- 5.5 The result of the RFST. Top: molecular hydrogen mass fraction. Bottom: energy per unit of mass. The radius is arbitrary. Each point represents a gas particle in the NB-TSPH code. . . 173
- 5.6 The result of the RFST. Top: gas density in g/cm^3 . Bottom: gas temperature in K. The radius is arbitrary. Each point represents a gas particle in the NB-TSPH code. 174
- 6.1 Cooling function dependence on the total metallicity Z for a given ($T = 10^{5.5}$ K) temperature for distribution of abundances present on a cosmological self-consistent simulation with metal enrichment. The solid line represents the cooling according to [122]. 181
- 6.2 The map representing the Markovian matrix M (see text for details). The labels inside the circles are XY where X represents the temperature classification (H=hot, W=warm, C=cold) and Y the ionization status (H=high, M=intermediate, L=low), e.g. HM represents a hot gas with an intermediate degree of ionization. The labels near the arrows are the percent probability to move from one state to another following the direction of the arrow itself. e.g, WH \rightarrow CM has a probability of 75.5% to happen. The circular arrows represent a status that remain the same. Transition with probability of 0% are omitted. . . . 186

List of Tables

- 2.1 The characteristics of the different phases of the interstellar medium, where MC indicates molecular clouds, n_0 is the gas density, T is the typical temperature ϕ_v is the volume filling factor (fraction), which is uncertain and controversial, M is the total mass in $10^9 M_\odot$, $\langle n_0 \rangle$ is the average mid-plane density in cm^{-3} (note that for WIM $\langle n_0 \rangle$ is represented by a Gaussian, while WIM and HII are represented with an exponential), H is the Gaussian scale height and Σ is the surface density in the solar neighborhood in $M_\odot \text{pc}^{-2}$. Note that CNM is here intended as a diffuse cloud. More details within the text. . . . 31
- 2.2 The characteristics of the energy sources of the ISM. P is expressed as 10^{-12} dyne cm^{-2} , the energy density is in eV cm^{-3} and finally the heating rate is in $\text{erg s}^{-1} \text{H-atom}^{-1}$, and is represented as $a(b) = a \times 10^b$. Note that the heating rate for the thermal process is an energy loss. From [124]. 34
- 2.3 Luminosities of some sources in the Milky Way in (L_\odot). We adopt $a(b) = a \times 10^b$ as usual. From [124]. 35
- 2.4 Hugoniot data and vaporization threshold data. ρ_0 is the density of the material, c_0 is its sound speed, s is an adimensional parameter (details within the text), ϵ_v is the specific vaporization energy, P_t is the pressure threshold and v_t is the velocity threshold. Note that the specific vaporization energy is indicated in units of 10^{11} , and the pressure is in units of 10^{12} . Note that graphite and amorphous carbon have the same properties. From [125]. 67

3.1	Elemental species used in ROBO and their indexes. In the first row the species based only on hydrogen (from 1 to 5), in the second row the species on helium (from 6 to 8), in the third row metals and their ions (from 9 to 16), fourth row contains species based on deuterium (from 17 to 22), the fifth row contains the species that belongs exclusively to the CO network (23 to 27) and, finally, in the last row the electrons (the 28th specie).	82
3.2	The reaction rates among hydrogen, deuterium and helium. All the rates are in cm^3/s . The gas temperature T is in Kelvin; the electron temperature T_e is in eV. References: reactions 1 to 20 [60], reaction 21 [57]	83
3.3	Continuation of Table 3.2. The reaction rates among hydrogen, deuterium and helium. All the rates are in cm^3/s . The gas temperature T is in Kelvin; the electron temperature T_e is in eV. References: for reactions 22, 23, 24 and 27 see [60], for 25 and 26 see [57].	84
3.4	Continuation of Table 3.3. Reaction rates among hydrogen, deuterium and helium. All the rates are in cm^3/s . The gas temperature T is in Kelvin; the electron temperature T_e is in eV. References: 28 to 34, 36 and 37 [57], 34 and 35 [1]	85
3.5	Continued from 3.4. Reaction rates for processes where metals are involved and where cosmic ray (CR) interact with the ISM. All the reaction rates are in s^{-1} . The gas temperature T is in Kelvin; the electronic temperature T_e is in eV. The functions for recombination (Φ_{rec}) and collisions (Φ_{col}) are described in the text. The cosmic ray field is $\zeta_{\text{CR}} \text{ s}^{-1}$ and it is the rate of H_2 ionization by cosmic rays. References: 38, 40, 42 and 44 [128], 39, 41, 43 and 45 [129], 46 to 48 and 49 to 54 [59], 48 [140] and, finally, 55 to 57 [133].	86
3.6	Fit coefficients for the charge transfer reaction $\text{H}_2 + \text{H}^+ \rightarrow \text{H}_2^+ + \text{H}$ as described in the Eqn. (3.6). Coefficients are in the form $a(b) = a \times 10^b$. All the temperature ranges are shown. . .	89
3.7	Reaction rates for reactions belonging to the CO network. $T_{300} = T/300$, with T in K. References: 58 to 63 [138] and 64 [107]; For reactions 58 to 61 see text for details.	91

3.8 Cross sections of photochemical processes in cm^2 . The energy E is in eV. The various quantities in use are: $\xi = E/E_{th}$, $\Phi_{\text{ph}}(a_f, y_w, x_f, y_a, P) = [(x_f - 1)^2 + y_w^2]y^{0.5P-5.5}[1 + \sqrt{y/y_a}]^{-P}$, $y = \sqrt{x_f^2 + a_f^2}$, $x_f(a, b) = E/a - b$, and $x_{Si} = 1.672 \times 10^{-5}$. See Table 3.9 for notes and references. 94

3.9 Notes and references for the reactions listed in Table 3.8. (a) [59], (b) [128]. See these papers for further references. 95

3.10 Coefficients c_{ij} used in the Eqn. (3.23) and taken from [87]. 97

3.11 Heating processes. References: all from [59] except the photoelectric effect. See this papers for more references. 104

3.12 The value used to compute the formation efficiency of H_2 and HD. E_{phy} and E_{ch} are in K, a_{pc} is in \AA . From [25]. 108

3.13 Initial values for the number densities of the hydrogen and helium elemental species and the deuteroids. They are either fixed to a constant value or based upon the number density of one of the *free* hydrogen species n_{H} , n_{H_2} and n_{H^+} via the f_{D} factor. Since H^- and H_2^+ are constant, then also D^- and HD^+ are fixed. Values are indicated as $a(b) = a \times 10^b$. See also the text for details. 125

4.1 Results of the PCA analysis on the output data. 159

4.2 Initial values for the number densities of the hydrogen and helium elemental species and the deuteroids. They are either fixed to a constant value or based upon the numerical abundance of one of the *free* hydrogen species n_{H} , n_{H_2} and n_{H^+} via the f_{D} factor. Since H^- and H_2^+ are constant, then also D^- and HD^+ are fixed. Values are indicated as $a(b) = a \times 10^b$. See also the text for details. 159

6.1 The nine possible XY combination for a gas with two properties each one classified with three states. Temperature are hot (H), warm (W) and cold (C), while ionization are high (H), intermediate (M) and low (L). 183

A.1 The number of the atomic levels considered in our model for different species. 193

Chapter 1

Introductory outline

A Universe simple enough to be understood is too simple to produce a mind capable of understanding it.

John D. Barrow¹

Galaxy formation and evolution is a crucial topic in the present day astrophysics. The Λ CDM cosmological model (also known as *concordance* model) predicts that the heterogeneous Universe observed today formed out of an initially homogeneous distribution of matter². In this scenario, the galaxy formation process is a result of tiny quantum fluctuations produced by the Big Bang. The simplest model proposed to explain these features is the Λ CDM cosmology, which is in general agreement with the observed Universe.

The large-scale structures and the galaxies were formed as a consequence of the growth of these primordial fluctuations (small local inhomogeneities in the density field). In the Λ CDM model, the Universe matter content is $\sim 84\%$ Dark Matter and 16% baryonic matter (gas). The Dark Matter fluctuations grow in mass and ultimately detach from the expanding Universe, forming halos in which gas can condense and collapse, provided it can cool enough to make its pressure negligible with respect to the gravitational attraction.

When the first halos form, the Universe gas content is almost exclusively composed of hydrogen and helium, with traces of the other light elements [121, 9, 131]. The first proto-galaxies are believed to assemble at this stage, from the condensation of this primordial mixture into the first stars, and the first proto-galactic systems.

¹The World Within the World. Oxford: Oxford University Press, 1990. pp. 342-343. ISBN 0-19-286108-5.

²The homogeneity of the temperature of the early Universe is one of the most important results from the observation of the CMB [137, 139].

During the very first stages of the growth of the density perturbations, it is possible to use an analytical approach to follow the problem. This is the *linear* phase which is well described by the Zel'dovich approximation. However, after this period the evolution of the system become strongly non-linear and any analytical approach would be misleading.

The most widely adopted approach to cope with the non-linearity issue is the use of numerical N-body simulations. In Padova, a complete N-body code has been written over the years by many researchers [23, 86]. The last release is named EvOL [98]. The code is based on two concepts, the *tree-code* and the *smoothed particle hydrodynamics* (SPH). The tree-code describes the gravitational interactions with the aid of a data structure (namely the tree) that allows to handle the system efficiently. The SPH is a mesh-free Lagrangian method used for simulating hydrodynamics of fluid flows, and in this kind of code it is used to describe the gas. This methodology is called N-body/Tree SPH, and in this work we refer to this class of codes as NB--TSPH codes. With the aid of such a code, the infall of the baryonic matter into the potential well formed by the Dark Matter, can be described with accuracy even into the non-linear regime, and hence the baryonic matter (i.e. the gas) can begin to form the stars. Unfortunately the modeling of this last phenomenon is not so simple as it might seems.

The main problem resides in the fact that it is extremely complicated to model the physics and the chemistry of the gas. The primordial gas, and later (after the formation of the first stellar objects) the so-called *interstellar medium* (ISM), plays a key role in the evolution of the galaxies. Unfortunately, a large number of chemical and mechanical processes take place in the ISM, and many of them are both complex to model and partially unknown, despite their complete understanding would be necessary to correctly describe the evolution of the galaxies (and in particular their star formation history).

The complexity of the phenomena makes this study a formidable challenge. First, we need to know which processes are the most important ones and which we may neglect for our current purposes. Moreover, it is to understand how these processes could be modeled, and to do this we also need accurate data (for example, the rate coefficients of any chemical reaction). Then, we must describe our models with sophisticated algorithms: at the same time, they should be clever enough to save as much computational loadwork as possible, since the evolution of the ISM is only a part into the already CPU-demanding NB-TSPH framework. However they need a good level of accuracy to produce reasonable models.

The present day chemical/physical codes are quite accurate but any code must balance the accuracy of the processes described and the computational

weight of its algorithms. The developers of the numerical models try to find the trade-off between accuracy and speed, which is a well-known problem among those who study complex aspects of Nature through simulations³.

To summarize, the main object of the present study is the ISM, its processes and its modeling. In particular, we will describe what kind of trade-off we have chosen, proposing a model (and a code) to describe the ISM and developing a new tool to overcome the accuracy/speed dichotomy.

The next Chapter introduces the ISM in a general way, first with a qualitative description of the phenomena, then with an analysis of the chemistry, the cooling and heating processes, and finally the dust content.

The Chapter 3 describes in details our approach to the ISM, introducing our ISM model and its companion code, called ROBO. Here, for each topic of the previous Chapter (i.e. chemistry, cooling, heating and dusts) a detailed description will be presented.

Since the numerical simulations of formation and evolution of the galaxies in the Universe are the framework of the present work in the Chapter 4 we suggest how to embed a complex code like ROBO in a NB-TSPH model, introducing the Artificial Neural Networks (ANN).

The following Chapter is dedicated to some tests of the the NB-TSPH model together with the ANN. We also give a brief description of the evolutionary code (EVOL).

In the last part we show some new ideas for future developments and some ideas for successive projects.

³It is also worth pointing out that present-day machines are about to reach the energy consumption limit, and building larger CPU/GPU cluster is not suitable. This is a further challenge to develop efficient algorithms and to study some new and better ways to model the physics of the astrophysical simulations.

Chapter 2

The Interstellar Medium

It seems to be a natural consequence of our points of view to assume that the whole of space is filled with electrons and flying electric ions of all kinds. [...] It does not seem unreasonable therefore to think that the greater part of the material masses in the universe is found, not in the solar systems or nebulae, but in "empty" space.

Kristian Birkeland¹

The Interstellar Skie.. hath .. so much Affinity with the Starre, that there is a Rotation of that, as well as of the Starre.

Francis Bacon²

2.1 ISM: Introduction

In the solar neighborhood, the Sun and its planetary system only fill 3×10^{-10} of the total space available. All of the remaining space to the next stars is filled with the so called *interstellar medium* or shortly ISM. In general, this

¹The Norwegian Aurora Polaris Expedition, H. Aschehoug & Co., 1902-1903.

²*Sylva sylvarum*, or, a natural history in ten centuries: whereunto is newly added the History naturall and experimentall of life and death, 1626. section 354-345.

is a tenuous gas of hydrogen and helium with a small amount of heavier atoms. These elements can be both neutral or ionized and can also be found in molecules, like H_2 and CO . These components may belong to a gas phase or to a solid phase. The gas forms some peculiar objects as the HII regions, the reflection nebulae, the dark clouds and the supernova remnants; it can be divided into different thermal phases, such as cold molecular clouds, cool HI clouds, warm intercloud gas and hot coronal gas. It also exchanges energy with the external environment through heating and cooling; the heating is due to photons, cosmic rays and X-rays, whereas the cooling depends on the physical conditions of the different regions. This last process produces the emission spectra that is a great source of information to determine the physical characteristics of the observed region.

As explained before, the ISM plays a central role in the history of a galactic system. The gas is in constant evolution, since new atoms are injected in the ISM from stars both through SN explosions and stellar winds. The stars which form from the enriched gas change their characteristics as the gas changes its physical parameters. This tight connection between stars and gas heavily determines the evolution of a galaxy.

Before starting to describe in detail the physics, we will briefly recall the observed interstellar objects, the components of the ISM, its energy sources, and some characteristics of the Milky Way.

2.1.1 Interstellar objects

We start our short overview from the *HII regions*, which are clumps of ionized gas formed by young massive stars with $T_{\text{eff}} > 25\,000$ K which emit a great number of photons beyond the Lyman limit ($h\nu > 13.6$ eV); these highly energetic photons ionize the surrounding gas. Hence the presence of this ionized gas usually indicates a massive ongoing star formation. These nebulae are bright and clearly visible in the Milky Way like luminous and cloudy objects. Well known examples are the Great Nebula in Orion (M42) and the Lagoon Nebula (M8), and fainter examples are the California Nebula and IC 434. These different objects show how HII regions can have different brightness.

The gas that form these region is ionized by the embedded stars and has a temperature of $\sim 10^4$ K. Densities range from $10^3 - 10^4 \text{ cm}^{-3}$ for compact HII regions, with a diameter of approximately 0.5 pc, to 10 cm^{-3} for more diffused and extended nebulae, that are about 20 times larger. Two examples are the Orion Nebula (compact), and the North America Nebula (diffuse).

The optical spectra of these objects are dominated by hydrogen and helium recombination lines and optical forbidden line emission from ions like

[OII], [OIII] and [NII]. Another clear component is the free-free thermal radio emission from the ionized gas, and IR due to warm dust that re-emits the UV radiation from the young stars located there.

Another class of objects are the *reflection nebulae*. These nebulae reflect the light from nearby bright stars; NGC 2024 in Orion, and the Pleiads (which appears like a group of stars surrounded by a faint nebulosity) are typical examples. In both cases the observed light is reflected starlight, hence it is not due to hot gas like in the HII regions.

Another difference from the previous class of objects is that radio emissions are absent, and the IR emission is fainter. Their density is about 10^3 cm^{-3} for compact objects and the stars that are nearby these objects have spectral types later than B1. Even the regions around hot stars present reflected starlight, but their emission is fully dominated by the component from the ionized gas, making the reflected component less evident.

To conclude, there are three hypotheses for the origin of such objects: (i) the nebula is a remnant of the materials where the stars were formed, like NGC 2023 and NGC 7023; (ii) the nebulae is a chance encounter between the stars and the gas as for the Pleiads; (iii) the ejecta of late-type stars form the reflection nebula, like IC 2220 or the Red Rectangle.

Dark nebulae are regions in which few stars are observed. Looking at the center of the Milky Way the presence of such objects is manifest. Two examples of dark cloud are the roundish Coalsack near the Southern Cross and the Horse Head Nebula, that is visible because is back-lighted by IC 434 (a HII region in the background of the dark cloud). The size of these regions ranges from tens-of-parsecs to 10^{-2} pc for tiny objects. Dark clouds are not completely dark, as the name suggests, but, even if they don't host stars, they show some faint reflected light. Also, they are bright at mid-IR and far-IR wavelengths. However, some dense clouds are opaque even at mid-IR wavelengths and are dark in absorption against background galactic mid-IR emission. These objects are called infrared dark clouds (IRDC).

If we only consider the visible light, the Galaxy is dominated by HII regions and reflected nebulae, but in the infrared wavelengths the sky is dominated by the *photo-dissociation regions* or, shortly, PDR.

These objects are atomic-molecular zones that separate ionized and molecular gas near bright O-B stars. Some examples are the Orion bar and NGC 2023. In these regions the far-ultraviolet radiation penetrates into the gas; this is the reason why these regions are also known as *photo-dominated regions* (with the same acronym PDR). The photons dissociate and ionize the molec-

ular species and, even if most of the photons are absorbed by dusts, a small fraction of the gas reaches few hundreds of degrees through the photoelectric effect. These processes make the PDRs bright in the IR dust continuum and in the part of the spectra due to atomic fine-structure cooling lines. Molecular lines are also present, since in these regions the cooling through molecular processes is non negligible. In general, any region reached by a FUV field can be considered a PDR. Therefore, these are regions where the chemistry and the physics of the gas is largely determined by the action of the FUV photons.

The last objects in this short list are the *supernova remnants*, formed by the material ejected by a SN explosion. The SNR's spectrum is that of a high velocity shock; the emission is dominated by radio radiation due to relativistic electrons spiraling around magnetic field, a process called *synchrotron emission*. These objects are also bright in the X-rays wavelengths since they are composed by hot gas, with temperature of about one million of Kelvins. Famous examples are the SN1987A in the Large Magellanic Cloud, and SN1054 (better known as Crab Nebula) that was the first astronomical object identified with a historical supernova explosion.

2.1.2 ISM components

In the previous Section we have described some classes of objects to show how the ISM is observed in the Milky Way or in nearby galaxies. In this Section we present the different material components of the ISM, to briefly describe the range of the physical properties of the interstellar gas. The properties of the different phases are listed in Table 2.1, see the caption for the details.

A first component is the *neutral atomic gas* that is traced by the 21 cm line, and also can be observed in optical and UV through absorption lines of various element toward bright background stars. The neutral atomic gas can be divided into two sub-classes, the cold diffuse HI gas, also called cold neutral medium (CNM), and the warm intercloud gas, analogously called warm neutral medium (WNM). The first has a temperature of about 100 K, while the second reach approximately 8000 K. A standard HI cloud (Spitzer-type cloud) has a typical density of 50 cm^{-3} and a size of 10 pc. The density of the WNM is much less namely 0.5 cm^{-3} . In our Galaxy, 80% of the gas between 4 kpc and 8 kpc from the galactic center is in the cold neutral medium, distributed in a layer with a Gaussian scale height of about 100 pc. At higher latitudes, a large fraction of the neutral hydrogen is in the WNM component, with a larger scale height of 220 pc. In average, these two phases of the ISM have quite similar surface density. Locally we observe that the total WNM

column density toward the North Galactic Pole is about 2.5 times that of the CNM; this is because our Sun is located into a local bubble. In the outer part of the Galaxy this component rapidly increase its scale height.

When some energy source is present, the gas can become *ionized*. It is detected through dispersion of pulsar signals, optical and UV absorption line when a background source is present, or it can be traced through emission in the H α recombination lines. Most of the H α observed in our Galaxy is due to distinct HII regions, but almost all of the mass of the ionized gas resides in a diffuse component. The physical characteristics of this warm ionized medium (WIM) are the low density, about 0.1 cm^{-3} , and the quite high temperature of approximately 8000 K. Its volume filling factor is 0.25, while its scale height is around 1 kpc. Since the OI line at 6300 \AA is generally very weak, we argue that the gas is nearly fully ionized, but its source of ionization is not entirely clear. The most suitable candidate are the photons coming from bright young stars that escape from the associated HII regions and travel for hundreds of parsecs to ionize the WIM. The problem with this scenario is that these photons must travel without being absorbed by the neutral hydrogen.

A fundamental component of the ISM is the *molecular gas*. It is detected through the CO $J = 1 \rightarrow 0$ transition at 2.6 mm, a feature that is commonly used to trace the quantity of molecular gas into a galaxy. Most of the molecular gas of the Milky Way is located into giant molecular clouds with a typical size of 40 pc, a mass of $4 \times 10^5 M_{\odot}$, high densities (about 200 cm^{-3}) and temperatures of 10 K, but is worth to notice that these clouds can span over a large range of physical parameters. Molecular clouds are characterized by high turbulent pressures as indicated by the large linewidths of the emission lines. These clouds are also self-gravitating objects rather than being in pressure equilibrium with the other components of the ISM. Such objects are stable over time scales of about 3×10^7 years, and are site of massive star formation. While CO is the most evident feature of the molecular clouds, H $_2$ is thought to be the dominant molecular species, with a H $_2$ /CO ratio of 10^3 to 10^4 . In addition to this more than 200 molecules have been detected through their rotational emission lines. These species are generally simple, unsaturated, radicals or ions. The most observed molecules are the acetylenic carbon chains, but their high abundance could be originated from an observational bias, since this species possess large dipole moments and a relatively small partition function. These two characteristics make these molecules easily detectable at microwave lengths.

Recently the HERACLES survey containing an atlas of 18 nearby galaxies

has found a very good correlation between CO and HI kinematics, and the CO emission is compatible with optically thick clouds with $T = 10$ K [82]. In M82 the spectral line energy distribution reveals gas at high temperature $T = 500$ K, where the main coolant is the molecular hydrogen. In these regions the peak of the emission of the CO is in the level $J = 7$, that suggests the presence of an AGN and a strong X-ray heating [106]. It is also interesting to notice that galaxy formation models requires strong feedback to limit the star formation. In particular, these feedback could be molecular outflows as M82 suggests. Recently, this molecular flows have been observed in the nearby of the quasar Mrk 231, driven by the AGN activity [48]. The velocity found suggests that the gas around the nucleus will be depleted in few tens of Myr.

At high redshifts the CO is also detected and there is a good correlation between FIR and CO fluxes. It is interesting to note that many of the objects detected with CO at high redshifts are AGNs, suggesting a tight correlation between these phenomena. For a review on molecular gas at high redshift see [28].

The *hot coronal gas* can be traced through UV absorption lines of highly ionized species like CIV, SVI, NV and OVI, when a bright background sources is present. This gas also emits through such processes as bremsstrahlung and radiative recombination for the continuum, but also from collisional excitations and recombination for the emission lines at extreme UV and X-ray wavelengths. This hot intercloud medium (HIM) is tenuous (about 10^{-3} cm $^{-3}$) and has a temperature of 10^5 to 10^6 K. This gas is heated and ionized through shocks driven by stellar winds from early type stars and by supernova explosions. The HIM fills most of the volume of the halo, and in the disk its distribution is quite irregular. Our Sun is located into an hot bubble of about 100 pc.

The ISM is not composed only by gas, but also *dusts* are present. This component re-processes starlight into IR wavelengths, and causes the reddening and the extinction of distant sources - the ISM is indeed bright at IR wavelengths because of the continuum emission of the cold dust grains. It also polarizes the light since the magnetic fields align the elongated grains causing a phenomenon called *dichroic absorption*.

Dusts are also connected to reflection nebulae, because the light scattered by the dusts produces this class of objects. A detailed analysis shows that many of the refractory elements, like C, Si, Mg, Fe, Al, Ti and Ca, are locked up in dust. Dusts are in radiative equilibrium when we consider large grains, with sizes > 100 Å and temperatures of about 15 K, but when they are close to some bright stars they can reach higher temperatures, like some 75 K for

Table 2.1: The characteristics of the different phases of the interstellar medium, where MC indicates molecular clouds, n_0 is the gas density, T is the typical temperature ϕ_v is the volume filling factor (fraction), which is uncertain and controversial, M is the total mass in $10^9 M_\odot$, $\langle n_0 \rangle$ is the average mid-plane density in cm^{-3} (note that for WIM $\langle n_0 \rangle$ is represented by a Gaussian, while WIM and HII are represented with an exponential), H is the Gaussian scale height and Σ is the surface density in the solar neighborhood in $M_\odot \text{pc}^{-2}$. Note that CNM is here intended as a diffuse cloud. More details within the text.

Phase	n_0 (cm^{-3})	T (K)	ϕ_v	M	$\langle n_0 \rangle$	H (pc)	Σ
HIM	0.0003	10^6	0.5	-	0.0015	3000	0.3
WNM	0.5	8000	0.3	2.8	0.1	220	1.5
WIM	0.1	10^6	0.25	1.0	0.0025	900	1.1
CNM	50.0	80	0.01	2.2	0.4	94	2.3
MC	> 200.0	10	0.0005	1.3	0.12	75	1.0
HII	$1 - 10^5$	10^4	-	0.05	0.015	70	0.05

a typical HII region. If the grains are smaller than 100 \AA their temperature fluctuates, since they absorb single UV photons and re-emit them at mid-IR wavelengths.

2.1.3 Energy sources

There are many sources of energy of the ISM and their presence and efficiency is largely dependent on the region we are considering. These sources have similar energy density but, which is more important, different heating rates. This quantity depends on the ISM process coupled with the energy sources, hence it is of prime importance to describe the physics of these phenomena to deeply understand the characteristics of the ISM and its evolution. Before analyzing the ISM through a detailed description, we continue reviewing the features of the ISM. This Section is dedicated to some of the energy sources and their main characteristics.

A first source of energy is the *radiation field*. The ISM is permeated by photons at many different wavelengths. The spectrum can be divided into several frequency ranges depending on the involved processes. The hot gas with many emission lines is responsible for the shorter wavelengths. OB stars

emit photons with longer wavelengths and dominate the far-UV. The visible region of the spectrum is dominated by A-type stars and late type stars at far-IR and near-IR wavelengths. PAHs and dusts affect the far-IR, since they absorb the light at higher frequencies and emits at longer wavelengths. Finally, beyond the millimeters wavelengths we find the CMB emission at 2.7 K. This complex radiation field is has the highest heating rate with respect to the other sources of heating.

Another source of energy and pressure is the *magnetic field*, which can heavily influence the dynamics of the gas. As already mentioned, the magnetic field is traced by the polarization of the light scattered by dusts aligned with the field. In the solar neighborhood the strength of the field is about $5 \mu\text{G}$ and increases to $8 \mu\text{G}$ in the molecular ring at 4 kpc. Considering the synchrotron emission, as a proxy for the magnetic field lines of force, we find a thin-disk component associated with the gaseous disk, and a thick-disk component associated with the halo. The magnetic field has a uniform and a non-uniform component. The first is roughly circular with a strength of about $1.5 \mu\text{G}$ in the solar neighborhood. The non-uniform component is associated with expanding superbubbles and their shocks. The strength of the magnetic field depends on the density of the bubble as $B \propto n^\alpha$ with $\alpha \approx 0.5$ and typically $B \approx 30 \mu\text{G}$ at $n \approx 10^4 \text{ cm}^{-3}$. This means that denser bubbles have stronger magnetic fields.

However, we point out that in this work we do not consider magnetic fields, and the description in this Section is only added for completeness. The reason is twofold. First, a detailed theory of cosmological magnetic fields is still lacking, and since we are interested in the formation of galaxies, the inclusion of a magnetic field would be essentially arbitrary. Second, the NB-TSPH code EVOL does not include magnetic fields. An accurate description of this problem would require the introduction of some dynamics into the chemical code. This remark will become clearer in the Chapter 3, which is dedicated to the detailed description of the chemical code ROBO.

Cosmic rays (CR) are a third energy source in the ISM; they can be subdivided into high energy cosmic rays ($\geq 100 \text{ MeV}$) and low energy cosmic rays ($\approx 100 \text{ MeV}$). High energy CR greatly contribute to the energy density of the ISM. They are mainly composed of relativistic protons, helium nuclei, heavier elements and electrons. The relative abundance of the elements in the cosmic rays is non-solar, suggesting that they are formed from stellar material (e.g. SNe) or in sputtered grains. When a high energy proton interacts with the ISM, a gamma ray is emitted through the π^0 meson decay emission (if the energy of the proton is $1 - 10 \text{ GeV}$, the gamma ray has $E_\gamma \geq 50 \text{ MeV}$),

while high energy electrons interacting with the ISM produce gamma rays through bremsstrahlung and inverse Compton scattering. Thus, it is easy to understand why gamma rays are used to retrieve the presence of CR. There is also a tight connection between magnetic fields and cosmic rays, since CR in the MW are generally confined to a disk of radius 12 kpc with a thickness of 2 kpc. The origin of the high energy CR is believed to be the explosions of SN, which give energy to CR with an efficiency of $\sim 10\%$ of the kinetic energy of the ejecta. The pressure exerted by CR also provides support against gravity for the gas in ISM.

Low energy CR are important in the ISM energy balance since they heat the ISM. Unfortunately, it is difficult to obtain an accurate measure of their flux, since it is strongly modulated by the solar wind. It is difficult to directly measure the interstellar cosmic ray rate flux, but observations of simple molecules like OH can help, because their formation is catalyzed by the presence of the cosmic rays. These considerations, together with the observations, give a primary cosmic ray ionization rate of $\zeta_{\text{CR}} \approx 2 \times 10^{-16}$ (see Section 2.4.1 for more details).

Finally, another source of energy in the ISM is its *kinetic energy*, which derives from the action of winds from early-type stars and from supernovae explosions. Compared to the other sources, it contributes a small amount of energy, but if we consider the solar neighborhood, the turbulent energy of the HI (about 6×10^{51} erg/kpc $^{-2}$) provides support for the gas against the gravity. Observing our Galaxy is also possible to notice an ordered vertical flow of HI and infalls at higher latitudes. Note that even if the amount of heating is small, the expanding shells around OB the stars have an important influence on the morphology of the ISM, sweeping and compressing the surrounding ISM. These gas motions are often unstable to Rayleigh-Taylor and Kelvin-Helmholtz instabilities generating turbulence, which in turns can support dense atomic and molecular clouds against self-gravity.

All the properties presented in this Section are summarized in Table 2.2.

2.1.4 The ISM and the Milky Way

Comparing the different characteristics of the Galaxy with those of the other galaxies, the Milky Way appears to be an average spiral system and, in the Hubble classification, it could fall between the SBb-type and the SBc-type. This classification also shows that our Galaxy has a bar. The luminosities of the sources used as tracers of the ISM phases of the Milky Way are listed in

Table 2.2: The characteristics of the energy sources of the ISM. P is expressed as 10^{-12} dyne cm^{-2} , the energy density is in eV cm^{-3} and finally the heating rate is in $\text{erg s}^{-1} \text{H-atom}^{-1}$, and is represented as $a(b) = a \times 10^b$. Note that the heating rate for the thermal process is an energy loss. From [124].

Source	P	Energy density	Heating rate
Thermal	0.5	6.0	$-5(-26)$
UV	-	0.5	$5(-26)$
Cosmic ray	1.0	2.0	$3(-27)$
Magnetic fields	1.0	0.6	$2(-26)$
Turbulence	0.8	1.5	$1(-26)$
2.7 K background	-	0.25	—

Table 2.3.

The distribution of the atomic gas is rather flat out to 18 kpc, while the molecular gas has a peak at about 4.5 kpc (the so called *molecular ring*). When considering the rim where the Sun is located, the surface density of the molecular gas is somewhat larger than that of the atomic gas, but the outer regions of the galaxy are dominated by the latter component. The total mass of the HI is about 5 times the mass of H_2 .

An interesting feature of the Galaxy is the thinness of the disk, since the height scale is small compared to the radial scale length. The molecular gas has a thickness of ≈ 75 pc compared with a radial scale of 4 kpc. In the inner Milky Way the height scale is two or three times larger, while in the outer regions the neutral gas reaches a thickness of about 1 kpc.

It is difficult to study the structure of the Milky Way using the atomic gas since there are non-circular velocity components, but fortunately molecules are better tracers, also because they are limited to the arms of the spiral. Both tracers show long structures and the Sagittarius-Carina arm is evident. Nevertheless, the real structure of the Galaxy is still debated (e.g., it is still unclear whether it is composed of two or four spiral arms).

The overall distribution of the ISM can be easily studied in the other galaxies, e.g. M31, which is similar to the Milky Way and quite close to us. In this system, the bright HII regions, the atomic and the molecular gas, and the dust, are all located mostly in spiral arms. The interarm regions are more obscured, and the HI is present throughout the disk as well.

NGC 891, an Sb-type edge-on galaxy very similar to the MW, also shows an HI component that is more extended than that of our Galaxy.

Table 2.3: Luminosities of some sources in the Milky Way in (L_{\odot}). We adopt $a(b) = a \times 10^b$ as usual. From [124].

Source	Luminosity
<i>Stars</i>	
All stars	4.0(10)
OBA	8.0(9)
<i>Gas and dust</i>	
CII 158 μm	5.0(7)
FIR	1.7(10)
Radio	1.5(8)
γ -rays	3.0(5)
<i>Mechanical luminosities</i>	
SN	2.0(8)
WR	2.0(7)
OBA	1.0(7)
AGB	1.0(4)

2.1.5 The ISM and the stars

The visible part of galaxies is composed of stars and gas, and to understand how galaxies form and evolve we must understand how the ISM and the stars interact with one another. Stars of any mass pollute the ISM during their lives with gas, dust and metals. If we exclude the small amount of heavy elements produced by the Big Bang nucleosynthesis we can assert that the stars are the main drivers of the chemical enrichment of the ISM. The gas mass return rate is dominated by low-mass red giants, since in our Galaxy the low-mass stars dominate the total stellar mass. However, the stars that are more efficient in producing heavy elements are the massive ones, that eject O and Si. Furthermore, AGB stars produce carbon through the triple- α process, as well as the s process elements (slow neutron capture). Finally, Type-I supernovae (which have low-mass progenitors) inject a large quantity of Fe into the ISM. Type-I SN are also the main producers of dust grains. However, within the local interstellar gas ($8 \times 10^6 M_{\odot} \text{ kpc}^{-2}$) the amount of dust produced corresponds to a dust-to-gas ratio of $\approx 1.5\%$, that is larger than the real measured dust-to-gas ratio; this means that also Type-II super-

novae inject heavy elements into the interstellar gas. The time scale needed to form stars from the molecular gas is $\sim 2 \times 10^8$ years, while the time scale to exchange material between different phases is quite small being 3×10^7 years. These time scales are shorter than the lifetime of the Galaxy, about 1.2×10^{10} years. It means that such phenomena are very important when we consider the evolution of the Milky Way.

Another source of gas in the Galaxy is the surrounding environment, that come both from primordial material (but the value of this accretion is still controversial), and also from satellite galaxies (e.g., the Magellanic Stream from the Magellanic Cloud, which has an accretion rate of about $150 M_{\odot} \text{ kpc}^{-2} \text{ Myr}^{-1}$).

The scenario depicted over this Chapter shows that the ISM plays a key role in the evolution of the Galaxy, and all the aforementioned cyclic processes largely determine its star formation history. Winds from low-mass stars control the total mass balance of the ISM contributing to the injection of dust and PAH. High-mass stars dominate the mechanical energy injection through stellar winds and SNe explosions, giving also the turbulent pressure to support clouds against the gravity. Massive stars control the amount of FUV and the cosmic rays injection, and also the formation of the hot coronal gas phase. Finally, massive stars forms the elements needed to create the dust and this dust with its opacity permits to the molecules to survive. The cooling of the molecules is in turn fundamental to the star formation process.

To summarize, it is clear that there is a tight connection between the ISM and the stars, because these ingredients have a reciprocal influence through a large number of phenomena. The properties of the ISM are determined almost completely by the nearby stars and by the the star formation history. In particular, high-mass stars represent the influence of the present star formation activity, while the low-mass stars represent the past star formation activity. On the other side the star formation rate, the IMF, and all of the stellar populations properties are deeply influenced by the properties of ISM in which they are formed.

This makes the study of the ISM a formidable challenge. However, given its importance, this is a necessary task. If the model describes one or more phenomena in an incomplete or wrong way, or fails to reproduce some fundamental aspect of the complex network of interactions, the resulting description of the galaxy evolution will be - at best - inaccurate. Unfortunately, obtaining a detailed analysis of the ISM is extremely difficult: first, the range of parameters spans many orders of magnitude (e.g. the temperature of the gas ranges from few to tens of millions of Kelvins); second, the involved physical phenomena are complex and often poorly understood; finally, mod-

eling such phenomena needs sophisticated algorithms that are generally CPU-demanding. The aim of the next Sections is to give a better description of the mentioned topics in these introductory lines: we start with the chemical network, passing then to the energy processes, i.e. the cooling and the heating, and finally to the dusts.

2.2 ISM: Chemistry

One of the most important topics of research in the study of the ISM is the chemistry, describing the complex evolution and interaction of the ionized, neutral, atomic or molecular species populating the ISM. In this work we use the word *species* both for atoms and molecules (including their ions). Therefore, within the context of this work, we will usually refer to the term *chemistry* as the group of the processes that deal with the reactions between different species and leads to the transformation of a set of chemical species to a new one. The reactions and the species form the *chemical network*, that can be represented as a graph, which is an abstract representation of a set of objects (the species) where some pairs of the objects are connected by links (the reactions).

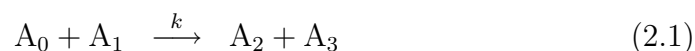
The description of the chemistry is generally complex because there are many species involved in a large number of reactions [138], and also because such reactions are fast compared to the time-scale in which the ISM evolves [59, 27, 1].

It follows that the reaction network becomes hard to describe when many reactions are involved. A first chemistry model could be made only with hydrogen-based atoms (H, H⁺) and Helium (He, He⁺, He⁺⁺), taking into account all their neutral and ionized atomic species as in [27], or more complicated, including metals, their ions and molecules like H₂, CO, CH_x and many others (see [132] for a review). If our model is going to include more and more species as desirable, consequently the network will have to deal with a rapidly growing number of reactions.

But why including many reactions complicates the scenario? To answer to this question we must discuss how a chemical network is (mathematically speaking) represented.

2.2.1 The chemical network

A single reaction can be summarized as:



where A_i is the number density of the generic atom or molecule in suitable units. It means that two species (namely the reactants) A_0 and A_1 react to form one or more species, in the example above A_2 and A_3 (the products). The efficiency of the reaction is described by a parameter k called the *rate coefficient* that determines the quantity of products formed. It is defined as the inverse of a number density and of a unit of time. The parameter k is therefore the probability that the reaction (2.1) occurs. The Equation (2.1) implies the mass conservation, but not the number density conservation. In other words, if the mass of the i -th species A_i is m_i , the sum of the masses $\sum_i m_i A_i$ of the products must be equal to the analogue sum done on the masses of the reactants. In this example $A_0 m_0 + A_1 m_1 = A_2 m_2 + A_3 m_3$. This is not necessarily verified with the analogue for the number density $\sum_i A_i$.

A practical example of this issue is the reaction $\text{H} + \text{e}^- \rightarrow \text{H}^+ + \text{e}^- + \text{e}^-$. Here the mass of the reactants and the mass of the products are equal, and they are

$$\underbrace{\text{H}}_{m_e + m_p} + \underbrace{\text{e}^-}_{m_e} = \underbrace{\text{H}^+}_{m_p} + \underbrace{\text{e}^-}_{m_e} + \underbrace{\text{e}^-}_{m_e},$$

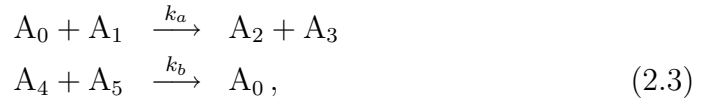
where m_e and m_p are the masses of the electron and the proton. In this example the mass is conserved (and the charge too), but not the total number density that is $3/2$ greater for the products.

For the aforementioned example, the Equation (2.1) brings four differential equations, one for each of the species involved, namely

$$\frac{dA_i}{dt} = \pm k A_0 A_1, \quad (2.2)$$

with $i \in [0, 3]$ and the LHS term is expressed in units of a number density over units of time. The RHS term has the sign plus if the i -th species is a product, or minus if the i -th species is a reactant. This is because the reactants are destroyed during the reactions (minus sign), and the products are formed (plus sign).

The simple model shown here can be easily extended to a complex network composed of multiple reactions. In that case each reaction will have a parameter k_j , and the expression (2.2) will be a sum over all the reactions that involve the i -th species. An example with two reactions will clear what we just stated. If we extend the previous model we analogously have



where k_a and k_b are the rate coefficients of the two reactions. To analyze how the species A_0 changes after an infinitesimal time interval dt we write the

differential equation as

$$\begin{aligned} dn_0(t + dt) = & - k_a n_0(t) n_1(t) dt \\ & + k_b n_4(t) n_5(t) dt, \end{aligned} \quad (2.4)$$

with n_i the number density of the species A_i . In this Equation the positive term is due to the second reaction (between A_4 and A_5) that increases the total quantity of A_0 , while the negative term is due to the first reaction in which A_0 is destroyed because it reacts with A_1 to form A_2 and A_3 . The system of ordinary differential equations describing the network (2.3) is made by six equations, one for each species involved.

This approach can be generalized to a system of differential equations in which each equation is a Cauchy problem (a differential equation with initial conditions) of the form

$$\frac{dn_i(t)}{dt} = \sum_{lm} k_{lm} n_l(t) n_m(t) - \sum_j k_{ij} n_i(t) n_j(t), \quad (2.5)$$

where $n_i(t)$ is the number density of the i -th species with known initial value $n_i(0)$. In Eqn. (2.5) k_{lm} is the rate of the reaction between the l -th and the m -th species expressed in units of number density per unit of time. Eqn. (2.5) is written as the sum of all the reactions forming the i -th species ($\sum_{lm} k_{lm} n_l(t) n_m(t)$) minus the sum of all the reactions destroying the i -th species ($\sum_j k_{ij} n_i(t) n_j(t)$). The indexes i, j, l , and m run over all the elemental species.

The system of Equations (2.5) and the set of initial parameters $n_i(0)$ represent the whole problem.

Another aspect that must be underlined is that the rate coefficients are usually environment-dependent. A very common case is when a rate coefficient depends on the temperature, as in the collisional ionization shown above ($H + e^- \rightarrow H^+ + 2e^-$) where k is actually a function of the temperature $k(T)$. Since the chemistry is strictly connected to the cooling and heating processes, it means that a dn_i/dt implies a dT/dt that influences the chemistry via $k(T)$. This last remark will be more clear in the Section dedicated to the cooling processes.

2.2.2 Photoionization

The rate coefficients depend also on the quantity of radiation that reaches the gas volume where the model is settled. This is the case of reactions like $A + \gamma \rightarrow A^+ + e^-$ where γ is a photon of energy $h\nu$. We define Γ_{ph} as the rate

coefficient for the photoionization reactions. This coefficient is quite different from the already mentioned k , being involved in the differential equation

$$\frac{dA_i}{dt} = \pm \Gamma_{\text{ph}} A_j, \quad (2.6)$$

with the usual meaning of the symbols as in similar equations. In this case we are considering a reaction that involves the i -th and the j -th species in the form $A_j + \gamma \rightarrow A_i^+ + e^-$.

Since in the LHS there is the variation of the number density over time, the rate coefficient Γ_{ph} will be expressed as the inverse of the time (e.g. s^{-1}). Although the standard rate coefficient k discussed above changes with the environment, because it is controlled by the temperature, this is not the default situation for the photoionization coefficient. The dependence on the environment of Γ_{ph} is eventually included into a varying radiation field impinging on the ISM, thus changing during time the energy flux able to ionize our species. If the ionizing flux is constant than our photo-ionization rate coefficient will not vary. Let us now discuss this coefficient in detail. In general, the reaction rate is given by

$$\Gamma_{\text{ph}} = 4\pi \int_{E_{\text{th}}}^{\infty} \frac{\sigma(E)J(E)}{E} e^{-\tau(E)} dE, \quad (2.7)$$

where $J(E) = J(h\nu)$ is the energy flux per unit of frequency and solid angle of the impinging radiation field, $\sigma(E)$ is the cross-section of the considered reaction, which has the unit of an area, $\tau(E)$ is the gas optical depth at the energy E and $f(E)$ is a numerical factor accounting for the effects of the secondary ionization, that are negligible if the UV radiation is not dominated by X-rays [59]. From the dimensional analysis we see that the rate is in $[\text{s}^{-1}]$. Once included into a numerical code the integral in Eqn. (2.7) must be calculated at each time-step if the radiation field changes with time, or once for all if the radiation field remains constant.

There are different ways to describe the impinging UV flux, depending on the region considered. A widely used method for the far-ultraviolet (FUV) flux (which is the part of the radiation spectrum that mainly influences the photoionization process) is to consider the ratio between the flux involved and a standard radiation field named Habing's radiation field. This latter is simply $1.2 \times 10^{-4} \text{ erg/cm}^2/\text{s}/\text{sr}$. The average interstellar radiation field is 1.7 times the Habing field. This is a simple representation of the interstellar radiation field that is composed of different processes, namely the infrared and the sub-millimetric emission from dust, the millimetric one from CMB, the UV and the FUV from OB stars, the extreme-ultraviolet (EUV) with

numerous emission lines from hot gas and, finally, the extragalactic contribution at the hardest energies. This means that the radiation flux needs a more detailed model. To cope with this issue, we can use a polynomial fit in the form $N_{\text{ISRF}}(\lambda) = \sum_i c_i \lambda^{-i}$ in units of surface, time, frequency and solid angle with λ the wavelength and c_i the fit coefficients - see for more details [124].

If the model is included in some cosmological framework the flux could be for example redshift dependent: indeed [42, 127, 103] have proposed a flux that is redshift dependent. It is described by

$$J(\nu) = 10^{-21} J_{21}(z) \left(\frac{\nu_{\text{H}}}{\nu} \right)^{\alpha_{\text{UV}}}, \quad (2.8)$$

with the dependency on the redshift given by

$$J_{21}(z) = \frac{J_{21}}{1 + [5/(1+z)]^4}. \quad (2.9)$$

The term α_{UV} , that describes the slope of the flux, is usually equal to one, and the factor J_{21} is the intensity of the flux. As usual, z is the redshift. The expression (2.9) represents a flux that increases with the redshift (i.e. smaller at recent epochs), that is equal to J_{21} when $z \rightarrow \infty$ and it is $\approx 1.6 \times 10^{-3} J_{21}$ at $z = 0$. The photoionization process and its inclusion in our model will be discussed more in detail during this Thesis when we will describe our code/model ROBO.

An important role is also played by dust: it crucially affects the chemical behavior of the interstellar medium and, like the chemistry and the photoionization process, it gives its contribution to the system of differential equations. Since interstellar dust plays a key role, this issue will be skipped for now and it will be described accurately in the Section 2.5.

2.2.3 Chemistry: numerical issues

*mi fiderò di te
quando anche tu ti fiderai di me,
ma chi dei due inizia per primo?*

Bluvertigo³

As shown in the previous Sections, the velocity of the reaction rates is crucial to define the computational complexity of the system to study. When a large number of species and reactions is used, the whole system becomes

³Pop Tools, Mescal, 2001

extremely complicated; the chemical time-scales can be shorter than the typical dynamical time-scales by several order of magnitude. The rate coefficients are usually expressed in units of cm^3/s , and from (2.5) we see that this rate, multiplied by the numerical densities of the two reactants, gives the speed of the reaction, which is the amount of variation of the number density. Thus we obtain cm^{-3}/s , which is exactly what we define as the speed of the reaction. Because of their sudden variations, fast reactions complicate the solution of the system of Eqns. (2.5).

Consider for example a reaction with a rate coefficient of $k = 10^{-10} \text{cm}^3/\text{s}$, at some given temperature. It follows that $dn = kn_1n_2 dt = 10^{-10}dt$ if $n_1 = n_2 = 1 \text{cm}^{-3}$. In other words, if we want to integrate with a precision of $dn = 10^{-10}$ the time-step must be $dt = 1 \text{s}$, that is extremely small compared to a typical time step of a cosmological NB-TSPH code which is approximately $\Delta t = 10^4 \text{yrs} \approx 3 \times 10^{11} \text{s}$ or more. Moreover, using such small time-steps the stiffness of the system of equations increases.

Note that the real situation is generally worse than this, because in this example we have considered small densities and a small rate coefficients. Higher densities imply faster reactions, and (keeping the accuracy constant) faster reactions require even smaller time-steps.

To solve this problem we need an ordinary differential equations solver ables to work with such complicated systems.

In our model we only deal with ordinary differential equations (ODE)⁴.

During this work we often deal with *stiff equations*. The exact definition of stiff equation would require heavy mathematical formalisms; for our aims, it is sufficient to define it as a differential equation for which some solver algorithms are numerically unstable, unless the step size is taken to be extremely small⁵.

There are many methods to solve a stiff system of ODEs; for example the Eulerian method, the Runge-Kutta, the Adams-Bashforth, the Adams-Moulton and the Backward Differentiations Formulae (BDF). The first three methods are not suited for our problem, while the others give better results. In particular the BDF method is the most accurate for this class of problem.

⁴An ODE is a differential equation in which the unknown function (the dependent variable) is a function of a single independent variable. In the simplest form, the unknown function is a real or complex valued function. ODEs are further classified according to the order of the highest derivative of the dependent variable with respect to the independent variable appearing in the equation; the most important cases for scientific applications are first-order and second-order differential equations. A further distinction exists between differential equations explicitly solved with respect to the highest derivative and differential equations in an implicit form.

⁵This definition is not accurate since in principle we should define the expressions *numerically unstable* and *extremely small*!

The BDF belongs to the class of the *multistep methods*. A single initial value problem is

$$y' = f(t, y) \quad y(t_0) = y_0, \quad (2.10)$$

where y' represents the differential of y , t is the independent variable. y_0 is the initial value assigned to the dependent variable. If we apply the BDF method to this problem [4], we obtain the general formula for the multistep problem

$$\sum_{i=0}^k a_i y_{n-i} = h \sum_{i=0}^k b_i f_{n-i}, \quad (2.11)$$

where h is the step size, f_j is $f(t_j, y_j)$, while a_i and b_i determine the particular linear multistep method. The BDF have $b_i = 0$ for $i > 0$, thus we have

$$\sum_{i=0}^k a_i y_{n-i} = h b_0 f_n. \quad (2.12)$$

Since BDF is an implicit method, it requires the solution of non-linear equations at each step. To cope with this a modified Newton's method is used.

The BDF method allows to find a solution of the ODE system formed by the reactions belonging to the chemical networks. This is one of the most CPU-demanding task. Finding a fast way to solve the ODE system is crucial, because it often requires about the 90% of the computational time. The BDF method (implemented in the DVODE routine, see [14, 19, 73]) has proven to be the most efficient for our purposes.

2.3 ISM: Cooling

A fundamental ingredient in the models of the ISM is the cooling. This process has a great importance because (together with the heating) rules the temperature variations inside a generic gas volume considered in the model. We have already seen that the chemistry depends on the temperature, because the rate coefficients are temperature-dependent and they change their values by several order of magnitude at varying the temperature. We will see in this Section that the cooling is heavily influenced by the chemistry, since its effectiveness depends on the quantity of species that populate the ISM.

Its role is important also in the star formation context. The star formation process is the result of a gravitational collapse of a cloud of gas: the collapsing force is usually balanced by the thermal energy of the gas that increases

during its collapse along with the density of the cloud. The thermal energy is the result of the collisions between the chemical species that form the gas and this thermal effect, that is density-dependent, would halt the collapse if no other process would reduce its power. In this framework the cooling plays a fundamental role reducing the thermal energy of the gas and thus reducing the resistance of the gas cloud to the collapse. It is therefore of primary importance to study how the ISM changes its temperature during its evolution, because the intensity of the cooling strongly influences the total amount of the stars being formed.

The ISM lowers its temperature because photons of frequency ν escape from the gas and consequently their energy $h\nu$ is lost. The process that describes this phenomenon could be summarized by these two reactions



Here the species A collides with the species B and the energy exchanged during the collision excites the species B (the asterisk at the superscript means that the species is excited). After the collision the species B releases a photon (γ) of frequency $\nu = E/h$, and E is the energy lost in the whole process.

In order to have an efficient cooling process there are some criteria that must be satisfied. First of all (i) there must be frequent collisions and a large number of collision partners. This is obvious since the drivers of the process represented in the system of reactions (2.13) are the collisions between the gas particles. (ii) The excitation energy must be less or equal the kinetic energy. If this condition is not satisfied the collisions are non-influential and not able to excite the species involved. (iii) Another point that should be satisfied is that the probability that a collision excites the species must be high enough. This is because the efficiency of the process could be low even if the first and the second conditions are satisfied. (iv) The probability that an excitation occurs is not the only probabilistic aspect of the process and also the probability that a photon is emitted from an excited species plays its own role. This probability must guarantee that a photon is emitted before another collision occurs. (v) The last condition is that the photons emitted are not re-absorbed. In other words: the gas must be optically thin. If this condition is not satisfied the gas cannot cool since no energy can escape from the volume of gas considered.

These criteria are important to understand what are the most important coolants. Even if a coolant is very abundant, its efficiency could not be so high as expected because, for example, its probability of being excited is very low.

An interesting example is the cooling by CO and its isotope ^{13}CO . The CO is a very efficient coolant, but the criteria (v) is not satisfied (self-shielding occurs) and when the gas becomes optically thick, the cooling efficiency is low. This is not true for ^{13}CO which is optically thin, but the abundance of this isotopic molecule, criteria (i), is lower than CO, so their net cooling becomes comparable for two different reasons.

When we consider the cooling by molecules another striking aspect is that their structure determines the efficiency of the cooling. This is true for vibro-rotational spectra, when the dipole moment of the molecule plays a key role in the cooling process. This topic will be discussed in detail in the Section 2.3.2.

2.3.1 Atomic Cooling

What is the link between the chemistry and the cooling? How is affected the cooling process by the chemical composition of the interstellar medium? To answer to these questions we must first know how the atoms and molecules behave.

An atom has discrete energetic levels that can be populated by its electrons. When an electron moves from an higher level (called excited level) to a lower one, the difference of energy ΔE between the levels is emitted as a photon of energy $\Delta E = h\nu$, where ν is the energy of the photon and h is the Planck's constant. If this atom belongs to a given volume of interstellar medium, the escaping photon brings away the energy ΔE from the gas and consequentially the gas cools down by $\Delta E/k_B$ Kelvin (or any equivalent unit of temperature, depending on k_B that is the Boltzmann constant).

In particular, when an electron hits an atom there is a probability that such an atom reaches an excited state. As already mentioned, the atom after a while returns to a not excited state and releases a photon. An atom has a probability ϵ to emit a photon due to a de-excitation of an electron that moves from the level i to a lower level j . The probability that an atom emits a photon, is described by the emission coefficient ϵ that is

$$\epsilon = \frac{h\nu}{4\pi} n_i A_{ij}$$

where n_i is the number density of the electrons that populate the i -th level, and A_{ij} is the Einstein coefficient for spontaneous emission, which is the process that lets an electron moving spontaneously from a level to a lower one. A spontaneous emission occurs when the external processes are not involved in the transition. The Einstein coefficient is the probability that such an event occurs.

The collisional excitation is the process by which an electron makes a transition from a low energy level to an higher one, due to a collision between the atom considered and a collider (electrons, molecules or other atoms). This process is characterized by a coefficient γ that describes the probability of an electronic transition between two levels. In general the de-excitations and the collisional excitations both contribute to populate or de-populate the atomic levels. In particular we have

$$n_i \sum_j P_{ij} = \sum_j n_j P_{ji} \quad (i \neq j), \quad (2.14)$$

where P_{ij} represents a transition from the i -th to the j -th level, and n_i is the number density of the atoms in the i -th energy state. This last Equation is a balance between the de-populating and populating effects acting between the different levels.

To complete the picture we need a conservation equation which is

$$\sum n_i = n_x, \quad (2.15)$$

where n_x is the total number density of the atom considered. The combined use of both Equations (2.14) and (2.15) allows to know the number density of each excited level.

A two level system will be described as

$$\begin{cases} n_1 + n_2 = n_x \\ \sum_k n_1 n_j \gamma_{12}^k - \sum_k n_2 n_k \gamma_{21}^k - n_2 A_{21} = 0, \end{cases}$$

where the sums run on the colliders. The meaning of the symbols is already discussed except for γ_{ij}^k which is the collisional rate from the i -th to the j -th level for the k -th type of collider that hits the atom.

If the atom has more than two levels the system of equations is more complicated but based also in this case on Equations (2.14) and (2.15). The Equation (2.15) remains the same, but Equation (2.14) will be replicated $N - 1$ times for each atomic level, where N is the number of levels considered. The resulting system is described by a matrix multiplication $A \times \bar{n} = B$ where A is the matrix of the coefficients of the equations, \bar{n} is the array containing the N unknown variables and, finally, B is the array containing the constant coefficients. The last array is made by zeros, except for the term n_x corresponding to the continuity equations, and the matrix A is

$$A = \begin{cases} \sum_k M_{ik} & i = j \\ -M_{ij} & i \neq j, \end{cases} \quad (2.16)$$

where

$$\begin{aligned} M_{ji} &= \sum_l \gamma_{ji}^l n_l + A_{ji} \\ M_{ji} &= \sum_l \gamma_{ji}^l n_l. \end{aligned} \quad (2.17)$$

In both the Equations the sums run over the colliders. The solutions of the matrix multiplication are the numerical densities of each excited population (see Appendix A for all the details on the metal cooling matrices).

Obtaining the cooling is now a straightforward task, because it is given by

$$\Lambda = \sum_{1 < i} \sum_{0 \leq j < i} n_i A_{ij} \Delta E_{ij}, \quad (2.18)$$

where n_i represents the number density belonging to the i -th state, A_{ij} is the Einstein coefficient describing the transition between the i -th and j -th level and ΔE_{ij} is the energy difference between the i -th and j -th level.

This multi-levels model is particularly suited for metals, which have a complicated fine structure: a characteristic that makes metals one of the strongest coolant in astrophysics. Indeed, the metals cool the gas by several hundreds of kelvins implying that they are a key ingredient in the star formation process. However, in the first-stars formation scenario, the metals are not present since they are a product of the continuous process of birth and death of the stars with consequent enrichment of the ISM; so there must be a coolant efficient enough to cool the gas and to permit the formation of these zero-metallicity stars. This is the role played by the molecules which are discussed in the next Section.

2.3.2 Molecular Cooling

We have already stressed that molecular cooling could be a valid alternative to the metal cooling. This is possible since the molecules have a complicated behavior and also smaller activation energies than atoms: these characteristics make molecules suitable coolants. The molecules have a complex roto-vibrational spectrum due to the rotation and the vibration of the atoms that form the molecule. Fortunately, the most common astrophysical molecules are CO and H₂, that are linear diatomic molecules. Their simple structure allows to make some basic assumptions that simplifies the model developed to describe their behaviour. For this reason, in this work we describe only the physics of this particular class of molecules.

The two physical phenomena that justify our interest for this class of molecules are the rotational and the vibrational cooling, due to the rotation and stretching of the two atoms of the molecule. In the next Sections these

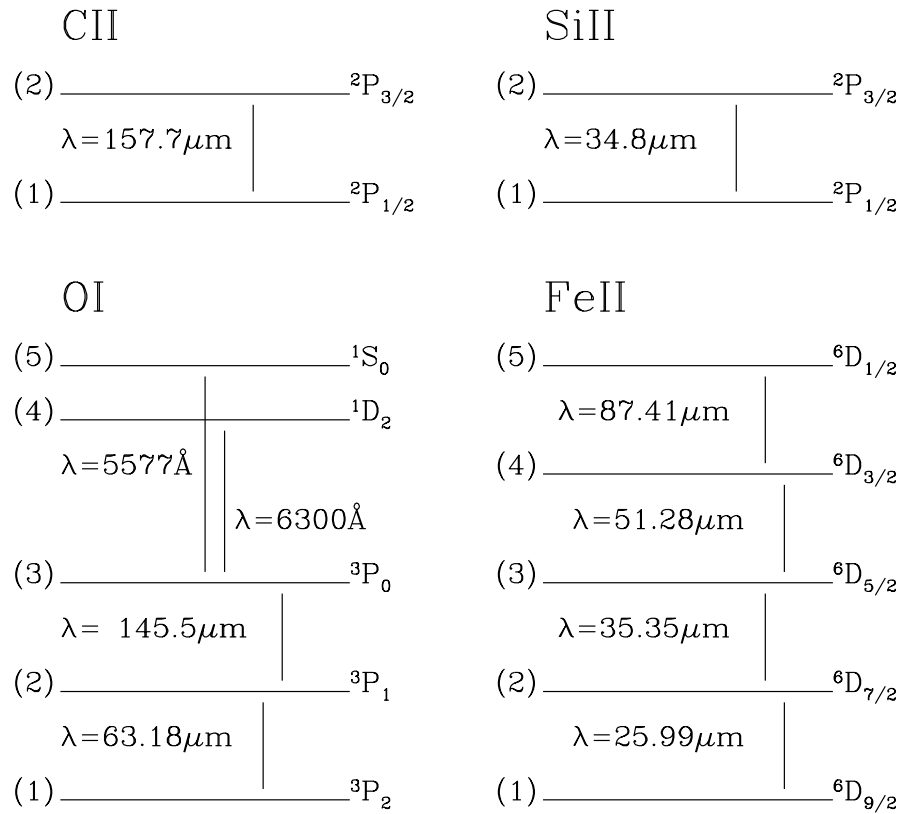


Figure 2.1: Some of the fine-structure lines included in our cooling model for the ions C^+ , O , Si^+ and Fe^+ . From [89].

two processes will be described in detail, while in the Section 3.3 we describe how this issue could be embedded in a model for the study of the ISM.

Rotational Cooling

The physical quantity involved in the rotational cooling is the moment of inertia. A molecule has three moments of inertia, one for each mutually orthogonal axes (I_a , I_b and I_c). Since we are dealing with molecules of astrophysical interest that are linear diatomic molecules, and thus they have a cylindrical symmetry, we have $I_a \ll I_b = I_c$, making the solution of the set of equations trivial.

The simplest assumption that we can make to describe the observation of the rotational spectroscopy is the rigid rotor. The rotation kinetic energy of a molecule is quantized, and it is the main driver of its rotational spectrum. If we consider a molecule made by two atoms of masses m_1 and m_2 which are separated by a distance R , its rotational energy is described by

$$\tilde{E}(J) = \tilde{B}_e J(J+1), \quad (2.19)$$

where $J = 1, 2, 3, \dots$ are the rotational quantum numbers and \tilde{B}_e is the rotational constant which is

$$\tilde{B}_e = \frac{h}{8\pi^2 c I}, \quad (2.20)$$

where h and c are the Planck's constant and the speed of light respectively. I is the moment of inertia given by

$$I = \mu R^2 = \frac{m_1 m_2}{m_1 + m_2} R^2, \quad (2.21)$$

in which the reduced mass μ shows that the moment of inertia is calculated respect to the center of mass of the system. Since we are dealing with quantized moments, we need a selection rule for the J terms. This is $\Delta J = \pm 1$, which means that the change of a unity is a rule valid both for emission (plus sign) and for absorption (minus sign). This last statement provides the method to find the positions of the lines in the molecular spectrum. Indeed, we have

$$\tilde{\nu}_{J' \leftrightarrow J''} = \tilde{E}(J') - \tilde{E}(J'') = 2\tilde{B}_e (J'' + 1), \quad (2.22)$$

with $J'', 1, 2, 3, \dots$, where $\tilde{\nu}$ is the frequency of the expected lines. Note that the frequency is expressed as the inverse of a space, which is very common in spectroscopy. To obtain an energy in standard units we must simply use $E = c h \tilde{\nu}$, where c and h are the speed of light and the Planck's constant. The frequency in standard units is then $\nu = c \tilde{\nu}$.

The rigid rotor model produces some discrepancies when the predicted lines are compared to the real ones. If the rigid rotor model would be correct, the lines of the spectrum should be equally spaced: however, when we observe a spectrum of a linear model, the lines have different distances. To cope with this we introduce the non-rigid rotor model in which the moment of inertia changes because of some secondary order effects. The most important correction is the centrifugal distortion.

When a molecule rotates, the distance between its atoms increases due to the centrifugal force that pulls the atoms apart. In the Equation (2.21) this phenomenon increases the distance R and consequentially the momentum of inertia I . From Equation (2.20), we can see that increasing R brings a decrease in \tilde{B}_e . The final effect can be described as

$$\tilde{E}(J) = \tilde{B}_e J(J+1) - \tilde{D}_e J^2(J+1)^2, \quad (2.23)$$

where \tilde{D}_e is the centrifugal distortion constant, where $J = 0, 1, 2, \dots$ are the rotational quantum numbers. The line spacing for the rotational mode is now

$$\tilde{\nu}_{J' \leftrightarrow J''} = 2\tilde{B}_e(J''+1) - 4\tilde{D}_e(J''+1)^3, \quad (2.24)$$

with $J'' = 0, 1, 2, \dots$ as usual.

In the Section 3.3 we describe more in detail how to obtain the rotational cooling from quantum-mechanical calculations, and also how to describe and include this process in a code developed to study the evolution of the ISM.

Vibrational Cooling

Molecules can also stretch. The degrees of freedom for this process depend on the number of atoms that form a molecule, causing the normal modes of vibration. For a molecule with n atoms, the number of normal modes of vibration is $3n - 6$, and each mode is independent. As already mentioned we deal only with simple molecules like CO and molecular hydrogen, which are linear and diatomic. For linear molecules the number of modes of vibration is $3n - 5$, as rotation about its molecular axis cannot be observed and if the molecule is diatomic as the ones we are dealing with, $n = 2$ and we get $3n - 5 = 1$. A diatomic molecule has therefore just one normal mode of vibration: this simplifies the model for the molecular vibrational cooling.

To have a vibration of frequency ν a molecule must absorb a quantity of energy that is $E = h\nu$. The model that allows to describe the phenomenon is the simple harmonic motion. With this approximation is possible to solve the Schrödinger's wave equation, obtaining the energy states

$$E_n = \left(n + \frac{1}{2}\right) \frac{h}{2\pi} \sqrt{\frac{k}{m}}, \quad (2.25)$$

where $n = 1, 2, 3, \dots$ are the quantum numbers, k is the force constant (Hooke's law) and m is the mass, which in a diatomic molecule is the reduced mass

$$m = \frac{m_1 m_2}{m_1 + m_2}, \quad (2.26)$$

with m_1 and m_2 the masses of the two atoms that form the molecule. The selection rule is $\Delta n = \pm 1$, meaning that a transition happens only when the quantum number n changes by one unity.

As far as the rotational spectroscopy is concerned, the model presented here is too rough, and when the predicted spectrum is compared to the observed one, some differences arise. These discrepancies are the result of the anharmonicity of the oscillator. This phenomenon is clear in the hot transitions (transitions between two states of a single normal mode of vibration, neither of which is the overall ground state) that are shifted to lower frequencies.

To conclude, the actual spectrum is much more complex since the transitions are not only due to the vibrational component, but are also from rotation. The resulting energy for a diatomic molecule is given by

$$E(v, J) = \omega \left(v + \frac{1}{2} \right) + \tilde{B}_e J(J + 1), \quad (2.27)$$

with v and J the vibrational and the rotational quantum numbers respectively, and ω the vibrational frequency. Three sets of bands are observed corresponding to $\Delta J = 1$ (R branch), $\Delta J = 0$ (Q branch) and $\Delta J = -1$ (P branch). In particular, considering $v = 1 \rightarrow 2$ and the rules above, we have $\nu = \omega + 2B(J + 1)$ for R branch and $\nu = \omega - 2BJ$ for P branch. The Q branch is simply $\nu = \omega$. This demonstrates how sets of absorption bands are separated by the rotational constant. Note that no centrifugal distortion effects (already discussed) nor coupling between rotation and vibration are included. The last effect is due to the change of the moment of inertia due to the vibrational stretching of the molecular bond. If these effects are present there is a shift in the bands, and a separation of the individual Q branch. Even if there is this discrepancy with observed lines the Equation (2.27) represents still a valuable approximation.

2.4 ISM: Heating

To complete the picture of the thermal balancing of the interstellar medium, we describe how external phenomena increase the gas temperature through

energy injection. The main driver of this process is the photoionization of the chemical species by the radiation coming from outside the given volume of gas. The energy of the photons is converted into kinetic energy of the ionized electrons. This process is therefore strictly connected to the chemistry as already described in the Section 2.2.2.

The dust is involved in a similar process, but it is more complicated than atomic and molecular ionization, thus (as for the dust chemistry) we will describe this effect in an appropriate Section hereinafter.

Another phenomenon that heats the gas is the ionization by cosmic rays. They yield their kinetic energy to the gas in a way similar to the photoionization process. Their energy is transferred to the ionized electrons.

The last source of heating that will be discussed in this Thesis is the heating due to the turbulence of the gas, that dissipates the energy of the smallest elements of fluid into the gas, increasing its temperature.

2.4.1 Heating by Cosmic Rays

Cosmic rays are subatomic particles that permeates the space: they are mostly protons (90%), alpha particles (9%) and electrons (1%). It is difficult to describe this particles field as there are no precise measures of its intensity in different regions of the Universe. The assumptions made to describe the cosmic rays are based on the measurement on the Earth considering that the field found is a mean field valid in the most of the regions of the Universe. It is important to underline that cosmic rays are influenced by magnetic field, since they are usually made by charged particles, and also their formation mechanism is unknown. These last remarks made the description of the cosmic rays an hard task.

The cosmic rays heat the ISM through the ionization and the excitation of the species that form the gas. It is worth noticing that cosmic rays can penetrate the gas in depth due to their nature: in this way they can heat the ISM also in high optical depth regions of the clouds that are usually opaque to the UV photons. The most efficient cosmic rays are the low-energy ones, which are in the energy range 1 – 10 MeV, and they are the most efficient because of their number, since in nature the low energy cosmic rays are more than the high energy ones. The mechanism that heats the gas is the exchange of the kinetic energy of the particle with the gas through a direct collision with free electrons, or through the ionization and/or excitation of the target species.

The total ionization rate could be described using

$$n\xi_{\text{CR}} = n\zeta_{\text{CR}} [1 + \phi^{\text{H}}(E, x_e) + \phi^{\text{He}}(E, x_e)] , \quad (2.28)$$

where ζ_{CR} is the primary ionization rate, $\phi(E, x_e)$ is the average number of secondary ionizations of the given species (in this case H and He), E is the energy of the primary ionization and x_e is the electron fraction.

Considering only the first ionization we can derive the heating rate as

$$n\mathcal{H}_{\text{CR}} = n\zeta_{\text{CR}}E_{\text{h}}(E, x_e), \quad (2.29)$$

where $E_{\text{h}}(E, x_e)$ is the heat deposited per primary ionization, that for low degrees of ionization is $E_{\text{h}}(E, x_e) \approx 7 \text{ eV}$. The cosmic ray heating rate is then

$$n\mathcal{H}_{\text{CR}} = 3 \times 10^{-27} n \left[\frac{\zeta_{\text{CR}}}{2 \times 10^{-16}} \right], \quad (2.30)$$

here in $\text{erg/cm}^3/\text{s}$.

2.4.2 Heating by Turbulence

A turbulent fluid is described by its Reynold's number that is defined by:

$$\mathcal{R} = \frac{vL}{\nu}, \quad (2.31)$$

where v is the mean velocity, L is a characteristic scale length, and ν is the kinematic viscosity. \mathcal{R} represents the ratio between the inertial forces and the viscous forces of a fluid flow. A fluid could be considered turbulent if $\mathcal{R} > 3000$: the ISM has typically $\mathcal{R} \approx 10^6 - 10^8$ which is clearly turbulent.

The kinetic energy of the fluid is dissipated at small scales through eddies of size ℓ , that are the smallest elements in size of the fluid. The smallest scale is set by viscosity, and it is typically 10^{16} cm for the WNM and 10^{13} cm for molecular clouds. The power-spectrum is the Kolmogorov one which is

$$E(k)dk = \frac{2}{3} (2\pi\dot{\epsilon})^{2/3} k^{-5/3} dk, \quad (2.32)$$

where $\dot{\epsilon} = \text{constant}$ is the rate of energy dissipation and $k = 2\pi/\ell$ is the scale size.

The characteristic length of the turbulence determines the heating as

$$n\mathcal{H}_{\text{turb}} = \frac{1}{2} \frac{nm_{\text{H}}v^2}{\ell/v}, \quad (2.33)$$

which is environment-dependent as ℓ and v show. For the WNM we have $v = 10 \text{ km/s}$ on a scale length of 200 pc giving

$$n\mathcal{H}_{\text{turb}} = 2.8 \times 10^{-30} n, \quad (2.34)$$

and for molecular clouds ($v \approx 1 \text{ km/s}$ and $\ell = 1 \text{ pc}$) we have

$$n\mathcal{H}_{\text{turb}} = 3 \times 10^{-28} n, \quad (2.35)$$

both in $\text{erg/cm}^3/\text{s}$.

2.5 ISM: Dust

Another one bites the dust

Queen⁶

Interstellar dust is a key ingredient in the chemistry and physics of the ISM. This solid component is involved in a lot of important phenomena and is a very broad subject with many topics, among which we can cite: extinction of the stellar light and emission in the near-IR/mid-IR/far-IR; dust formation (by accretion in the ISM, in remnant of SNe and in the envelopes of AGB stars) and destruction (by SNe shocks); charging, sputtering, shattering, heating and cooling of dust grains; heating of interstellar gas by photoelectrons ejected from dust grains; electron transfer from dust grains to metal ions and alignment of dust grains by the magnetic field. In particular, since we are dealing with a chemical description of the ISM, we will be mainly interested on processes like for instance the chemistry on dust surface (called grain-phase chemistry) and the gas heating through photo-ionization.

The role of the dust grains is in particular complicated because their formation and destruction is a cumbersome process not easy to include in detail into the models: the population of dust is formed by different grains of different size and most of all different chemical composition. Unfortunately these discrepancies lead to a different physical behaviour of the different families of grains and it is therefore mandatory to know how the dust population is characterized. For instance, the size influences the formation and destruction of the grains, their temperature and the rate of the chemistry reactions on such grains. The chemical composition, on the other side, is a crucial detail since the physical properties of the grain (like for example molecular hydrogen formation on its surface) strongly change if the dust grain belongs to the family of carbon-based grains or silicon-based ones (if we suppose to roughly divide dust in these two types).

The taxonomy of the grains is wide because they also include the PAH (Polycyclic Aromatic Hydrocarbons) which is a class of molecules that are formed by carbon atoms arranged in a honeycomb hexagon-based structure, that is planar. These carbon hexagons are connected each other and surrounded externally with H atoms. Some representative PAHs are pyrene ($C_{16}H_{10}$), the more complex ovalene ($C_{32}H_{14}$), naphthalene ($C_{10}H_8$) and pentacene ($C_{22}H_{14}$). Just to complete the PAHs classification they are divided into catacondensed, which have hexagons that share only two carbon atoms and form elongated chains ($C_{10}H_8$ is the simplest), and pericondensed, more

⁶The Game, EMI/Parlophone, 1980

compact, in which hexagons share more than two carbon atoms (pyrene is the simplest one, while coronene $C_{24}H_{12}$ is one of the most studied). Cata-condensed PAHs are thought to be poorly resistant to UV photons, leaving pericondensed ones as the more suitable ones to populate the ISM with their compact resistant form. As it can be easily seen, the structure of these constituents is more complex than the molecules discussed until now, which were linear and with two atoms only. PAHs have been introduced into dust models because they provide a natural explanation for the observed emission spectrum of dust in the MIR, where the excitation is assumed as the result of the internal conversion of energy because of the absorption of an energetic photons.

However, introducing the PAHs in a model of the ISM as the one described in this Thesis goes beyond the aims of this work. For this reason, this topic will not be discussed anymore. Hereinafter when we deal with dust, we only consider a simple classification of dust which consists in dividing dust grains into the big families of the carbonaceous grains (carbon-based grains like diamonds, graphite, amorphous carbon) and silicates (silicon-based grains like olivines and pyroxenes).

In our model we will focus our interest on the following specific topics dust-related. First of all we are interested in how grains are formed and destroyed, and in particular what is their size distribution as a result of the interplay between these two processes. Second, another fundamental ingredient in the dust description is how grains interact with a incident radiation field, since this is a key element to calculate the temperature of the grains. The temperature determines then the quantity of molecules that could be formed onto the grain surface. Finally, we describe how the dust heats the ISM through photoelectric ejection of electrons into the ISM, including the analysis of the charge distribution over the grain lattice.

All these points will be discussed as general physical phenomena in the next Sections, and then they will be examined again in the Chapter dedicated to the code ROBO itself, paying attention to their numerical implementation.

2.5.1 Size distribution

The observations show that the extinction of the light by dust increases with the spectral frequency, strongly rising from the infrared to the far-UV. Since the extinction saturates when the size a becomes comparable with the wavelength λ , it means that dust grains exist in different sizes. The involved range of wavelengths allow us to fix the sizes of the grains, from 2000 Å in the visible part of the spectrum, up to 50 Å when the Far-UV extinction is considered. Since the grain abundance, their size and the extinction efficiency

are related, if we consider the extinction efficiency $Q_v \approx 1$ for $\lambda = 2000 \text{ \AA}$ we obtain an abundance of dust grains of 4×10^{-13} . Analogously in the FUV region we obtain 2×10^{-9} for $\lambda = 100 \text{ \AA}$. Similarly, inverting the observed extinction curve we can obtain the grain size distribution in the ISM. Even if this argument is correct the result strongly depends on the characteristics of the grain population involved. In particular, we need to know what is their dominant component, their shape(s) and their optical properties. Once these are known it is possible to retrieve the distribution of the grains. The simplest and most widely used model for the size distribution of dust grains is the one developed by Mathis, Rumpl and Nordsieck (usually called MRN model, see [93]). It consists in a power-law size distribution of graphite and silicate grains usually in the range $50 - 2500 \text{ \AA}$:

$$n_C(a)da = A_C n a^{-3.5} da, \quad (2.36)$$

both for graphite and silicates, eventually varying the upper and lower limit. Other possibilities could be adopted like the recent Weingartner distribution, however for our purposes the MRN distribution is fully adequate and reproduce the general trend with smaller grains much more abundant in nature than the bigger ones. A caveat that must be underlined is that for small sizes ($< 200 \text{ \AA}$) the extinction is in the Rayleigh limit, which means that is not size-dependent and therefore the range of the smallest grain dimensions is more uncertain. We need in any case a population of very small grains (VSGs) as is inferred from the studies of extinction curves and near-IR/mid-IR emission of the Galaxy.

Another way to determine grain size distribution is to use the grain polarization. The wavelength of the maximum polarization is related to the size following this relation:

$$\lambda_p = 2\pi(n - 1)a. \quad (2.37)$$

It has been observed that in the IR range the polarization decreases, reflecting the fact that the number of large grains is smaller than the number of small ones. Beside, for the UV, another decline has been observed in the polarization: in principle it seems that this decline could suggest a rapid decline in the number of small grains, if the same criterium of large grains is applied. However, the contribution of the small grains to the polarization is negligible. This depends on the alignment and on the shape of the grains. The conclusion is therefore that small grains do not contribute to the polarization and we get no clue in order to eventually lower their number from the UV polarization decline.

2.5.2 Formation

The formation of the dust can be subdivided into two main processes. The first one is the formation of the dust and its injection in the ISM from stellar objects that behave as dust factories more or less efficient in some particular evolutionary stages. In particular SNe and AGB stars play by far the major role, and only a very small contribution comes from other evolutionary stages. The second process occurs along the evolution of the ISM: it is the grain formation through the accretion of the atoms that are present in the ISM, and it not depends on the origin of the dust, even if dust injected by AGB/SNe continuously refuels the ISM with seeds over which the accretion process can take place. The inclusion of the first process into the models mainly depends on the calculation of a set of chemical dusty yields able to determine the relative fraction of gas and dust injected in the ISM either in the AGB phase or during the SNe explosions. In this Section anyway, we will focus and describe only the second process of dust formation by accretion, because it concerns directly our ISM model, while the amount of stardust already in site and injected into the ISM by stars will be an input parameter entering into our ISM calculations.

The formation of the dust in the ISM derives from the accretion of atoms over seeds already present. This process depends on the number of atoms in the gas phase and on the characteristics of the dust, as the surface (i.e. the size) of the seed where atom should stick. Indeed, as we have already seen in the previous Section, the grains have different sizes and their distribution function is a power-law like $dn(a) \propto a^{-3.5}da$: therefore the available area for impinging atoms will clearly be different. Another key parameter are the physical properties of the grain, that change with the different types of seeds: in our simple description we will deal only with carbonaceous grains and silicates.

All these physical characteristics are generally summarized by a function that represents the probability that the accretion process occurs. This function depends on different parameters, such as the temperature of the gas, the temperature of the dust and the kind of seed involved. The variation of the number density of a grain of size a per unit of time is

$$\dot{n}(a) = c_{\text{env}}\varphi\pi a^2 n_{\text{g}} n_{\text{d}} v_{\text{g}}, \quad (2.38)$$

where πa^2 represents the cross section of the grain, n_{g} is the number density of the considered element in the gas phase, n_{d} is the dust number density, v_{g} is the velocity of the gas due to the thermal motion, c_{env} is a parameter determined by the environment and, finally, φ is the aforementioned function. The last two terms will be better discussed in the next lines.

The Eqn. (2.38) is a general description for the accretion: it depends on the seed involved, and in our case produces two equations, one for the carbonaceous grains and one for the silicates. Also, in the Eqn. (2.38) the size of the grains determines the probability that the accretion occurs and the velocity also increases such a probability.

The number densities in Eqn. (2.38) represent first of all the fact that the more dust we have, the more dust will form, and second the more atoms we have available to accrete on the seeds (e.g. carbon atoms available to accrete on carbonaceous grains already in situ), the more dust will form. If at least one of the densities is equal to zero the dust accretion will halt.

But the most interesting part of the Eqn. (2.38) is the φ function that depends on the physical properties of the dust, that are different for different types of seeds. The variable of the function φ are the temperature of the dust, that modifies the sticking probability of a given atom over a given seed, and the temperature of the gas. A practical description will be given in the Section 3.5.3 where the φ is actually a function $\alpha(T_g, T_d)$ of the gas and dust temperatures.

Finally c_{env} is the influence of the environment on the process, that modifies the probability of the dust accretion. The following point must be now underlined: in the previous lines we have analyzed the influences from dust/gas temperature and the lattice. However, for the ISM this description could not be accurate enough, since some other phenomena are present, like the UV field, the shocks and many others, that would hamper dust formation. Including such phenomena in a theoretical model is complicated, but they can be parametrized under a sort of *delaying factor*. This term reduce the efficiency of the formation of dust, simulating the presence of some process that prevents the formation of dust grains into the volume of ISM considered.

During this Thesis this parameter will not be discussed anymore (from a theoretical point of view) and it will be considered as a static term (see Section 3.5.3 for further details). However, using a static parameter is clearly not accurate and just a first order approximation, because it implies that this delaying factor is the same in all the regions of the Universe. We are aware of the importance of this term and of the roughness of our description, thus in a future work it will be better developed, including its environmental dependence.

2.5.3 Temperature

The dust temperature, as already seen, plays an important role in the dust properties, since the accretion of the grains is a function that strongly depends on this parameter (Sections 2.5.2 and 3.5.3). The role of the tempera-

ture will be also discussed in the other Sections of this Thesis, when we will introduce the formation of molecules over the surface of the grains.

The temperature of the grains depends mainly on the radiation field impinging on the volume of the ISM considered. The temperature is calculated considering dust grains in thermal equilibrium, that is the amount of energy that the grains absorb and emit is the same. We neglect the well known and widely studied and modelled behaviour of very small grains that fluctuate in temperature assuming on average a wide temperature probability distribution (differently from big grains whose distribution is more like a delta of Dirac at low temperatures) and reaching even high temperatures. For the purposes of this Thesis this description would be too complicated to be included, since it requires a full calculation of the probability distribution via the transition matrix between the energy states. If we consider a generic radiation field $J(\lambda)$ with an absorption efficiency of $Q(\lambda)$ the energy absorbed is

$$\Gamma_{\text{abs}} = 4\pi\sigma_{\text{d}} \int_0^{\infty} Q(\lambda)J(\lambda)d\lambda, \quad (2.39)$$

where σ_{d} is the cross section of the grain.

The emission of the grain is analogously described by

$$\Gamma_{\text{em}} = 4\pi\sigma_{\text{d}} \int_0^{\infty} Q(\lambda)B(T, \lambda)d\lambda, \quad (2.40)$$

where $B(T, \lambda)$ is the Planck function for a given temperature T and a given wavelength λ . Comparing Eqn. (2.39) and Eqn. (2.40) we see that a grain absorbs radiation at any wavelengths (weighted by the $Q(\lambda)$ function), and emits the energy absorbed as a blackbody with temperature T .

Since $\Gamma_{\text{abs}} = \Gamma_{\text{em}}$ it is possible to retrieve the dust temperature. If we assume that the efficiency follows a simple power-law like $Q(\lambda) \propto (\lambda/\lambda_0)^\beta$ with $\lambda_0 = 2\pi a$ and $\beta = 1$ we obtain

$$T(a) = \xi_d \left(\frac{J}{a} \right)^{1/5}, \quad (2.41)$$

where ξ_d is a term that includes all the constants, J is the integrated mean intensity and a the size of the grain. With more detailed considerations (as the correct value for absorption efficiency for UV and visible) a reasonable approximation for silicate is

$$T_{\text{sil}}(a) = 13.6 \left(\frac{1 \mu\text{m}}{a} \right)^{0.06} \text{ K}. \quad (2.42)$$

Graphite has a similar equation

$$T_{\text{gra}}(a) = 15.8 \left(\frac{1 \mu\text{m}}{a} \right)^{0.06} \text{ K}. \quad (2.43)$$

From this model is also possible to calculate the IR emission considering dust of different sizes to obtain

$$I(\lambda) = \int_r \int_a n_d(r, a) \pi a^2 Q(\lambda, a) B(T, \lambda) da dr, \quad (2.44)$$

along the line of sight r . This will be the total IR intensity observed neglecting the extinction.

An interesting situation is when a dusty cloud is heated by stars, but it is optically thick in the IR. As we have just seen, dust grains will radiate as a black body with temperature T_{BB} , so the peak of the wavelength is known being $\lambda_m T_{\text{BB}} \approx 3 \times 10^{-1} \text{ cm K}$. The FUV radiation emitted by the stars that are embedded in the cloud is absorbed by the dust and then re-emitted away as IR radiation. But if the cloud is optically thick we can even have a phenomenon of absorption of the dust IR radiation itself. This scenario is interesting since it happens when the stars form in very dense clouds, it must be carefully taken into account with radiative transfer models and it could eventually be used to get clues on star forming regions.

To conclude, this Section clearly shows that it is crucial an accurate photons diffusion model within a galaxy formation and simulation code, since the temperature of the grains is influenced only by the radiation field that flows through the ISM. Dust temperature is also an important parameter when we consider the processes where interstellar dust is involved, like its evolution and the formation of molecules such as H_2 and HD, that are known to be important coolants when the gas is metal-free. Because these coolants strongly influence the star formation, it is clear how much a detailed description of the radiation field is a critical issue.

2.5.4 Destruction

The dust distribution is not static during the evolution of the ISM: it is strongly influenced by the environment. A dust destruction process has been defined in [75] as any interaction between a grain and another “particle” (grain, atom, ion, nucleus, electron or photon) that leads to a net baryon loss from the grain - the resultant grain mass loss may be total.

In this work we deal with two kinds of destruction processes, i.e. (i) destruction by shocks and (ii) destruction via thermal sputtering. The first one

depends on the environment, and it is difficult to model within the framework of the NB-TSPH simulations, the second one depends only on the local gas parameters of the considered ISM volume and can be easily modeled.

In this Section these two destruction processes will be discussed in detail, while their implementation into our model will be presented in the Section 3.5.4.

Shock sputtering (low speed)

The physical explanation of this process is quite trivial; the dust is accelerated by a shock front, and when the grains impact together they are destroyed or damaged.

Note that we are not interested in what is the origin of the shock. To be more accurate, we assume that a shock front makes the ISM turbulent. This means that the shock changes the property of the ISM, or better, it changes the scenario, regardless of the characteristics of the shock itself. This remark will be clear in Section 3.5.4 where the model will be presented within the computational framework.

The model proposed in this work is mainly based on [68]. First, we consider a volume of ISM with a dust function distribution that is a power-law (i.e. $dn \propto a^{-3.5} da$). When a shock front perturbs this volume of gas, the dust grains accelerate to a given speed that depends on their mass. Small grains move faster than the bigger ones. This last assumption of a drift between different dimensions, allows us to introduce a relative motion between big and small grains, and to model therefore the dust population as a steady cloud of large grains that becomes the target of a moving cloud of small grains. This assumption permits to classify the grains into targets (the steady ones) and projectiles (the moving ones).

Generally speaking, the impact is determined by the number of the targets (n_t), the number of the projectiles (n_p) and a factor that depends on the properties of the grains, the rate coefficient (α_{impact}). The change in the number density of the grain population is therefore:

$$\dot{n} = \alpha_{\text{impact}} n_p n_t, \quad (2.45)$$

where α_{impact} is in cm^3/s , and the number density is in cm^{-3} , resulting in $\text{cm}^{-3}\text{s}^{-1}$ for \dot{n} as expected.

First we must consider the effects of the projectiles on the target grains. We assume that the masses and the velocities of the grains involved in the collisions determine the physics of the impact. Regardless of the relative speed of the colliders we have two cases. (a) If the mass of the projectile is small compared to the target mass the target will be partially damaged, while the

projectile will be totally destroyed. (b) On the other hand, if the mass of the projectile is similar to the target mass the target will be destroyed as the projectile. The model is shown in Fig. 2.2.

Thus, we have that the case (a) is when $m_{\text{proj}}/m_{\text{target}} < \tilde{m}$ and (b) if $m_{\text{proj}}/m_{\text{target}} \geq \tilde{m}$, where in both cases $0 < \tilde{m} < 1$ is a constant value that determines the limit between the two cases. This is usually $\tilde{m} = 0.5$.

When the ratio is lower than the \tilde{m} the target loses a fraction of its mass and the grain becomes smaller since $m = 4/3\pi a^3 \rho_{\text{gr}}$, where a is the grain size, ρ_{gr} is the mass density of the material (e.g. graphite or silicate for carbonaceous grains and silicates respectively). So, if a grain of mass m loses a fraction of mass fm , the mass after the impact will be $\hat{m} = m - fm = m(1 - f)$ and consequently its size becomes $\hat{a} = a(1 - f)^{1/3}$.

In the other case ($m_{\text{proj}}/m_{\text{target}} \geq \tilde{m}$) all the mass of the target goes in fragments and no residuals are present because $f = 1$.

In both cases the mass fraction fm goes into fragments according to the hypothesis that the fragments follow a power-law. This power-law is related to the total number density of the fragments after an impact as

$$n_{\text{frag}} = C_{\text{frag}} \int_{a_{\text{low}}}^{\hat{a}} a^{-3.5} da, \quad (2.46)$$

where a_{low} is the lower limit of the dust distribution, and C_{frag} is calculated considering that the total mass of the residuals is fm .

In the case (a) the target becomes smaller and consequentially, if we divide our dust distribution in bins of different size, the target grain moves from one bin to another. The i -th bin occupied by the grain before the impact obeys to $a_i < a < a_{i+1}$, but after the impact the new bin (j -th) will be determined by the relation $a_j < \hat{a} < a_{j+1}$.

After this analysis we expect that a grain population starting with a given power-law will change its distribution increasing the number of small dust grains, since all the processes described here destroy the grains. An example of this is described in the Section 3.5.4.

Another ingredient that has been neglected until now is the speed of the grains. This latter one influences the effectiveness of the impact, and we expect that slow grains have a smaller probability of damaging a target (as in the lower limit $v = 0$). In particular, under a certain speed, the impact is irrelevant. We define this speed as v_{frag} . The impact is therefore significant only when $v_{\text{pt}} > v_{\text{frag}}$, where v_{pt} is the relative speed between the projectile and the target.

A quantitative description of the effect of the velocity on the impact

process is described by an impact parameter. We define this as

$$\alpha_{\text{impact}} = \begin{cases} \sigma_{\text{pt}} v_{\text{pt}} & v_{\text{pt}} > v_{\text{frag}} \\ 0 & \text{else,} \end{cases} \quad (2.47)$$

where σ_{pt} is the geometric cross section, simply $\sigma_{\text{pt}} = \pi(a_{\text{p}} + a_{\text{t}})^2$, with a_{p} and a_{t} the sizes of the projectile and the target respectively. As indicated by the term σ_{pt} , the velocity increases the probability of an impact, and also the size of the colliding partners determines the probability of the impact, simply assuming that larger grains have more chances to impact.

All these ingredients gives the variation of the dust population per unit of time. A given bin of the dust distribution will change its number density in the following way that we describe considering three terms: (i) the mass lost that goes into fragments, (ii) the mass lost through remnants that change their size from a to \hat{a} and, finally, (iii) the mass gained from larger grains destroyed and forming smaller grains belonging to the considered bin. The equation describing the evolution for the i -th bin is therefore:

$$\dot{n}(i) = -\dot{n}_{\text{frag}}(i) - \dot{n}_{\text{rem}}(i) + \dot{n}_{\text{gain}}, \quad (2.48)$$

where the RHS corresponds to the three terms indicated above, and \dot{n}_{gain} sums the contribution from other bins.

The Eqn. (2.48) will be better discussed (with its implementation in the chemical code) in the Section 3.5.4.

Shock sputtering (high speed)

In the previous Section the sputtering model is based only on low velocities. The subject of this Section is the shock sputtering at higher speeds. At these velocities grains are destroyed and vaporized giving a part of their material back to the gas phase. The role of the sputtering is important in the physics of the ISM and a correct model should allow to find the average time scales for the destruction of the grains. According to [76], the time required to replenish the ISM with dust through stellar winds and SNe is about 2.5×10^9 yr. On the other side, dust grains are destroyed by SNe shocks, and their lifetime is about 5×10^8 yr according to [116, 96]. These values would reproduce a very small dust-to-gas ratio: the observed average one in the MW is small, but not so much, for this reason is more likely that the two time scales, at least for part of the history of the galaxy are similar. Indeed, similar time scales are adopted in chemical evolution model of dust for the MW like [38], where the two time scales are related by a factor of two. It follows that the

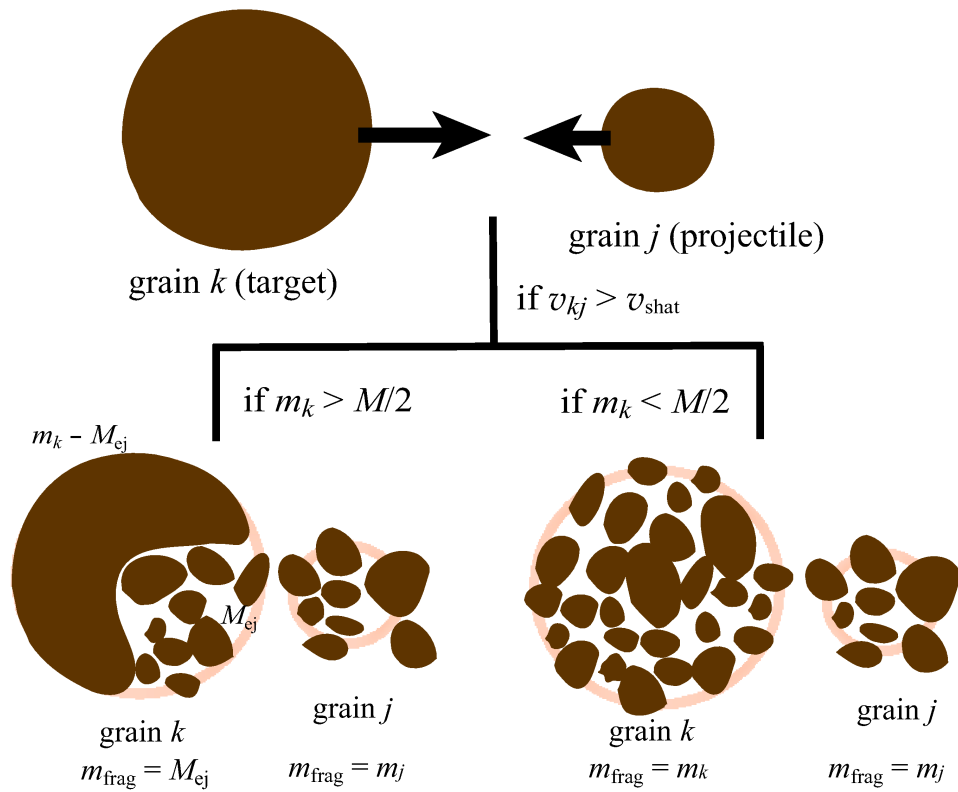


Figure 2.2: Target-projectile interaction. If the mass of the projectile is lower than the half of the mass of the target, the target is partially damaged (left), else the target is totally destroyed (right). In this picture $\tilde{m} = m_{\text{target}}/2$. From [68].

model used to describe the shocks is crucial to determine the abundance of dusts: the interplay between the destruction/accretion processes will rule dust evolution in the ISM.

Also in this case we consider that a small grain (projectile) hits a larger grain (target) and we consider the relative velocity between the collision partners.

An high-velocity impact can lead the shocked material to a multitude of phase transformations, including the transition between the low-pressure solid phase to the high-pressure solid phase, but also to melting and vaporization. The vaporization has a crucial importance in our model since it permits the interface between the gas-phase and the dust-phase.

An impact compresses the target up to a maximum value given by the strength of the shock generated by the impact. Hence, the shocked material will release itself and a rarefaction wave occurs. During such an expansion the material passes through different phases including the gas/vapor phase.

The kinetic energy of the shock is converted both in thermal and elastic energy. This latter one is totally converted into kinetic energy of the accelerated material upon the expansion. The thermal component is expended in performing the work of the rarefaction and again partially transformed into kinetic energy. Only the remaining thermal energy is used for vaporization. To summarize, the impact always increases the internal energy of the projectile, but only that part of the energy, that remains as thermal energy after the rarefaction, will lead to a vaporization process.

The impact creates different regions in the target: the material presents itself in many phases, going from fully vaporized to molten. Since it is difficult to keep track of all these intermediate phases, a good compromise is to assume a pressure threshold. When the pressure is above this limit, the vaporization occurs.

This scenario has been applied to the grain-grain collisions in the interstellar shocks by [125] to calculate the vaporized volume of material. Their analysis is based on three steps: (i) calculating the volume of vaporized material as a function of the velocity for given sizes of the target and the projectile. (ii) The volume is then averaged over the impact angle, since glancing collisions transfer smaller quantity of energy. (iii) This volume is also integrated over the speed distribution of the shock.

We are interested in the first two steps, since the third one depends on the velocity distribution that could be a free parameter of the chemical code (see Section 3.5.4 for further details about the method applied to the code ROBO).

To give an overview of the problem we discuss here in detail the model proposed by [125]. They consider a projectile of size (a_p) and a target (a_t)

with relative speed v , and a collision angle θ . These two objects collide and the impact forms a shock wave inside the target. When the rarefaction occurs, the result is that part of the material is vaporized, as we have just described. We can define a vaporization threshold v_t as

$$v_t = (1 + \mathcal{R})\sqrt{2\epsilon_v}, \quad (2.49)$$

where \mathcal{R} is the ratio between the pre-shock and post-shock densities which is $\mathcal{R} = 1$ if the projectile and target are composed by the same material. ϵ_v is the specific vaporization energy. The fraction of vaporized material on the projectile is

$$f_{v1} = \frac{M_{v1}}{M_P} = \frac{1}{2}(1 + 2\mathcal{R})\frac{h}{\sigma_{1i}}, \quad (2.50)$$

with h the overlapping volume $h = a_t/(a_p + a_t)$ and σ_{1i} a parameter that depends on the Mach's number of the shocking material.

The vaporized target mass relative to the projectile mass is

$$f_{v2} = \frac{M_{v2}}{M_P} = 0.78 \frac{1 + 2\mathcal{R}}{(1 + \mathcal{R})^{16/9}} \frac{1}{\sigma_{1i}^{1/9}} \left(\frac{\mathcal{M}_r^2}{\sigma_1 \mathcal{M}_1^2} \right)^{8/9} \mathcal{R}^{0.18}, \quad (2.51)$$

where the numbers of Mach are defined as

$$\begin{aligned} \mathcal{M}_r &= \frac{v_r}{c_0} \\ \mathcal{M}_1 &= \frac{v_1}{c_0}, \end{aligned} \quad (2.52)$$

with the relative speed defined as $v_r = v_1 + v_{1p}$, where v_1 is the target speed and v_{1p} is the projectile speed. Finally, c_0 is the sound speed in the given material.

The vaporized fraction is then

$$F_v = \frac{M_v}{M_T} = \frac{f}{1 + f}, \quad (2.53)$$

where f is

$$f = \left[f_{v1} + f_{v2} \left(1 - \frac{v_t}{v} \right)^{1/2} \right] \frac{M_P}{M_T}, \quad (2.54)$$

considering that this Equation is valid when $v \geq v_t$. The aforementioned parameters for different material are indicated in the Table 2.4.

We have presented here the model proposed by [125], adapted in such a way to simply describe the vaporization when a strong shock occurs in

Table 2.4: Hugoniot data and vaporization threshold data. ρ_0 is the density of the material, c_0 is its sound speed, s is an adimensional parameter (details within the text), ϵ_v is the specific vaporization energy, P_t is the pressure threshold and v_t is the velocity threshold. Note that the specific vaporization energy is indicated in units of 10^{11} , and the pressure is in units of 10^{12} . Note that graphite and amorphous carbon have the same properties. From [125].

Material	ρ_0 (g cm ⁻³)	c_0 (km s ⁻¹)	s	ϵ_v (erg g ⁻¹)	P_t (dyn cm ⁻²)	v_t (km s ⁻¹)
Silicate	3.3	5.0	1.23	4.8	5.4	19
Graphite	2.2	1.8	1.9	6.4	5.8	23
SiC	3.1	7.7	1.1	8.1	8.6	25
Ice	1.0	2.0	1.4	0.54	0.092	6.5

the ISM. The original model is really complicated because they consider many free parameters. Indeed, the intent of the authors was to generalize the problem starting from a set of basic equations. Since this approach would be too complicated for the purposes of this Thesis, in this Section we have proposed a simpler version. We suggest to the reader to refer to the original paper to deeply understand all the details of this accurate model. We then successfully applied this model to the chemical code ROBO as it will be shown later on in the next Chapter of this Thesis (details in the Section 3.5.4).

Thermal sputtering

The last process we describe is the thermal sputtering, that is dominant in the hot gas ($T > 10^6$ K). This process is important since it gives its contribute to the destruction of the dust grains in the ISM. As we already stressed, determining the destruction rate of the grains has a crucial importance to understand the evolution of the ISM, since the dust take part to many processes in the gas. Moreover, a large fraction of many of the heavy elements (e.g. Mg, Si, C and Fe) resides in the dust (the so-called phenomenon of the depletion of the elements in the gas), thus it is very important to quantify the amount of the material (mainly metals) released back from the dust to the gas phase in the destruction process. Indeed, the metals in the gas phase act as strong coolants, thus the thermal sputtering (and the destruction processes in general) plays a key role in the evolution of the ISM.

The processes that affect the dust when the ISM temperature overcomes

the 10^6 K threshold are various and can be described through the sputtering yield $Y(E, \theta)$ that is a function of the kinetic energy E and of the incident angle θ .

The low energy sputtering yield has been proposed by [36] as a semi-empirical formula for a normal incidence of the gas particles over the grains ($\theta = 0$). It is

$$Y(E, \theta = 0) = A \frac{(\epsilon - \epsilon_0)^2}{1 + (\epsilon/30)^{4/3}} \quad \epsilon > \epsilon_0, \quad (2.55)$$

where

$$\begin{aligned} \epsilon &= \eta E U_0^{-1}, \\ \eta &= 4\xi \frac{M_P M_T}{(M_P + M_T)^2} \end{aligned} \quad (2.56)$$

and

$$\epsilon_0 = \max[1, 4\eta], \quad (2.57)$$

where M_P is the projectile mass, M_T is the target mass, U_0 the mean binding energy per atom, and $\xi \leq 1$ is an efficiency factor which is unitary for atomic solids. $A \approx 8.3 \times 10^{-4}$ is a constant that is found to be independent of the projectile-target combination. The mean binding energy is $U_0 = 7.38$ for the graphite, $U_0 = 5.70$ for the silicates and $U_0 = 4.13$ for the iron .

Analogously, at high energies the sputtering yield has been calculated by [117] as

$$Y(E, \theta = 0) = \lambda s_n(E/E_A), \quad (2.58)$$

where

$$\lambda = 0.262\alpha \left(\frac{M_P}{M_P + M_T} \right) \frac{Z_P Z_T}{\sqrt{Z_P^{2/3} + Z_T^{2/3}}} \frac{I_H}{U_0}, \quad (2.59)$$

and $s_n(E/E_A)$ is the reduced nuclear stopping power from the Thomas-Fermi model. In the Eqn. (2.59) α is a parameter of order of one that depends on M_T/M_P (see [117], Fig. 13), Z_P and Z_T are the atomic numbers of the projectile and target respectively.

Even if the Eqns. (2.55) and (2.58) do not join smoothly, [36] have calculated the sputtering rates using these Equations. With this result they also give the lifetime for dust grains in an environment with $T \geq 10^6$, obtaining

$$\tau = \frac{a}{|da/dt|} \approx 2 \times 10^4 \frac{a}{0.01 n_H} \text{ yr}, \quad (2.60)$$

where a is the grain size in μm and n_H is the density of the gas in cm^{-3} .

2.5.5 Formation of molecules

The presence of dust has been observed up to redshift $z \approx 6.2$ [90] using the light from a QSO located at this redshift and the trend of the observations seems to confirm the presence of galaxies already in place and highly obscured by dust at high redshift. The kind of dust that usually explain the main features of the observations is the classical mixture based on the two components silicates and some kind of amorphous carbon, like graphite (respectively called in this work silicates and carbonaceous grains). These observations confirm that dust is already present when the formation of the earlier structure occurred, and underlines the importance of the dust analysis also when we study the evolution of the large structure of the Universe at high redshift. In the actual high- z scenario, the appearance of the PAH features and graphite extinction bump in the UV are both connected to the delayed injection of carbon by AGB stars, as it has been shown with observations of galaxies of different metallicity [39, 40, 53, 41]. In the early Universe before that most massive AGB stars start to contribute to the dust budget, only SNe are injecting dust, mainly silicates, in the ISM. Recently, it has been also shown in [41] and [34], that anyway even in these high redshift galaxies there should be enough time such that a significant amount of dust may be produced by accretion in the ISM and therefore dust would not simply be stardust. The role played by SNe could be in that case to mainly inject seeds for the grain growth in the ISM.

In this Section we will describe a key aspect of the dust in the ISM: the formation of molecules catalyzed by the dust. If dust is available in the high redshift Universe, this formation channel of the molecules may happen and this is crucial because the cooling by molecules is of primary importance.

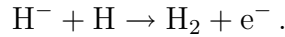
In the previous Section we described how the formation of molecules like H_2 and HD is very important during the evolution of the ISM. In particular, the molecules are important coolant when the gas is metal-free, because without the contribution of such molecules a metal-free gas can not reduce its temperature enough to form stars. This is the case of a primordial gas where the abundances of the elements are only due to the Big Bang nucleosynthesis, which produces hydrogen, helium, deuterium and lithium, as well as their ions. These atoms can not cool the ISM, but they allow the formation of linear molecules as the aforementioned H_2 and HD.

The molecular hydrogen allows the ISM to cool down to a temperature of few hundred of kelvins, since its first rotationally excited state is at about 500 K. The HD permits a lower cooling (below 100 K) because it has a non-zero dipole moment, being formed by two different atoms. The first excited state

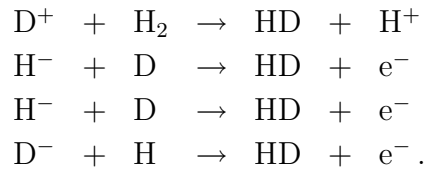
here is about at 150 K. So, the molecular hydrogen is important in the first cooling phase and, when the gas is cold enough, the HD turns to be more important than the H₂.

There are in general two ways to form these molecules, through the reactions of the gas phases and through the chemistry of the dust phase.

In the gas-phase the formation of H₂ is boosted by the presence of free electrons. The electrons allow the formation of the H⁻ that is one of the reactants of the highly efficient reaction



For the HD we have in the gas-phase



These coolants are important until the gas is metal-free, but once the pollution of the metals occurs, the metals and the dust assume a key role. The metals are important because they are direct coolants through atomic lines, and their effect on the temperature is strong (see [113, 89]). The dust is not an efficient coolant by itself, but its role in the formation of the main coolants has been demonstrated (e.g. [26] and their subsequential studies).

To understand the mechanism of the processes that allow the formation of molecules over the grain lattice, we introduce the description proposed by [26] for the molecular hydrogen, that can be extended also to HD. We propose their model with its formalism, with the purpose to show the differences and the similarities between the gas phase and the dust phase. Their analysis of the H₂ formation over the dust is modelled with the Langmuir kinetics, a semi-analytical isothermal model for gases adsorbed by solids. It is based on four assumptions: (i) the surface of the adsorbent is uniform or, analogously, all the adsorption sites are equivalent. The adsorption sites are where the reactants take part to the reaction. (ii) Adsorbed molecules do not interact. (iii) All the adsorption occurs through the same mechanism. (iv) At the maximum adsorption, only a single layer is formed: molecules of adsorbate do not deposit on already adsorbed molecules of adsorbate, but only on the free surface of the adsorbent.

To summarize, the Langmuir model asserts that over the grain lattice the species (a) accrete, (b) migrate, (c) react and (d) evaporate if the thermal energy is enough to produce such a process. The model applied to dust grains

has two assumptions more, namely: (i) atomic mobility is a combination of quantum tunneling and thermal diffusion and (ii) atoms can bind to the surface in the chemisorption (CA) sites or in the physisorption (PS) sites. The chemisorbed atoms are strongly bound to the surface and become free to move only at high temperatures (few hundred Kelvins), and the chemisorbed atoms are weakly bound and need only few Kelvins to move.

Since they deal only with H_2 , they use CA and PS hydrogen and PS molecular hydrogen. Using three differential equations, it is possible to retrieve the H_2 quantity over the lattice and, with this datum, to calculate the quantity of desorbed (unbound from the lattice and then restituted back to the gas) molecular hydrogen.

In particular, the first Equation is

$$\dot{H}_p = F(1 - H_p - H_2 - \alpha_{pc}) - 2\alpha_{pp}H_p^2 + \alpha_{cp}H_c(1 - H_p) - \beta_p H_p, \quad (2.61)$$

where F is the incoming flux of H atoms to the surface, α_{ij} is the diffusion rate from the i -th site to the j -th site (with i and j that can be PS sites or CA sites, indicated with p and c respectively) and β_k is the desorption rate of the k -th population, namely $\beta_k \propto \exp(-E_k/k_b T)$ with E_k the desorption energy of the k -th species, T the lattice temperature and k_b the Boltzmann constant. Eqn. (2.61) asserts that the variation of the H_p over a time-step is given by the incoming flux (F), the rate of atoms going to CA sites (α_{pc}), the recombination of PS atoms with PS atoms (α_{pp}), the recombination of PS atoms with atoms coming from CA sites (α_{cp}), the atoms coming from CA sites into free PS sites and, finally, the evaporation rate of the PS atoms (β_p). This mechanism is consistent with the model described above where the lattice is formed by PS sites and CA sites, and the atoms move from site to site. The incoming flux and the evaporation rate represent the exchange with the gas phase.

Analogously \dot{H}_c has a similar equation

$$\dot{H}_c = \alpha_{pc}H_p F(1 - H_c) - \alpha_{cp}H_c + \alpha_{pc}H_c - \alpha_{pc}H_p H_c - 2\alpha_{cc}H_c^2 - \beta_c H_c, \quad (2.62)$$

but in this case the RHS term is given by atoms coming from PS sites to empty CA sites (α_{pc}), CA atoms going into PS sites (α_{cp}), the recombination of CA atoms with atoms coming from PS sites (α_{pc}), the recombination of CA atoms with other CA atoms (α_{cc}) and, finally, the evaporation rate of CA atoms (β_c).

The last of the three differential equations describes the variation of the molecular hydrogen

$$\dot{H}_2 = \mu(2\alpha_{pp}H_p^2 + \alpha_{cp}H_c H_p + \alpha_{pc}H_p H_c + \alpha_{cc}H_c^2) - \beta_2 H_2, \quad (2.63)$$

with μ the fraction of molecular hydrogen that remains attached to the surface after its formation. The other terms have the same meaning as in the previous Equations, except $\beta_2\text{H}_2$ which is the evaporation rate of the molecular hydrogen.

These Equations are then integrated to obtain the molecular hydrogen formed. Furthermore, this model can be extended to HD and D₂, once considered also the CA and the PS sites for the deuterium. In this case there are four more Equations, i.e. \dot{D}_p , \dot{D}_c , \dot{D}_2 and \dot{HD} , that are similar to the previous ones.

This model permits to obtain the formation rate for the molecular hydrogen H₂ in the ISM for different temperatures of the gas and dust. These data can be used to create a temperature depending (both from dust and gas) function f to retrieve the rate of formation as $R_{\text{H}_2} = f(T_g, T_d)n_{\text{H}}$, where n_{H} is the number density of the hydrogen in the gas phase, while T_g and T_d are the temperatures of the gas and dust respectively. Note that HD has its own analogous equation. This is the approach used in our code ROBO: this method avoids to solve the system of differential Equations formed by Eqns. (2.61), (2.62) and (2.63), using less CPU-time and consequently being more versatile. In the Chapter dedicated to ROBO this aspect will be discussed in detail.

To conclude, it is worth stressing again the following point: the dust phase is strictly connected to the metallicity. Indeed, dust is mainly formed by metals produced by stars that continuously enrich the ISM, generation after generation. We can not have dust if the ISM is not at least a bit enriched in metals. Once we have dust, we can form molecules via the channel we just described. However, the metal cooling is more efficient than the molecular cooling. It follows that in principle if the environment is highly enriched, the presence of the metals could make the catalyzing effect of the dust negligible and the cooling by molecules could be overwhelmed by the metals. This is clearly not the case of the very low-metal environments (like it could happen for high- z young environments), where the dust produce a significant amount of molecules, and their contribution is fundamental.

2.5.6 Heating and cooling

When the dust grains are impinged by a radiation field of far-ultraviolet photons, the photoelectric effect may eject electrons from the dust to the gas phase. If the photoelectric emission occurs at the surface of the dust grain, the ejected electron will have some eV of energy. This value is the difference

between the energy $h\nu$ of the photon and the work function W of the grain material, that is $E = h\nu - W$, where $W \approx 5$ eV. If this process reaches an high efficiency the total effect is non negligible, but becomes important.

Indeed, the photoelectric heating through photoelectric emission is thought to be one of the dominant effect in the heating of the ISM, warming the nearby ISM. This effect is observable in the photons dominated regions (also known as photo-dissociated regions - PDR) where the FUV photons are the dominant heating source of the gas, and the fine structure lines show that only the 0.1 – 1% of the incoming energy is converted into heating.

The simple description proposed above with $E = h\nu - W$ is quite rough. Actually, a fraction of the energy absorbed is dissipated to overcome the W . Another part of the energy is lost in inelastic collisions of the excited electron with the atoms of the grain while it moves toward the surface of the grain. The last effect that requires energy is the Coloumb potential due to the positive charge formed by the lack of the electrons already ejected. The remaining energy is then converted to heating via inelastic collisions with the species in the gas phase.

The effective heating Ψ depends on the charge and size of the grains and it is

$$\Psi(a) = \sum_Z [H(a, Z) - C(a, Z)] f(a, Z) n(a) a, \quad (2.64)$$

that is a function of the grain size a . $H(a, Z)$ is the heating that depends on the size and charge of the given grain (this term will be discussed in detail in the Section 3.5.5); The term $C(a, Z)$ is the energy removed by the recombination of the electrons with the dust grains (i.e. a cooling, that will be discussed later in this Section). The last terms are the function $f(a, Z)$ that represents the probability of finding a grain in the state characterized with the charge Z and the size a , and, finally, $n(a)$ is the number density of the grains of size a . The sum runs over all the possibly charge states. The distribution of the charge of a grain is represented by a Gaussian function peaked at some Z , depending on the size of the grain (see Fig. 2.3 for an example).

The $\Psi(a)$ allows us to find the net heating simply through the following Equation

$$H_{\text{net}} = \int_{a_-}^{a_+} \Psi(a) da, \quad (2.65)$$

where a_{\pm} are the upper and the lower size limits of the dust distribution. The meaning of this Equation is straightforward.

From the Eqn. (2.64) it is clear that the distribution of the charge plays an important role in the whole process. This means that knowing the distri-

bution of the charge over the grain is rather fundamental. This point will be discussed in the Section 3.5.5, giving a detailed description of the process.

The other phenomenon connected with the energy exchange between dust grains and gas particles is the cooling, that depends on the fact that grains act as sinks for the energy. Let us consider an atom in the gas phase with a kinetic energy equivalent to a temperature of 100 K. If it sticks to a grain with a temperature of 20 K, the equivalent energy of $100 - 20 = 80$ K is lost from the gas. This energy is radiated away and this process is actually a cooling. A simple calculation shows that the energy lost is density dependent:

$$\Lambda_d \approx 3 \times 10^{-31} n^2 \frac{T}{100 \text{ K}} \text{ erg cm}^{-3} \text{ s}^{-1}, \quad (2.66)$$

and it is clearly not important in the low-density regions.

2.6 ISM: Conclusions

The purpose of this Chapter was to introduce the reader of the Thesis to the chemistry of the ISM, giving a description of the ISM processes and their peculiar issues. It is easy to recognize that modelling the ISM is a formidable task, because there are many processes that interact together, and also because such processes are not known in detail. This last problem is frequent in astrophysics, since, even if the single physical process is well-known, the parameters that control it are usually obscure. This fact is striking when we deal with the ISM. For instance, the rate coefficient for the chemistry reactions are not completely determined in the ISM conditions and in such a case the errors give different results when applied to ISM modelling (see [57] for a review). When we deal with or we introduce the dust into the models, the scenario becomes even more complex, since the dust grains behavior is poorly known in the different regions of the Universe, in particular at high redshift.

The problem resides in the fact that all these ingredients are mixed together and their uncertainties could be amplified when we create a complex model that considers the chemistry, the cooling and heating, the dust grains, the UV radiation and many more processes. Mixing together all these different ingredients, it is a complicated task since these phenomena interact with a complicate behavior and each one of them has an elaborate description.

This complicated interaction becomes even more clear when we implement the model into the algorithms. In particular, as we have already seen, the chemistry needs a stiff network of differential equations. If we add the cooling

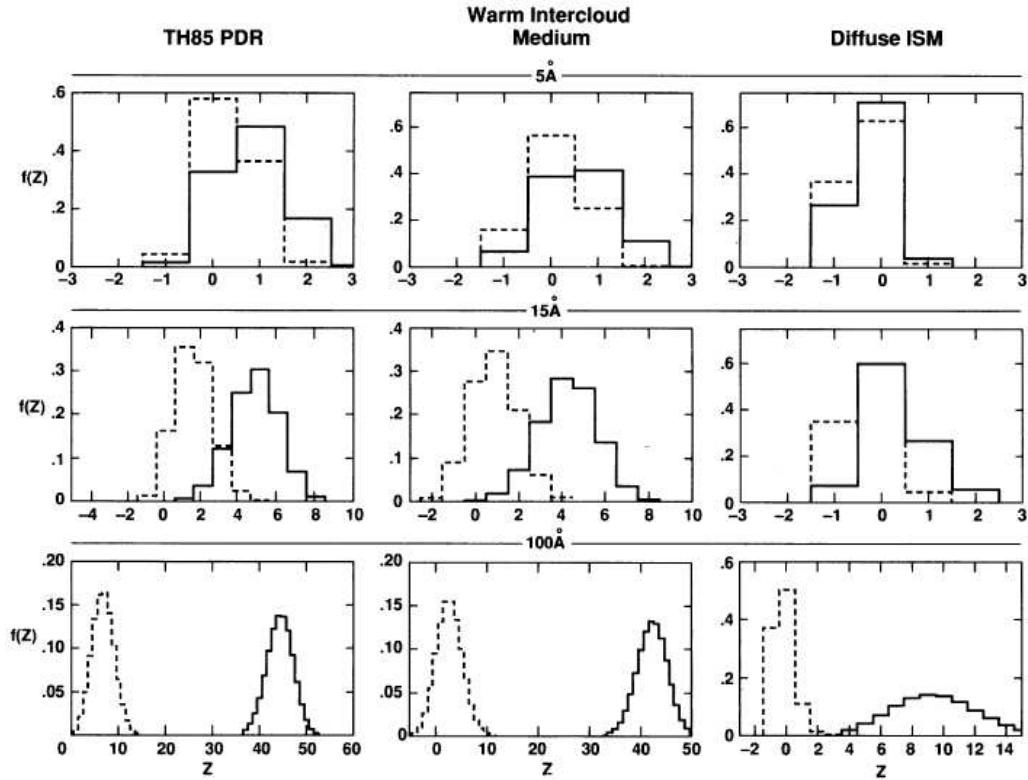


Figure 2.3: The distribution of charge in different environments (PDR, WIM and diffuse ISM), and for different grain sizes (5, 15 and 100 Å). The solid lines represent spherical grains of a given radius, while the dashed lines are for planar particles of the same radius. The purpose of this picture is to illustrate the shape of the distribution of charge. From [5] (in the same paper are also given the physical properties of the environments considered - see their Table 2).

process, we must consider that at each integration time-step the cooling needs to solve a linear system to determine the number density of the different quantum states for each species, in order to calculate the actual cooling.

Our volume of gas interacts also with the external UV radiation which means, numerically speaking, integrating the impinging radiation field together with the photo-ionization cross-sections over all the wavelengths considered.

This scenario becomes more intricate introducing dust. Dust grains are a non-negligible component of the ISM and they are difficult to analyze as we have seen in the previous Sections. The dusty component interacts with the chemistry of the gas, first catalyzing the formation of H_2 and HD, and then exchanging the carbon and the silicon/magnesium/iron atoms with the gas-phase through accretion and vaporization (considering only graphite grains and silicates). Dust grains have their own evolution too, that is size depending, and is determined by the shocks and the temperature of both gas and dust. Finally, the grains also interact with the UV field that changes the temperature of the dust and also determines the heating through photoelectric ejection of electrons. This latter process requires to know the distribution of the electric charge on the grains, meaning that we must solve a linear system at each integration step.

The scenario described above has been developed into a code called ROBO, that is the subject of the following Chapter.

Chapter 3

ROBO

“Forty-two!” yelled Loonquawl. “Is that all you’ve got to show for seven and a half million years’ work?”

“I checked it very thoroughly,” said the computer, “and that quite definitely is the answer. I think the problem, to be quite honest with you, is that you’ve never actually known what the question is.”

The Hitchhiker’s
Guide to the Galaxy¹

3.1 Introduction

Modeling the gas chemistry is an important step towards correctly describing the growth of cosmological structures, the formation and evolution of galaxies, and star formation in general. For instance, the molecular hydrogen is one of the most efficient coolant and its abundance eventually determines the total amount of stars in the Universe. Both structure growth and galaxy formation and evolution are customarily investigated by means of large numerical simulations in which a wide set of chemical reactions taking place in the ISM should be considered to get and follow the key molecules (elemental species in general) eventually governing the efficiency of the star formation and gas cooling. However, we must face the growing standard complexity of a typical NB-TSPH model which includes: particles of dark matter, particles

¹Douglas Adams, The Hitchhiker’s Guide to the Galaxy, 1979, Pan Books, ISBN 0-330-25864-8

of baryonic matter (this latter in form of stars and gas in turn divided in several thermal and chemical phases, such as cold, warm and hot, atomic and molecular, neutral and ionized), sources of energy heating and cooling, energy feed-back and easily many other physical processes. For this reason too a detailed chemical description of the ISM would drastically reduce the computational performances of any numerical algorithm (code) one may adopt to this purpose. This requires a strategy to optimize the chemical accuracy of the ISM model and the computational speed.

In this Chapter we present a new model of the ISM and the associated code we have developed to explore the ISM properties over large ranges of the physical parameters and at the same time to cope with the above difficulties. The model and companion code are named ROBO².

The model deals with an ideal ISM element of unit volume, containing gas and dust in arbitrary initial proportions, whose initial physical conditions are specified by a set of parameters, which is let evolve for a given time interval. The history leading the element to that particular initial physical state is not of interest here. The ISM element is mechanically isolated from the host environment, i.e. it does not expand or contract under the action of large scale forces, however it can be interested by the passage of shock waves originated by physical phenomena taking place elsewhere (e.g. supernova explosions). Furthermore, it does not acquire nor lose material, so the conservation of total mass applies, even if its chemical composition can change with time. It is immersed in a bath of UV radiation generated either by nearby or internal stellar sources and in a field of cosmic ray radiation. It can generate its own radiation field by internal processes and so it has its own temperature, density and pressure, each other related by an Equation of State (EoS). If observed from outside, it would radiate with a certain spectral energy distribution. For the aims of this study, we do not need to know the whole spectral energy distribution of the radiation field pervading the element, but only the UV component of it. Given these hypotheses and the initial conditions, the ISM element evolve toward another physical state under the action of the internal network of chemical reactions changing the relative abundances of elemental species and molecules, the internal heating and cooling processes, the UV radiation field, the field of cosmic rays, and the passage of shock waves. In view of the future applications of this model in dynamical simulations of galaxies, the integration time interval is chosen in such a way that (i) it is sufficiently long to secure that the secular evolution of the gas properties is achieved, (ii) it is short enough to secure that the physical properties of the ISM at each instant are nearly independent of the external variations of the

²The name means “thing” in some northern Italy dialects.

large scale properties of the system hosting the ISM element. In other words, ROBO associates to any initial state (a point in the multidimensional space of the physical parameters) a final state (another point in the same space) through a path. The model is like an operator determining in the space of the physical parameters conditions the vector field of the local transformations of the ISM from one initial state to a final one.

The new ISM model stands on recipes of the internal physical processes falling in between those developed by [59] and [118]. The first one follows the thermal and chemical evolution of the low metallicity gas in large numerical simulations. The chemical network includes a detailed treatment of H and He but neglects the molecules formed with heavy elements (like CO and similar). Dust is included to compute its contribution to the formation of molecular hydrogen, however its evolution is not calculated. The chemical code is an on-the-fly routine, running as part of a wider code following cosmological simulations of structure growth.

The model proposed by [118] uses the non-equilibrium treatment for hydrogen-like species and the standard equilibrium approximation for all the remaining chemical species. It does not take any type of dust into account. To calculate the cooling rates [118] use CLOUDY [47] and get the cooling rates as a function of temperature, density and metallicity. By doing this, it is possible to include a large chemical network and a wide set of coolants, but the price to pay is that several over-simplifications of the problem are mandatory, e.g. the assumption of ionization equilibrium.

Our ISM model and associated code ROBO not only can describe in great detail the gas evolution but also includes large chemical networks and the presence of various types of dust of which they follow the chemistry and the complex interplay between grain destruction and formation. Many gas and dust components are taken into account, among which we recall the molecular hydrogen and the metal coolants [113, 89] or HD [95]. To track the evolution of these components the ISM model and ROBO take into account various physical processes that may affect the behavior of the whole system. For instance, dust is very efficient in forming both H₂ and HD [24]. The inclusion of dust formation and destruction is a formidable task. Among other processes, dust can be destroyed by shocks that deserve special care to be properly modeled. Here we have considered two different approaches. The first one make use of a mean shock speed that is assumed to be the same for all gas particle, neglecting the effects of the environment. In reality this is too crude a description. The second approach starts from the notion that the shocks develop when the motion of the gas particles becomes turbulent and that the distribution of turbulent velocities is well described by the Kolmogorov law. This is significantly better than the previous case and it is

the approach we prefer.

In this Chapter we describe in detail the physics of the ISM model that is used by ROBO. The problem and associated code are divided in three parts, mirrored by the structure of the Sections of this Chapter: gas chemistry, cooling and heating and finally dusts. All these aspects are mutually coupled and overlapped.

3.2 ROBO: chemistry

The kernel of the numerical code modeling the gas chemistry is the network of chemical reactions among different elemental species (atoms and molecules, neutral or ionized dust grains of different type) and free particles (such as the electrons), the network of photo-chemical reactions between the above elemental species, and the radiation field. In addition to this, we must include all the processes creating and destroying molecules and dust grains with particular attention to those most efficient for the cooling of the gas. For this reason our chemical network follows species like H_2 , HD and metals (C, O, Si, Fe, and their ions).

The number of reactions depends on how many species are tracked and how many details are included in their description. A number of codes study the behavior of the ISM [27, 77, 52, 3, 60] each of which with a different number of species to follow and a different degree of sophistication of the physical processes taken into consideration.

We keep track of the following 23 elemental species plus the free electrons: H, H^+ , H^- , H_2 , H_2^+ , He, He^+ , He^{++} , C, C^+ , Si, Si^+ , O, O^+ , Fe, Fe^+ , D, D^+ , D^- , D_2 , HD, HD^+ , and e^- . We add CO, CH, CH_2 , CH_2^+ and CH_3^+ , reaching the total of 27. The last molecules are introduced as intermediate reactants/products of the minimal CO network described below.

These species are divided into five groups. The first one contains hydrogen-only based species. The second group lists helium and its ions. Carbon, oxygen, silicon and iron with their ions form the third group. The last group is composed by deuterium-based species, in which HD plays the key-role in the gas cooling. The last one, as already described, hosts the molecules participating to the CO network. Electrons constitute the link between the five groups.

The reactions in which all the above species are involved are

- collisional ionization ($A + e^- \rightarrow A^+ + 2e^-$),
- photorecombination ($A^+ + e^- \rightarrow A + \gamma$),

- dissociative recombination ($A_2^+ + e^- \rightarrow 2A$),
- charge transfer ($A^+ + B \rightarrow A + B^+$),
- radiative attachment ($A + e^- \rightarrow A^- + \gamma$),
- dissociative attachment ($A + B^- \rightarrow AB + e^-$),
- collisional detachment ($A + e^- \rightarrow A + 2e^-$),
- mutual neutralization ($A^+ + B^- \rightarrow A + B$),
- isotopic exchange ($A_2^+ + B \rightarrow AB^+ + A$)
- dissociations by cosmic rays ($AB + CR \rightarrow A + B$),

where A and B are two generic atoms.

The chemical network governing the ISM model is a classical system of differential equations in which each equation is a Cauchy problem of the form

$$\frac{dn_i(t)}{dt} = \sum_{lm} R_{lm}(T)n_l(t)n_m(t) - \sum_j R_{ij}(T)n_i(t)n_j(t), \quad (3.1)$$

where $n_i(t)$ is the number density of the i -th species with known initial value $N_i(0)$. In Eqn. (3.1) $R_{lm}(T)$ is the rate of the reaction between the l -th and the m -th species expressed in units of cm^3/s . Eqn. (3.1) is written as the sum of all the reactions forming the i -th species

$$\sum_{lm} R_{lm}(T)n_l(t)n_m(t), \quad (3.2)$$

minus the sum of all the reactions destroying the i -th species

$$\sum_j R_{ij}(T)n_i(t)n_j(t). \quad (3.3)$$

The indexes i, j, l , and m run from 1 to 27 as in the list of elemental species and free electrons we have already mentioned. The one to one correspondence between the indexes in the Eqn. (3.1) and elemental species is given in Table 3.1.

To clarify the meaning of Eqn. (3.1) we show the case of a two-reaction system

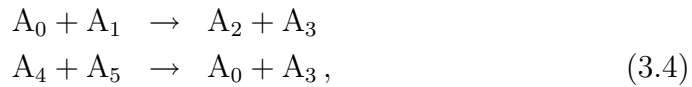


Table 3.1: Elemental species used in ROBO and their indexes. In the first row the species based only on hydrogen (from 1 to 5), in the second row the species on helium (from 6 to 8), in the third row metals and their ions (from 9 to 16), fourth row contains species based on deuterium (from 17 to 22), the fifth row contains the species that belongs exclusively to the CO network (23 to 27) and, finally, in the last row the electrons (the 28th specie).

H-based (1-5)	H	H ⁺	H ⁻	H ₂	H ₂ ⁺			
He-based (6-8)	He	He ⁺	He ⁺⁺					
Metals (9-16)	C	C ⁺	O	O ⁺	Si	Si ⁺	Fe	Fe ⁺
D-based (17-22)	D	D ⁺	D ⁻	D ₂	HD	HD ⁺		
CO network (23-27)	CO	CH	CH ₂	CH ₂ ⁺	CH ₃ ⁺			
Electrons (28)	e ⁻							

where A_i is the numerical density of the generic species in unit of cm^{-3} . Looking at the density variation of the species A_0 over the time step dt the density n_{A_0} changes as

$$\begin{aligned}
 dn_{A_0}(t + dt) = & - k_{01}(T)n_{A_0}(t)n_{A_1}(t)dt \\
 & + k_{45}(T)n_{A_4}(t)n_{A_5}(t)dt.
 \end{aligned}
 \tag{3.5}$$

In this Equation the positive term is due to the second reaction (between A_4 and A_5) that increases the total quantity of A_0 (and also A_3), while the negative term is due to the first reaction in which A_0 is destroyed because it reacts with A_1 to form A_2 and A_3 .

We adopt here a minimal description containing only the 27 species listed in Table 3.1 and the 57 reactions listed in Tables 3.2, 3.4, 3.5, and 3.8 and described below in some detail. The Tables 3.2, 3.4, and 3.5 also sample the chemical reactions according to the same four groups in which we have separated the elemental species depending on the type of reaction and the information to our disposal to derive the reactions rates. In doing this, the notation in use may appear rather intrigued. This is made on purpose and the main motivation is that we want to keep the same formalism adopted in literature for the sake of easy comparison. First of all, there are 64 reactions among particles either atoms or molecules or free electrons. Each reaction is identified by a progressive number going from 1 to 64 and so the associated reaction rate named k_n (with n from 1 to 64). Each reaction will be a term of the right hand side of the 27 differential equations of system (2.5) and the associated reaction rate will coincide with one of the R_{ij} terms of Eqns.

Table 3.2: The reaction rates among hydrogen, deuterium and helium. All the rates are in cm^3/s . The gas temperature T is in Kelvin; the electron temperature T_e is in eV. References: reactions 1 to 20 [60], reaction 21 [57]

Reaction	Reaction Rate
1 $\text{H}_2 + \text{D} \rightarrow \text{H} + \text{HD}$	if($T \leq 2 \times 10^3 \text{K}$) $k_1 = \text{dex}[-56.4737 + 5.88886 \log(T) + 7.196292 \log(T)^2 + 2.25069 \log(T)^3 - 2.16903 \log(T)^4 + 0.317887 \log(T)^5]$ if($T > 2 \times 10^3 \text{K}$) $k_1 = 3.17 \times 10^{-10} \exp(-5207/T)$
2 $\text{HD} + \text{H} \rightarrow \text{H}_2 + \text{D}$	if($T \leq 200 \text{K}$) $k_2 = 5.25 \times 10^{-11} \exp(-4430/T)$ if($T > 200 \text{K}$) $k_2 = 5.25 \times 10^{-11} \exp[(-4430/T) + (173900/T^5)]$
3 $\text{D}^+ + \text{H}_2 \rightarrow \text{H}^+ + \text{HD}$	$k_3 = 10^{-9} [0.417 + 0.846 \log(T) - 0.137 \log(T)^2]$
4 $\text{H}^+ + \text{HD} \rightarrow \text{D}^+ + \text{H}_2$	$k_4 = 1.1 \times 10^{-9} \exp(-488/T)$
5 $\text{H}^+ + \text{D} \rightarrow \text{D}^+ + \text{H}$	if($T \leq 2 \times 10^{10} \text{K}$) $k_5 = 2 \times 10^{-10} T^{0.402} \exp(-37.1/T) - 3.31 \times 10^{-17} T^{1.48}$ if($T > 2 \times 10^5 \text{K}$) $k_5 = 3.44 \times 10^{-10} T^{0.35}$
6 $\text{H} + \text{D}^+ \rightarrow \text{D} + \text{H}^+$	$k_6 = 2.06 \times 10^{-10} T^{0.396} \exp(-33/T) + 2.03 \times 10^{-9} T^{-.332}$
7 $\text{HD} + \text{D}^+ \rightarrow \text{D}_2 + \text{H}^+$	$k_7 = 10^{-9}$
8 $\text{H}^+ + \text{D}_2 \rightarrow \text{D}^+ + \text{HD}$	$k_8 = 2.1 \times 10^{-9} \exp(-491/T)$
9 $\text{H}_2 + \text{H}^+ \rightarrow \text{H}_2^+ + \text{H}$	$k_9 = 10^A$ with $A = \sum_{i=0}^7 a_i \log(T)^i$, with a_i as in Table 3.6
10 $\text{H} + \text{H}^+ \rightarrow \text{H}_2^+ + \gamma$	$k_{10} = \text{dex}[-19.38 - 1.523 \log(T) + 1.118 \log(T)^2 - 0.1269 \log(T)^3]$
11 $\text{H} + \text{H}_2^+ \rightarrow \text{H}_2 + \text{H}^+$	$k_{11} = 6.4 \times 10^{-10}$
12 $\text{H} + \text{HD}^+ \rightarrow \text{H}_2 + \text{D}^+$	$k_{12} = 10^{-9}$
13 $\text{H}^+ + \text{e}^- \rightarrow \text{H} + \gamma$	$k_{13} = 2.753 \times 10^{-14} (315614/T)^{1.5} [1 + (1115188/T)^{0.407}]^{-2.242}$
14 $\text{D}^+ + \text{e}^- \rightarrow \text{D} + \gamma$	$k_{14} = k_{13}$
15 $\text{H}_2^+ + \text{e}^- \rightarrow 2\text{H}$	if($T \leq 617 \text{K}$) $k_{15} = 10^{-8}$ if($T > 617 \text{K}$) $k_{15} = 1.32 \times 10^{-6} T^{-0.76}$
16 $\text{HD}^+ + \text{e}^- \rightarrow \text{H} + \text{D}$	$k_{16} = 7.2 \times 10^{-8} T^{-0.5}$
17 $\text{H} + \text{e}^- \rightarrow \text{H}^- + \gamma$	$k_{17} = \text{dex}(-17.845 + 0.762 \log(T) + 0.1523 \log(T)^2 - 0.03274 \log(T)^3)$
18 $\text{D} + \text{e}^- \rightarrow \text{D}^- + \gamma$	$k_{18} = k_{17}$
19 $\text{H} + \text{e}^- \rightarrow \text{H}^+ + 2\text{e}^-$	$k_{19} = \exp[-32.71396786 + 13.5365560 \ln(T_e) - 5.73932875 \ln(T_e)^2 + 1.56315498 \ln(T_e)^3 - 0.287705600 \ln(T_e)^4 + 3.48255977 \times 10^{-2} \ln(T_e)^5 - 2.63197617 \times 10^{-3} \ln(T_e)^6 + 1.11954395 \times 10^{-4} \ln(T_e)^7 - 2.03914985 \times 10^{-6} \ln(T_e)^8]$
20 $\text{D} + \text{e}^- \rightarrow \text{D}^+ + 2\text{e}^-$	$k_{20} = k_{19}$
21 $\text{H}^- + \text{H} \rightarrow \text{H}_2 + \text{e}^-$	$k_{21} = 10^{-9} \xi$, $\xi = [0.65, 5.0]$,

Table 3.3: Continuation of Table 3.2. The reaction rates among hydrogen, deuterium and helium. All the rates are in cm^3/s . The gas temperature T is in Kelvin; the electron temperature T_e is in eV. References: for reactions 22, 23, 24 and 27 see [60], for 25 and 26 see [57].

Reaction	Reaction Rate
22 $\text{D}^- + \text{H} \rightarrow \text{HD} + \text{e}^-$	$k_{22} = 10^{-9}\xi/2, \xi=[0.65, 5.0]$
23 $\text{H}^- + \text{D} \rightarrow \text{HD} + \text{e}^-$	$k_{23} = k_{22}$
24 $\text{D}^- + \text{D} \rightarrow \text{D}_2 + \text{e}^-$	$k_{24} = k_{21}$
25 $\text{H}^+ + \text{D}^- \rightarrow \text{HD}^+ + \text{e}^-$	$k_{25} = 1.1 \times 10^{-9}(T/300)^{-0.41}$
26 $\text{D}^+ + \text{H}^- \rightarrow \text{HD}^+ + \text{e}^-$	$k_{26} = k_{25}$
27 $\text{H}^- + \text{e}^- \rightarrow \text{H} + 2\text{e}^-$	$k_{27} = \exp[-18.01849334 + 2.36085220 \ln(T_e)$ $-2.82744300 \times 10^{-1} \ln(T_e)^2$ $+1.62331664 \times 10^{-2} \ln(T_e)^3$ $-3.36501203 \times 10^{-2} \ln(T_e)^4$ $+1.17832978 \times 10^{-2} \ln(T_e)^5$ $-1.65619470 \times 10^{-3} \ln(T_e)^6$ $+1.06827520 \times 10^{-4} \ln(T_e)^7$ $-2.63128581 \times 10^{-6} \ln(T_e)^8]$

Table 3.4: Continuation of Table 3.3. Reaction rates among hydrogen, deuterium and helium. All the rates are in cm^3/s . The gas temperature T is in Kelvin; the electron temperature T_e is in eV. References: 28 to 34, 36 and 37 [57], 34 and 35 [1]

	Reaction	Reaction Rate
28	$\text{H}^- + \text{H} \rightarrow 2\text{H} + \text{e}^-$	if($T_e \leq 0.1$ eV) $k_{28} = 2.5634 \times 10^{-9} T_e^{1.78186}$ if($T_e > 0.1$ eV) $k_{28} = \exp[-20.372609 + 1.13944933 \ln(T_e) - 0.14210135 \ln(T_e)^2 + 8.4644554 \times 10^{-3} \ln(T_e)^3 - 1.4327641 \times 10^{-3} \ln(T_e)^4 + 2.0122503 \times 10^{-4} \ln(T_e)^5 + 8.6639632 \times 10^{-5} \ln(T_e)^6 - 2.5850097 \times 10^{-5} \ln(T_e)^7 + 2.4555012 \times 10^{-6} \ln(T_e)^8 - 8.0683825 \times 10^{-9} \ln(T_e)^9]$
29	$\text{H}^- + \text{H}^+ \rightarrow 2\text{H}$	if($T \leq 10^4$ K) $k_{29} = 2.4 \times 10^{-6} T^{-0.5} (1 + 2 \times 10^{-4} T)$
30	$\text{H}_2^+ + \text{H}^- \rightarrow \text{H}_2 + \text{H}$	$k_{30} = 5 \times 10^{-7} \sqrt{100/T}$
31	$\text{H}^- + \text{H}^+ \rightarrow \text{H}_2^+ + \text{e}^-$	if($T_e \geq 1.719$ eV) $k_{31} = 8.4258 \times 10^{-10} T_e^{-1.4} \exp(-1.301/T_e)$ if($T_e < 1.719$ eV) $k_{31} = 2.291 \times 10^{-10} T_e^{-0.4}$
32	$\text{H}_2 + \text{e}^- \rightarrow 2\text{H} + \text{e}^-$	$k_{32} = 5.6 \times 10^{-11} \sqrt{T} \exp(-102124/T)$
33	$\text{H}_2 + \text{H} \rightarrow 3\text{H}$	$k_{33} = 1.067 \times 10^{-10} T_e^{2.012} \exp[-(4.463/T_e)(1 + 0.2472 T_e)^{3.512}]$
34	$\text{He} + \text{e}^- \rightarrow \text{He}^+ + 2\text{e}^-$	$k_{34} = \exp[-44.09864886 + 23.91596563 \ln(T_e) - 10.7532302 \ln(T_e)^2 + 3.05803875 \ln(T_e)^3 - 0.56851189 \ln(T_e)^4 + 6.79539123 \times 10^{-2} \ln(T_e)^5 - 5.00905610 \times 10^{-3} \ln(T_e)^6 + 2.06723616 \times 10^{-4} \ln(T_e)^7 - 3.64916141 \times 10^{-6} \ln(T_e)^8]$
35	$\text{He}^+ + \text{e}^- \rightarrow \text{He} + \gamma$	$k_{35} = k_{35}^d + K_{35}^e$ $k_{35}^d = 1.544 \times 10^{-9} T_e^{-1.5} \exp(-48.596/T_e) \times [0.3 + \exp(-8.1/T_e)]$ $K_{35}^e = 3.925 \times 10^{-13} T_e^{-0.6353}$
36	$\text{He}^+ + \text{e}^- \rightarrow \text{He}^{++} + 2\text{e}^-$	$k_{36} = \exp[-68.71040990 + 43.93347633 \ln(T_e) - 18.4806699 \ln(T_e)^2 + 4.70162649 \ln(T_e)^3 - 0.76924663 \ln(T_e)^4 + 8.113042 \times 10^{-2} \ln(T_e)^5 - 5.32402063 \times 10^{-3} \ln(T_e)^6 + 1.97570531 \times 10^{-4} \ln(T_e)^7 - 3.16558106 \times 10^{-6} \ln(T_e)^8]$
37	$\text{He}^{++} + \text{e}^- \rightarrow \text{He}^+ + \gamma$	$k_{37} = 3.36 \times 10^{-10} T^{-0.5} (T/1000)^{-0.2} [1 + (T/10^6)^{0.7}]^{-1}$

Table 3.5: Continued from 3.4. Reaction rates for processes where metals are involved and where cosmic ray (CR) interact with the ISM. All the reaction rates are in s^{-1} . The gas temperature T is in Kelvin; the electronic temperature T_e is in eV. The functions for recombination (Φ_{rec}) and collisions (Φ_{col}) are described in the text. The cosmic ray field is $\zeta_{\text{CR}} \text{ s}^{-1}$ and it is the rate of H_2 ionization by cosmic rays. References: 38, 40, 42 and 44 [128], 39, 41, 43 and 45 [129], 46 to 48 and 49 to 54 [59], 48 [140] and, finally, 55 to 57 [133].

	Reaction	Reaction Rate
38	$\text{C}^+ + \text{e}^- \rightarrow \text{C} + \gamma$	$k_{38} = \Phi_{\text{rec}}(T, 6.85 \times 10^{-8}, 0, 11.3, 0.193, 0.25)$
39	$\text{C} + \text{e}^- \rightarrow \text{C}^+ + 2\text{e}^-$	$k_{39} = \Phi_{\text{col}}(T_e, 6.556 \times 10^{-10}, 65.23, 2.446 \times 10^7, 0.7567)$
40	$\text{Si}^+ + \text{e}^- \rightarrow \text{Si} + \gamma$	$k_{40} = \Phi_{\text{rec}}(T, 3.59 \times 10^{-8}, 0, 13.6, 0.073, 0.34)$
41	$\text{Si} + \text{e}^- \rightarrow \text{Si}^+ + 2\text{e}^-$	$k_{41} = \Phi_{\text{col}}(T_e, 8.616 \times 10^{-10}, 119.1, 4.352 \times 10^7, 0.7563)$
42	$\text{O}^+ + \text{e}^- \rightarrow \text{O} + \gamma$	$k_{42} = \Phi_{\text{rec}}(T, 1.88 \times 10^{-7}, 1, 8.2, 0.376, 0.25)$
43	$\text{O} + \text{e}^- \rightarrow \text{O}^+ + 2\text{e}^-$	$k_{43} = \Phi_{\text{col}}(T_e, 1.517 \times 10^{-9}, 360.1, 1.329 \times 10^8, 0.7574)$
44	$\text{Fe}^+ + \text{e}^- \rightarrow \text{Fe} + \gamma$	$k_{44} = \Phi_{\text{rec}}(T, 2.52 \times 10^{-7}, 0, 7.9, 0.701, 0.25)$
45	$\text{Fe} + \text{e}^- \rightarrow \text{Fe}^+ + 2\text{e}^-$	$k_{45} = \Phi_{\text{col}}(T_e, 2.735 \times 10^{-9}, 1314.0, 4.659 \times 10^8, 0.7568)$
46	$\text{O}^+ + \text{H} \rightarrow \text{O} + \text{H}^+$	$k_{46} = 4.99 \times 10^{-11} T^{0.405} + 7.54 \times 10^{-10} T^{-0.458}$
47	$\text{O} + \text{H}^+ \rightarrow \text{O}^+ + \text{H}$	$k_{47} = [1.08 \times 10^{-11} T^{0.517} + 4 \times 10^{-10} T^{0.00669}] \exp(-227/T)$
48	$\text{O} + \text{He}^+ \rightarrow \text{O}^+ + \text{He}$	if($T < 6000$ K) $k_{48} = 4.991 \times 10^{-15} \left(\frac{T}{10^4}\right)^{0.3794} \exp\left(-\frac{T}{1.121 \times 10^6}\right)$ if($T \geq 6000$ K) $k_{48} = 2.780 \times 10^{-15} \left(\frac{T}{10^4}\right)^{-0.2163} \exp\left(\frac{T}{8.158 \times 10^5}\right)$
49	$\text{C} + \text{H}^+ \rightarrow \text{C}^+ + \text{H}$	$k_{49} = 3.9 \times 10^{-16} T^{0.213}$
50	$\text{C}^+ + \text{H} \rightarrow \text{C} + \text{H}^+$	$k_{50} = 6.08 \times 10^{-14} \left(\frac{T}{10^4}\right)^{1.96} \exp\left(-\frac{1.7 \times 10^5}{T}\right)$
51	$\text{C} + \text{He}^+ \rightarrow \text{C}^+ + \text{He}$	if($T \leq 200$ K) $k_{51} = 8.58 \times 10^{-17} T^{0.757}$ if($200 < T \leq 2000$ K) $k_{51} = 3.25 \times 10^{-17} T^{0.968}$ if($T > 2000$ K) $k_{51} = 2.77 \times 10^{-19} T^{1.597}$
52	$\text{Si} + \text{H}^+ \rightarrow \text{Si}^+ + \text{H}$	if($T \leq 10^4$ K) $k_{52} = 5.88 \times 10^{-13} T^{0.848}$ if($T > 10^4$ K) $k_{52} = 1.45 \times 10^{-13} T$
53	$\text{Si} + \text{He}^+ \rightarrow \text{Si}^+ + \text{He}$	$k_{53} = 3.3 \times 10^{-9}$
54	$\text{Si} + \text{C}^+ \rightarrow \text{Si}^+ + \text{C}$	$k_{54} = 2.1 \times 10^{-9}$
55	$\text{H} + \text{CR} \rightarrow \text{H}^+ + \text{e}^-$	$k_{56} = 0.46 \zeta_{\text{CR}}$
56	$\text{H}_2 + \text{CR} \rightarrow 2\text{H}$	$k_{57} = 1.50 \zeta_{\text{CR}}$
57	$\text{H}_2 + \text{CR} \rightarrow \text{H}_2^+ + \text{e}^-$	$k_{58} = 0.96 \zeta_{\text{CR}}$

2.5). To establish the exact correspondence is a matter of patient work, not of primary interest here. Most of these reaction rates are taken from [1] and [60] to whom we refer for all details. Some of these reactions are discussed in this Section paying major attention to those rates that are vividly debated in literature.

3.2.1 Reaction by reaction: notes on a few cases

In this Section we examine in some detail a few chemical reactions that are widely debated in literature and are affected by large uncertainties. The reaction numbers are the same as those used in Tables 3.2, 3.4, 3.5, and 3.8 for the sake of an easy identification.

$\text{H}_2 + \text{H}^+ \rightarrow \text{H}_2^+ + \text{H}$ (REACTION 9). Each author has his own favored rate for this reaction so that the overall uncertainty is large. Our prescription is as follows. Up to 3×10^4 K we adopt the data of [114], based on the latest and most accurate quantum-mechanical calculations of the vibrationally resolved cross sections for the charge transfer $\text{H}_2 + \text{H}^+ \rightarrow \text{H}_2^+ + \text{H}$ at the center-of-mass collision energies from the threshold (~ 1.8 eV) up to 10 eV. For higher collision energies, up to approximately 10^4 eV, we derive the cross section following the suggestions by [7] and [74], which stand on the best known experimental (see for instance [54]) and theoretical data as well as on the recent measurements by [79]. These data were smoothly matched to those of [78] at low energies, thus yielding the most updated cross section for charge transfer from H to H_2^+ in the vibrationally ground state. This cross section is shown in the top panel of Fig. 3.1. Following [114], from this cross section we calculate the rate coefficients for temperatures from the threshold up to 10^8 K, as shown in the bottom panel of Fig. 3.1.

We fit the reaction rate (in units of cm^3s^{-1}) with the analytical expression

$$\log [k_9(T)] = \sum_{i=0}^7 a_i \log(T)^i, \quad (3.6)$$

where T is the temperature in Kelvin. Two intervals are considered for the temperature, i.e. $T = [10^2, 10^5]$ K and $T = [10^5, 10^8]$ K and two different fits are derived. The coefficients a_i for the two fits are given in Table 3.6. The rates obtained from this analytical fit are compared to those derived from the numerical data. No difference can be noticed as shown in the bottom panel of Fig. 3.1.

ASSOCIATIVE DETACHMENTS OF H^- AND D^- (REACTIONS 21 TO 24).

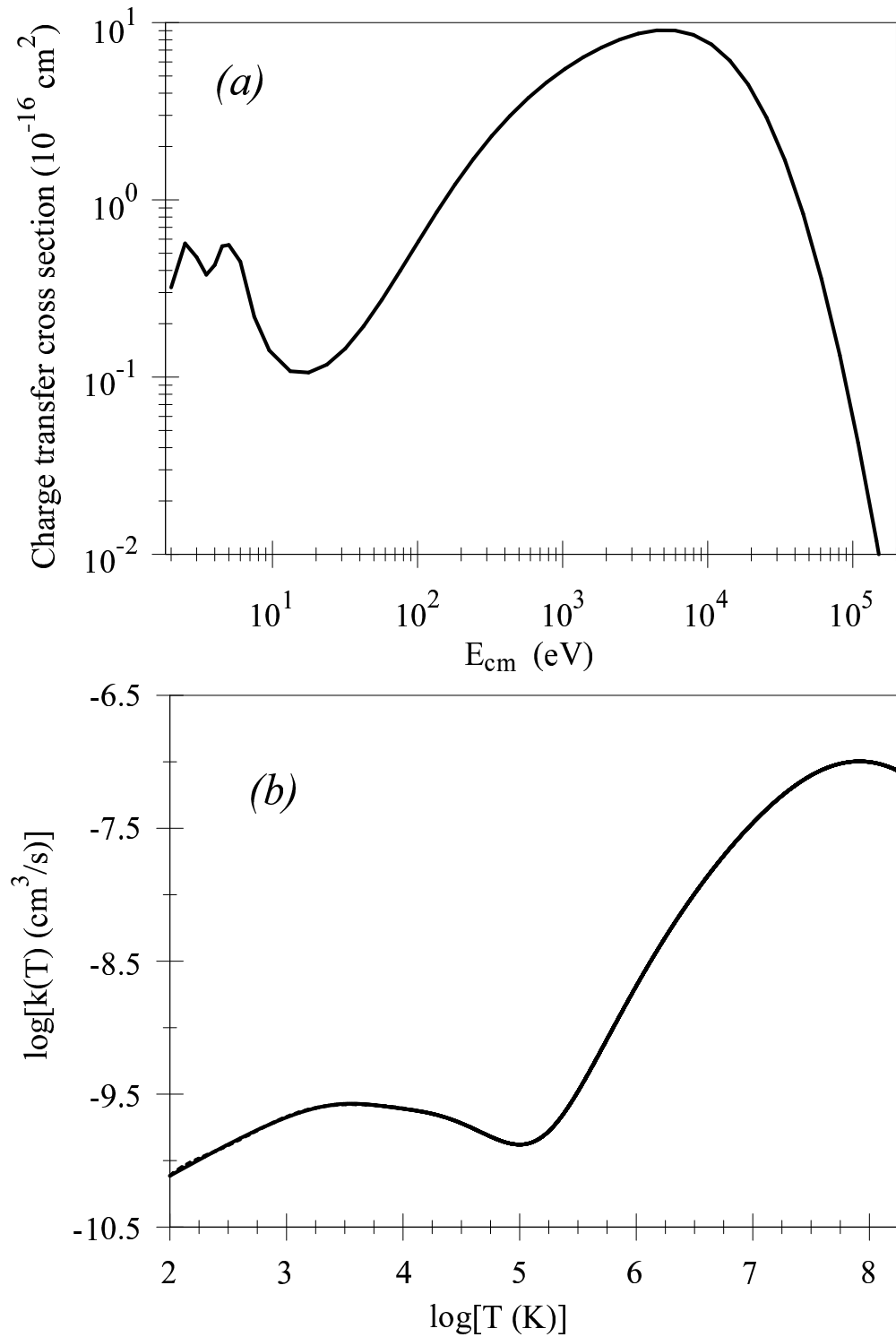
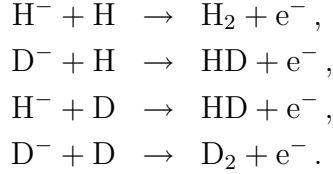


Figure 3.1: Top panel: charge transfer cross section for the reaction $\text{H}_2 + \text{H}^+ \rightarrow \text{H}_2^+ + \text{H}$. Bottom Panel: Rate coefficient $k(T)$ derived from the cross section in the top panel. The fits of $k(T)$ (dashed line) given by Eqn. (3.18) and Table 3.6 cannot be visually distinguished from $k(T)$.

Table 3.6: Fit coefficients for the charge transfer reaction $\text{H}_2 + \text{H}^+ \rightarrow \text{H}_2^+ + \text{H}$ as described in the Eqn. (3.6). Coefficients are in the form $a(b) = a \times 10^b$. All the temperature ranges are shown.

a_i	$10^2 \leq T < 10^5$ K	$10^5 \leq T \leq 10^8$ K
a_0	-1.9153214(+2)	-8.8755774(+3)
a_1	4.0129114(+2)	1.0081246(+4)
a_2	-3.7446991(+2)	-4.8606622(+3)
a_3	1.9078410(+2)	1.2889659(+3)
a_4	-5.7263467(+1)	-2.0319575(+2)
a_5	1.0133210(+1)	1.9057493(+1)
a_6	-9.8012853(-1)	-9.8530668(-1)
a_7	4.0023414(-2)	2.1675387(-2)

These processes include the following four reactions



Following [56] and using their notation, the reaction rate is expressed as $k = \text{const} \times \xi$ where ξ is a parameter taking values in the interval $[0.65, 5.0]$. In our case we obtain $k_{21} = k_{24} = 10^{-9} \xi$ and $k_{22} = k_{23} = 10^{-9} \xi/2$. In ROBO the parameter ξ can be varied in the above interval to investigate its effects on the overall results. In the present study we adopt $\xi = 0.65$.

$\text{H}^+ + \text{H}^- \rightarrow \text{H} + \text{H}$ (REACTION 29). For the mutual neutralization of H^- we adopt the cross section given by [31] and [57]. The mutual neutralization rate is related to the rate of the associative detachment $\text{H}^- + \text{H} \rightarrow \text{H}_2 + \text{e}^-$, in competition for the available H^- ions. Both rates are important for the formation of H_2 (see [57] for more details). It is worth recalling here that other estimates for this reaction rate have been reported by [57]. In brief [102] proposed the rate $k = 5.7 \times 10^{-6} T^{-0.5} + 6.3 \times 10^{-8} - 9.2 \times 10^{-11} T^{0.5} + 4.4 \times 10^{-13} T \text{ cm}^3 \text{ s}^{-1}$, whereas [32] gave $k = 7.0 \times 10^{-7} T^{-0.5} \text{ cm}^3 \text{ s}^{-1}$.

$\text{He}^+ + \text{e}^- \rightarrow \text{He} + \gamma$ (REACTION 35). This process can occur either via direct radiative recombination or di-electronic recombination, followed by radiative relaxation. Therefore, the reaction rate is the sum of two terms

$$k_{35} = k_{35}^{\text{d}} + k_{35}^{\text{e}}, \quad (3.7)$$

in units of cm^3s^{-1} . The first term is the di-electronic recombination rate, described by

$$k_{35}^{\text{d}} = 1.544 \times 10^{-9} T_e^{-1.5} \exp(-48.596/T_e) \times [0.3 + \exp(-8.1/T_e)], \quad (3.8)$$

where T_e is the temperature expressed in eV. The second term is the radiative recombination rate whose temperature dependence is

$$k_{35}^{\text{e}} = 3.925 \times 10^{-13} T_e^{-0.6353}. \quad (3.9)$$

Both terms are taken from [1].

$Z^+ + e^- \rightarrow Z + \gamma$ (REACTIONS 38, 40, 42, 44). An important process to include is the metal recombination. The metals considered by our ISM model and ROBO are C, Si, O, and Fe. The recombination rates of the metals are calculated according to the formalism proposed by [128]

$$\Phi_{\text{rec}}(T, A, \tau_0, \tau_1, b) = \frac{A}{T_0 (1 + T_0)^{1-b} (1 + T_1)^{1+b}}, \quad (3.10)$$

in units of cm^3s^{-1} , where T is the temperature, $T_0 = \sqrt{T/\tau_0}$ and $T_1 = \sqrt{T/\tau_1}$. In Table 3.5 we give the fit coefficients A , b , τ_0 and τ_1 for each metal.

$Z + e^- \rightarrow Z^+ + 2e^-$ (REACTIONS 39, 41, 43, 45). For the collisions between electrons and metals we use the fit proposed by [129] which is

$$\Phi_{\text{col}}(T, A, P, \Delta E, X, K) = A \frac{1 + P\sqrt{U}}{X + U} U^K e^{-U}, \quad (3.11)$$

in units of cm^3s^{-1} , where $U = \Delta E/T$ in which ΔE is the energy difference between the two atomic levels involved in the process, and T is the temperature. Both ΔE and T are in eV. The parameters A , P , ΔE , X , and K are given in Table 3.5.

3.2.2 Minimal CO network

Since CO has a key role we have included in ROBO a simplified CO-network based on [104]. They use an simplified model considering intermediate reactions, included in an implicit way. For our purposes we explicit such reactions to use a six-reactions network. We also add a seventh reaction to consider the destruction by colliders at high temperatures [107]. These reactions are listed in Tab. 3.7 and their rate coefficients [138]. Note that $T_{300} = T/300$, with T in K.

Table 3.7: Reaction rates for reactions belonging to the CO network. $T_{300} = T/300$, with T in K. References: 58 to 63 [138] and 64 [107]; For reactions 58 to 61 see text for details.

	Reaction	Reaction Rate
58.	$C^+ + H_2 \rightarrow CH_2^+ + \gamma$	$k_{58} = 4 \times 10^{-16} T_{300}^{-0.2}$
59.	$CH_2^+ + e^- \rightarrow CH + H$	$k_{59} = 1.6 \times 10^{-7} T_{300}^{-0.6}$
60.	$CH_2^+ + H_2 \rightarrow CH_3^+ + H$	$k_{60} = 1.6 \times 10^{-4}$
61.	$CH_3^+ + e^- \rightarrow CH_2 + H$	$k_{61} = 6.6 \times 10^{-11}$
62.	$CH + O \rightarrow CO + H$	$k_{62} = 7.58 \times 10^{-8} T_{300}^{-0.5}$
63.	$CH_2 + O \rightarrow CO + 2H$	$k_{63} = 1.33 \times 10^{-10}$
64.	$CO + e^- \rightarrow C + O + e^-$	$k_{65} = 2.86 \times 10^{-3} T_{300}^{-3.52} \exp(-112700/T)$

Tab. 3.7 shows how CO is formed from C^+ and O species, using CH, CH_2 , CH_2^+ and CH_3^+ as intermediate products/reactants, and H_2 and e^- as other reactants.

Our model includes UV radiation, so we must consider the photo-dissociation of the molecules included in the network. The effects on radiation are on carbon-based molecules. For this reason we use the photo-ionization rates

$$\Gamma_{CO} = G_0 10^{-10} \text{ s}^{-1}, \quad (3.12)$$

and

$$\Gamma_{CH_x^{(+)}} = G_0 5 \times 10^{-10} \text{ s}^{-1}, \quad (3.13)$$

where in both the Equations G_0 is the ratio between the UV flux in RO-BO and Habing's flux, which is $I_{\text{Hab}} = 1, 2 \times 10^{-4} \text{ erg/cm}^2/\text{s}/\text{sr}$. The $CH_x^{(+)}$ expression indicates that we are dealing (in this case) with CH, CH_2 , CH_2^+ and CH_3^+ molecules.

Following the Eqn. (3.13) we must consider the products of all the $CH_x^{(+)}$ molecules involved in the implicit reactions (i.e. $CH_x^{(+)} + \gamma \rightarrow \text{products}$). At this stage we are not interested in the detail of these reactions. For this reason we introduce the parameter $\beta(G_0)$ (from [104]) that determines the efficiency of the reactions numbered from 58 to 61 in Table 3.7. This parameter is defined as $\beta(G_0) = \exp[G_0 \cdot \ln(\xi)]$ with $\xi = 5 \times 10^{-10}$ from Eqn. (3.13). In this way, when radiation is not present ($G_0 = 0$) we have $\beta = 1$, which represents the scenario where photons do not reduce the formation of the various $CH_x^{(+)}$. When $G_0 = 1$ we have $\beta = \xi$, that describes reactions of formation having reduced efficiency. Finally when $G_0 \rightarrow \infty$ (not physical) we obtain $\beta \rightarrow 0$, meaning that the $CH_x^{(+)}$ are totally destroyed before any

possible interaction. The coefficient of the i th reactions now reads $k'_i = \beta \cdot k_i$, with $i \in [58, 61]$, and Eqn. (3.13) is not directly implemented into the code.

3.2.3 Photochemistry

In addition to this, we consider the group of photo-chemical processes listed in Table 3.8 for which we provide the cross section of the reaction and the analytical expression to derive the reaction rate as function of the existing radiation field.

In the present model of ISM we do not include the chemical reactions with lithium and its compounds (e.g. LiH and LiH⁺) because according to [109] and [101] they are not important coolants. Neglecting lithium and compounds, the number of species to follow, including metals and deuterium compounds, amounts to the 27 we have considered.

There is some interest in the CO molecule because it is an important coolant at very low temperatures. Among others, recipes for the formation of the interstellar CO are presented by [111] and [58]. However, explicitly following the formation of the CO molecule would be too complicated for our aims. Therefore we will limit ourselves to propose a simple model with two channels following [104].

In our chemical network we also include the effect of the cosmic ray radiation field. For convenience, we list in Table 3.5 the ionization rates for cosmic rates given by [133]. Cosmic rays are important for the cooling because they can destroy molecules that contribute to it, thus lowering the temperature of the interstellar medium (see the reactions shown in Table 3.5). In particular, cosmic rays are able to destroy H₂ and HD, and to ionize atoms. The role of the cosmic rays is still largely unknown because the strength of their radiation field in various regions and epochs of the Universe is not firmly determined. While their effect can be explored in the vicinity of a strong source, for a random sample of the Universe there are no exact measurements of the cosmic ray radiation field. Furthermore, most NB-TSPH simulators like EvOL do not contain the full description of cosmic rays, but simply consider their presence as a parameter. Therefore, even if these reactions have been considered and their rates presented in Table 3.5. they have not been included in practice in the system of equations (2.5).

Photo-chemical reactions

For the photo-chemical reactions we adopt the model and rates of [59] and [128]. In general the reaction rate is given by

$$R_{\text{photo}} = 4\pi \int_{E_{\text{th}}}^{\infty} \frac{\sigma(E)J(E)}{E} e^{-\tau(E)} [1 + f(E)] dE, \quad (3.14)$$

where $J(E) = J(h\nu)$ is the energy flux per unit frequency and solid angle of the impinging radiation field, $\sigma(E)$ the cross section, $\tau(E)$ is the gas opacity at the energy E and $f(E)$ is a numerical factor accounting for the effects of the secondary ionization, that are negligible if the UV radiation is not dominated by X-rays [59]. The rate is in s^{-1} .

The cross sections $\sigma(E)$ are expressed in two different ways according to the reaction under consideration. The reactions and associated rates are listed in Table 3.8. For the reactions from 1 through 8 we note (i) the quantity $\epsilon = \sqrt{(E/E_{\text{th}}) - 1}$; (ii) for H_2 and HD photo-dissociation we use the model proposed by [59]. We have

$$\sigma_{\text{H}_2} = 1.38 \times 10^9 J(h\bar{\nu}) f_s, \quad (3.15)$$

where

$$f_s = \frac{0.965}{(1 + N_{\text{H}_2}/b_5)^2} + \frac{0.035}{\sqrt{1 + N_{\text{H}_2}}}, \quad (3.16)$$

where N_{H_2} is the column density and $b_5 = b/10^5$ with $b = 9.12 \times 10^5 \sqrt{T_{\text{gas}}/10^4}$. For HD we have

$$\sigma_{\text{HD}} = 1.5 \times 10^9 J(h\bar{\nu}), \quad (3.17)$$

with $h\bar{\nu} = 12.87$ eV.

For the remaining reactions involving metals (i.e. from 9 through 12), the rates contain the fits given by [128] using the expression

$$\begin{aligned} \Phi_{\text{ph}}(a_f, y_w, x_f, y_a, P) &= [(x_f - 1)^2 + y_w^2] \\ &\times y^{0.5P-5.5} \left[1 + \sqrt{\frac{y}{y_a}} \right]^{-P}, \end{aligned} \quad (3.18)$$

where $y = \sqrt{x_f^2 + a_f^2}$. The meaning of the various symbols is given in Table 3.8. More details on the reactions and companion quantities and symbols are given by [59] and [128]. See also the references therein.

The UV radiation field is calculated as in [42], [127] and [103]. In particular we have

$$J(\nu) = 10^{-21} J_{21}(z) \left(\frac{\nu_{\text{H}}}{\nu} \right)^{\alpha_{\text{UV}}}, \quad (3.19)$$

where z is the redshift, $\nu_{\text{H}} = E_{\text{H}}/h$ is the frequency corresponding to the hydrogen first level energy threshold, $\alpha_{\text{UV}} = 1$ and $J_{21}(z)$ is

Table 3.8: Cross sections of photochemical processes in cm^2 . The energy E is in eV. The various quantities in use are: $\xi = E/E_{th}$, $\Phi_{\text{ph}}(a_f, y_w, x_f, y_a, P) = [(x_f - 1)^2 + y_w^2]y^{0.5P-5.5}[1 + \sqrt{y/y_a}]^{-P}$, $y = \sqrt{x_f^2 + a_f^2}$, $x_f(a, b) = E/a - b$, and $x_{Si} = 1.672 \times 10^{-5}$. See Table 3.9 for notes and references.

	Reaction	Cross Section
1	$\text{H} + \gamma \rightarrow \text{H}^+ + \text{e}^-$	$\sigma_1 = 6.3 \times 10^{-18} \xi^4 \exp(4 - 4\epsilon^{-1} - \arctan \epsilon) [1 - \exp(-\frac{2\pi}{\epsilon})]^{-1}$
2	$\text{D} + \gamma \rightarrow \text{D}^+ + \text{e}^-$	$\sigma_2 = \sigma_1$
3	$\text{He} + \gamma \rightarrow \text{He}^+ + \text{e}^-$	$\sigma_3 = 3.1451 \times 10^{-16} \xi^{7/2} [1.0 - 4.7416 \xi^{1/2} + 14.82 \xi - 30.8678 \xi^{3/2} + 37.3584 \xi^2 - 23.4585 \xi^{5/2} + 5.9133 \xi^3]$
4	$\text{H}^- + \gamma \rightarrow \text{H} + \text{e}^-$	$\sigma_4 = 2.11 \times 10^{-16} (E - E_{th})^{3/2} E^{-3}$
5	$\text{H}_2 + \gamma \rightarrow \text{H} + \text{H}$	see text
6	$\text{H}_2^+ + \gamma \rightarrow \text{H} + \text{H}^+$	if $(2.65 < E < 11.27)$ $\sigma_5 = \text{dex}[-40.97 + 15.9795 \xi - 3.53934 \xi^2 + 0.2581155 \xi^3]$ if $(11.27 < E < 21)$ $\sigma_5 = \text{dex}[-30.26 + 7.3935 \xi - 1.29214 \xi^2 + 0.065785 \xi^3]$
7	$\text{H}_2 + \gamma \rightarrow \text{H}_2^+ + \text{e}^-$	if $(15.4 < E < 16.5)$ $\sigma_6 = 9.560 \times 10^{-17} \xi - 9.4 \times 10^{-17}$ if $(16.5 < E < 17.7)$ $\sigma_6 = 2.16 \times 10^{-17} \xi - 1.48 \times 10^{-17}$ if $(17.7 < E < 30.0)$ $\sigma_6 = 1.51 \times 10^{-17} \xi - 2.71$
8	$\text{HD} + \gamma \rightarrow \text{H} + \text{D}$	see text
9	$\text{C} + \gamma \rightarrow \text{C}^+ + \text{e}^-$	$\sigma_7 = 5.027 \times 10^{-16} \Phi_{\text{ph}}(1.607, 0.09157, x_f, 62.16, 5.101)$
10	$\text{O} + \gamma \rightarrow \text{O}^+ + \text{e}^-$	$\sigma_8 = 1.745 \times 10^{-15} \Phi_{\text{ph}}(0.1271, 0.07589, x_f, 3.784, 17.64)$
11	$\text{Si} + \gamma \rightarrow \text{Si}^+ + \text{e}^-$	$\sigma_9 = 2.506 \times 10^{-17} \Phi_{\text{ph}}(0.4207, 0.2837, x_f, 20.57, 3.546)$
12	$\text{Fe} + \gamma \rightarrow \text{Fe}^+ + \text{e}^-$	$\sigma_{10} = 3.062 \times 10^{-19} \Phi_{\text{ph}}(0.248, 20.69, x_f, 2.671 \times 10^7, 7.92)$

$$J_{21}(z) = \frac{J_{21}}{1 + [5/(1+z)]^4}, \quad (3.20)$$

where in our case $J_{21} = 1$.

Finally, to derive the reaction rates, we integrate Eqn. (3.14) from $E = E_{\text{th}}$ to $E = \infty$ over the energy range of the radiation field photons.

The integrals must be calculated at each time-step if the radiation field changes with time or once for all at the beginning of the simulation if the radiation field remains constant. The integrals are calculated using Romberg's integration method.

Table 3.9: Notes and references for the reactions listed in Table 3.8. (a) [59], (b) [128]. See these papers for further references.

	Reaction					Note	Ref
1	H	+	γ	\rightarrow	H ⁺ + e ⁻	$E_{th} = 13.6$	a
2	D	+	γ	\rightarrow	D ⁺ + e ⁻	$E_{th} = 13.6$	a
3	He	+	γ	\rightarrow	He ⁺ + e ⁻	$E_{th} = 24.6$	a
4	H ⁻	+	γ	\rightarrow	H + e ⁻	$E_{th} = 0.755$	a
5	H ₂	+	γ	\rightarrow	H + H	see text	
6	H ₂ ⁺	+	γ	\rightarrow	H + H ⁺	$E_{th} = 2.65$	a
7	H ₂	+	γ	\rightarrow	H ₂ ⁺ + e ⁻	$E_{th} = 15.4$	a
8	HD	+	γ	\rightarrow	H + D	see text	
9	C	+	γ	\rightarrow	C ⁺ + e ⁻	$E_{th} = 11.26$ $x_f(2.144, 1.133)$	a;b
10	O	+	γ	\rightarrow	O ⁺ + e ⁻	$E_{th} = 13.62$ $x_f(1.240, 8.698)$	a;b
11	Si	+	γ	\rightarrow	Si ⁺ + e ⁻	$E_{th} = 8.152$ $x_f(23.17, x_{Si})$	a;b
12	Fe	+	γ	\rightarrow	Fe ⁺ + e ⁻	$E_{th} = 7.902$ $x_f(0.05461, 138.2)$	b

3.3 ROBO: cooling

3.3.1 Which are the sources of cooling to consider?

Our first idea was to use the formulation proposed by [27] which includes the following mechanisms:

- collisional ionization - H, He, He⁺, He(2³S)
- recombination - H⁺, He⁺, He⁺⁺
- dielectronic recombination - He
- collisional excitation - H(all n), He⁺($n = 2$), He($n = 2, 3, 4$)
- bremsstrahlung - all ions,

All the rates for these processes can be found in [27] (thereinafter C92).

In addition to this cooling treatment which is suited for non-equilibrium model for H and He chemistry, we add the formulation by [122] (thereinafter SD93). The latter is used only for metals subtracting off the values in the Z=0 case.

In any case both apply to high temperatures, say greater than 10⁴ K. We refer to them by the acronyms C92 or SD93. In addition to this, SD93 provide the dependence of cooling on the gas metallicity. This makes this source of data very interesting to our purposes.

A difference between C92 and SD93 is that in the former the cooling rate is described by numerical fits (no further interpolations are needed), whereas in the latter, one has to interpolate in temperature and metallicity huge tabulations of data. To this aim we used a surface fit (routine SFIT in IDL) where the plane surface passes through four points originated corresponding to two discrete values in temperature and two discrete values in metallicity. The analytical expression of this plane yields the cooling rate. Given the two pairs of interpolating points, (T_0, ρ_0) , (T_0, ρ_1) , (T_1, ρ_0) and (T_1, ρ_1) , the analytical function that describes the surface can be written in the form

$$\Lambda_{\text{SD93}}(T, \rho) = a_0 + a_1\rho + a_2T + a_3T\rho, \quad (3.21)$$

with a_i the fit coefficients. So, for a generic point (T, ρ) , for which $T_0 \leq T \leq T_1$ and $\rho_0 \leq \rho \leq \rho_1$, cooling is given by Eqn. (3.21)

Table 3.10: Coefficients c_{ij} used in the Eqn. (3.23) and taken from [87].

	$i = 0$	$i = 1$	$i = 2$	$i = 3$	$i = 4$
$j = 0$	-42.56788	0.92433	0.54962	-0.07676	0.00275
$j = 1$	21.93385	0.77952	-1.06447	0.11864	-0.00366
$j = 2$	-10.19097	-0.54263	0.62343	-0.07366	0.002514
$j = 3$	2.19906	0.11711	-0.13768	0.01759	-0.00066631
$j = 4$	-0.17334	-0.00835	0.0106	-0.001482	0.000061926

3.3.2 H₂ cooling.

The H₂ cooling requires a different description. [69] first evaluated the molecular hydrogen cooling. A modern, widely used source of H₂ cooling is by [52]. Although this cooling function is quite accurate, we prefer to add some more details by including the function found by [57], which takes in account not only the H₂ – H interaction, but also the collisions with He, H⁺, H₂ and free electrons. It is described by

$$\Lambda_{\text{H}_2} = \sum_k \sum_i \text{dex} [a_{ik} \log(T_3)^i] n_{\text{H}_2} n_k \text{ erg cm}^{-3} \text{ s}^{-1}, \quad (3.22)$$

where $T_3 = T/10^3$ K with T the gas temperature, a_{ik} is the i -th fit coefficient of the k -th species ($k = \{\text{H}, \text{H}^+, \text{H}_2, \text{e}^-, \text{He}\}$) and n are the numerical densities. The orto-para ratio is assumed to be 3 : 1. Outside the temperature range of the fits we use the molecular hydrogen cooling by [52].

3.3.3 HD cooling.

To describe the cooling by the deuterated molecular hydrogen we use the model proposed by [87]. It includes HD roto-vibrational structures, radiative and collisional transitions for $J \leq 8$ rotational levels, and the vibrational levels $v = 0, 1, 2, 3$. It has been found that including the roto-vibrational transitions increases the cooling efficiency of HD. The fit provided by the authors depends on the gas density and temperature. It can be parameterized as

$$\Lambda(T, n)_{\text{HD}} = \sum_{i=0}^4 \sum_{j=0}^4 c_{ij} \log_{10}(n)^i \log_{10}(T)^j, \quad (3.23)$$

where c_{ij} is the matrix whose elements are given in Table 3.10.

Using Eqn. (3.23) is particularly convenient from a numerical point of view as it provides fast evaluations of the cooling by the HD molecule.

3.3.4 Cooling by the CO molecule

Modeling the CO formation and the cooling through this molecule is not trivial since introducing the CO in the chemical network needs a large number of auxiliary molecules and consequently a large number of new reactions, even some minimal network has been proposed (see the references in this Chapter introduction). In this sense some models adopt cooling that are not network-dependent.

As an example we describe an early formulation adopted by [23] that is

$$\Lambda_{\text{CO}} = 1.6 \times 10^{-29} 10^{([\text{Fe}/\text{H}] - 1.699)} T^{0.5} \text{ erg cm}^3 \text{ s}^{-1}, \quad (3.24)$$

where T is the temperature in Kelvin, $[\text{Fe}/\text{H}]$ is the gas metallicity and $\Lambda(\text{CO})$ is the cooling due to carbon monoxide molecules. This should be divided by n^2 (the numerical density of the gas squared) to be consistent with the other cooling processes presented in this work. This Equation is valid in the temperature range $10 < T < 100$ K and from no metals up to $[\text{Fe}/\text{H}] = 0.5$.

Even if this simply representation could be useful (although not accurate), for ROBO we use a different approach. considering the rotational and the vibrational components of the CO cooling. Since we are dealing with a unitary volume of ISM, we use the optical thin limit model.

In this sense the steady-state equations in [97] are adopted together with the rate coefficients calculated using the $L \rightarrow 0$ coefficients in [115] with [61] method, including the [33] correction (see the paragraph at the end of this Section for further details).

To calculate the total rotational cooling we use the equation of statistical equilibrium from [97]:

$$n_j[A_j + n_{\text{H}_2} \sum_i \gamma_{ji}] \quad (3.25)$$

$$- \left[n_{\text{H}_2} \sum_i \gamma_{ij} n_i + n_{j+1} A_{j+1} \right] = 0, \quad (3.26)$$

with n_j the density of molecule in state $j = J$, n_{H_2} is the molecular hydrogen density, γ_{ij} is the rate coefficient of the transition, and A_j is the A -coefficient

from state j to $j - 1$. The system of equation is completed with the normalization $\sum_j n_j = n_{\text{CO}}$. The solution of this linear system is straightforward. The emission of the transition J to $J - 1$ is

$$I_J = \frac{h\nu}{4\pi} \frac{A_J n_J}{n_{\text{CO}}} \text{ erg/s/molecule/sr}, \quad (3.27)$$

from which we can retrieve the total cooling rate $\Lambda_{\text{rot}} = n_{\text{CO}} \sum_J I_J$.

The vibrational component is taken from [70], considering collisions with H_2 giving the rate coefficients:

$$\begin{aligned} \gamma_{01} &= 4.3 \times 10^{-14} T \exp(-68/T_3) \exp(-E_{10}/kT) \\ \gamma_{02} &= 2.7 \times 10^{-13} T \exp(-172/T_3) \exp(-E_{20}/kT), \end{aligned} \quad (3.28)$$

with $E_{10}/k = 0.5E_{20}/k = 3080 \text{ K}$, $T_3 = T^{1/3}$ and k is the Boltzmann's constant.

Complete calculation of the CO cooling rates

We describe here the complete calculation of the CO cooling rates from [115] with [61] method.

As seen in this Section to calculate the statistical equilibrium of the CO levels we need to know the coefficients γ_{ij} that indicate the probability of a transition between the i -th and the j -th level.

The cooling rate from level $J \rightarrow J'$ ($\gamma_{JJ'}$) is calculated using the ground state γ_{L0} because the levels are not completely independent. In [61] we have:

$$\gamma_{JJ'} = (2J' + 1) \sum_L (2L + 1) \left(\begin{array}{ccc} J & L & J' \\ 0 & 0 & 0 \end{array} \right)^2 \gamma_{L0} \quad J' < J, \quad (3.29)$$

where the 2×3 matrix is the Wigner 3j-symbols which are quantities that arise in considering coupled angular momenta in two quantum systems. We consider the special case

$$W_{3j} = \left(\begin{array}{ccc} j_1 & j_2 & j_3 \\ 0 & 0 & 0 \end{array} \right) \quad (3.30)$$

that obeys to $|j_1 - j_2| \leq j_3 \leq j_1 + j_2$ and for our purposes it is defined as

$$W_{3j} = \begin{cases} (-1)^{g/2} W_a^{1/2} W_b & \text{if } g \text{ even} \\ 0 & \text{if } g \text{ odd} \end{cases} \quad (3.31)$$

where $g = j_1 + j_2 + j_3$, W_a is

$$W_a = \frac{\prod_{i=1}^3 (g - 2j_i)!}{(g + 1)!} \quad (3.32)$$

and W_b

$$W_b = \frac{(g + 1)!}{\prod_{i=1}^3 (g/2 - j_i)!}. \quad (3.33)$$

The rest of the matrix is calculated as any atomic system with many levels using

$$\gamma_{J'J} = \gamma_{JJ'} \frac{2J + 1}{2J' + 1} \exp\left(\frac{-\Delta E_{JJ'}}{k_b T}\right) \quad (3.34)$$

where $2J + 1$ is the degeneration of the J -th atomic level, $\Delta E_{JJ'} = |E_J - E_{J'}|$, k_b is the Boltzmann's constant and, finally, T is the gas temperature.

Eqn. (3.34) is an approximation that becomes inaccurate at higher rotational levels since the energy splitting is not constant at increasing J . To cope with this we introduce the correction by [33] which is

$$A(L, J) = \frac{6 + \Omega(L)^2}{6 + \Omega(J)^2}, \quad (3.35)$$

with

$$\Omega(y) = 0.13y\tilde{B}\ell \left(\frac{\mu'}{T}\right)^{1/2}, \quad (3.36)$$

with the rotational constant $\tilde{B} = 1.878 \text{ cm}^{-1}$, the scattering length $\ell = 3 \text{ \AA}$ and the reduced mass $\mu' = 6.86 \text{ uma}$. The Eqn. (3.29) will be then multiplied by $A(L, J)^2$ to include the correction.

With these ingredients we have calculated the rate coefficients matrices for different temperatures (5, 10, 30, 50, 70, 100, 300, 500, 700, 1000, 1500, 2000) K that are used to calculate the CO cooling (see Fig. 3.2).

3.3.5 Cooling by the Metals

The cooling process by the metals is included using the list of the metals adopted by [89], namely CII, SiII, OI and FeII (see the Appendix B in [89]). This source of cooling is particularly important for temperatures lower than 10^2 K . The cooling is due to the fine structure level transitions of the ionized carbon $2P(3/2) \rightarrow 2P(1/2)$, and similarly for the ionized silicates. There are two other species that take part in this process: neutral oxygen (nine transitions between levels 1S_0 , 1D_2 , 3P_0 , 3P_1 and 3P_2) and ionized iron (five

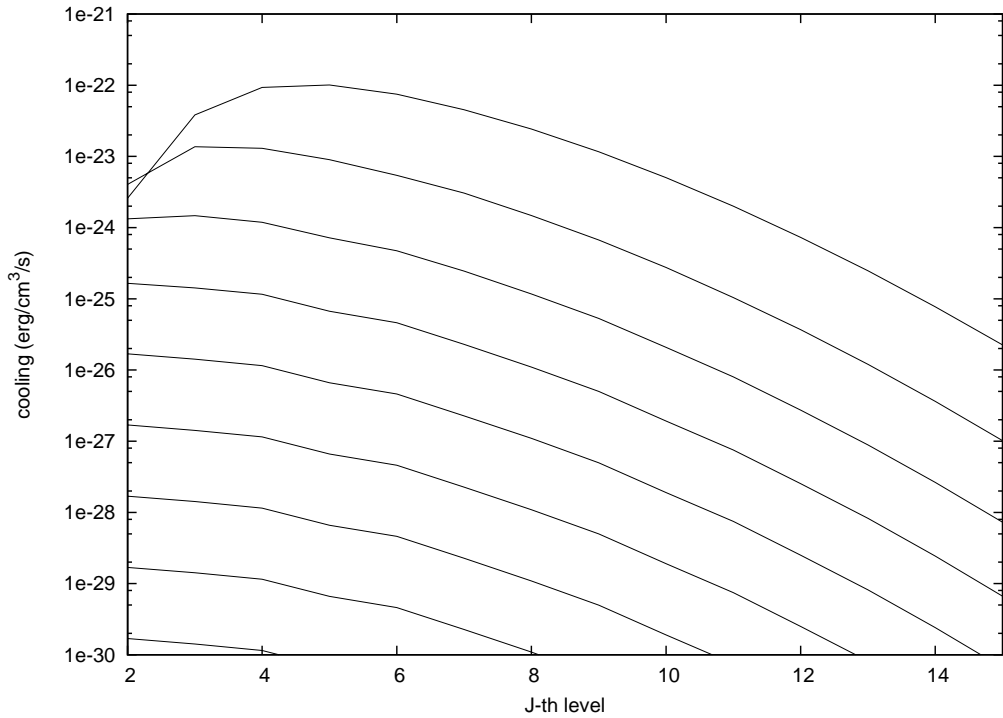


Figure 3.2: The cooling calculated for different rotational quantum numbers J with the method proposed in the Section 3.3.4. The Figure is for $T = 100$ K accounting for the collisions with ortho-molecular hydrogen. Each line represents the cooling at a different number density of H_2 . In particular we have $n_{\text{H}_2} = 10^5 \text{ cm}^{-3}$ for the upper line and $n_{\text{H}_2} = 10^{-3} \text{ cm}^{-3}$ for the lower line. Each step in density is logarithmic.

transitions between levels ${}^6\text{D}_i$ with i odd in the range $[1, 9] \in \mathbb{N}$). The cooling from each transition is additive and is given in erg/s by

$$\Lambda_i = \frac{\gamma_{ji}^{\text{H}} + \gamma_{ji}^{\text{e}} n_{\text{e}}/n_{\text{H}}}{\gamma_{ji}^{\text{H}} + \gamma_{ij}^{\text{H}} + (\gamma_{ji}^{\text{e}} + \gamma_{ij}^{\text{e}}) n_{\text{e}}/n_{\text{H}} + A_{ij}/n_{\text{H}}} A_{ij} \Delta E_{ij} \quad (3.37)$$

where γ_{ij}^{H} is the reaction rate for the hydrogen and γ_{ij}^{e} is the same but for electrons, A_{ij} is the Einstein coefficient between the i -th and j -th levels, ΔE_{ij} is the energy difference between the levels and, finally, n_{H} and n_{e} are the hydrogen and electrons number density respectively. To complete the Equation we need to know

$$\gamma_{ji} = \frac{g_i}{g_j} \gamma_{ij} \exp[-\Delta E_{ij}/(k_B T_{\text{gas}})] , \quad (3.38)$$

both for hydrogen and electrons; g_i and g_j are the level statistical weights, k_B is the Boltzmann's constant and T_{gas} is the gas temperature.

To obtain the total cooling by metals we use $\Lambda_{\text{metals}} = \sum_i \Lambda_i$ where i indicates a generic level transition for any of the four metals we have included.

The cooling proposed by [89] is improved implementing the cooling rates by [59]; in particular we use the de-excitation rates calculated for the collisions with ionized and molecular hydrogen when available. We also include the cooling from neutral C, Si (as in [59]), Fe and ionized O (as in [70]).

3.3.6 Total cooling

The cooling rate by all the above processes is additive and can be described by

$$\Lambda_{\text{tot}} = \Lambda_{\text{CEN92}} + \Lambda_{\text{SD93}} + \Lambda_{\text{H}_2} + \Lambda_{\text{HD}} + \Lambda_{\text{CO}} + (\Lambda_{\text{C}} + \Lambda_{\text{O}} + \Lambda_{\text{Si}} + \Lambda_{\text{Fe}} + \text{ions}) . \quad (3.39)$$

where the Λ s are functions of the temperature. Λ_{H_2} and Λ_{HD} are the cooling functions of the two molecular species, and the terms in brackets are the cooling of the metals.

The overall rate of temperature change, due to the heating and cooling, is given by the following Equation

$$\frac{dT}{dt} = \frac{\gamma - 1}{k_B \sum_i n_i} (\Gamma - \Lambda) \text{ K/s} , \quad (3.40)$$

where Γ is the heating source (if present), Λ is the cooling source, n_i are the numerical densities (the sum is over all the elements), k_B is the Boltzmann constant and γ is the adiabatic index defined in [100] as

$$\gamma = \frac{5x_{\text{H}} + 5x_{\text{He}} + 5x_{\text{e}^-} + 7x_{\text{H}_2}}{3x_{\text{H}} + 3x_{\text{He}} + 3x_{\text{e}^-} + 5x_{\text{H}_2}}, \quad (3.41)$$

where x is the numerical fraction of the element in the subscript. For an ideal gas of pure hydrogen this value is 5/3. If the gas is made only of molecular hydrogen we have $\gamma = 7/5$.

In Eqn. (3.41) we use for the adiabatic index of H_2 under $\log(T) \leq 2.6$ a linear fit of the data proposed by [11] (see also the erratum [12]), considering a 3:1 ortho/para ratio mix.

Γ is a generic heating term. It can be used to introduce heating phenomena like SNe feedback, cosmic ray, and others. In the current version of ROBO, Γ is used as a free parameter that is kept constant during a single run. In any case, the Γ term can be specified by the user according to his scientific aims.

3.4 ROBO: heating

Heating by photo-dissociation of molecular hydrogen and UV pumping, H and He photo-ionization, H_2 formation in the gas and dust phase and, finally, ionization from cosmic rays are modeled as in [59]. All these processes are listed in Table 3.11. To describe the heating by the photoelectric effect we adopt the model proposed by [5] and discuss it separately in the Section 3.5.5 below.

H and He photo-ionizations increase the gas energy at the rate

$$\Gamma = 4\pi \int_{E_0}^{\infty} \frac{\sigma(E)J(E)}{E} e^{-\tau(E)} (E - E_0) \eta(E - E_0) dE, \quad (3.42)$$

where $\sigma(E)$ is the reaction cross section, $J(E)$ is the photon flux, $e^{-\tau(E)}$ is the optical depth for a photon of energy E , η is the efficiency of the process (i.e. the fraction of energy converted to heat) and $(E - E_{th})$ is the difference between the energy of the photon and the energy of the atomic ground level. The rates Γ are given in Table 3.11.

3.5 ROBO: dusts

Dust grains take part to the process of molecule formation, e.g. HD and H_2 form on the surface of dust grains. Therefore, all physical processes involv-

Table 3.11: Heating processes. References: all from [59] except the photoelectric effect. See this papers for more references.

Process	Heating (Γ)
H ₂ photo-dissociation	$6.4 \times 10^{-13} R_d n_{\text{H}_2}$
UV pumping of H ₂	$2.7 \times 10^{-11} R_d n_{\text{H}_2} \left(\frac{n}{n+n_{\text{cr}}} \right)$
H photo-ionization	see text
He photo-ionization	see text
Gas-phase H ₂ formation	$\left(2.93 \times 10^{-12} k_{21} n_{\text{H}^-} + 5.65 \times 10^{-12} k_{11} n_{\text{H}_2^+} \right) \left(\frac{n}{n+n_{\text{cr}}} \right)$
Dust-phase H ₂ formation	$7.16 \times 10^{-12} k_{\text{dust}} n n_{\text{H}} \left(\frac{n}{n+n_{\text{cr}}} \right)$
Cosmic-ray ionization	$3.2 \times 10^{-11} \zeta_{\text{tot}} n$
Photoelectric effect	see Sect. 3.5.5

ing the dust must be described and treated with the highest accuracy. To understand how grains take part to the process of molecule formation, we need to know the mechanisms of grain formation and destruction, and the distribution of the grain temperature and size.

Given an initial set of dust composition and abundances, our dust model follows the evolution of the dusty components during the history of the ISM due to the creation of new grains and the destruction of the existing ones. Creation of new dust grains is governed by several processes that have different efficiencies depending on the size of the dust particles. The same applies for destruction which is mainly due to the thermal motion of the gas particles and shocks from supernovæ. Thermal destruction is quite easy to model, because the only parameter at work is the gas temperature. Shock disruption is more difficult to evaluate. The main uncertainty comes from the fact that discrete numerical hydrodynamical simulations can only follow shocks up to a given (often too coarse) resolution, yet insufficient for the microscopic description required here. To cope with this, we have followed a “statistical” approach. In brief, once identified the gas particles of the NB-TSPH simulations with their turbulent velocities (suggested by their velocity dispersion), we assume that all the shocks inside them follow the Kolmogorov law. See below for more details.

Furthermore, grain destruction may depend on their size. This is the case of the destruction by thermal motions, where the small grains are destroyed before the large ones. As a consequence of this, the size distribution function and the abundances of dust grains of different type are continuously changing with time. The ever changing size distribution function plays an important role in the formation mechanism of HD and H₂ that are among the most

efficient coolants. In brief, changing the distribution function of the dust grains means changing the quantity of key-role molecules produced by dust, as shown in [25].

We analyze here the different aspects of the grain evolution and their role in the formation of coolant molecules. First we focus on the distribution function of the dust grains, than we describe the formation of coolants on grains. Finally, we analyze the destruction and the formation of dust as well as the effects of the grains temperature.

3.5.1 Size distribution function of dust grains

We adopt a simple power law MRN-like grain size distribution function [93, 35]. This is given by $dn(a)/da \propto a^{-\lambda}$, with a the grain dimension, $n(a)$ the numerical fraction and $\lambda = 3.5$; this distribution covers the range $5 \text{ \AA} < a < 2500 \text{ \AA}$ and is extended to the smallest grain dimensions in such a way to include the typical polycyclic aromatic hydrocarbons (PAHs) region [84]. Even if more complicated distributions have been proposed [134], our simple choice is suitable as initial condition for the purposes of this work.

Indeed, it is worth pointing out here that the initial size distribution function changes with time due to dust destruction and formation, which in turn depend on the grain size. Consequently, the power law we started with does no longer apply. This will soon affect the formation of H_2 or HD. For this reason, the knowledge of the current size distribution function is of paramount importance.

First of all, we split the interstellar dust in two main components: the carbon-based (thereinafter simply carbonaceous grains) and the silicon-based grains (thereinafter the silicates). These have different roles in the formation of molecular hydrogen as well as different formation and destruction rates. In principle, there should be an additional group to consider, namely the PAHs, because the three types of dust have different efficiencies in the H_2 and HD formation. However, there is the lucky circumstance that PAHs and graphite grains have similar efficiencies as shown by Fig.2 of [25]. Basing on this, we lump together graphite grains and PAHs and treat separately the silicates. Therefore, thereinafter we refer to the mixture graphite grains plus PAHs as “carbonaceous grains”.

3.5.2 Dust-driven H_2 and HD formation

The model we adopt to describe the so called dust phase is the one proposed by [25]. In brief, the dust phase has its own network of reactions that establish the relative abundances of the various types of dust and govern the formation

of H₂ and HD (we can neglect the presence of other molecules like CO). The newly formed H₂ and HD are fed to the gas phase and enter the system of equations governing the abundances of the ISM and viceversa. In reality, the two phases should be treated simultaneously, governed by a unique system of differential equations determining the number densities of the elemental species, dusty compounds and free electrons at once. In practice this is hard to do because in general the time scales of the various processes creating and destroying the elemental species of the gas phase are much different from those governing the formation/destruction of dust grains. To cope with this difficulty, the [25] model separates the two phases, provides the results for the dust phase, and more important provides a link between the two phases that allows to determine the formation rate of H₂ and HD by the dusts as a function of gas temperature T_g and dust temperature T_d . This link is named the “Sticking Function $S(T_g, T_d)$ ”. The sticking function somehow quantifies the probability that an hydrogen atom striking a grain will stick to the surface (i.e. physisorbed), rather than simply bouncing off. The sticking function characterizes the probability for an atom to remain attached to a grain. Here we strictly follow this way of proceeding.

According to the [25] model, the rate at which H₂ molecule forms over the grain surface is:

$$R_d(\text{H}_2) = \frac{1}{2}n(\text{H})v_g n_d \sigma \epsilon_{\text{H}_2} S(T_g, T_d) \text{ cm}^{-3} \text{ s}^{-1}. \quad (3.43)$$

where $n(\text{H})$ is the density of hydrogen in the gas phase, $v_g = \sqrt{8kT_g/m_{\text{H}}}$ is the gas thermal speed (k is the Boltzmann constant and m_{H} is the hydrogen mass), n_d is the dust number density, σ the grain cross section (i.e. πa^2), ϵ_{H_2} the intrinsic efficiency of the process, and $S(T_g, T_d)$ the sticking function. This latter in turn is a function of the dust and grain temperatures

$$S(T_g, T_d) = \left[1 + 0.4 \left(\frac{T_g + T_d}{100} \right)^{0.5} + 0.2 \left(\frac{T_g}{100} \right) + 0.08 \left(\frac{T_g}{100} \right)^2 \right]^{-1}. \quad (3.44)$$

where T_g and T_d are in Kelvin. With this function the probability for a gas molecule to remain stuck on a dust grain is higher in a cold gas than in a hot one. This probability is even higher for the cold grains. For HD the expressions are similar.

Eqn. (3.43) contains the intrinsic efficiency ϵ_{H_2} (or as ϵ_{HD} for HD), that

is the probability for the process to occur. In our case it is the probability that atoms, which are stuck to a grain, react to form H₂ or HD.

For the carbonaceous grains, the efficiencies ϵ_{H_2} and ϵ_{HD} coincide and are equal to:

$$\epsilon_{\text{C}} = \frac{1 - T_{\text{H}}}{1 + 0.25 \left(1 + \sqrt{\frac{E_{\text{ch}} - E_{\text{S}}}{E_{\text{phy}} - E_{\text{S}}}}\right)^2 e^{-\frac{E_{\text{S}}}{T_{\text{d}}}}}, \quad (3.45)$$

The efficiency for the silicates ϵ_{Si} is

$$\epsilon_{\text{Si}} = \frac{1}{1 + \frac{16T_{\text{d}}}{E_{\text{ch}} - E_{\text{S}}} e^{-\frac{E_{\text{ph}}}{T_{\text{d}}}} e^{\beta_{\text{d}} \text{apc} \sqrt{E_{\text{phy}} - E_{\text{S}}}}} + \mathcal{F}, \quad (3.46)$$

where $\beta_{\text{d}} = 4 \times 10^9$ for H₂ and $\beta_{\text{d}} = 5.6 \times 10^9$ for HD. The term \mathcal{F} is a function of the gas temperature and can be written as

$$\mathcal{F}(T) = 2 \frac{e^{-\frac{E_{\text{phy}} - E_{\text{S}}}{E_{\text{phy}} + T}}}{\left(1 + \sqrt{\frac{E_{\text{ch}} - E_{\text{S}}}{E_{\text{phy}} - E_{\text{S}}}}\right)^2}. \quad (3.47)$$

The expression T_{H} is given by

$$T_{\text{H}} = 4 \left(1 + \sqrt{\frac{E_{\text{ch}} - E_{\text{S}}}{E_{\text{phy}} - E_{\text{S}}}}\right)^{-2} \exp\left(-\frac{E_{\text{ch}} - E_{\text{S}}}{E_{\text{ch}} + T_{\text{g}}}\right). \quad (3.48)$$

The various quantities appearing in the above relationships are listed in Table 3.12. For more details on these Equations see [25]. Comparing Eqns. (3.45) and (3.46) we see that the efficiency is high when the dust temperature is low. For the silicates the efficiency window is smaller than for the carbonaceous grains. For the silicates the efficiency is high for temperatures up to 20 K and then falls by two orders of magnitude. The carbonaceous grains are efficient for temperatures up to 100 K, where the efficiency is still 0.1 (instead of 0.01 as for the silicates). Finally, it is worth noticing that the efficiency profile is smoother for the carbon grains.

From all these considerations it follows that cold dust and warm carbon-dominated dust in a cold gaseous environment are the most efficient drivers for the formation of coolant molecules like H₂ and HD.

3.5.3 Grain formation

Here we briefly examine the formation of dust grains. We start with an initial number density with the size distribution given in Section 3.5.1 and with a

Table 3.12: The value used to compute the formation efficiency of H₂ and HD. E_{phy} and E_{ch} are in K, a_{pc} is in Å. From [25].

Surface	E_{phy}	E_{ch}	E_{S}	a_{pc}
Carbons	800 K	7000 K	200 K	3 Å
Silicates	700 K	15000 K	-1000 K	1.7 Å

given ratio between the silicates and the carbonaceous grains. This latter is a free parameter varying in the range $[0, 1]$, where zero stands for dust made of sole carbon grains; one is for dust made of sole silicates.

According to [38], the temporal variation of the size distribution function of grains caused by accretion is given by

$$\frac{dn(a)}{dt} = c_d \alpha(T_g, T_d) \pi a^2 n_g n_d(a) v_g \quad (3.49)$$

where all the quantities have the same meaning as in Eqn. (3.43) but for $\alpha(T_g, T_d)$ and c_d .

The quantity $\alpha(T_g, T_d)$ is a sort of sticking coefficient depending on the gas and dust temperature and the type of dust. This coefficient is therefore forced to change in the course of the evolution. Furthermore, n_d (and consequentially n) are functions of a . Eqn. (3.49) is similar to Eqn. (3.43) because the process is similar, except that now we this mathematical description is applied to the carbon atoms that remain stuck to the carbon lattice of the grain. Our the expression slightly differs from the original of [38] because the parameter c_d is introduced in Eqn. (3.49) to take some considerations made by [38] himself into account. Inserting $c_d = 1$ we can obtain the time scale of the process. In a standard cold gas this time scale is $\tau \approx 2 \times 10^4$ yrs, which is significantly smaller than the observational estimates. Normal evaporation, caused by cosmic rays or UV heating and grain-grain collisions can halt the growing of the dust grains. The factor c_d somehow takes this phenomena into account. It is estimated to be of the order of $c_d = 10^{-3}$. We name c_d the delay factor.

For the sticking coefficient $\alpha(T_g, T_d)$ we make use of the data by [81], considering a carbon atom of the gas phase as impinging on a carbon lattice. The Equation fitting the data has the form

$$\begin{aligned} \alpha(T_g, T_d) &= 0.0190 T_g (0.0017 T_d + 0.4000) \\ &\times \exp(-0.0070 T_g), \end{aligned} \quad (3.50)$$

where T_g and T_d are the gas and dust temperatures respectively (see Fig.

3.3). The sticking coefficient $\alpha(T_g, T_d)$ has no dimensions. The data of [81] provide a good dependence on the gas temperature T_g , but a poor one on the dust temperature T_d . Therefore an accurate fit is not possible. The above relationship can be used in the temperature intervals $10 \text{ K} \leq T_g \leq 1000 \text{ K}$ and $3 \text{ K} \leq T_d \leq 300 \text{ K}$. At present we use the same model also for silicate grains even though this approximation might not be accurate. We plan to improve upon this point in the future.

With this model the formation efficiency is higher when the interstellar medium has a temperature $T \approx 100 \text{ K}$ and when the dust grains have a temperature of about 300 K . For dust grains with temperature higher than 300 K or lower than 3 K , the formation efficiency is unknown. Though the fits from [81] are not very accurate, they are enough for our purposes as we are only interested in the shape and maxima of the curves in Fig. 3.3.

Finally, we note that we have described the formation of dust by means of a general process of accretion in the ISM leaving aside other sites of dust formation like the envelopes of obscured AGB stars, Wolf-Rayet stars and remnants of supernovæ [38]. The reason behind this is that all of these are external sources of dust eventually enriching in dust content the ISM and determining therefore a different initial dust content as input for ROBO. Indeed, for our purposes, only the internal sources of dust in the unit volume are important. The information about the initial conditions of the dust mixture should be provided to ROBO by the companion NB-TSPH code EVOL properly taking into account the dusty yields coming from the stars.

3.5.4 Grain destruction

Destruction by shocks:

to introduce the shattering of dust grains by shocks we use a description based on [68]. In our model when the ISM is turbulent, the small grains (projectiles) impact the larger grains (targets). We divide the dust grains in $N = 100$ density bins of different masses, to have

$$n_{\text{dust}} = b_{\text{norm}} \int_{a_{\text{low}}}^{a_{\text{up}}} n(a) da \Leftrightarrow n_{\text{dust}} = \sum_{i=0}^{N-1} n_i, \quad (3.51)$$

with b_{norm} the normalization constant, and $n(a) \propto a^{-3.5}$. Note that for our purposes we consider the grain mass related to the grain size as $m = 4/3\pi a^3 \rho_{\text{gr}}$, where $\rho_{\text{gr}} = 2.3 \text{ g/cm}^3$ the density of the graphite that forms a grain.

When a projectile of mass m_j hits a target of mass m_i , the target loses a fraction of mass $f_{\text{sh}} m_i$ if $m_j < m_i/2$ or it is totally destroyed if $m_j \geq m_i/2$

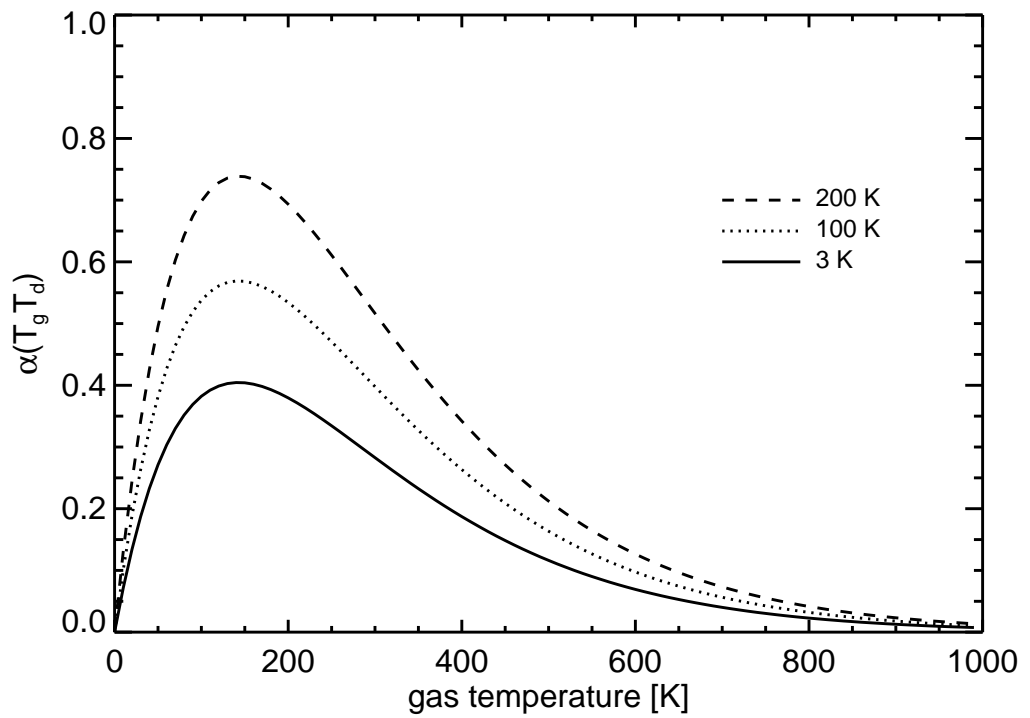


Figure 3.3: The sticking coefficient for the carbon molecules over a carbon lattice derived from [81]. The different lines indicate a different dust temperature: 3 K (solid), 100 K (dotted) and 200 K (dashed). T_g is the gas temperature in Kelvin.

(i.e. $f_{\text{sh}} = 1$). In both cases the projectile is destroyed. The lost mass (fragments) is redistributed using the usual power-law distribution. The remaining parts of the target (remnants) will be inserted in another bin of smaller mass corresponding to $(1 - f_{\text{sh}})m_i$.

So the density variation of the i -th bin is

$$\frac{dn_i}{dt} = \left(\frac{dn_i}{dt}\right)_L + \left(\frac{dn_i}{dt}\right)_F + \left(\frac{dn_i}{dt}\right)_R, \quad (3.52)$$

where the L subscript indicates the term representing the mass lost in fragments, F the mass gained from the fragmentation and finally R the mass of the remnants that move from other bins to the i -th. Note that the first term must be negative.

In our case we are interested in using densities instead of masses. From a statistical point of view we must consider the probability of an impact. This is determined by the density of the targets n_i , the density of the projectiles n_j , their relative speed v_{ij} and their sizes (a_i and a_j). The assumptions on speed will be discussed later in this Section. For the targets belonging to the i -th bin we have that the mass lost in fragments correspond to a density change of

$$\left(\frac{dn_i}{dt}\right)_L = - \sum_j^{j \leq i} \epsilon_{ij} \alpha_{ij} n_i n_j \quad (3.53)$$

where

$$\epsilon_{ij} = \begin{cases} \frac{f_{\text{sh}} n_i + n_j}{n_i + n_j} & \text{if } m_j > m_i/2, \\ 1 & \text{if } m_j \leq m_i/2. \end{cases} \quad (3.54)$$

and the impact coefficient is

$$\alpha_{ij} = v_{ij} \pi (a_i + a_j)^2. \quad (3.55)$$

Consequently the total density of the fragments is

$$\frac{dn_{\text{frag}}}{dt} = \sum_i \frac{dn_i}{dt} \quad (3.56)$$

and this will be distributed among the bins with a power-law to obtain the $(dn_i/dt)_F$ of each bin.

The other positive term is the density of the remnants given by

$$\left(\frac{dn_k}{dt}\right)_R = (1 - \epsilon_{ij}) \frac{dn_i}{dt}, \quad (3.57)$$

where k is the bin index defined as

$$k = \text{int} \left[\frac{m_i(1 - f_{\text{sh}}) - m_{\text{low}}}{\Delta m} \right], \quad (3.58)$$

with i the index of the shuttered bin and Δm the size of each bin, viz. $(m_{\text{up}} - m_{\text{low}})/N$.

The speed obeys to a Kolmogorov-like distribution

$$\xi(v) = \int_{v_{\text{low}}}^{v_{\text{up}}} \phi(v) dv, \quad (3.59)$$

with

$$a_{\text{norm}} \int_{v_{\text{low}}}^{v_{\text{up}}} \phi(v) dv = 1. \quad (3.60)$$

where v_{low} and v_{up} are the limits of the shock velocities over which the normalization of $\phi(v)$ applies, thus fixing the constant a_{norm} . The relative speed v_{ij} of the grains is obtained considering the speed distribution in Eqn. (3.59) in the range $v_{\text{low}} = 1$ km/s and $v_{\text{up}} = 200$ km/s for a total of 30 speed bins. The quantity $\xi(v)$ permits to weight the contribution of the dn/dt computed at each speed bin.

Vaporization

since we deal also with high velocity shocks, we are interested in the vaporization process, in which a dust grain is vaporized into the gas-phase. We use the formalism of [125] considering the impact of carbon grains. The fraction of vaporized material is

$$F_v = \frac{f_{\text{vap}}}{1 + f_{\text{vap}}} \quad (3.61)$$

defining

$$f_{\text{vap}} = \left[f_{v1} + f_{v2} \sqrt{1 - \frac{v_t}{v}} \right] \frac{m_j}{m_i}, \quad (3.62)$$

where $v_t = 23$ km/s is the shock threshold velocity, m_i and m_j are the masses of target and projectile respectively. The Eqn. (3.62) must satisfy the relation $v \geq v_t$. We also have

$$f_{v1} = 2.59 \frac{a_i}{a_i + a_j}, \quad (3.63)$$

and

$$f_{v2} = \frac{2.11}{\sigma_1^{8/9}}, \quad (3.64)$$

where

$$\sigma_1 = \frac{0.3 (s + \mathcal{M}^{-1} - 0.11)^{1.3}}{(s + \mathcal{M}^{-1} - 1)}, \quad (3.65)$$

with \mathcal{M} the Mach's number of the shuttered material and $s = 1.9$ from [125].

Destruction by thermal sputtering

To evaluate the fraction of grains destroyed by thermal sputtering, we adopt the approximation by [37]. A grain of dust in a medium with temperature $T \leq 10^6$ K has a destruction time (i.e. its lifetime)

$$\tau_{\text{dist}} \approx 10^3 a(\text{nm}) / n_{\text{H}} \text{ yr.}$$

From this we can obtain the destruction rate per second. The above relation is only valid for high temperatures.

To include the temperature dependence of the destruction rate we refer to [125] and with the aid of this latter we model the dependence on the gas temperature of the lifetime of the dust. As expected, dust grains with lower temperature have a longer lifetime. Finally, according to the [37], the small grains have a shorter lifetime than the large ones in the same environment.

The grain temperature depends on the radiation field generated by all the stellar sources. However, for the sake of simplicity, in this study we have used a fixed value for the grain temperature. Therefore, a great improvement would be given by including a description of the photon diffusion (e.g. [92]). Our choice is partially justified by the fact that the companion NB-TSPH code EVOL does not yet include photon diffusion. This fact leads us to postpone the implementation of different grain temperatures to when photon diffusion will be included in EVOL.

3.5.5 Heating by photoelectric ejection of electrons from dust grains

The photoelectric ejection of electrons by dust grains is an important source of heating. The model proposed here is based on [5] (hereafter BT94) and [135]. The photoelectric heating is given by

$$\begin{aligned} H(N_C, Z) &= W \pi \int_{\nu_Z}^{\nu_H} \sigma_{\text{abs}}(N_C) Y_{\text{ion}}(N_C, IP_Z) \\ &\times F(\nu) g(N_C, IP_Z) d\nu, \end{aligned} \quad (3.66)$$

where W is the FUV dilution factor, σ_{abs} the photon absorption cross section, Y_{ion} the photoelectric ionization yield, $F(\nu)$ the UV radiation flux and

$g(N_C, IP_Z)$ the kinetic energy partition function. N_C is the number of carbon atoms that form the dust ($0.5 a^3$ with a the size in Å) and IP_Z the ionization potential of a grain of charge Z . ν_H is the Lyman frequency and ν_Z the frequency corresponding to IP_Z . In our model the range of grain size is 5Å to 100Å, since the total heating is mostly due to small grains (see BT94 for details).

The FUV absorption cross section is $\sigma_{\text{abs}} = \pi a^2 Q_{\text{abs}}$, where Q_{abs} is calculated using a combination of PAH and graphite grains, see Eqn. (3.81) and Eqn. (3.82).

The photoelectric ionization yield depends on the grain size and on the IP_Z the ionization potential of a grain of charge Z . The yield is

$$Y_{\text{ion}} = Y_{\text{inf}} \frac{1 - IP_Z(Z, N_C)}{h\nu} f_\gamma(N_C), \quad (3.67)$$

where $Y_{\text{inf}} = 0.14$, h the Planck constant and ν the frequency of the UV radiation. The ionization potential of a grain of charge Z changes with the shape of the grain (disc/sphere) and it is

$$IP_Z(Z, N_C) = \begin{cases} 4.4 + 25.1(Z + 0.5)(N_C)^{-1/2} & \text{discs} \\ 4.4 + 11.1(Z + 0.5)(N_C)^{-1/3} & \text{spheres,} \end{cases} \quad (3.68)$$

both in eV.

The enhancing factor $f_\gamma(N_C)$ is

$$f_\gamma(N_C) = \left(\frac{\zeta}{\alpha}\right)^2 \left(\frac{\alpha^2 - 2\alpha + 2 - 2e^{-\alpha}}{\zeta^2 - 2\zeta + 2 - 2e^{-\zeta}}\right), \quad (3.69)$$

with

$$\begin{aligned} \alpha &= \frac{a}{\ell_{\text{att}}} + \frac{a}{\ell_{\text{esc}}} \\ \zeta &= \frac{a}{\ell_{\text{att}}}, \end{aligned} \quad (3.70)$$

where a is the size in angstrom, $\ell_{\text{att}} = 100 \text{ \AA}$ is the photon attenuation length and $\ell_{\text{esc}} = 10 \text{ \AA}$ is the electron escape length.

Finally, to complete the list of the terms in Eqn. (3.66), we define the partition function as

$$g(N_C, IP_Z) = \frac{1}{2} \frac{h\nu - IP_Z}{h\nu}, \quad (3.71)$$

where the symbols have the same meaning as above. In order to have more details on the Equations listed above see the papers cited in this Section.

The total photoelectric heating is

$$\Gamma = \int_{N_-}^{N_+} \sum_Z H(N_C, Z) f(N_C, Z) n(N_C) dN_C, \quad (3.72)$$

where $f(N_C, Z)$ is the probability to find a grain composed of N_C carbon atoms at a certain charge Z . This can be computed considering the collisions with electrons and ions. The detailed balance yields

$$f(Z) [J_{\text{pe}}(Z) + J_{\text{ion}}(Z)] = f(Z + 1) J_e(Z + 1), \quad (3.73)$$

with J_{pe} the rate of photoelectron emission, J_{ion} and J_e the accretion rates of ions and electrons.

The detailed calculation of $f(Z)$ shown in the very next lines are from BT94. To obtain $f(Z)$ we apply

$$f(Z > 0) = f(0) \prod_{Z'=1}^Z \frac{J_{\text{pe}}(Z' - 1) + J_{\text{ion}}(Z' - 1)}{J_e(Z')} \quad (3.74)$$

and

$$f(Z < 0) = f(0) \prod_{Z'=Z}^{-1} \frac{J_e(Z' + 1)}{J_{\text{pe}}(Z') + J_{\text{ion}}(Z')}. \quad (3.75)$$

The rates J_{ion} and J_e are from [135] and can be both described as

$$J_i(Z) = n_i s_i \left(\frac{8k_b T}{\pi m_i} \right)^{1/2} \pi a^2 \tilde{J} \left(\tau = \frac{ak_b T}{q_i^2}, \nu = \frac{Ze}{1_i} \right), \quad (3.76)$$

with n_i the number density of the type i charged particle, $s_i = 1$ its sticking coefficient and m_i its mass. T is the temperature, q_i the charge of the particle and, finally, k_b is the Boltzmann constant.

The function \tilde{J} assumes different values depending on its arguments, in particular we have for $\nu = 0$

$$\tilde{J}(\tau, \nu = 0) = 1 + \left(\frac{\pi}{2\tau} \right)^{1/2}, \quad (3.77)$$

for $\nu < 0$

$$\tilde{J}(\nu < 0) \approx \left(1 - \frac{\nu}{\tau} \right) \left[1 + \left(\frac{2}{\tau - 2\nu} \right)^{1/2} \right], \quad (3.78)$$

that have an accuracy of $\pm 5\%$ for $\nu \leq -1$ and $10^{-3} < \tau < \infty$ since it is the result of a fit. Analogously the $\nu > 0$ case gives

$$\tilde{J}(\nu > 0) \approx [1 + (4\tau + 3\nu)^{1/2}]^2 \exp(-\theta_\nu/\tau), \quad (3.79)$$

with an accuracy of $\pm 4\%$ and the value of the potential maximum as

$$\theta_\nu = \frac{\nu}{1 + \nu^{-1/2}}. \quad (3.80)$$

As the FUV absorption cross section σ_{abs} depends on the absorption efficiency of FUV photons by the grains, we use the data of [35] and [80] for the graphite grains and [83, 84, 85] for the PAHs. We also use the model proposed by [83, 84, 85] to create a mixed population of PAHs and graphite grains. Following their paper the total absorption efficiency is

$$Q_{\text{abs}}(a, \lambda) = \xi(a)Q_{\text{abs}}^{\text{PAH}}(a, \lambda) + [1 - \xi(a)]Q_{\text{abs}}^{\text{gra}}(a, \lambda), \quad (3.81)$$

defining

$$\xi(a) = (1 - q)\min\left[1, \left(\frac{a_0}{a}\right)^3\right], \quad (3.82)$$

with $q = 0.01$ and $a_0 = 50 \text{ \AA}$ (see [83, 84, 85] for more details).

In the same way we can also obtain the cooling associated with the electron recombination. This is given by

$$C(N_C, Z) = n_i s_i \sqrt{\frac{8kT}{\pi m_i}} \pi a^2 \hat{\Lambda}(\tau, \nu), \quad (3.83)$$

where n_i is the density of the charged particle with sticking coefficient $s_i = 1$ and mass m_i and a is the grain size. The term $\hat{\Lambda}(\tau, \nu)$ is described in detail in BT94. The total cooling is obtained as in Eqn. (3.72).

In Fig. 3.4 we show the results from a simple model with a grain distribution with $n_{\text{dust}} = 10^{-5} \text{ cm}^{-3}$ and a gas with a temperature of 10^2 K .

3.6 ROBO: the code

The code has been developed with IDL³. Its user friendly features help the development of applications that are otherwise difficult to build in FORTRAN⁴. The code is divided in self-explanatory procedures (routines) that are grouped in four classes (gas chemistry, dusts, cooling, and general code behavior). The main routine calls all other sub-routines that are needed to calculate the gas evolution (see Fig. 3.5).

³IDL is a product of ITT Visual Information Solutions, <http://ittvis.com/>

⁴It is worth to notice that ROBO has its own FORTRAN counterpart called ROFO - see Sect. 5.3 for further details.

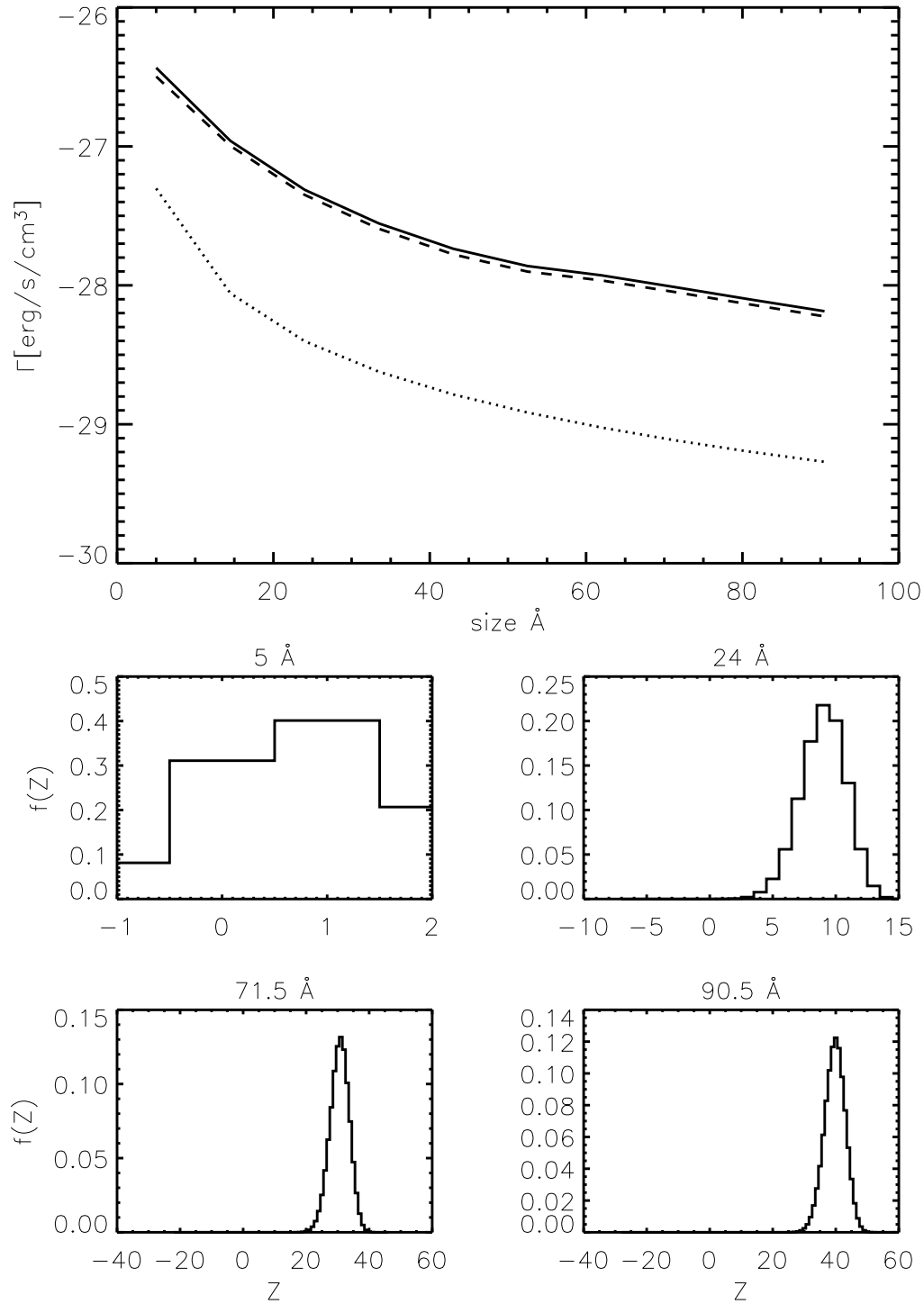


Figure 3.4: Top Panel: heating by dusts (solid line), cooling (dotted line) and the difference between heating and cooling (dashed line) for different diameters of the dust particles. Bottom Panel: the probability of finding a grain with a certain charge Z as a function of the grain dimensions.

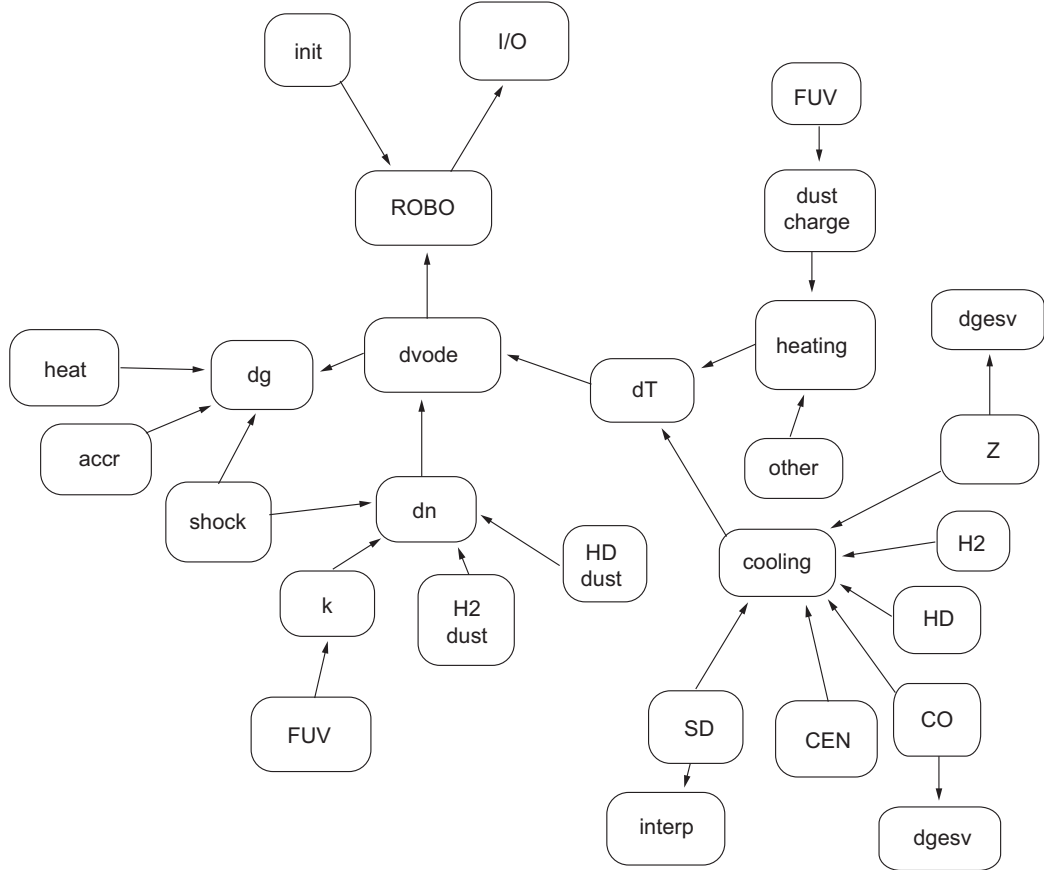


Figure 3.5: The structure of the code ROBO. *Dvode* is the solver for the ordinary differential equations, *dn*, *dT* and *dg* are the differential functions for the species, the temperature and the dust bins, *init* is the initialization of the parameters of the different models and *I/O* is the interface with the input/output devices. *Heat* represents the dust destruction by heating, *accr* is the dust accretion and *shock* represents the processes related to shocks. *k* are the rate coefficients, *FUV* is the impinging radiation, *H₂* and *HD dust* are the contribution of molecules of the dust to the gas-phase. *Heating* and *cooling* are self-explanatory. The cooling is determined by metals (*Z*), molecular hydrogen cooling (*H₂*), *HD*, *CO*, *CEN* [27] and *SD* [122]. *CO* and *Z* need a linear system solver, namely *dgesv*, while *SD* needs a subroutine to interpolate (*interp*). The arrows are for illustrative purposes only, and do not represent the actual code data-flow.

3.6.1 Mass conservation

The total mass per unit volume of the ISM at time t is $M(t) = \sum_i n_i(t) m_i$, where $n_i(t)$ is the current number density of the i -th species, m_i is its molecular or atomic mass and the sum is over all the species. While the number densities can vary with time, the total mass must be conserved. In the numerical integration of the system of differential Eqns. (2.5), the conservation of the total mass is not always guaranteed, because it depends on the physical processes, the choice of initial parameters and the time-step. Particular care is paid in our test computations to secure and to check run by run the conservation of the total mass, i.e. $|M(t_0) - M(t)|/M(t_0) \ll \mathcal{O}(10^{-10})$ where $M(t_0)$ is the initial total mass of the system per unit volume.

3.6.2 Time-step

Even with short time-steps, it may happen that some species reach negative values in a single time-step: this is because the differential of a species could be negative and its absolute value larger than the relevant numerical density. This problem could be solved by forcing the species to be positive. This would cause difficulties with the mass conservation, then in the subsequent time-step the solver would change again the sign of the species abundance and, finally, the cooling would produce some non physical effects. In brief, a negative value of the abundance of the species would artificially turn the cooling into heating, which is clearly impossible. The obvious way out is to suitably choose the time-step.

3.6.3 Numerical Solver

In our system of differential equations (2.5) there are 57 reactions to deal with, so a fast and accurate solver is needed. We use the routine LSODE of IDL. LSODE uses adaptive numerical methods to advance the solution of a system of ordinary differential equations by one time-step [67, 108], optimizing the process for user-defined time steps. In our case LSODE absolute tolerance is 10^{-40} and the relative one is 10^{-12} .

The number densities of all the particles (atomic species, molecules, dusty components and free electrons) are governed by the balance between creation and destruction processes and, even more important, span very wide ranges of values.

3.6.4 Ranges of applicability

ROBO can be safely used in the following intervals for temperature, density, and metallicity: $10 \leq T \leq 10^7$ K, $10^{-12} \leq n \leq 10^3$, and $10^{-12} \leq Z \leq 10$. The density range is somewhat limited towards the high value end, observational; estimates of the density in molecular clouds can indeed reach higher values. Work is in progress to extend the density range. Furthermore, let us remind the reader that $Z = 1$ means $[\text{Fe}/\text{H}] = 0$, the solar case, and $Z = 10$ means $[\text{Fe}/\text{H}] = 1$, i.e. the ratio of number densities (Fe/H) equal to ten times solar. Finally, as not all reaction rates cover the whole ranges of values, some extrapolation is required.

3.6.5 Free parameters

ROBO contains 47 parameters governing the physics, the mathematics, and the numerical procedure. Here we briefly comment the most important ones.

- *Ionized fraction of metals*: it fixes the fraction of C, O, Si and Fe in the first ionization level.
- *Metallicity*: the metallicity of the gas is defined as $Z = 10^{[\text{Fe}/\text{H}]}$. It is worth recalling here that $Z = 1$ is the solar case $[\text{Fe}/\text{H}] = 0$ (see below for more details).
- *Number densities*: the number density of the 27 elemental species and/or molecules, free electrons and dusty components are all in cm^{-3} .
- *Fraction of carbon dusts*: the percentage of carbonaceous grains. If it is equal to 1 all the dust is made by graphite grains and PAHs; if this parameter is equal to 0 all the dust is made by silicates. Intermediate values are also possible.
- *Gas temperature*: the temperature of the gas depends on the cooling and heating processes and changes during the gas evolution.
- *Dust temperature*: the temperature of the dust is kept constant during each run. It controls the formation of molecules on the surface of the grains and also the accretion of the dust grains themselves.
- *CMB temperature*: the gas temperature can not go below the temperature of the Cosmic Microwave Background (CMB). At present the CMB temperature is kept constant during each run.

- *Cosmic ray field*: the field formed by the cosmic rays that populate the gas. It destroys or ionizes molecules like H_2 . This field is expressed in s^{-1} , thus corresponding to the rate of ionization of the H_2 by the cosmic rays.
- *Total integration time of a model*: the total time of each run in s.
- *Time step*: the time step used in the models. A typical value is 10^3 years. However, it can be changed by the routine LSODE.
- Finally, there is a number of flags activating or switching off the different sources of heating and cooling and the mechanisms of dust formation and destruction we have described in the previous Sections.

3.7 ROBO: tests

To validate ROBO we have calculated two groups of models of gas evolution: the first one consists of 480 dust-free cases. Each case corresponds to a different combination of the parameters. The second group consists of 32 models of gas evolution but in which the presence of dust grains is taken into account.

The aim here is to investigate the evolution of the same elemental species in presence or absence of the dust. In addition to this, the large number of cases per group allow us to investigate the model response at varying the key parameters. Indeed, owing to the large number of parameters to our disposal it is not possible to explore the whole parameter space.

Finally, it is worth noticing that the choice of the parameters for the two groups of models is somehow guided by the fact that ROBO is mainly designed to become a sort of ancillary tool for NB-TSPH codes. Therefore, in view of this, the two groups of models use the same parameter space adopted by EVOL.

3.7.1 Dust-Free Models

Each model is a simulation of a unitary volume of gas in absence of dust. The results consist of 480 (see below) evolutionary models of the gas temperature and number densities of the 27 species under consideration plus the free electrons. As already emphasized, in each model special care is paid to secure the mass conservation and to avoid unphysical negative number densities. The models of this set are calculated neglecting the presence of any type of dust and they are meant to check the internal consistency of ROBO.

Set up of the parameters

Each model gives the thermal and density history of the gas for an assigned set of parameters. The number of parameters and the values assigned to each of them determine the total number of models to calculate. This is given by $N_m = \prod_{i=1}^N p_i$ where N_m is the total number of models, p_i is the number of different values for the i -th parameter, and N is the total number of the parameters, that in our case amounts to 47 (see Sect. 3.6.5).

For all the models we must specify the initial value of metallicity, the number densities n_{H_2} , n_{H^+} , n_{e^-} , and the gas temperature. We adopt four values for the metallicity $Z = 10^{[\text{Fe}/\text{H}]}$: $\{0, 10^{-6}, 10^{-3}, 1\}$; four values for the H_2 number density: $\{10^{-10}, 10^{-6}, 10^{-2}, 10^{-1}\} \text{ cm}^{-3}$; three values for the H^+ number density: $\{10^{-10}, 10^{-1}, 1\} \text{ cm}^{-3}$; two values for the electron number density: $\{10^{-10}, 10^{-1}\} \text{ cm}^{-3}$; five values for the gas temperature: $\{10, 10^3, 10^4, 10^6, 10^8\}$ K. More details on the metallicity are given below when we discuss the number densities of the metals. All the other parameters of the models have a constant value.

In all the models, the following quantities have a fixed initial value. They are: $n_{\text{H}} = 1.0$ for the neutral hydrogen, $n_{\text{H}^-} = 10^{-9}$ for the hydride, $n_{\text{H}_2^+} = 10^{-11}$ for the molecular hydrogen and $n_{\text{He}} = 0.1$ for the helium. No helium ions are present at the beginning, so we have $n_{\text{He}^+} = n_{\text{He}^{++}} = 0$. The initial values of all the deuteroids are set to 10^{-25} ; these are deuterium atom, its ions (D^+ and D^-), the molecules HD and D_2 , and the ion HD^+ .

Metals (i.e. C, O, Si, Fe and their ions C^+ , O^+ , Si^+ and Fe^+) are computed from the metallicity as follows⁵. We start from the general

$$[\text{Fe}/\text{H}] = \log_{10} \left(\frac{n_{\text{Fe}}}{n_{\text{H}}} \right) - \log_{10} \left(\frac{n_{\text{Fe}}}{n_{\text{H}}} \right)_{\odot}, \quad (3.84)$$

where n_{Fe} and n_{H} are the number densities of iron and hydrogen, and the definition of metallicity we have adopted, namely $Z = 10^{[\text{Fe}/\text{H}]}$. It must be emphasized that this notation for Z is different from the commonly used definition of metallicity, that is $Z = 1 - X - Y$ with X and Y hydrogen and helium weight fractions. In the usual meaning Z is therefore the weight fraction of all the species heavier than helium. In our definition Z is simply related to the iron content $[\text{Fe}/\text{H}]$ by the expression $Z = 10^{[\text{Fe}/\text{H}]}$. With this notation, Z can be higher than one: $Z = 1$ corresponds to the solar iron abundance. Considering now a generic metal indicated by X we can write

$$\frac{n_{\text{Fe}}}{n_{\text{X}}} = \left(\frac{n_{\text{Fe}}}{n_{\text{X}}} \right)_{\odot}, \quad (3.85)$$

⁵ROBO lets also insert the value for single metallic species without using the total metallicity.

and

$$n_X = Z n_H \left(\frac{n_X}{n_H} \right)_{\odot}, \quad (3.86)$$

Therefore if we know the ratio $(n_X/n_H)_{\odot}$, the total metallicity Z and the number density n_H of hydrogen in the model, we can derive the number density of the generic metal X . Note that by doing this we assume that for any metallicity the relative abundances of elements follow the solar partition. In other words we do not consider here the possibility that the gas may have distribution of heavy elements with respect to hydrogen different from that in the Sun (α -enhancement problem).

We use the same method to derive the number density of metal ions given by

$$n_{X+} = \kappa Z n_H \left(\frac{n_X}{n_H} \right)_{\odot}, \quad (3.87)$$

where κ represents the ionized fraction n_{X+}/n_X of the metal X . In the present models we set $\kappa = 0$, so that all the metals start as neutral species. Hot gas can ionize them in the early stages of the model computation.

The temperature of the gas is a free parameter, but cannot be smaller than the temperature of the CMB. For the present models we set $T_{\text{CMB}} = 2.73$ K, the present day measured value [10, 49].

Each model of the ISM is followed during a total time of 3.15×10^{14} s which approximately corresponds to 10^7 yrs. This choice stems from the following considerations. Each model of the ISM is meant to represent the thermal-chemical history of a unit volume of ISM whose initial conditions have been established at certain arbitrary time and whose thermal-chemical evolution is followed over a time scale long enough for secular effects to develop but short enough to closely correspond to a sort of instantaneous picture of large scale evolution of the whole system hosting the ISM unit volume. The initial physical conditions are fixed by a given set of parameters each of which can vary over wide ranges. One has to solve the network of equations for a time scale long enough to reveal the variations due to important phenomena such star formation, cooling and heating, but not long to allow to the system to depart from the instantaneous situation one is looking at. The value of 10^7 yr resulted to be a good compromise.

The initial value of the time-step is 3.15×10^{10} s $\approx 10^3$ yrs. This time-step determines the minimum number of steps required to cover the time spanned by a model. It means that each simulation needs at least 10^4 iterations to be completed. The LSODE integrator may introduce shorter time steps depending on the complexity of the problem; so 10^4 is the minimum number of

required steps. This value for the time-step seems to keep the system stable during the numerical integration.

While integrating, all the sources of cooling are kept active: metal cooling, H_2 cooling according to the prescriptions by [52] and [57], and, finally, the cooling from deuterated hydrogen.

More in general, the initial values of the number densities fall in three groups: (i) the elemental species with constant initial values, the same for all the models (namely H^- , H_2^+ , He^+ and He^{++}); (ii) the elemental species whose initial values are derived from other parameters (namely He, all the deuteroids and the metals, like for instance C and O, that depend on the choice of the total metallicity \tilde{Z}) and, finally, (iii) the elemental species with free initial conditions (namely H, H_2 , H^+ , and e^-).

Hydrogen group: H, H^+ , H^- , H_2 and H_2^+ . The initial values of the species H^- and H_2^+ are $n_{\text{H}^-} = n_{\text{H}_2^+} = 10^{-10} \text{cm}^{-3}$ [109], while the other three hydrogen species have free initial values.

Deuterium group: D, D^+ , D^- , D_2 , HD and HD^+ . The number densities of the deuteroids are calculated from their hydrogenoid counterparts. For the single atom species we have $n_{\text{D}} = f_{\text{D}} n_{\text{H}}$, $n_{\text{D}^+} = f_{\text{D}} n_{\text{H}^+}$ and $n_{\text{D}^-} = f_{\text{D}} n_{\text{H}^-}$, where $f_{\text{D}} = n_{\text{D}}/n_{\text{H}}$. For the molecules, we can consider the ratio f_{D} as the probability of finding an atom of deuterium in a population of hydrogen-deuterium atoms. This assumption allows us to calculate the HD, D_2 and HD^+ number densities as a joint probability; for HD and HD^+ we have $n_{\text{HD}} = f_{\text{D}} n_{\text{H}_2}$ and $n_{\text{HD}^+} = f_{\text{D}} n_{\text{H}_2^+}$, but for D_2 is $n_{\text{D}_2} = f_{\text{D}}^2 n_{\text{H}_2}$ as the probability of finding two deuterium atoms is f_{D}^2 . This is valid as long as $f_{\text{D}} \ll 1$.

Helium group: He, He^+ , He^{++} . The ratio $n_{\text{He}}/n_{\text{H}}$ is set to 0.08, thus allowing to the initial value of n_{He} to vary accordingly to the initial value for n_{H} . The initial number densities of the species He^+ , He^{++} are both set equal zero and kept constant in all the models.

Metals group: C, C^+ , O, O^+ , Si, Si^+ and Fe, Fe^+ . The Fe number density of the ISM is

$$n_{\text{Fe}} = n_{\text{H}} \cdot \text{dex} \left\{ [\text{Fe}/\text{H}] + \log \left(\frac{n_{\text{Fe}}}{n_{\text{H}}} \right)_{\odot} \right\}, \quad (3.88)$$

where $(n_{\text{Fe}}/n_{\text{H}})_{\odot}$ is the iron-hydrogen ratio for the Sun. To retrieve the number density of a given metal X we use $n_{\text{X}} = n_{\text{Fe}} \cdot f_{\text{X}}$, where f_{X} is the metal-iron number density ratio in the Sun.

The list of the species whose initial number densities are kept constant in all the models of the ISM is given in Table 3.13. The chemical composition of the ISM is typically primordial with the by mass abundances of hydrogen $X = 0.76$, and helium $Y = 0.24$ and all metals $Z \simeq 0$. The helium to hydrogen number density ratio corresponding to this primordial by mass

Table 3.13: Initial values for the number densities of the hydrogen and helium elemental species and the deuteroids. They are either fixed to a constant value or based upon the number density of one of the *free* hydrogen species n_{H} , n_{H_2} and n_{H^+} via the f_{D} factor. Since H^- and H_2^+ are constant, then also D^- and HD^+ are fixed. Values are indicated as $a(b) = a \times 10^b$. See also the text for details.

H^-	1.0(-12)	D	$f_{\text{D}}n_{\text{H}}$
H_2^+	1.0(-12)	D^+	$f_{\text{D}}n_{\text{H}^+}$
He	$0.8(-1) n_{\text{H}}$	D^-	$f_{\text{D}}n_{\text{H}^-}$
He^+	0.0(+0)	HD	$f_{\text{D}}n_{\text{H}_2}$
He^{++}	0.0(+0)	HD^+	$f_{\text{D}}n_{\text{H}_2^+}$
		D_2	$f_{\text{D}}^2n_{\text{H}_2}$

abundances is $n_{\text{He}}/n_{\text{H}} \simeq 0.08$. The adopted cosmological ratio for the deuterium is $f_{\text{D}} = n_{\text{D}}/n_{\text{H}} \simeq 10^{-5}$. With the aid of these numbers and the above prescriptions we get the number density ratios listed in Table 3.7.1 and the initial values of the number density in turn.

Results for dust-free models

In this Section we discuss the results we have obtained for the dust-free models. Together with this we also consider a side group of models calculated with some specific assumptions (e.g. without metal cooling and others to be explained in the course of the presentation) to underline some effects and to better understand the physical processes taking place in the ISM.

Special attention is paid to check whether there are some unexpected effects or drawbacks in the models and in ROBO. We also describe how different physical quantities affect the overall behaviour of gas. This is achieved by varying a single parameter at a time and keeping constant all the others.

Temperature and H_2 density. In Fig. 3.6 we compare the temperature evolution for different values of the initial molecular hydrogen densities in two cases with very different metallicity, i.e. $Z = 10^{-10}$ and $Z = 1$. The important role played by the metal cooling is soon visible comparing the two panels. In the bottom panel, cooling is so strong that all the models reach almost the same final temperature below 10 K. The opposite in the top panel. Comparing each curve with the others in both panels, the effect of the molecular hydrogen is evident: higher H_2 densities imply steeper cooling

curves. In the metal free models, the temperature systematically shifts to lower values at increasing the density of the molecular hydrogen (top panel of Fig. 3.6). The effect is similar but enhanced in the case of metal rich models (bottom panel of Fig. 3.6).

Metallicity. Fig. 3.7 shows the evolution of the temperature (top panel) and H_2 number density (bottom panel) of models with different metallicity Z . Each curve is characterized by a different initial metallicity. In these models the sources of UV radiation are at work. As in the previous Figure, the cooling strongly depends on the metallicity. The marked knee in the temperature-age relationship is caused by the cooling via the metallicity. Looking at the H_2 -age relationship we note that the formation of H_2 is favored when more free electrons are present (this effect becomes clear when considering Figs. 3.7, 3.8, and 3.9).

UV radiation. The UV radiation plays a key role in the H_2 density evolution. To cast light on the issue, we calculated models with no UV sources. They are displayed in Fig. 3.8. The top panel shows the temperature-age relationship, whereas the bottom panel shows the H_2 number density-age relationship. Comparing the bottom panel of Fig. 3.7 to that of Fig. 3.8 it is clear the effect of the UV radiation. When the UV radiation is present, H_2 is destroyed very early on, whereas when the UV radiation is absent the number density of H_2 remains nearly constant during the whole evolution. We also note that in the first case the effect of the cooling is stronger. This happens because the UV flux increases the density of free electrons, and since they act as colliders, the eventual higher number of collisions determines a marked improvement in the cooling process.

Ionized versus neutral metals. The difference in the cooling could be attributed to different efficiencies of the cooling by ionized and neutral metals. This is in contrast by the results shown in Fig. 3.10, where models with the metal cooling by ionized species (top panel) and the metal cooling by neutral species alternatively switched off (bottom panel) are compared. For each metallicity the curves in Fig. 3.7 are roughly the sum of the curves presented in Fig. 3.10 (both panels). In the top panel the effect of the cooling starts earlier when the contribution due to neutral metals is present and, in general, the cooling process varies more smoothly than the case without cooling by neutral species. Even if the two cooling histories are different, there is no evidence that the cooling by ionized metals is strong enough to justify the differences in cooling between models with UV (Fig. 3.7) and models without UV (Fig. 3.8).

Metallicity and Cooling. In Fig. 3.11 are plotted four different models with different combinations of metallicity (very high or very low) and cooling by

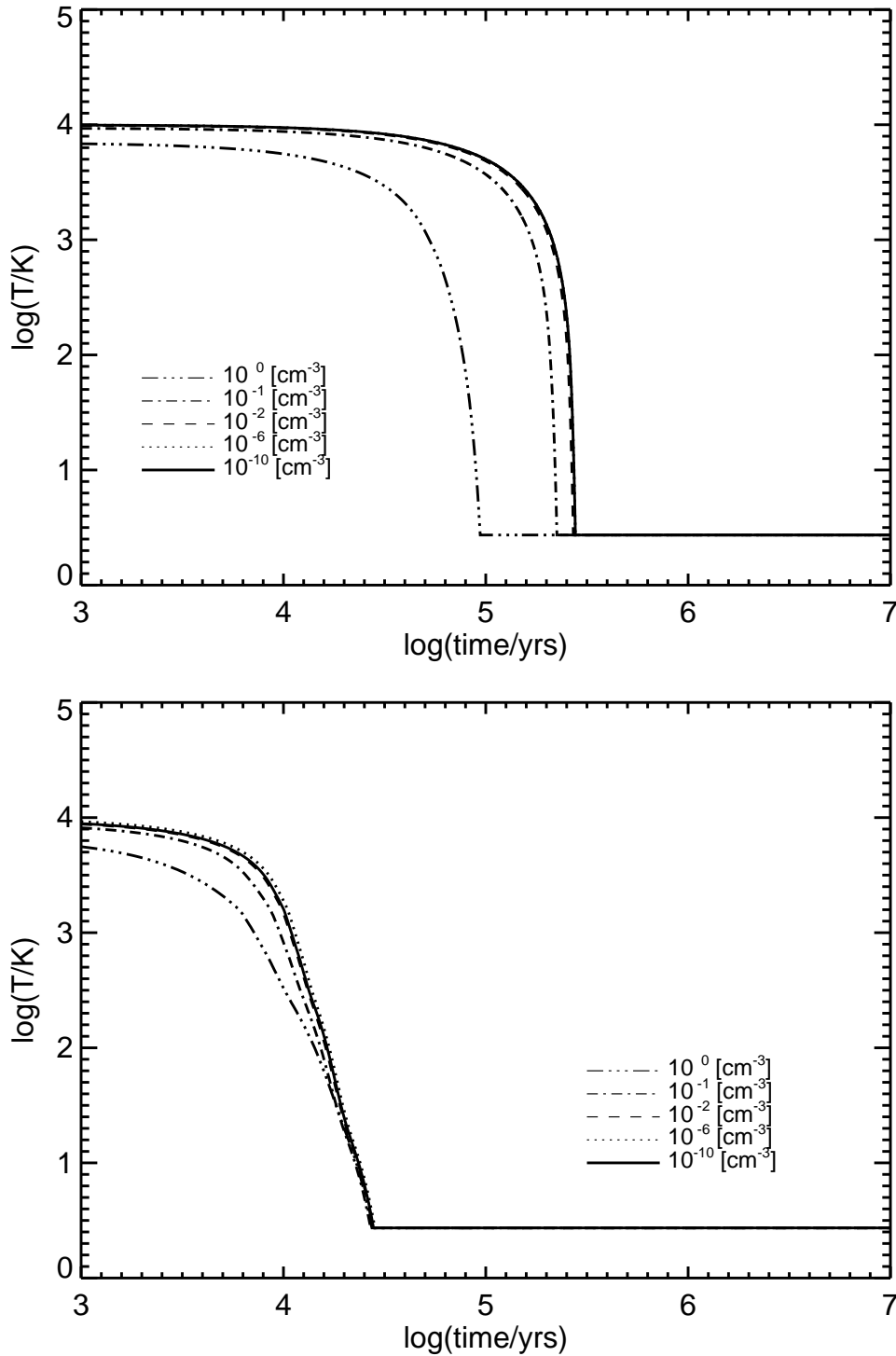


Figure 3.6: Temperature evolution for different values of the initial H_2 densities. The lines represent the time evolution in the cases $H_2 = 10^{-10}$ (solid line), $H_2 = 10^{-6}$ (dotted line), $H_2 = 10^{-2}$ (dashed line), $H_2 = 10^{-1}$ (dashed-dotted line) and, finally, $H_2 = 10$ (three dots-dashed line). All the densities are in cm^{-3} . Top Panel: the models with $Z = 10^{-10}$. Bottom Panel: the same as in the top panel but for $Z = 1$. See the text for more details.

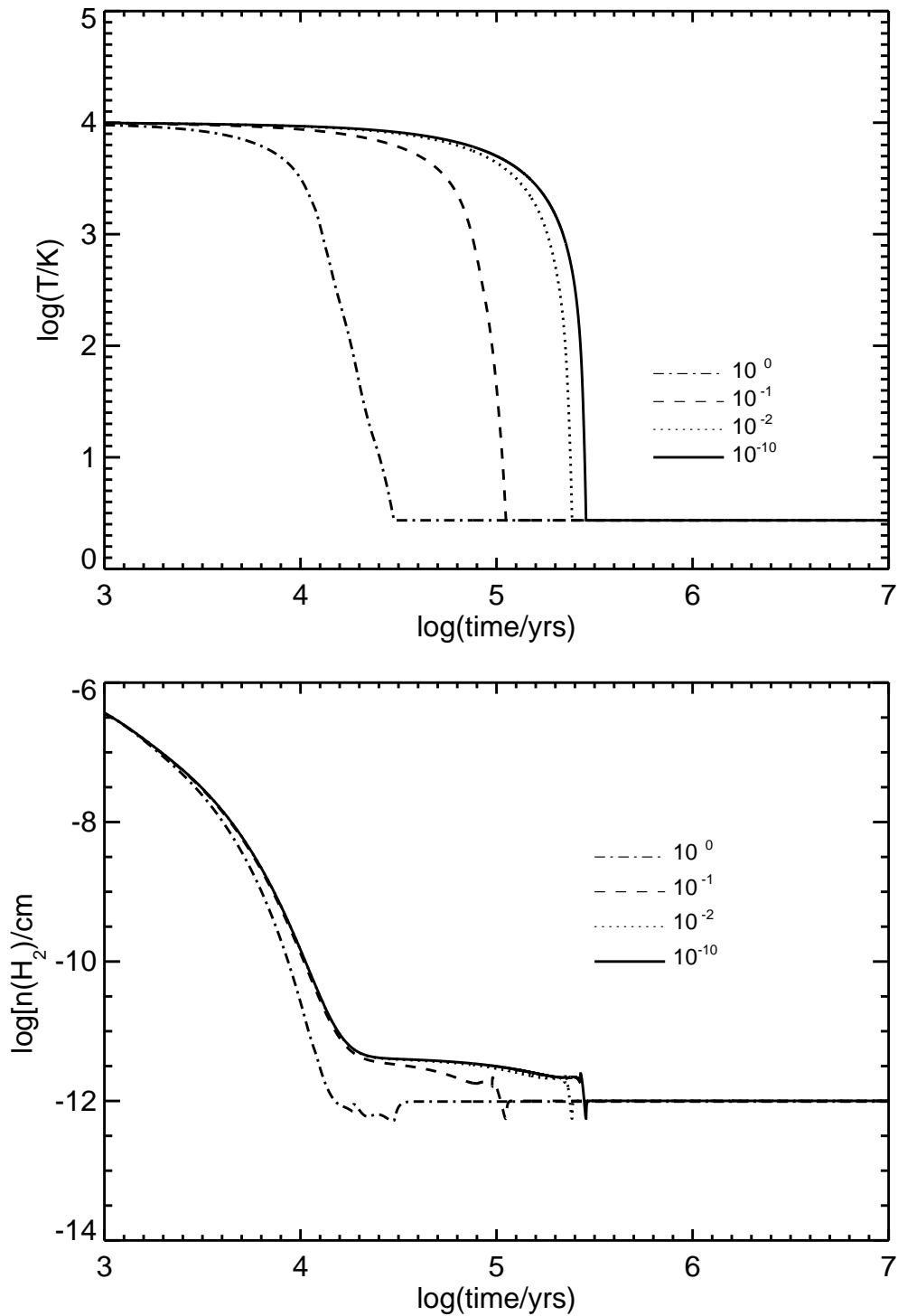


Figure 3.7: Top Panel: Temperature evolution for different metallicities Z and in presence of the UV radiation field. Bottom Panel: evolution of the number density of molecular hydrogen for the same set of parameters. We represent the cases $Z = 1$ (dot-dashed line), $Z = 10^{-1}$ (dashed line), $Z = 10^{-2}$ (dotted line) and, finally $Z = 10^{-10}$ (solid line). See the text for more details.

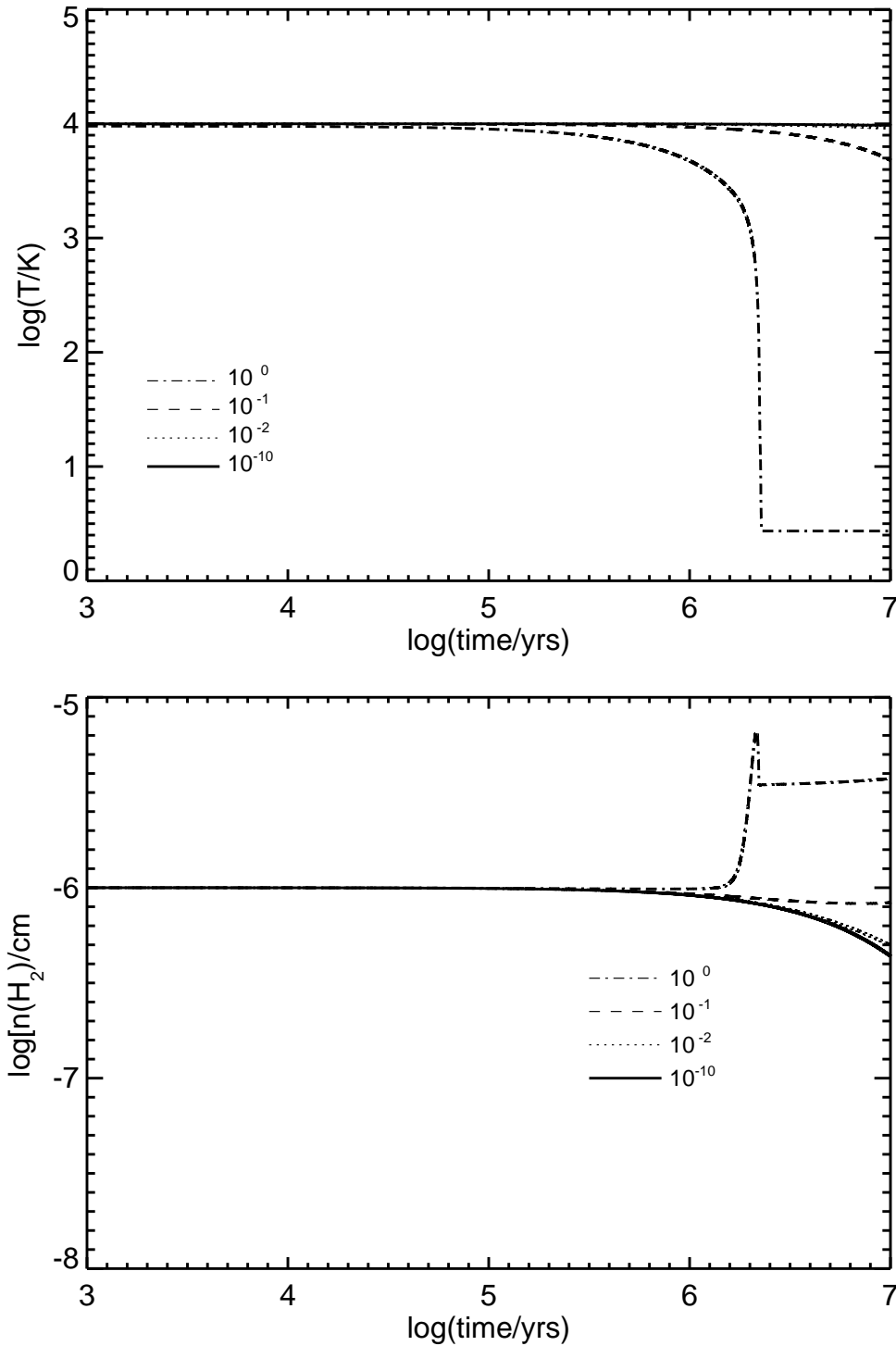


Figure 3.8: Top Panel: Temperature evolution for different metallicities Z but in absence of the UV radiation field. Bottom panel: evolution of the molecular hydrogen for the same set of parameters. We represent the following cases: $Z = 1$ (dot-dashed line), $Z = 10^{-1}$ (dashed line), $Z = 10^{-2}$ (dotted line) and, finally, $Z = 10^{-10}$ (solid line). See the text for more details.

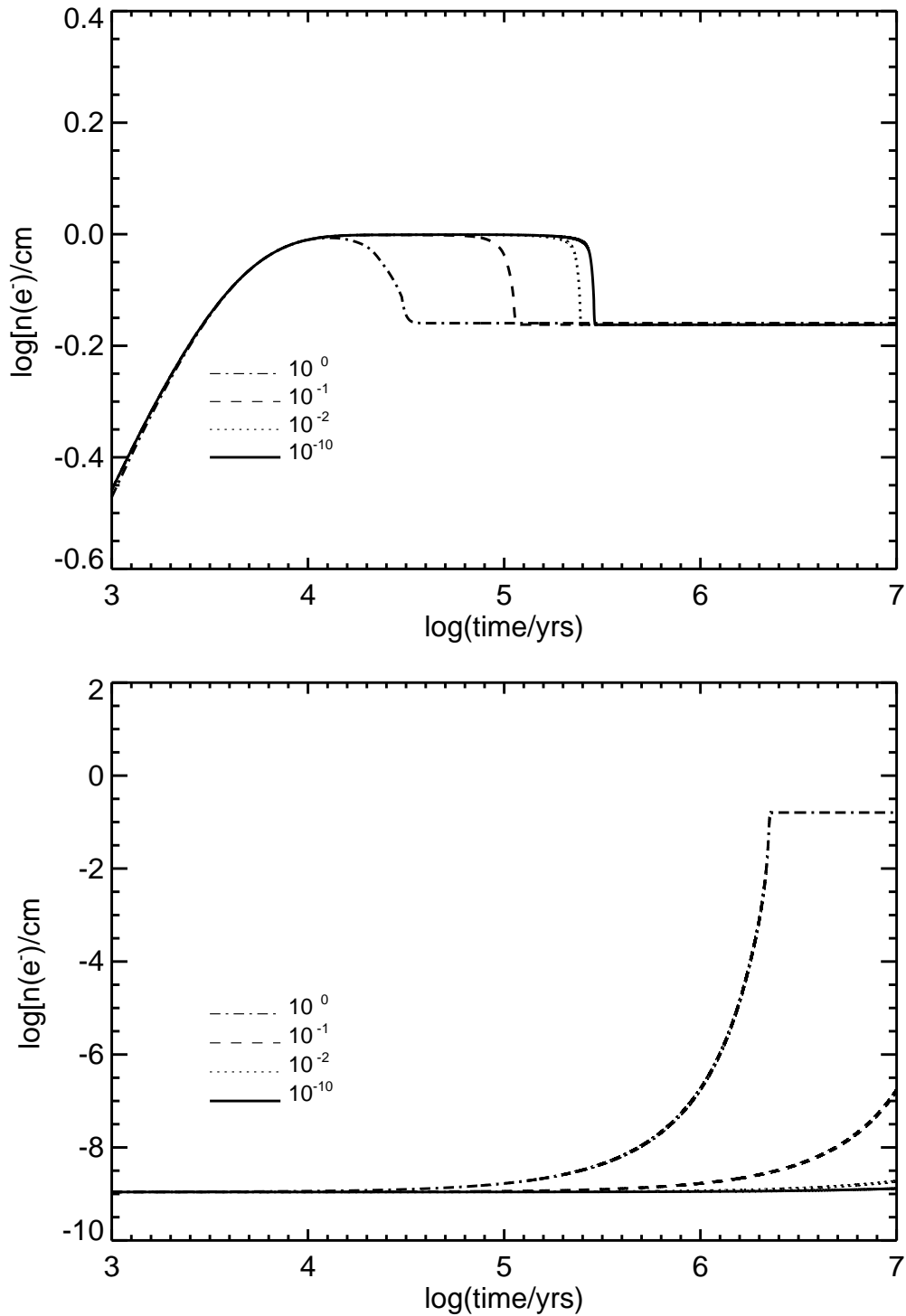


Figure 3.9: Temporal evolution of the electrons number density for different metallicities Z and in presence of the UV radiation field (top panel, related to Fig. 3.7) or without the UV field (bottom panel, same model of Fig. 3.8). The metallicities are $Z = 1$ (dot-dashed line), $Z = 10^{-1}$ (dashed line), $Z = 10^{-2}$ (dotted line) and, finally $Z = 10^{-10}$ (solid line). See the text for more details.

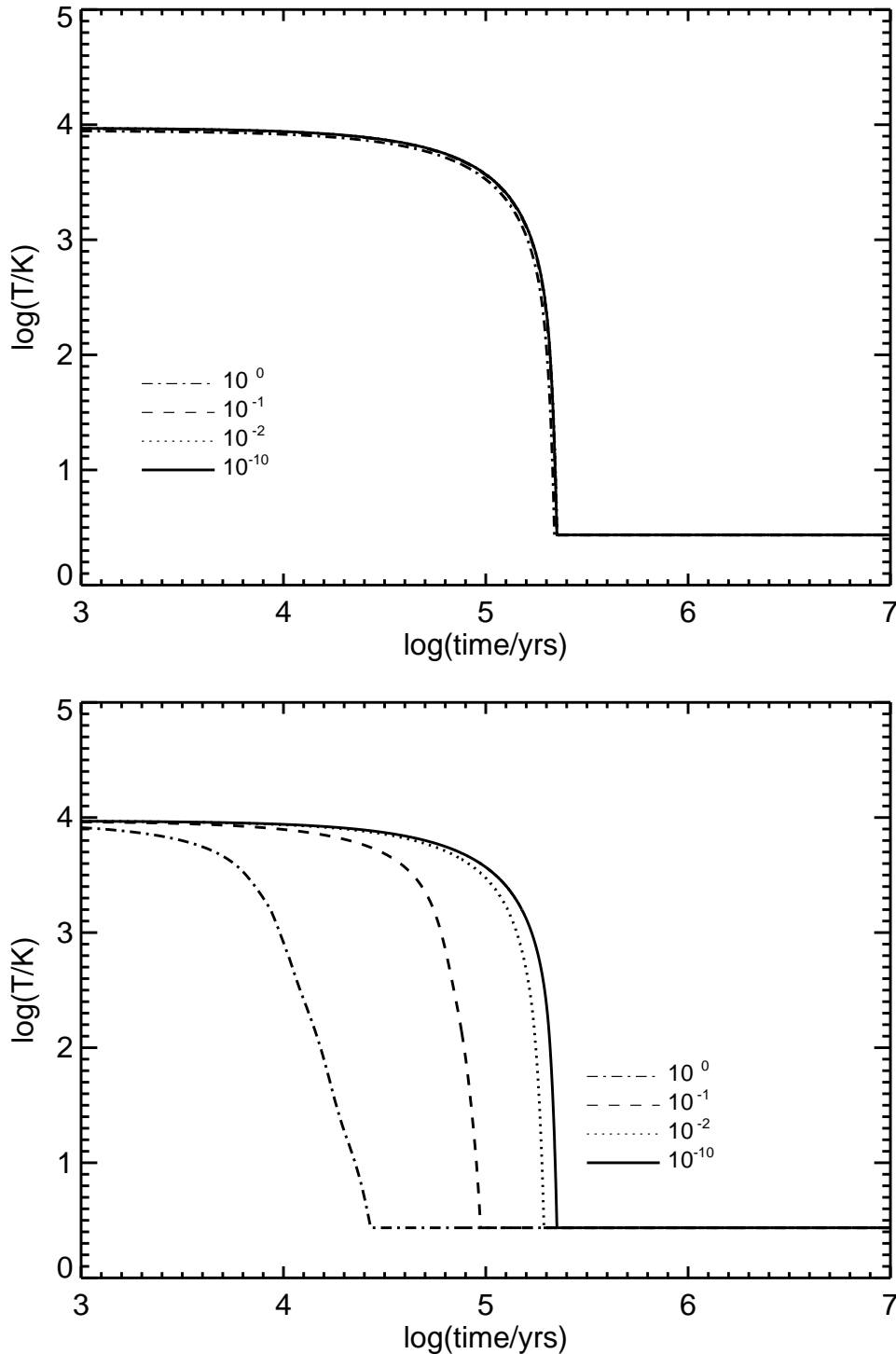


Figure 3.10: Temperature evolution for different metallicities Z and with the cooling contribution by ionized or neutral metals alternatively switched off. Top Panel: no cooling by ionized metals. Bottom panel: no cooling by neutral metals. In both panels the meaning of the lines is as follows: the dot-dashed line is for $Z = 1$, the dashed line for $Z = 10^{-1}$, the dotted line for $Z = 10^{-2}$, and the solid line for $Z = 10^{-10}$. See the text for more details.

metals (included or switched off) ⁶. This plot highlights how the cooling by metals affects the temperature and hence the physical status of the gas. As expected, the model with high metallicity and cooling by metals included, is the one experiencing the strongest cooling. The two models with very low metallicity have a similar behavior independently from the presence or absence of the cooling by metals. The last case, with high metallicity and no cooling by metals, is the one with the lowest temperature decrease. The reason for it is explained in Fig. 3.12, where the evolution of H₂ for the four cases under consideration is shown.

The model with high metallicity and no cooling by metals has the lowest H₂ density compared to the other three and consequently has low cooling. From Fig. 3.12 we also see that the model with high metallicity and cooling by metals has the highest H₂ density. This explains the results in the top panel of Fig. 3.11, in the sense that the cooling process here could be mainly due to the contribution coming from the molecular hydrogen. The bottom panel of Fig. 3.11 shows the same models with no cooling by H₂. In this case only the model with cooling by metals included and high metallicity undergo a significant cooling. This somehow opposes to the previous explanation.

3.7.2 Models with dust: parameter set up

In this Section we consider models in which the effect of the dust grains is taken into account. We adopt here the same values for the parameters as in the dust-free models.

The minimum initial metallicity is $Z = 10^{-6}$ and the initial number density of the molecular hydrogen is $n_{\text{H}_2} = 10^{-6} \text{ cm}^{-3}$. The number densities of electrons and H⁺ are free parameters; they are $n_{\text{H}^+} = \{10^{-10}, 10^{-1}\}$ and $n_{\text{e}^-} = \{10^{-10}, 10^{-1}\}$, both in units of cm^{-3} as usual. The initial temperature is set to $T = 10^4 \text{ K}$.

The only difference with respect to the previous models is the presence of dust. We adopt four values for the number density of dust grains, namely $n_{\text{dust}} = \{0, 10^{-3}, 10^{-2}, 10^{-1}\} \text{ cm}^{-3}$. In these models the composition of the dust mixture is 50% of carbonaceous grains and 50% of silicates.

We also calculate models with or without dust sputtering by shocks, in order to describe the behaviour of a turbulent gas particle with and without the grain depletion due to the shocks.

All the other parameters remain the same as in the dust-free models, such as the number densities of different elements and the cooling processes. In all

⁶In these models we switch off the C92 cooling to better highlight the sole effects due to different metallicities.

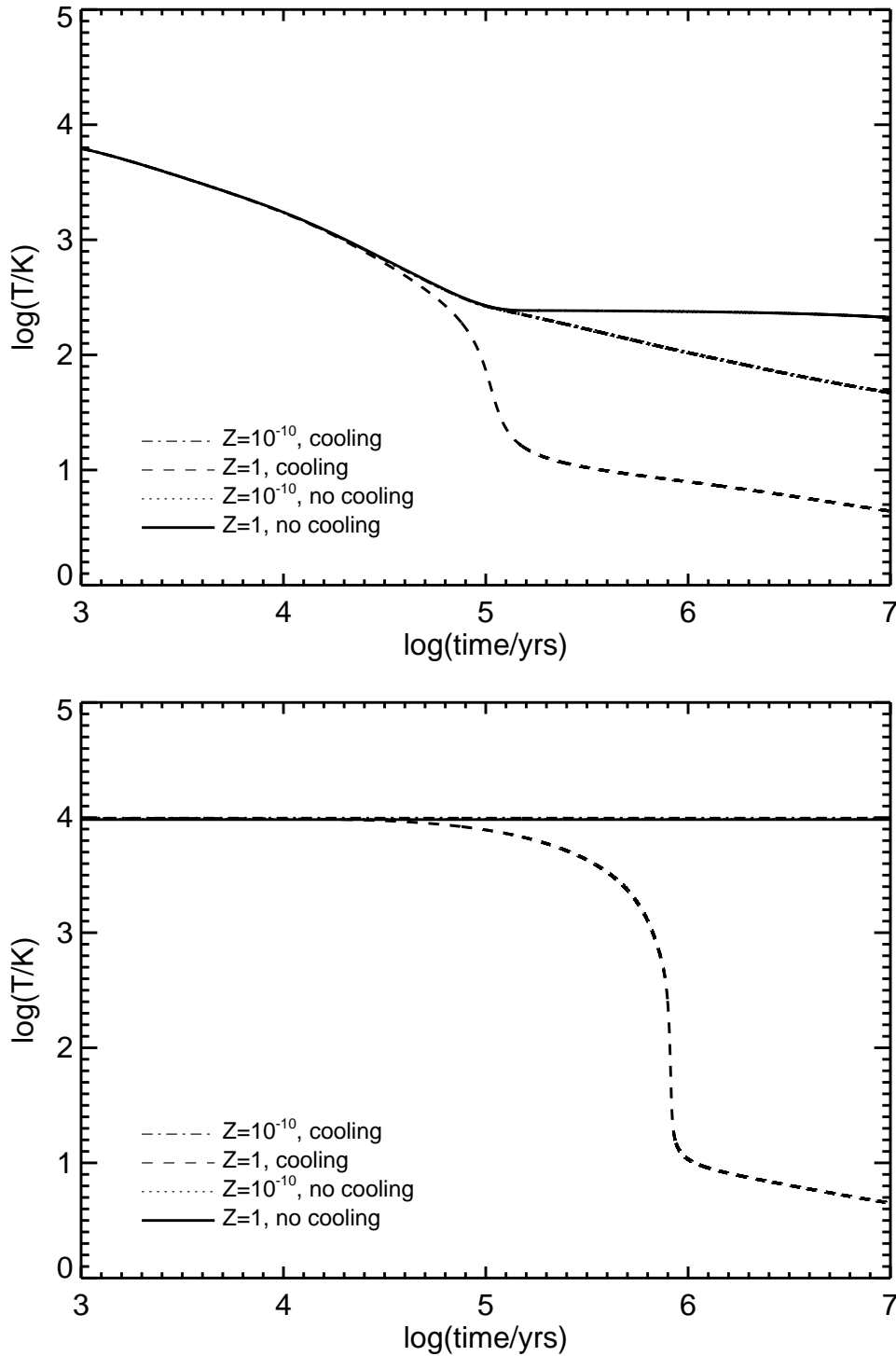


Figure 3.11: Temperature evolution with different metallicities Z and cooling options. The meaning of the lines is as follows: high Z and no cooling (solid line), low Z and no cooling (dotted line), high Z and cooling included (dashed line), low Z and cooling included (dashed-dotted). The dashed-dotted and dotted lines overlap. Top Panel: the H_2 cooling is enabled. Bottom Panel: the H_2 cooling is switched off. The cooling by Cen is switched off in both panels.

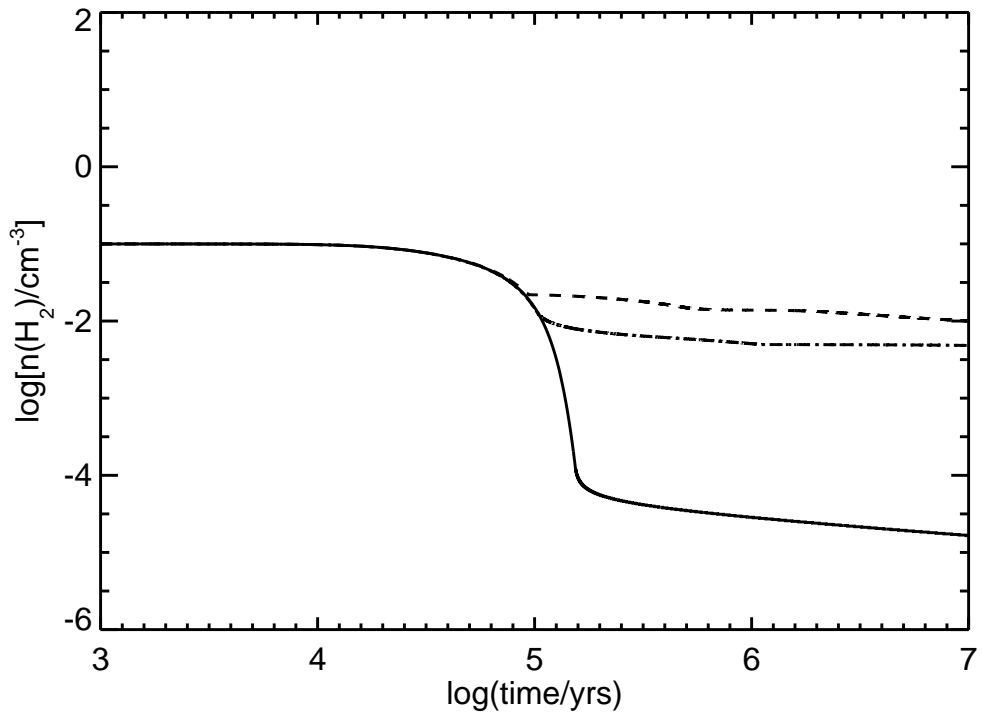


Figure 3.12: Evolution of the number density of molecular hydrogen for different initial metallicity Z and options for the cooling. The meaning of the lines is as follows: high Z and no cooling (solid line), low Z and no cooling (dotted line), high Z and cooling enabled (dashed line), low Z and cooling switched off (dashed-dotted line). The dashed-dotted and dotted lines overlap. The cooling by Cen is switched off in both panels.

$Z=10^{-10}$, cooling
 $Z=1$, cooling
 $Z=10^{-10}$, no cooling
 $Z=1$, no cooling

these models thermal sputtering and dust formation are active, so the dust properties are let change during the evolution of the interstellar medium.

Results for models with dusts

The series of plots going from Fig. 3.13 through Fig. 3.15 show the temporal evolution of three important quantities of the models, namely the gas temperature, the number densities of dust and molecular hydrogen for different amounts of initial dust and different initial metallicities. Clearly there is a tight relationship between the initial amount of dust, the temporal behaviour of temperature, and the number density of H_2 . First, at a given low metallicity, by increasing the dust fraction the temperature decreases earlier and faster (top panel of Fig. 3.13), whereas if the metallicity is high there is no remarkable effect due to the increased dust content (bottom panel of Fig. 3.13). Also, for the low metallicity, the trend is anticipated as the dust content increases.

Looking at the temporal evolution of the number density of H_2 shown in the panels of Fig. 3.14 we note that, in coincidence with the temperature fall off and subsequent gentle decrease, the H_2 number density first decreases and then increases forming a local minimum. This happens because the dust drives the formation of H_2 : models with more dust suffer more cooling and hence form more H_2 . Only if the metallicity is very high, the cooling effect of dust grains loses importance as shown by the bottom panel of Fig. 3.13. To conclude, the curves displayed in the top and bottom panels of Fig. 3.14 have nearly the same shape, but a different vertical offset. The position and depth of the minima depends on the temperature variation and the vertical offset clearly depends on the amount of dust present in the gas. This means that amount of dust and H_2 are closely related.

Finally, we calculate and present six models (three for each initial amount of the dust density) that include now the dust destruction by shock sputtering and vaporization. Their temporal evolution is limited to the first 10^5 years only. The results are shown in Fig. 3.16 (the gas temperature) and Fig. 3.17 (the dust grains number density as a function of the size of dust grains). Looking at Fig. 3.16, the temporal evolution of the gas temperature is the same as in the previous case with the sole thermal sputtering at work. In contrast, the dust number density undergoes big changes as shown in Fig. 3.17, because the shock sputtering is very efficient. Fig. 3.17 shows how the dust distribution changes with the time for the $n_{\text{dust}} = 10^{-3} \text{ cm}^{-3}$ case. Plotting the data of Fig. 3.17, the dust grains have been grouped in bins of according to their size⁷. The lines represent different distributions at different

⁷It worth noticing that even if the initial distribution of dust density per size bin is a

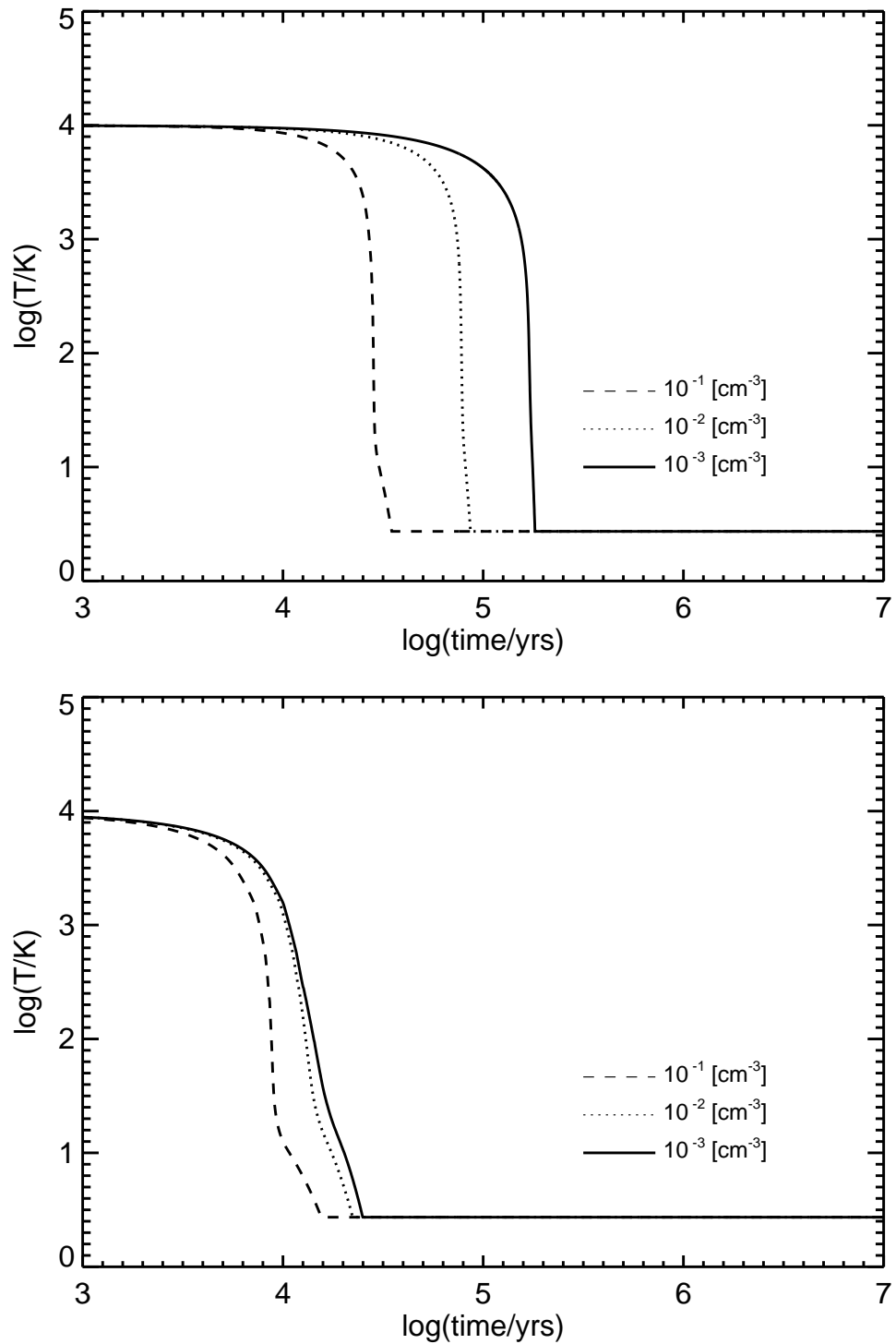


Figure 3.13: Temperature evolution for different amounts of initial dust. Top Panel: low metallicity cases. Bottom Panel: high metallicity cases. In both panels the meaning of the lines is as follows: the solid line is for $n_{\text{dust}} = 10^{-3}$, dotted line is for $n_{\text{dust}} = 10^{-2}$ and, finally, the dashed line is for $n_{\text{dust}} = 10^{-1}$. See the text for more details.

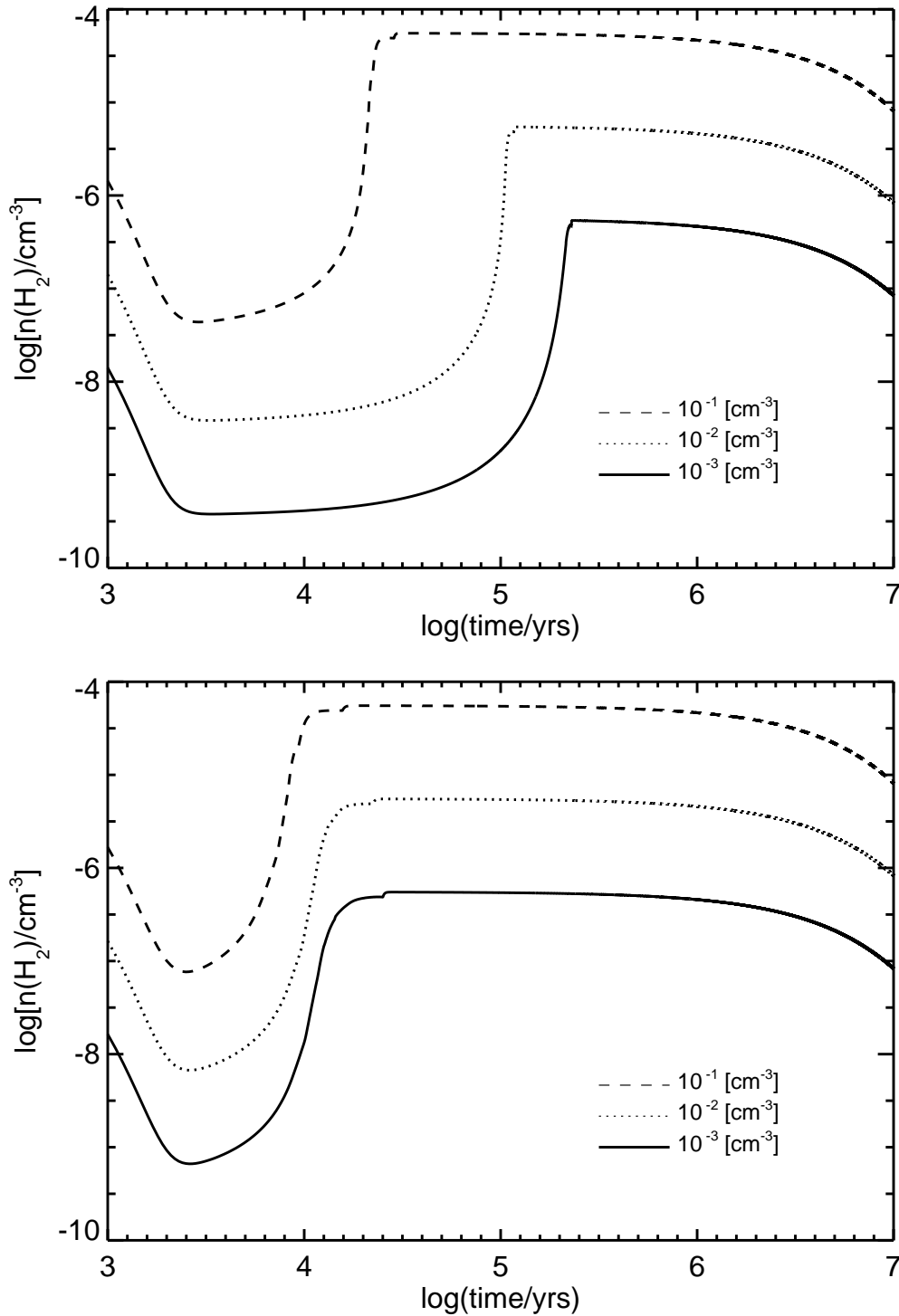


Figure 3.14: Evolution of molecular hydrogen for different amounts of initial dust. Top Panel: low metallicity cases. Bottom Panel: high metallicity cases. In both panels the meaning of the lines is the same as in Fig. 3.13. See the text for more details.

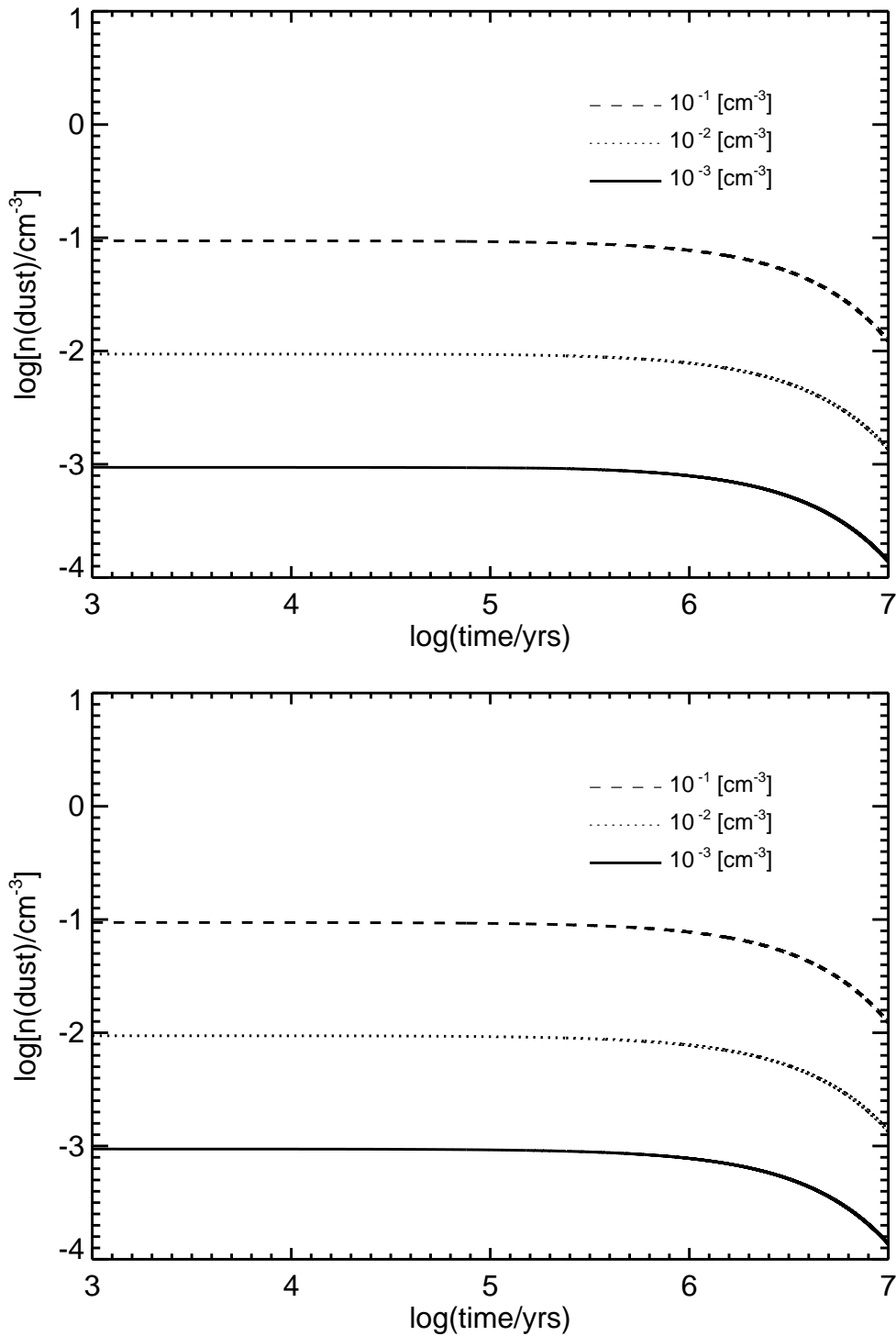


Figure 3.15: Dust density evolution for different initial amounts of dust. Top panel: low metallicity cases. Bottom panel: high metallicity cases. The meaning of the lines is the same as in Fig. 3.13. See the text for more details.

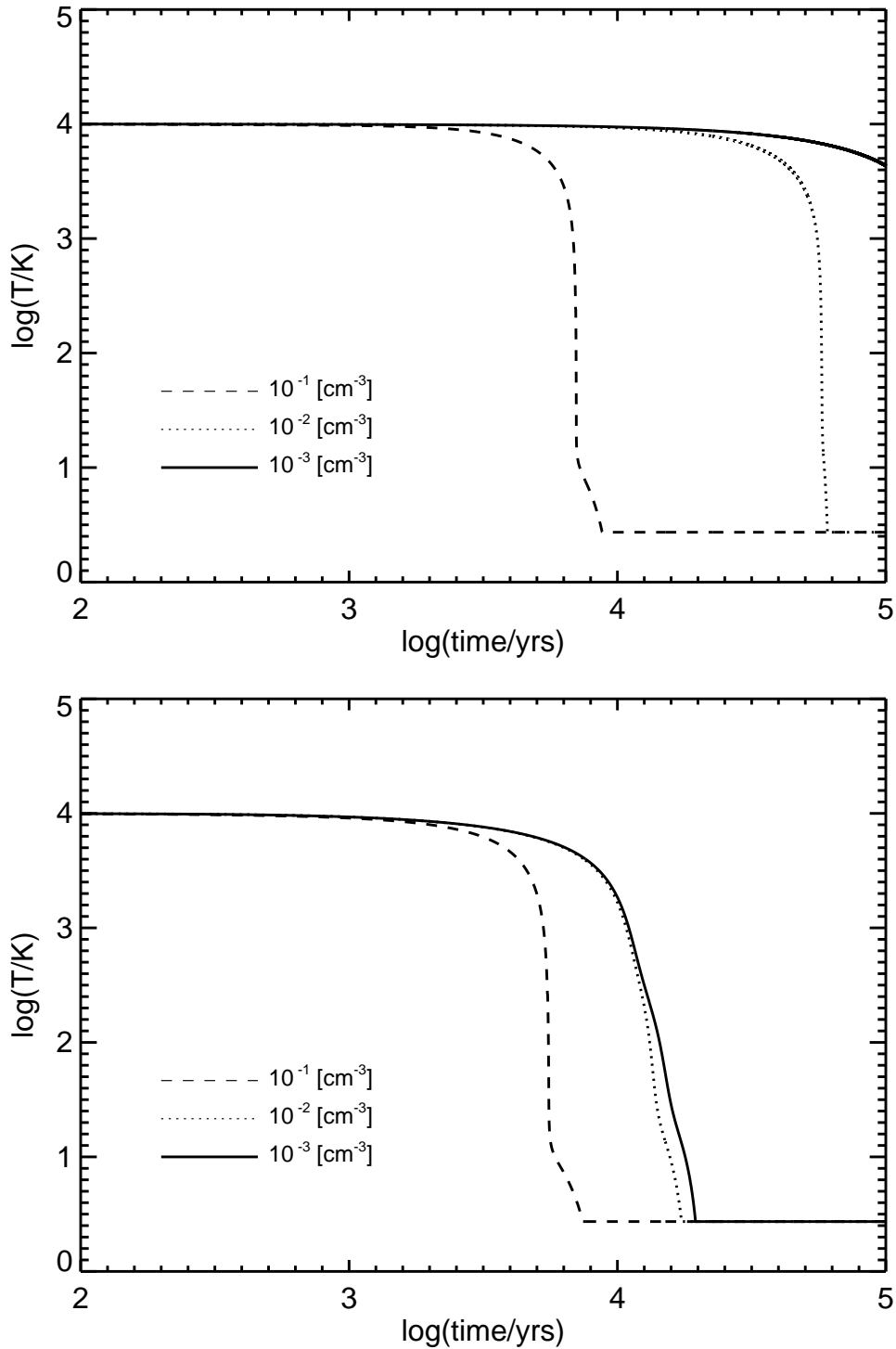


Figure 3.16: Temperature evolution for different amounts of dust. Shock disruption is enabled. Top panel: low metallicity cases. Bottom panel: high metallicity cases. The meaning of the lines is the same as in Fig. 3.13. See the text for more details.

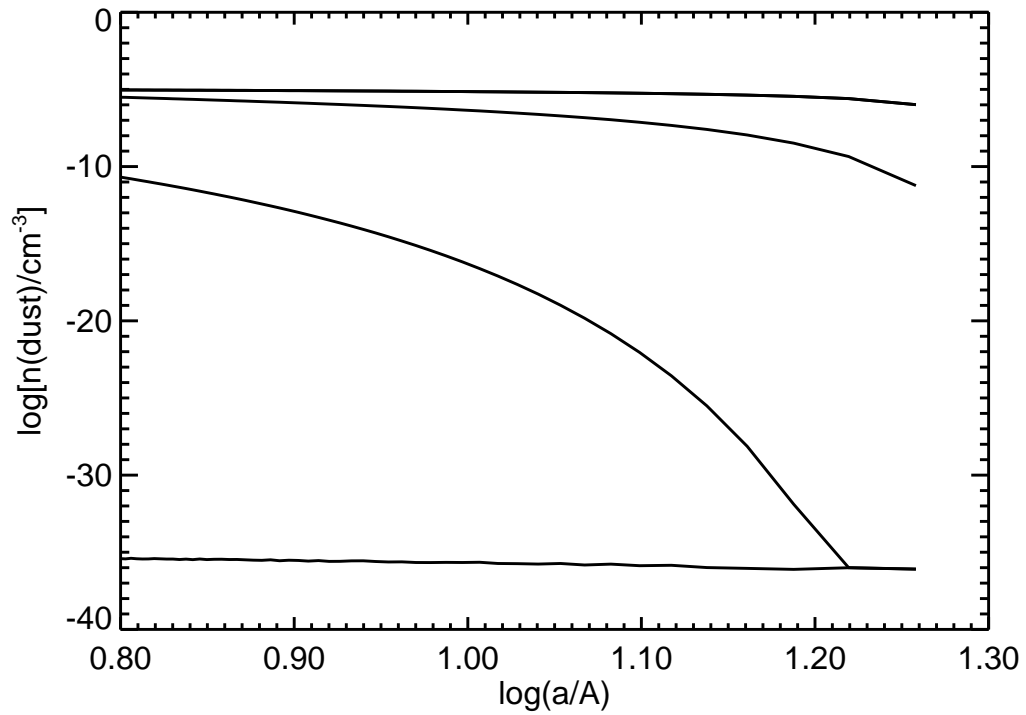


Figure 3.17: Dust density evolution for different dimension bins. Shock disruption is enabled. Lines represent the distribution of dust among the bins for different ages (from top to bottom, 10, 10^2 , 10^3 and 10^4 years). See the text for more details.

ages, namely 10, 10^2 , 10^3 and 10^4 years from top to bottom. As expected, the shock first destroys the large size grains and then the small ones.

power law, assuming that the dimension of the bin size is chosen in such a way that the density per bin is constant, the initial distribution shown in Fig. 3.17 appears to be flat.

Chapter 4

Interfacing ROBO with Nbody/TreeSPH

In this Chapter we describe some methods to interface ROBO to the NB-TSPH code EVOL. We first describe the two classes of solutions considered: (i) the classical methods, like direct integration and grids, and (ii) the methods based on the artificial intelligence paradigm, such as the Support Vector Machines and the Radial Basis Functions. Then we describe our choice, the Artificial Neural Networks, describing how they work and their algorithms.

4.1 Introduction

Even when the physics is described with the desired accuracy, the number of mass elements (particles) customarily used in large-scale simulations is large (typically 10^4 to 10^7), so that large amounts of computational workload are requested. Clearly, computing the internal evolution of each mass element in detail is extremely time-consuming, whatever the method chosen to follow it might be.

The aim of this Chapter is to present a method able to alleviate part of the above difficulties by approximating the exact solution of a detailed physical model and yet ensuring both a robust and sufficiently precise description of the gas properties, while maintaining the computational workload to an acceptable level.

The method stands on the model of the ISM and companion code ROBO described previously in this work. In brief, ROBO follows the evolution of a gas element during a given time interval Δt . In other words, given the initial physical and chemical state of a gas element as functions of its hydrodynamical properties, the relative abundances of its chemical constituents and the

kind of interactions with the surrounding medium, the model calculates the *final* state after some time interval Δt .

The straight implementation of ROBO into a generic hydrodynamical simulation (and companion code) to perform the on-the-fly computation of the ISM properties, although desirable, would be far too expensive in terms of computational costs. The easiest way of proceeding would be to store the results of ROBO as look-up tables (grids) where the values of interest (e.g. the physical parameters of the gas element: mass fractions of molecular, neutral, ionized hydrogen; temperature, density, pressure; the abundance of dust, and so on) are memorized for a given (large) set of initial configurations. However, each parameter to be stored corresponds to one dimension of the look-up table (grids). Thus, tracking N parameters requires a N -dimensional matrix. Such matrix is discrete, so an interpolation in a N -dimensional space is required to know the final state corresponding to a given initial state of a generic gas element. The all procedure when applied many times to a high number of gas particle would be very time consuming. A different strategy must be conceived.

To cope with this, we develop an algorithm based on the ANN technique to establish the correspondence between the *initial* + *final* state. The ANN technique can handle a large number of parameters without requiring a real-time interpolation. The ANNs require few floating point operations and “learn” to behave like the original physical models on which they are trained. The computational cost of it is easily affordable.

4.2 Possible methods to interface ROBO and a NB-TSPH code

The methods proposed in this Section are divided into two groups. The first group includes standard approaches, such as the direct integration of the system of differential equations, or the interpolation of a database of pre-compiled models using a grid method. The second group uses techniques that are successfully applied to many fields of research but are still largely unconsidered in astrophysical simulations. Such techniques are based on the artificial intelligence (AI) paradigm, and they permit to obtain fair results with simple and unspecific algorithms. We describe here the Support Vector Machines (SVM) and the Radial Basis Function (RBF). There are two other methods that belong to this group, the Artificial Neural Networks (ANN), that are described in the Section 4.3, and the Markov’s Chains (MC) that will be described in the Chapter 6 as a suggestion for future developments.

4.2.1 Classical methods

There are different methods to embed a complicated chemical code into a NB-TSPH code. The main problem (mentioned several times in the previous Sections) resides in the fact that a chemical code requires a large amount of CPU-time depending on its complexity, and a *direct integration* needs a fine optimization and a well-balanced parallelism. In the direct integration paradigm, a large part of the computational resources is used by the chemistry algorithms, and in particular by the chemical network solver, to an amount depending on the number of reactions that are included in the model or, more precisely, their stiffness. Even if the network included only a few reactions, if one of them had very high rates it could slow down the whole integration process.

At very low metallicities, the chemical network included in ROBO is quite fast; this is because the fastest reactions occur only at high Z . For this reason, the direct integration method can be used at very low metallicities. Unfortunately, when the gas becomes denser or reaches an higher Z the solver considerably slows down the whole code. Considering a galaxy simulation with 10^5 gas particles, and given that the solver should find a solution at every time-step for each particle, the total integration time would increase unacceptably.

A trivial objection is that the workload of the NB-TSPH could be split into many processors actually reducing the number of particles: this issue will be discussed later.

We propose an example in order to have a rough value for the time needed to complete a full simulation of a galaxy. We define τ the CPU-time, and we assume that $\Delta\tau$ is the CPU-time needed to integrate the chemical network over a time-step of $\Delta t = 10^4$ yr (analogously t is the simulation time). A simulation with $N_g = 10^5$ gas particles, takes $\tau_{\text{tot}} = N_g \Delta\tau$ seconds to evolve one time-step. Now, we consider that our simulation uses $P = 100$ CPUs, and a linear speed-up with the increasing of the CPUs number¹. This gives $\tau_{\text{tot}} = N_g \Delta\tau / P$. If the model galaxy is evolved for an Hubble time, approximately $t_H = 10^{10}$ yr, we have

$$\tau_{\text{tot}} = \frac{N_g t_H}{P \Delta t} \Delta\tau \approx 10^9 \Delta\tau, \quad (4.1)$$

considering only the time spent to integrate the system of differential equa-

¹ The speed-up is a number that indicates the efficiency of the parallel code respect to the serial code. It is usually defined as $S_p = T_s / T_p$ where T_s is the execution time of the serial code, T_p is the execution time of the parallel code with p processors. When $p = S_p$ we have the linear speed-up, also known as the ideal speed-up. This is a *very optimistic*, almost impossible assumption! It is adopted here only for simplicity.

tions based on the chemical network. It is clear that $\Delta\tau$ cannot be large. Note that this description of the problem is highly simplified, since a real NB-TSPH code allows a better optimization strategy to reduce the total workload. However, in this example we neglect the CPU-time spent to solve the linear systems that calculate the statistical equilibrium for the cooling of the metals and many other features that require a large amount of CPU.

The direct integration method could be substituted with some theoretical assumptions about the chemical evolution. The drawback of this method is that in some cases the system becomes non-linear; in these cases the analytical approximations is too rough to give correct results and the direct integration becomes unavoidable.

Another widely used technique is the *grid method*. It consists in creating a database of chemical models changing the initial parameters over a predefined range of values. This database is then interpolated on-the-fly during the NB-TSPH simulation to retrieve the evolved parameters at each time-step. Let's see step-by-step how this method works.

(i) The first step consists in choosing N free parameters x_i , each one in the range $[x_i^-, x_i^+]$. These parameters should be chosen considering their relative importance in determining the evolution of the chemistry of the ISM.

(ii) Each range is then sampled considering p_i discrete values, and the evolution of the gas for the desired time-step (in the previous example it was $\Delta t = 10^4$ yr) is then performed. We need a simulation for each combination of the initial parameters (x_1^0, \dots, x_N^0) ; therefore, the total number of models is then $M_{\text{tot}} = \prod_i p_i$.

(iii) The database now contains M_{tot} evolved models with the evolved parameters $(x_1^{\Delta t}, \dots, x_N^{\Delta t})$. The evolution could now be described as a function $f : S \rightarrow S$ with $S \subset \mathbb{R}^N$ that is defined as $(x_1^{\Delta t}, \dots, x_N^{\Delta t})_j = f[(x_1^0, \dots, x_N^0)_j]$ where j is the index of the j -th model. This surjective function connects two points in the parameter space, and replaces the detailed evolution and its intermediate steps of integration, that is what we need for the purposes of the NB-TSPH code.

(iv) At this point we choose an interpolation method, that is the main drawback of the grid method: interpolating with accuracy a dataset in many dimensions is not trivial, since it is strongly data dependent. To find the correct fitting method one must know how the data are distributed. Choosing the best fitting method in many dimensions with an unknown complexity of the distribution of the data, could not be straightforward.

To cope with these problems we choose a different method. Since we cannot define the multidimensional fitting function *a priori*, there are some

methods based on the AI paradigm that could help us. These methods are the subject of the next section.

4.2.2 AI-based methods

As we have seen in the previous Section, the main problem with the multidimensional fit resides in the fact that, in general, we have no clue on the shape of the fitting function. We introduce the AI-based methods to cope with this issue. These methods are developed to solve the classification problems (such as the written characters recognition), but they can also be extended to the regression problems².

In this Section we only describe the so-called *supervised learning* problems. A supervised learning problem is the task of inferring a function from supervised training data, i.e. a set of training examples. In the supervised learning technique, each example is a pair consisting of an input object and a *desired* output value. A supervised learning algorithm analyzes the training data and produces an inferred function, i.e. a *regression function*. The inferred function should predict the correct output value for any valid input object; this requires the learning algorithm to generalize from the training data to unseen situations in a “reasonable” way.

These methods permit to obtain a regression function that is easy to handle. The main drawback of this approach is that finding the regression function is an *ill-posed problem*. A *well-posed problem* is defined as a problem with the following properties [63]:

- (i) A solution exists
- (ii) The solution is unique
- (iii) The solution depends continuously on the data, in some reasonable topology

If one of these properties is not verified the problem is then *ill-posed*.

An example of well-posed problem is the study the evolution of a physical system using the direct integration method (see the previous Section). In this example the condition (i) is verified, as long as the algorithm does not diverge; the condition (ii) is also verified, because the system converges to a determined physical state after a user-defined time-step; the condition (iii) is determined by the fact that the algorithm cannot generate any discontinuity.

²The regression is the technique used to model through a function a relationship between a set of scalar variables and one or more variables (e.g. the fitting methods).

Conversely, the AI-based problems are ill-posed. These methods essentially consist in finding the absolute minimum in the multidimensional error surface that represents the problem in the space of the parameters. The algorithms that belong to this class of problem find the absolute minimum following the downhill direction of the error surface. The main trouble of this technique stems from the fact that the error surface must be convex, or the algorithm may fall in a relative minimum. These last remarks will be discussed in more details in Section 4.3.

In the next lines we describe some possible methods based on the AI paradigm.

Support Vector Machines

Support vector machines (SVMs) are a set of related supervised learning methods that analyze data and recognize patterns, generally used for classification and regression analysis. The original SVM algorithm was invented by Vladimir Vapnik and the current standard realization (soft margin) was proposed in [29].

The standard SVM takes a set of input data, and predicts, for each given input, which of two possible classes the input is a member of, which makes the SVM a non-probabilistic binary linear classifier. Since an SVM is a classifier, then given a set of training examples, an SVM training algorithm builds a model that predicts whether a new example falls into one category or the other. Intuitively, an SVM model is a representation of the examples as points in space, mapped so that the examples of the separate categories are divided by a clear gap that is as wide as possible. New examples are then mapped into that same space and predicted to belong to a category based on which side of the gap they fall on.

More formally, a SVM constructs a hyperplane or set of hyperplanes in a high or infinite dimensional space, which can be used for classification, regression or other tasks. Intuitively, a good separation is achieved by the hyperplane that has the largest distance to the nearest training data points of any class.

Whereas the original problem may be stated in a finite dimensional space, it often happens that in that space the sets to be discriminated are not linearly separable. For this reason it was proposed that the original finite dimensional space be mapped into a much higher dimensional space, hopefully making the separation easier in that space. SVM schemes use a mapping into a larger space so that cross products may be computed easily in terms of the variables in the original space making the computational load reasonable. The cross products in the larger space are defined in terms of a kernel func-

tion $K(x, y)$ which can be selected to suit the problem. The hyperplanes in the large space are defined as the set of points whose cross product with a vector in that space is constant.

The vectors defining the hyperplanes can be chosen to be linear combinations with parameters α_i of images of feature vectors which occur in the data base. With this choice of a hyperplane the points x in the feature space which are mapped into the hyperplane are defined by the relation:

$$\sum_i \alpha_i K(x_i, x) = \text{constant} . \quad (4.2)$$

Note that if $K(x, y)$ becomes small as y grows further from x , each element in the sum measures the degree of closeness of the test point x to the corresponding data base point x_i . In this way the sum of kernels above can be used to measure the relative nearness of each test point to the data points originating in one or the other of the sets to be discriminated. Note the fact that the set of points x mapped into any hyperplane can be quite convoluted as a result allowing much more complex discrimination between sets which are far from convex in the original space.

An alternate version of SVM for regression was proposed by [64, 18]; this method is called support vector regression (SVR). The model produced by support vector classification depends only on a subset of the training data, because the cost function for building the model does not care about training points that lie beyond the margin. Analogously, the model produced by SVR depends only on a subset of the training data, because the cost function for building the model ignores any training data close to the model prediction.

We have implemented this method with different kernels to interpolate our database. The first tests have obtained poor results, showing large errors in the regression function. Hence, we have abandoned this method to use the Artificial Neural Networks, since their results are more promising. However, before describing the ANN we introduce another regression method, namely the *Radial Basis Function*.

Radial Basis Function

Radial basis functions (RBF) are a group of functions used for interpolation aims. Their value depends only on the distance (this the reason of the word *radial* in the name) between the generic point and the centre of the domain of the particular function. They allow to obtain an interpolation $s(x)$ with

the form

$$s(x) = \sum_{j=1}^N c_j \phi(\|x - x_j\|), \quad (4.3)$$

where $\phi(r)_j$ is the RBF, and c_j is the real coefficients used to fit the interpolation over N sampling points x_j . Commonly used RBF are, defining $r = \|x - x_j\|$,

$$\phi(r) = \begin{cases} \exp(-\beta r^2) & \text{Gaussian for } \beta > 0 \\ \sqrt{r^2 + \beta^2} & \text{multiquadratic for } \beta > 0 \\ r^k & \text{polyharmonic spline for } k \text{ odd} \\ r^k \ln(r) & \text{polyharmonic spline for } k \text{ even} \\ r^2 \ln(r) & \text{thin plate spline.} \end{cases} \quad (4.4)$$

Note that the thin plate spline is an polyharmonic spline for $k = 2$.

Several researchers have investigated the main features of the RBFs [88, 17, 2]. These functions are very interesting because of their optimization properties, since they allow to interpolate scattered samples in arbitrary dimensional spaces. Their algorithms are simple and computationally cheap. Depending on the specific RBF chosen, the properties are of course different.

Even if this method is promising we choose to use the Artificial Neural Networks, that are efficient and versatile (see Section 4.3). The RBFs will be taken into account for future developments. For further details see the bibliography of this subsection.

4.3 Our choice: Artificial Neural Networks

Since we would like to include the gas model (and results of ROBO) into numerical simulations of galaxies in a simple way we use Artificial Neural Networks (ANN). Let us suppose that a numerical code is calculating the formation and evolution of a model galaxy from an initial stage at high redshift using the standard NB-TSPH technique. At each time-step, it requires an update of the chemical status of the gas particles. This is done for every gas particle of the simulation (typically from 10^4 up to 10^7 particles, depending on the simulation under consideration). As already mentioned we have two methods to our disposal. The first one is a real-time chemical updater. This approach must use simple physics and a powerful computer in order to save computing time. The second one is the use of grids of models, calculated in advance for a wide range of the input parameters, in such a way

to cover the plausible space of the initial conditions. Since increasing the parameters also increases the space dimensions of the grids, thus rendering the data handling a cumbersome affair, we make use of the ANNs technique to get rid of this difficulty. Once the ANNs are instructed to reproduce the (ROBO) results as a function of the parameters, ANNs replaces ROBO in the NB-TSPH simulator of galaxies.

As already mentioned, the ideal way of proceeding would be to insert ROBO into a code simulating the temporal evolution of large scale structures and to calculate the thermodynamical properties of the ISM component. In all practical cases, this would be unreasonably time consuming. To cope with it without loosing accuracy in the physical description of the ISM we construct an ANN able to replace ROBO in all cases.

In brief, ANNs are non-linear tools for statistical data modeling, used to find complex relationships between input and output data or to discover patterns in complex datasets. The first idea of an ANN is by [65]. In the early sixties [110] built the first algorithm based on the iterative penalty and reward method, and finally, after two decades of silence, new ideas were brought by [20, 21, 22] (adaptive resonance theory), [71, 72] (associative neural network) and [112, 94], who developed the *back-propagation algorithm*, today a common and widely used training scheme.

Demanding computational problems (e.g. multidimensional fits or classifications) can be easily solved using ANNs whereas other methods would require large computing resources. An ANN is based on a simple conceptual architecture inspired by the biological nervous systems. It looks like a network composed by *neurons* and linked together by synapses (numerical weights). This structure is modeled with a simple algorithm, designed to predict an *output state* starting from an original *input state*. To achieve this, the ANN must be *trained*, so that it can “learn” to predict the output state from a given set of initial configurations. The simplest way of doing it, is the so-called *supervised learning*: input-output values are fed to the network, then the ANN tentatively computes an output set for each input set, and the difference between the predicted and the original output (i.e. the error) is used to calculate penalties and rewards to the synaptic weights. If the convergence to a solution exists, after a number of iterations, the predicted output value gets very close to the original one: *the ANN has learned*.

The network stores the original data in some dedicated neurons, the so called *input neurons*, elaborates these data and sends the results to another group of neurons that are called *output neurons*. Thus, data flow from input to output neurons. There is another group of neurons, named *hidden neurons*, that help the ANN to elaborate the final output (see Fig. 4.1). Each neuron (or unit) performs a simple task: it becomes *active* if its input signal is

higher than a defined threshold. If one of these units becomes active, it emits a signal to the other neurons; for this reason, each unit can be considered as a *filter* that increases or decreases the intensity of the received signal. The connections between neurons simulate the biological synapses and this is the reason why they are called *synaptic weights* or, more simply, *weights*.

The whole process can be written as follows:

$$n_i = f(x) \left(\sum_j w_{ij} n_j - \theta_i \right), \quad (4.5)$$

where n_i is the i -th neuron value, $f(x)$ is the activation function, w_{ij} is the weight between i -th and j -th neuron, θ_i is the neuron threshold, and x is the signal. For the activation function we adopt a *sigmoid*

$$f(x) = \frac{1}{1 + e^{-\beta x}}, \quad (4.6)$$

where β is a parameter fixing the sigmoid slope. It is worth recalling that other expressions for the activation function can be used.

In general the ability of the network to reproduce the data increases with the number of the hidden units up to a certain limit otherwise the ANN gets too “stiff” so that predicting the original output values gets more difficult. *The ANN stops learning!* Another reason to avoid many hidden neurons is that the procedure becomes time consuming (one must remember that we are mainly dealing with with matrix products). On the other side, an ANN with too few hidden units gets “dull” in reproducing the original data. Therefore, there is an optimal number of hidden neurons for each ANN.

There are several possible ANN architectures, depending on the task the network is designed to perform. The already cited back-propagation algorithm [112] is among the most versatile methods, it is one of the most suited to the supervised learning stage and can be applied to a wide range of problems. The name stems from the fact that the error produced by the network is propagated back to its connections to change the synapsis weights and consequently to reduce the error. As a detailed description of the ANN technique is beyond the aims of this Thesis, we limit ourselves to describe in some detail only the particular algorithm we have adopted for our purposes.

MaNN is the network we built to reproduce the ISM output models calculated by ROBO. We use a layer of input neurons where each input value corresponds to a free parameter of the ROBO models, i.e. the ones described in the Chapter 3. The definition of the model in MaNN requires some clarifications. While ROBO calculates the whole temporal evolution of a model, MaNN needs only the set of initial parameters (the input model) and the set

of final results (the output model). Therefore, a MaNN model is made of two strings (vectors) of quantities: the initial conditions for the key parameters (the input vector) and the results for the quantities describing the final state, after that the assigned time interval has elapsed (the output vector). We refer to the input vector as the vector \bar{x} whose dimension, i.e. the number of input units, is n_x . We then choose the shape of the output layer of neurons having in mind an “optimal” number of parameters to be used in a typical dynamical simulation. We use \bar{y} to indicate these units and the number of the neurons belonging to this layer is n_y ³. For example, if the code generating the input data only tracks the abundance of neutral hydrogen and the temperature, the MaNN input vector will be $\bar{x} = \{n_{\text{H}}^t, T^t\}$ and the relative output vector will be $\bar{y} = \{n_{\text{H}}^{t+\Delta t}, T^{t+\Delta t}\}$, and consequently $n_x = n_y = 2$. In this example the number of inputs is equal to the number of outputs, but this is not a strict requirement. In general, to avoid degeneracies one should have $n_x \geq n_y$ (considering independent database parameters). The input parameters can be also different from the output parameters, so in the previous example it could be $\bar{y} = \{n_{\text{H}}^{t+\Delta t}, n_{\text{H}_2}^{t+\Delta t}\}$.

There are two more layers in the MaNN, both are hidden and generally with the same size, which in turn depends on the complexity of the task (for example, retrieving a single output value can be obtained with two hidden layers of five elements, or even less). The first layer is \bar{h} with n_h neurons and \bar{g} is the second one with n_g units. Each layer is connected with a matrix of weights. A $n_x \times n_h$ matrix named W_{xh} is situated between the input units and the first hidden layer. Similarly, there is a $n_h \times n_g$ matrix named W_{hg} and, finally, W_{gy} , which is a $n_g \times n_y$ matrix. The architecture of MaNN that we have described here is sketched in Fig. 4.1.

4.3.1 The learning stage

We don't need no education.

Pink Floyd⁴

The whole learning process is divided into two different steps; the first one is the so called *training stage*, where MaNN is trained with a randomly chosen set of data. In the subsequent *test stage* new, blank (i.e. never used

³ In practice, to chose the input and output vectors and their dimensions we pay attention to the characteristics of the code to which the MaNN is applied, namely the Padova Tree-SPH code EvOL by [98]. The same reasoning can be applied to the code generating the input data, ROBO in our case. However, the whole procedure can be generalized to any other type of codes.

⁴The Wall, 1979, Harvest Records/EMI Records.

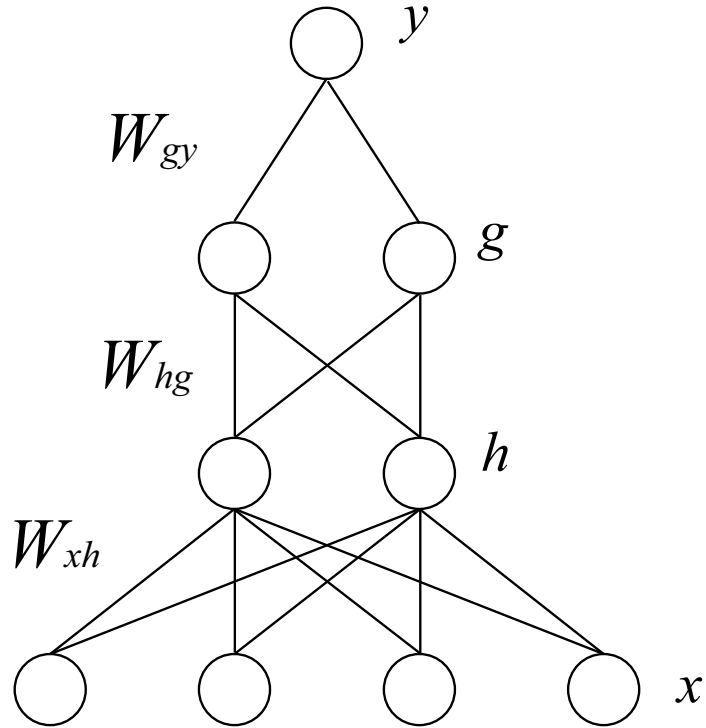


Figure 4.1: The architecture of MaNN. Circles indicate neurons, lines are connections (i.e. weights). Input units are labeled with the symbol \bar{x} , hidden neurons with \bar{h} if they belong to the first layer, and \bar{g} if they belong to the second one; finally, output units are indicated with \bar{y} . The matrix W_{xh} represents the weights between input and the first hidden units, W_{hg} are the connections between the first hidden units and the second hidden layer and W_{gy} connects the second layer of hidden units and the output. A single output is shown. In this Figure the forward propagation is from lower neurons to the upper ones. Back-propagation is from \bar{y} to \bar{x} neurons. Here $n_x = 4$, $n_h = n_g = 2$ and $n_y = 1$.

before) data are presented to MaNN to verify its behavior and the quality of the training. If MaNN retrieves the new data with a small (user defined) error, than the training stage is terminated. In case the error is still large, a new training stage is required. The training stage can also be stopped if the absolute error starts to increase again after an initial decrease (*early-stopping*). The aim is to avoid the so called *over-training*: a network is over-trained when it adapts too strictly to the data fed during the supervised learning, so that it cannot generalize the prediction to reproduce new cases of the test set of data, which contains data patterns that were not present in the previous stage.

At the beginning of the training process, each weight is initialized to a small, randomly chosen, value in the range $[-0.1, 0.1]$. The weights change under the action of MaNN. The rate at which MaNN changes its weights, otherwise known as the learning rate η , must be chosen carefully: for too high a value MaNN could oscillate without reaching a stable configuration, whereas for too small a value MaNN could take a long time to reach the desired solution or, even worse, be trapped in a false minimum of the error hyper-surface. We usually choose $0.1 \leq \eta \leq 0.9$.

The matrix of initial parameters contains N rows (the initial configurations of the input models); we randomly pick from this set $N_L < N$ rows for the training stage, which we refer to as L , and $N_T = N - N_L$ rows for the test stage, T .

A set \bar{s} of initial parameters randomly picked up from N_L is fed to the network as input vector $\bar{x} = \bar{s}$. The activation of each node belonging to the first hidden layer is then computed as

$$\bar{h} = f(\bar{x} \otimes W_{xh}) , \quad (4.7)$$

where \bar{h} is the vector of hidden neurons, f is the sigmoid function, W_{xh} is the weight matrix between the input and the first hidden neurons, and \otimes indicates the matrix product. If $\bar{c} = \bar{a} \otimes B$, where \bar{a} is a vector of n elements and B is a matrix $n \times m$, the size of the vector \bar{c} is m . The sigmoid function $f(\bar{v})$ has $\beta = 1$. Then the following relation holds

$$\bar{g} = f(\bar{h} \otimes W_{hg}) , \quad (4.8)$$

with obvious meaning of the symbols. Finally, the output vector of MaNN is given by

$$\bar{y} = f(\bar{g} \otimes W_{gy}) . \quad (4.9)$$

This first step is named the *forward-propagation*, because the algorithm calculates the output of the network for a given input vector $\bar{x} = \bar{s}$.

During the very first forward-propagation the output vector will contain nearly random values, because the weights are randomly generated. To improve upon it, we compute the error and back-propagate it to change the weights accordingly. The error at the output layer is

$$\bar{\delta}_y = (\bar{t} - \bar{y}) \dot{f}(\bar{A}_y) = (\bar{t} - \bar{y}) \bar{y}(1 - \bar{y}), \quad (4.10)$$

where \bar{A}_y is the vector of the activation functions for the output layer and the last equality is valid only with the activation function $f(\bar{v})$ with $\beta = 1$ that we have adopted. The error $\bar{\delta}_y$ is propagated back to the second hidden layer to become

$$\bar{\delta}_g = \dot{f}(\bar{A}_g) [\bar{\delta}_y \otimes W_{gy}] = \bar{g}(1 - \bar{g}) [\bar{\delta}_y \otimes W_{gy}], \quad (4.11)$$

with obvious meaning of all the symbols and expressions. Finally the error is propagated back for the last time giving

$$\bar{\delta}_h = \dot{f}(\bar{A}_h) [\bar{\delta}_g \otimes W_{hg}] = \bar{h}(1 - \bar{h}) [\bar{\delta}_g \otimes W_{hg}]. \quad (4.12)$$

Now that the error for each step between the various layers has been computed, the changes of the synaptic weights are

$$\begin{aligned} \Delta W_{xh} &= \eta [\bar{x} \otimes \bar{\delta}_h] + \alpha \Delta W_{xh}^o, \\ \Delta W_{hg} &= \eta [\bar{h} \otimes \bar{\delta}_g] + \alpha \Delta W_{hg}^o, \\ \Delta W_{gy} &= \eta [\bar{g} \otimes \bar{\delta}_y] + \alpha \Delta W_{gy}^o, \end{aligned} \quad (4.13)$$

The last terms at the RHS of the above Equations is called the *momentum* made by the product of a parameter α (to be tuned) and the variation of the corresponding weights at the previous step. ΔW_{xh}^o and the other similar terms indicate the values of the weights at the previous training step. The *momentum* is introduced to force the procedure to avoid false minima in the error hyper-surface. This loop must be repeated for each combination of the parameters in the set L .

To test the efficiency of the MaNN learning, the forward propagation is then applied to all the variables belonging to the set L . The RMS of the test data set is

$$\text{RMS} = \sqrt{\frac{\sum_{i=1}^{N_T} (y_i - t_i)^2}{N_T - 1}}, \quad (4.14)$$

where y_i is the output for the i -th test, t_i is the i -th correct test pattern and consequentially $y_i - t_i$ is the MaNN's error.

The training test loop will be repeated until the MaNN's learning reaches one of the following cases: (i) the RMS is lower than a certain limit chosen by the user, (ii) the RMS does not change for a sufficient number of loop cycles or, finally, (iii) the early-stopping condition is verified.

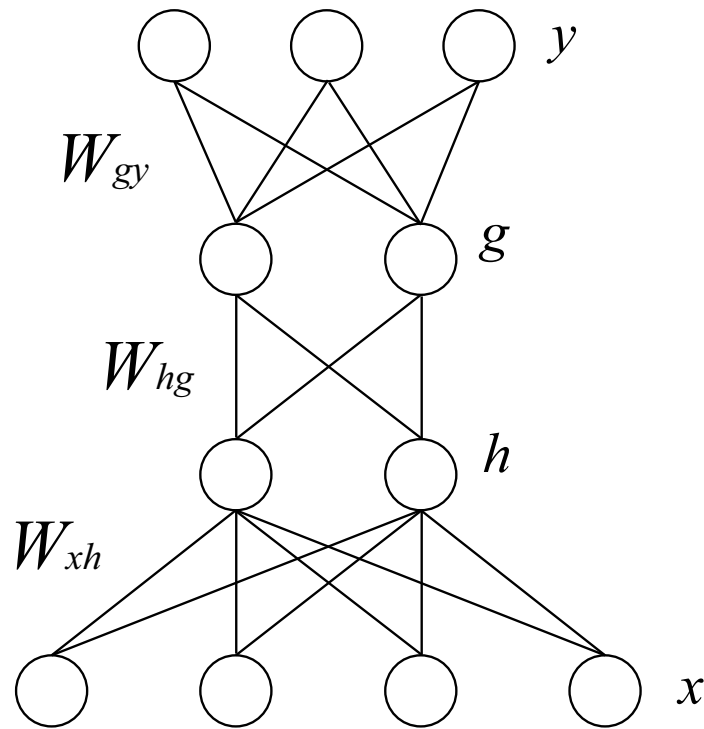


Figure 4.2: The architecture of a double hidden layer ANN. Circles indicate neurons, while lines represent the connections between the layers (i.e. weights). The input units are labeled with the symbol \bar{x} , the hidden neurons with \bar{h} if they belong to the first layer, and with \bar{g} if they belong to the second one; finally, the output units are indicated with \bar{y} . The matrix W_{xh} represents the weights between the output and the first hidden units, W_{hg} are the connections between the first hidden units and the second one and W_{gy} connects the second layer of hidden units and the output. Multiple outputs are shown. In this Figure the forward propagation is from the lower neurons to the upper ones. The back-propagation is from \bar{y} to \bar{x} neurons. Here $n_x = 4$, $n_h = n_g = 2$ and $n_y = 3$.

4.4 Training and testing MaNN

4.4.1 Input data from ROBO

As already stated, with ROBO we have calculated approximately 55000 models. For a given set of initial conditions and physical parameters, each model describes the state of an ISM element after $\Delta t = 10^4$ years of evolution. This time interval is short enough to secure that only small changes in gas abundances have occurred (a sort of picture of the physical state at given time), and long enough to be compatible with the typical time step in large-scale dynamical simulations.

For the purposes of the present analysis, we limit ourselves to track the following parameters: temperature T , metallicity $\tilde{Z} = 10^{[\text{Fe}/\text{H}]}$ of the gas⁵, and number densities of H, H₂, H⁺ and e⁻. This means that in addition to the temperature, MaNN is designed here to follow just these four species, whereas ROBO can actually follow twenty-three species including atoms, molecules and free electrons. The main motivation for this limitation is that in a large numerical dynamical simulation it is more convenient in terms of computing time and workload to follow in detail only those species (and their abundances) that are known to play a key role in the real evolution of the ISM (with particular attention to star formation and energy feedback) and to consider all the other species to remain nearly constant and small. In brief, the heavy elements are important coolants and the same holds for the molecular hydrogen, at least below $\sim 10^4$ K. The ionization fraction of hydrogen is also important, because free electrons are involved in a number of chemical reactions, and are the colliders that excite the coolants: this is the reason why n_{H^+} and n_{e^-} are considered. Moreover, the neutral n_{H} is in the list to ensure the mass conservation while changing the fractional abundances. Finally, the temperature determines the kind of physical processes that are important.

The initial values of the number densities. The initial values of the number densities fall in three groups: (i) the elemental species with constant initial values, the same for all the models (namely H⁻, H₂⁺, He⁺ and He⁺⁺); (ii) the elemental species whose initial values are derived from other parameters (namely He, all the deuteroids and the metals, like for instance C and O, that depend on the choice of the total metallicity \tilde{Z}) and, finally, (iii) the

⁵We call the attention of the reader on the definition of metallicity that we have adopted. It is related only to the iron content in the standard spectroscopic notation and not to the classical sum of the by mass abundances of all the species heavier than He, shortly indicated with Z and satisfying the relation $X + Y + Z = 1$, where X and Y are the by mass abundances of hydrogen and helium respectively.

elemental species with free initial conditions (namely H, H₂, H⁺, and e⁻).

HYDROGEN GROUP: H, H⁺, H⁻, H₂ and H₂⁺. The initial values of the species H⁻ and H₂⁺ are $n_{\text{H}^-} = n_{\text{H}_2^+} = 10^{-10} \text{cm}^{-3}$ [109], while the other three hydrogen species have free initial values.

DEUTERIUM GROUP: D, D⁺, D⁻, D₂, HD and HD⁺. The numerical densities of the deuteroids are calculated from their hydrogenoid counterparts. For the single atom species we have $n_{\text{D}} = f_{\text{D}} n_{\text{H}}$, $n_{\text{D}^+} = f_{\text{D}} n_{\text{H}^+}$ and $n_{\text{D}^-} = f_{\text{D}} n_{\text{H}^-}$, where $f_{\text{D}} = n_{\text{D}}/n_{\text{H}}$. For the molecules, we can consider the ratio f_{D} as the probability of finding an atom of deuterium in a population of hydrogen-deuterium atoms. This assumption allows us to calculate the HD, D₂ and HD⁺ number densities as a joint probability; for HD and HD⁺ we have $n_{\text{HD}} = f_{\text{D}} n_{\text{H}_2}$ and $n_{\text{HD}^+} = f_{\text{D}} n_{\text{H}_2^+}$, but for D₂ is $n_{\text{D}_2} = f_{\text{D}}^2 n_{\text{H}_2}$ as the probability of finding two deuterium atoms is f_{D}^2 . This is valid as long as $f_{\text{D}} \ll 1$.

HELIUM GROUP: He, He⁺, He⁺⁺. The ratio $n_{\text{He}}/n_{\text{H}}$ is set to 0.08, thus allowing to the initial value of n_{He} to vary accordingly to the initial value for n_{H} . The initial number densities of the species He⁺, He⁺⁺ are both set equal zero and kept constant in all the models.

METALS GROUP: C, C⁺, O, O⁺, Si, Si⁺ and Fe, Fe⁺. The Fe number density of the ISM is

$$n_{\text{Fe}} = n_{\text{H}} \cdot \text{dex} \left\{ [\text{Fe}/\text{H}] + \log \left(\frac{n_{\text{Fe}}}{n_{\text{H}}} \right)_{\odot} \right\}, \quad (4.15)$$

where $(n_{\text{Fe}}/n_{\text{H}})_{\odot}$ is the iron-hydrogen ratio for the Sun. To retrieve the number density of a given metal X we use $n_{\text{X}} = n_{\text{Fe}} \cdot f_{\text{X}}$, where f_{X} is the metal-iron number density ratio in the Sun.

The list of the species whose initial number densities are kept constant in all the models of the ISM is given in Table 4.2. The chemical composition of the ISM is typically primordial with the by mass abundances of hydrogen $X = 0.76$, and helium $Y = 0.24$ and all metals $Z \simeq 0$. The helium to hydrogen number density ratio corresponding to this primordial by mass abundances is $n_{\text{He}}/n_{\text{H}} \simeq 0.08$. The adopted cosmological ratio for the deuterium is $f_{\text{D}} = n_{\text{D}}/n_{\text{H}} \simeq 10^{-5}$. With the aid of these numbers and the above prescriptions we get the number density ratios listed in Table 4.4.2 and the initial values of the number density in turn.

Domains of the physical variables. In the present version of MaNN the variables in question span the following ranges: $\tilde{Z} = [10^{-12}, 10]$ for the metallicity, $n_{\text{H}} = n_{\text{H}^+} = n_{\text{e}^-} = n_{\text{H}_2} = [10^{-12}, 10^3] \text{cm}^{-3}$ for the numerical densities, and $T = [10, 10^7] \text{K}$ for the temperature.

Role of the dust. In this study, we neglect the presence of dust: in other words, the *dust density* is kept constantly equal to zero. This is because the current version of the NB-TSPH code EvOL does not include the treatment

of the dust component of the ISM. We plan to include silicates and carbonaceous dust grains both in EVOL and MaNN.

Other parameters. In addition to this, we do not consider the contribution by the *Cosmic Rays field*, the *background heating*, and the *UV ionizing field*. All of these processes, however, can be described by ROBO (see [62] for more details).

The CMB temperature is set to 2.725 K, the observed present value [49] and is kept constant in all the models. In the case of a cosmological use of MaNN one should include a redshift-dependent variation of the CMB temperature for a correct description of the CMB effects.

The parameters we have chosen form a \mathbb{R}^6 space: the input space of the MaNN. The large number of input models secures that the space of physical parameters is smoothly mapped.

Finally, in addition to the six-dimensional input vector, another input unit is dedicated to the so called *bias* which is always set to $x_0 = -1$; it gives the threshold θ in the Eqn. (4.5).

4.4.2 Compression of data?

To reduce the complexity of the problem, one can try to compress the input data, i.e. to reduce the number of variables and to obtain a new initial set easy-to-handle. A popular technique to reduce the number of dimensions of a data sample is the *principal component analysis* (PCA). The PCA is a transformation between the original data space and a new space (named PCA space). The aim of this method is to build this \mathbb{R}^n -dimensional subspace (with n less than the number of dimensions of the original space) so that its new PCA-variables are uncorrelated. In this way, only the most statistically significant parameters (i.e., the new variables that have the highest percentage of the total variance) are taken into consideration, instead of using the original parameters. PCA is useful when the data set is reduced to two or three modes. This is because two matrix products are needed, one to transform the input from the physical parameters space to the PCA space, and one to transform the output from the PCA space to the physical parameters space. These two operations have a non-negligible computational cost. In general, compressing the data with the PCA may improve the learning process of MaNN and its ability in reproducing the original data.

Analyzing the issue, we soon found that in our case the PCA method is not useful, and using the original data yields better results. Table 4.1 contains the results of the PCA analysis. It is easy to understand why reducing the number of parameters does not improve the situation: five modes cover approximately 87% of the total variance, and with the sixth mode the coverage reaches 94%.

Table 4.1: Results of the PCA analysis on the output data.

mode	Eigenvalue	Variance (%)
1	0.14585	36.9657
2	0.07454	18.8922
3	0.07006	17.7580
4	0.05606	14.2073
5	0.02871	7.2760
6	0.01934	4.9008

Table 4.2: Initial values for the number densities of the hydrogen and helium elemental species and the deuteroids. They are either fixed to a constant value or based upon the numerical abundance of one of the *free* hydrogen species n_{H} , n_{H_2} and n_{H^+} via the f_{D} factor. Since H^- and H_2^+ are constant, then also D^- and HD^+ are fixed. Values are indicated as $a(b) = a \times 10^b$. See also the text for details.

H^-	$1.0(-12)$	D	$f_{\text{D}}n_{\text{H}}$
H_2^+	$1.0(-12)$	D^+	$f_{\text{D}}n_{\text{H}^+}$
He	$0.8(-1) n_{\text{H}}$	D^-	$f_{\text{D}}n_{\text{H}^-}$
He^+	$0.0(+0)$	HD	$f_{\text{D}}n_{\text{H}_2}$
He^{++}	$0.0(+0)$	HD^+	$f_{\text{D}}n_{\text{H}_2^+}$
		D_2	$f_{\text{D}}^2n_{\text{H}_2}$

This means that the reduction of the number of parameters to obtain a \mathbb{R}^2 or \mathbb{R}^3 space is not possible. Note that only the PCA on the output data is shown, since the input data are random and they generate six modes with the same variance.

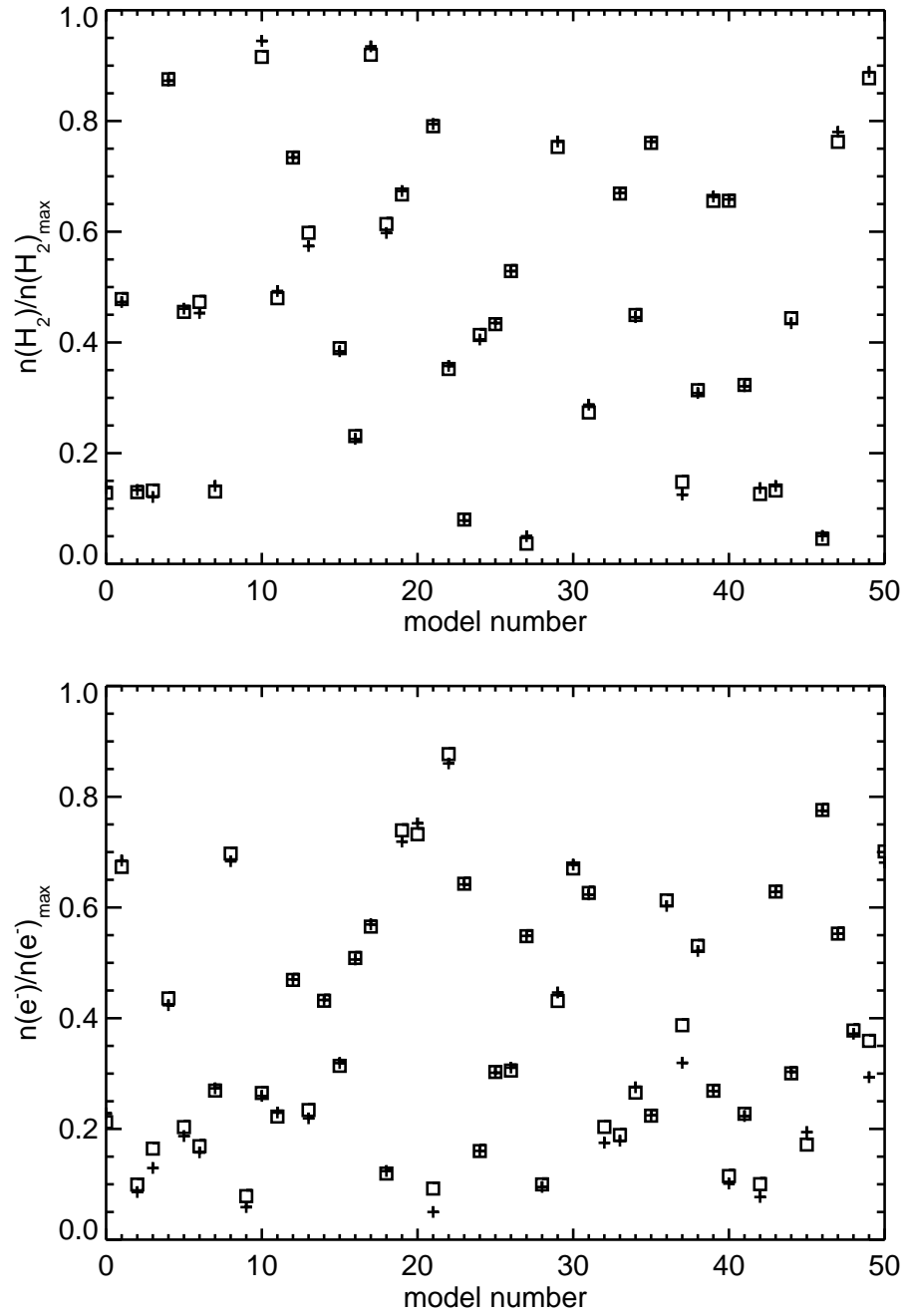


Figure 4.3: Comparison between normalized data from MaNN (cross) and ROBO (square), for molecular hydrogen density (left panel) and free electrons (right panel). We show only 50 randomly picked models. Similar results for the other outputs.

Chapter 5

Artificial Neural Networks in hydrodynamical numerical simulations

5.1 The NB-TSPH code: EvoL

The importance of numerical simulations in modern science is constantly growing, because of the complexity, the multi-scaling properties, and the non-linearity of many physical phenomena. When analytical predictions are not possible, we are forced to compute the evolution of physical systems numerically. Typical examples in astrophysical context are the problems of structure and galaxy formation and evolution. Over the past two decades, thanks to highly sophisticated cosmological and galaxy-sized numerical simulations a number of issues concerning the formation of cosmic systems and their evolution along the history of the Universe have been clarified. However, an equivalent number of new questions have been raised, so that complete understanding of how galaxies and clusters formed and evolved along the Hubble time is still out of our reach. This is especially true at the light of many recent observations that often appear at odds with well established theories (see for instance the long debated question of the monolithic versus hierarchical mechanism of galaxy formation and their many variants) and to require new theoretical scenarios able to match the observational data.

To this aim, more and more accurate and detailed numerical simulations are still needed. They indeed are the best tool to our disposal to investigate such complex phenomena as the formation and evolution of galaxies within a consistent cosmological context. A number of astrophysical codes for galaxy-sized and cosmological simulations are freely and publicly available. They

display a huge range of options and functions; each of them is best suited for a set of particular problems and experiments, and may suffer one or more drawbacks. Among the best known, we recall FLASH [51], GADGET [120] and its second release GADGET2 [119], GASOLINE [130], HYDRA [30], ENZO [105], and VINE [136].

We use the aforementioned code EVOL that is fully Lagrangian, parallel, and self-adaptive N-body code, written in Fortran95.

EVOL describes the dynamical evolution of a system of interacting discrete masses (particles) moving under the mutual gravitational forces and/or the gravitational action of external bodies, plus, when appropriate, under mutual hydrodynamical interactions. Such particles can represent real discrete bodies or a fluid contained in volume elements of suitable size. A numerical simulation of a physical system follows the temporal evolution of it using small but finite *time-steps* to approximate the equations of motion to a finite-differences problem. In the Lagrangian description, no reference grid is superposed to the volume under consideration, while the particles move under their mutual (or external) interactions. Each particles carries a mass, a position, a velocity, plus (when necessary) a list of physical features such as density, temperature, chemical composition, etc.

To simulate the dynamical evolution of a region of the Universe, one has to properly model the main different material components, namely Dark Matter, Gas, and Stars), representing them with different species of particles. Moreover, a physically robust model for the fundamental interactions (in addition to gravity) is required, at the various scales of interest. Finally, a suitable cosmological framework is necessary, together with a coherent setting of the boundary conditions and with an efficient algorithm to follow the temporal evolution of the system. EVOL is designed to respond to all of these requirements, improving upon the previous versions of the Padova Tree-SPH code under many aspects. The core of the old PD-TSPH code was written during the '90s by C. Chiosi, G. Carraro, C. Lia and C. Dalla Vecchia [23, 86]. Over the years, many researchers added their contribution to the development of the code. In its original release, the PD-TSPH was a basic Tree + SPH code, written in Fortran90, conceptually similar to TREE-SPH by [66]. Schematically, PD-TSPH used an early formulation of SPH [8] to solve the equations of motion for the gas component, and the [6] Tree algorithm to compute the gravitational interactions.

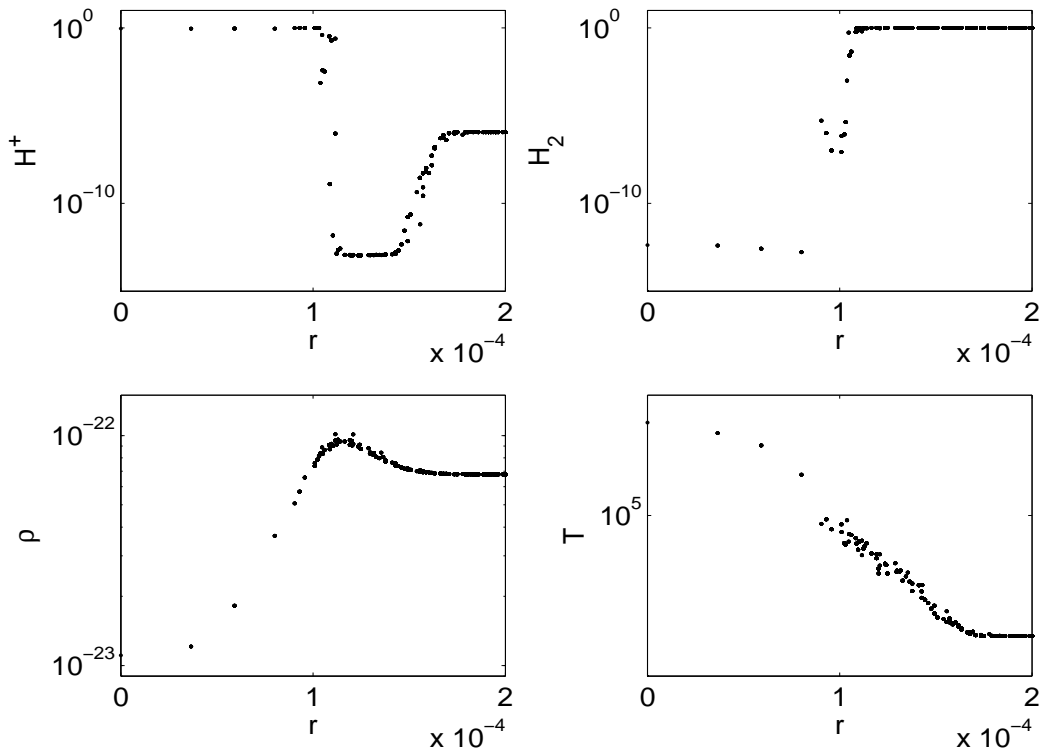


Figure 5.1: Sedov-Taylor OB-wind test with chemical evolution. Left to right, top to bottom: radial profiles of H^+ and H_2 mass fractions, ρ , and T , at $t = 0.5$ Myr. Plotted are all particles within the central 200 pc.

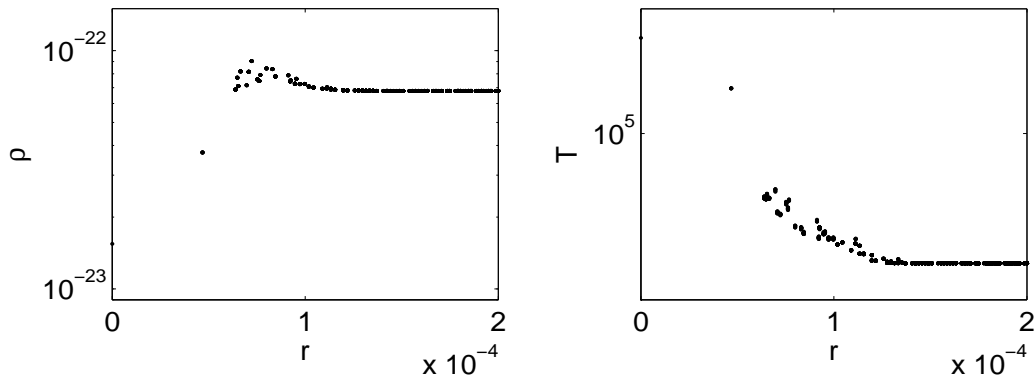


Figure 5.2: Sedov-taylor OB-wind test without chemical evolution. Left to right: radial profiles of ρ and T , at $t = 0.5$ Myr. Plotted are all particles within the central 200 pc.

5.2 ANN and EvOL

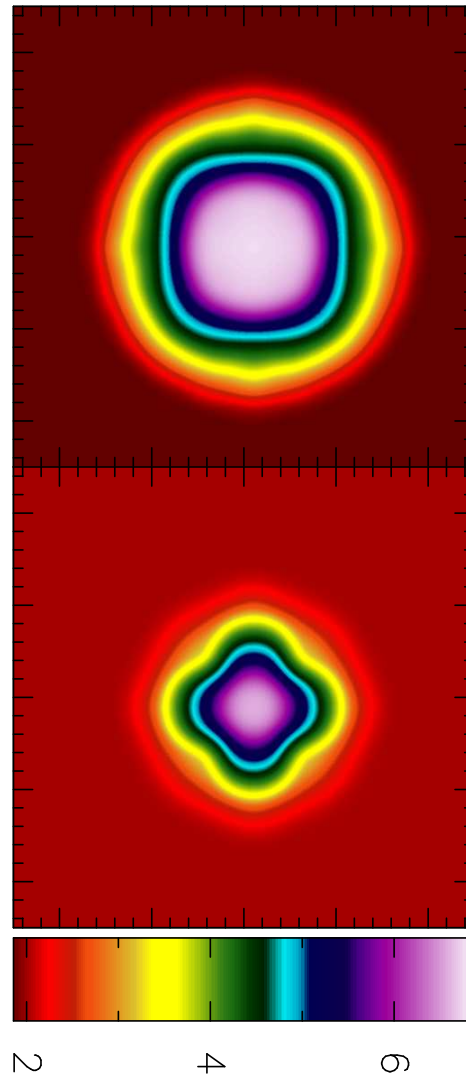
To evaluate the performance of MaNN in real large -scale numerical simulations we implemented it in the NB-TSPH code EvOL, and run a “realistic” version of the ideal Sedov-Taylor problem, which is known to be a rather demanding test.

MaNN tracks the evolution of the relative abundances of H, H⁺, H₂ and e⁻ within each gas particle of the SPH simulation. The MaNN routine is called by each active gas particle during the computation of its radiative cooling (which is in turn obtained from look-up tables, see [99] for details). Since the time interval $\Delta t = 10^4$ yr in between the initial and the final stage of any model in MaNN is usually smaller than the typical dynamical time step of a gas particle, the routine is called several times until the dynamical time step is covered. If the dynamical time step is not an integer multiple of the MaNN time interval, an interpolation is applied to the results of the last two calls of MaNN. During the whole procedure, all the physical parameters but the afore mentioned relative chemical abundances and the temperature (namely, total density, metallicity and mechanical heating rate) are kept constant.

Due to the detailed description of the chemical properties of each particle, the adiabatic index γ in the equation of state governing the gas pressure $P = (\gamma - 1)\rho u$ varies as a function of the relative abundances (see [62]). This will immediately reflect on the relationship between the internal energy and the temperature, and on the equation of the motion itself. Therefore, we expect an important change in the dynamical evolution of the whole system as compared to the case in which these chemical effects are ignored.

The test run is set up as follows. A uniform grid of 45^3 equal mass gas particles is displaced inside a periodic box of size $l = 1$ kpc. The mass of each mass element is $\simeq 10^4 M_{\odot}$, so the initial uniform density is $\rho \simeq 6.78 \times 10^{-23}$ g/cm³. The initial temperature is 200 K. The initial chemical mass fractions of each gaseous element are $[H^+] = 10^{-20}$, $[H_2] = 0.99$, $H = 1 - ([H_2] + [H^+])$. These initial conditions resemble a dense interstellar cloud of cold molecular material.

At time $t = 0$, the temperature of the central particle is instantaneously raised up to $T = 2 \times 10^7$ K, a temperature similar to that of the gas shocked by the winds ejected by O-B young stars. We name this physical case as the *Sedov-Taylor OB-wind*. At the same time, the chemical composition of the particle is changed to $[H_2] = 10^{-20}$, $[H^+] = 0.99$, $H = 1 - ([H_2] + [H^+])$. The temperature of the central particle is maintained constant, to mimic the continuous energy injection by the central star, and the system is let evolve freely under the action of hydrodynamic interactions and chemical reactions. We also include thermal conduction and radiative cooling that are usually



log Pressure (code units)

Figure 5.3: Sedov-taylor OB-wind test. Pressure field in a central slice of side $l = 500$ pc, with (left) and without (right) chemical evolution.

neglected in standard Sedov-Taylor explosion tests (see [98] for more details).

A region of hot material expands in the surroundings of the central particle. This is due to a spurious numerical conduction which, however, causes a numerical smoothing of the initial condition and favors the correct developing of the subsequent evolutionary stages. Then, a shock wave forms and moves outwards radially. Note that the continuous energy release from the central particle and the effect of radiative cooling, almost prevent the inward motion of shocked particles like in standard tests of the Sedov-Taylor explosion.

In Fig. 5.1 we show the state of the system after $\simeq 0.5$ Myr of evolution. The bottom panels display the density and temperature profiles, and the top panels the abundances of H^+ and H_2 . In the central hot and less dense region, the molecular hydrogen gets completely ionized (the abundance of H_2 falls to very low values), due to the high temperatures and low densities. The less dense cavity is surrounded by a layer of over-dense material (the shock layer) which in turn is surrounded by another layer with the initial density. The over-dense front is moving outwards. In the pre-shock region, near the shock layer, the density increase causes the H^+ to recombine into neutral hydrogen. These results fairly agree with the theoretical predictions.

To strengthen the above conclusion, we performed another simulation of the Sedov-Taylor OB-wind, in which the effects of the chemical composition and its changes on the gas particles are ignored (by the way this is exactly what is assumed in most if not all the cosmological simulations). In practice, all the gas particles are assumed to be composed of solely neutral H, so that the adiabatic index γ is fixed and equal to $5/3$. The results are shown in Fig. 5.2, in which the density and temperature profiles are displayed at the same age of the previous case presented in Fig. 5.1. Clearly, the dynamical evolution of the system is substantially different. The over-dense front moves at significantly lower speed. In particular, it is clear how the variable chemical composition ensures a higher pressure in the central region containing ionized particles, with respect to the outer region containing molecules. This causes the faster expansion of the central bubble with respect to present case. This is also supported by the pressure fields in the two cases shown in Fig. 5.3. The left panel shows the pressure field of the first case with evolving chemical composition of the gas particles, whereas the right panel shows the same but for constant chemical composition. The color code shows the value of the pressure in code units. Both pressure fields are measured at the same age of 0.5 Myr and on the surface of an arbitrary plane passing through the center of the computational box. There are a number of interesting features to note: (i) The pressure in the outskirts is lower in the case with chemical evolution, where the adiabatic index is $\gamma = 7/5$ for the bi-atomic molecule H_2 . At the same time, the pressure in the central region of the case with chemical evolu-

tion is higher by nearly a factor of two because the number of free particles (or equivalently the internal energy corresponding to a given temperature) is nearly doubled. (ii) The continuous energy release from the central particle, plus the action of the radiative cooling, almost prevent the inward motion of shocked particles (conversely to what happens in the standard Sedov-Taylor explosion test). Instead, they are compressed in a thin layer, which moves outwards under the action of the central source of pressure. For this reason, we are interested in the state of the system shortly after the beginning of the energy release, before the shock layer is pushed too far away from the central region. However, at that moment only a relatively small number of particles have already felt a strong hydrodynamical interaction. This explains the geometrical features that can be seen in Fig. 5.3. They are due to the initial regular displacement of the particles, whose effects are still to be smeared out by hydrodynamics interactions. Because the detailed chemical treatment implies a larger pressure gradient and, consequently, a faster expansion of the central bubble, after a given Δt the simulation without the inclusion of MaNN shows a stronger geometrical spurious asymmetry with respect to the “standard” case: this is simply because it is at a more primordial stage of its evolution.

5.3 ROFO or: how I learned to stop worrying and optimize ROBO

Measuring programming progress by lines of code is like measuring aircraft building progress by weight.

Bill Gates

As clearly depicted in the previous Sections, ROBO - an IDL code including a large number of physical processes and free parameters - is intended to be used with EvOL, the NB-TSPH developed to study the evolution of the large structures of the Universe. It is important to remark that ROBO creates a database of models, and this database is then used to train an Artificial Neural Network.

Presently, ROBO describes the ISM processes in much more detail than what can be done using a NB-TSPH code like EvOL. Generating thousands of physical models requires large computational resources. In our case one model requires a few seconds of computing time, and in particular, with a standard CPU ROBO takes less than one second to calculate simple models,

i.e. low density, low metallicity models, etc.; when the models become more complex, the CPU time per model can easily exceed 1 minute. This time can be reduced optimizing the code for particular purposes. This means developing a code similar to ROBO, but only including the physical features useful to EvOL.

For example, ROBO contains the UV field that influences the chemical network (the photo-ionization reactions) and the heating (the ejection of electrons from the dust grains). However EvOL still does not include the photon diffusion, so the UV analysis can be neglected in ROBO for the present purposes. Instead of switching off the parameters in ROBO, a better optimization can be obtained using a pre-processor, or directly writing a dedicated code.

Building an *ad hoc* code permits also to use a suitable programming language that enhances the performances. Since in the optimized version of ROBO the chemical network will be the core of the code, we have chosen Fortran and the DVODE library to solve the ordinary differential equations system. This library offers a great performances when embedded in the Fortran language.

Given these considerations, we have developed a code that is highly optimized for the present characteristics of EvOL. This code is named ROFO¹.

ROFO presents the following characteristics that, as already mentioned, are based on the features of the code EvOL. The chemical network is based on H, H⁺, H⁻, H₂, H₂⁺, He, He⁺, C, C⁺, O, O⁺, Si, Si⁺, Fe, Fe⁺ and e⁻; unlike ROBO, no deuterium-based species are included in ROFO, since these species are not included in the NB-TSPH code. CO is also ruled out for this test, as well as UV sources (this implies that the volume of the ISM considered does not receive any photons from the outside).

The cooling model is similar to the one used in ROBO. We included cooling from metals, H₂, and the cooling indicated as CEN92. However, we did not include CO and HD cooling, since these molecules are not considered, and SD93 cooling, that is not useful because we consider a temperature range of $10 < T < 10^4$ K.

Finally, no dust modelization has been included, since EvOL only considers a dust-free Universe.

The number of free parameters needs to be low, since the exploration of a parameters space with many free variables requires to generate a large number of models. To cope with this we only considered the temperature, the

¹We have simply changed a single letter in the name ROBO, choosing the letter F since the code is written in Fortran.

metallicity, the initial number density of H, H⁺ and H₂. These parameters are called *free*, while all the others initial parameters are *calculated* or *fixed*. Free parameters are given by the user. The *calculated* parameters derive from the free parameters using some physical assumptions (see below). The *fixed* ones are simply parameters that have the same constant value in all the models. In the next lines, the assumptions on the parameters will be discussed in more detail.

As already mentioned n_{H} , n_{H_2} and n_{H^+} are free parameters, each limited to the range $[10^{-12}, 10^3] \text{ cm}^{-3}$. At the moment we don't deal with very high densities, this fact is determined by the value of the higher density limit in the NB-TSPHcode EvOL. The lower bound is considered as the lower density bound for our simulations, and under this limit the species are considered negligible. This is also the reason why H⁻ has a fixed value of $n_{\text{H}^-} = 10^{-12} \text{ cm}^{-3}$. We then obtain a ionization parameter x_{ion} defined as

$$x_{\text{ion}} = \frac{n_{\text{H}}}{n_{\text{H}} + n_{\text{H}^+} + n_{\text{H}_2}}, \quad (5.1)$$

which is the ionization state of the ISM model. From x_{ion} we can retrieve the calculated parameter $n_{\text{H}_2^+} = n_{\text{H}_2} x_{\text{ion}}$, assuming that the ionization state is a property of the gas valid for all the ions present in the ISM model².

Helium is calculated considering the total density of H, and assuming a constant ratio $n_{\text{He}}/n_{\text{H}} = 0.08$, noticing that a fraction x_{ion} of this helium is ionized giving n_{He^+} .

Metals are retrieved using the definition of metallicity; they are therefore a function of the free parameter metallicity. Metallicity is given by

$$Z = [\text{Fe}/\text{H}] = \log \left(\frac{n_{\text{X}}}{n_{\text{H}}} \right) - \log \left(\frac{n_{\text{X}}}{n_{\text{H}}} \right)_{\odot}, \quad (5.2)$$

where X is a generic metal and n_{H} indicates all the hydrogen present in the gas. It gives

$$n_{\text{X}} = n_{\text{H}} \cdot \text{dex} \left[Z + \log \left(\frac{n_{\text{X}}}{n_{\text{H}}} \right)_{\odot} \right], \quad (5.3)$$

considering that a fraction x_{ion} of the metal found is ionized giving n_{X^+} . Finally, free electrons are $n_{\text{e}^-} = \sum_{\text{ions}} n_{\text{ions}}$.

The last free parameter is the temperature, which plays a key role in determining the evolution of the whole system, since it influences the rate coefficients in the chemical network as the cooling rates of the gas.

²This assumption will be improved in the future, since it is inaccurate, especially for what concerns the metal ions.

5.3.1 ROFO: an application to EvoL

We used a database of models produced with ROFO to a Sedov blast-wave test similar to the one proposed for ROBO (see Sect. 5.2). We refer to the previous test as RBST (ROBO Sedov Test), and to the second test as RFST (ROFO Sedov Test).

These tests are very similar to one another, yet there are some differences in the database and in the ANN training: (i) with ROBO we created the models with random initial values for the free parameters. For ROFO we preferred to produce a grid of models, with logarithmic spacing. (ii) In the RBST we used a double hidden layer ANN, while in RFST we use a single hidden layer ANN. (iii) In the RBST we decided to apply the MaNN architecture, while for RFST we choose the SaNN architecture. (iv) In RFST we also introduce a *validation stage* that is similar to the *test stage* used in RBST, but using some random models calculated outside the grid intersections³ to test the generalization of the ANN in a proper way. (v) Moreover, we use less free parameters than the previous case since the free electrons in RFST are a calculated parameters (see the beginning of this Section).

The results of the RFST are shown in Figs. 5.4, 5.5 and 5.6. The initial conditions are the same as for the RBST, where a fully ionized particle at $T = 10^8$ K is located at the centre of a cold cloud of molecular hydrogen. As in the standard Sedov blast wave test the hot particle causes the propagation of a shock wave through the gas. The Figures represent the situation of the model after an arbitrary time where the shock wave has propagated to a sufficient distance from the origin. We note that in the the post-shock region H and H^+ coexist in variable proportions. This mixture is dominated by the ionized hydrogen nearby the region where the shock reaches its highest density. The molecular hydrogen is partially destroyed by the shock and H_2 is still dominant in the region never reached by the shock wave.

It is worth to notice that the energy per mass of gas has a smooth curve (Fig. 5.5 bottom panel), while the temperature show some discontinuities (Fig. 5.6 bottom panel). The reason of this phenomenon resides in the fact that the temperature is related to the energy but also depends on the adiabatic index γ . Since different regions of gas are composed by different mix-

³Note that these models always range in the grid domain \mathbb{G} . If we imagine the i -th model of the validation set as a point v_i in the space of the parameters as $v_i(p_1, p_2, \dots, p_N)$, where p_j is the j -th parameter, we have $v_i \in \mathbb{G}^N \subset \mathbb{R}^N$, with N the number of parameters. Analogously the grid model $g_i(p_1, p_2, \dots, p_N)$ satisfies the expression $g_i \in \mathbb{G}^N \subset \mathbb{R}^N$. The set formed by all the v_i models is like a cloud that fills the domain of the grid based models. A v_i model cannot exceed the limits of the grid: we are not extrapolating data outside the problem domain.

tures of species, they have a different mean adiabatic index (see Section 3.3.6). Comparing Figs. 5.4, 5.5 and 5.6 (bottom), we notice that the temperature (Fig. 5.6 - bottom) globally follows the energy profile (Fig. 5.5 - bottom), but the temperature has also a clear connection with the relative abundances of elements in the gas (Fig. 5.4 and Fig. 5.5 - top).

similar feature should be visible also in the RBST results, while apparently no discontinuities are present in the temperature vs. radius plot (see Fig. 5.1). We believe the reason is that the chemical abundances show a smooth radial profile in this test compared to the RFST. The effect of the different adiabatic index is therefore smoother, resulting in a continue temperature profile.

In conclusion, this test shows interesting results. However, ANNs are still unreliable for a detailed analysis of the chemical evolution of the ISM within NB-TSPH codes. As the previous Figures show, the ANN causes the chemical profiles to be more noisy than theoretically expected. This effect could be caused by the intrinsic error of the ANN⁴, or by large differences in some regions of the data domain. Unfortunately these differences are often difficult to handle when the database hypercube includes many models and many parameters (i.e. dimensions) as it is in our case. For these reasons, we must conclude that using ANNs is still unfavourable, at least when the gas has a low metallicity. In the low metallicity case, ANNs may be easily substituted with a direct integration method optimized with some *ad hoc* algorithms or a suitable hardware choice (e.g. GPU). However, whenever the mean metallicity increases the direct integration method becomes really disadvantageous in terms of computational work-load, despite its accurate results: this is the case in which the ANNs could become crucial to study the evolution of the ISM within cosmological simulations. In the very next future, we plan to develop an hybrid method that uses a direct integrator at low metallicities and a ANN when the direct integration becomes not suitable.

5.4 Summary

In this Section we summarize the results of the tests of the Artificial Neural Network with the NB-TSPH code proposed in this Thesis.

In the Section 5.2 we show a Sedov blast-wave test performed by EvOL with an Artificial Neural Network based on a MaNN architecture and trained

⁴ANNs are closely related to the fitting functions and consequently ANNs have an error similar to the one of the fitting curves. Moreover, the ANN and the interpolation curves can be both interpreted as lossy data compressions: the error in both methods represents then a loss of information from the original data.

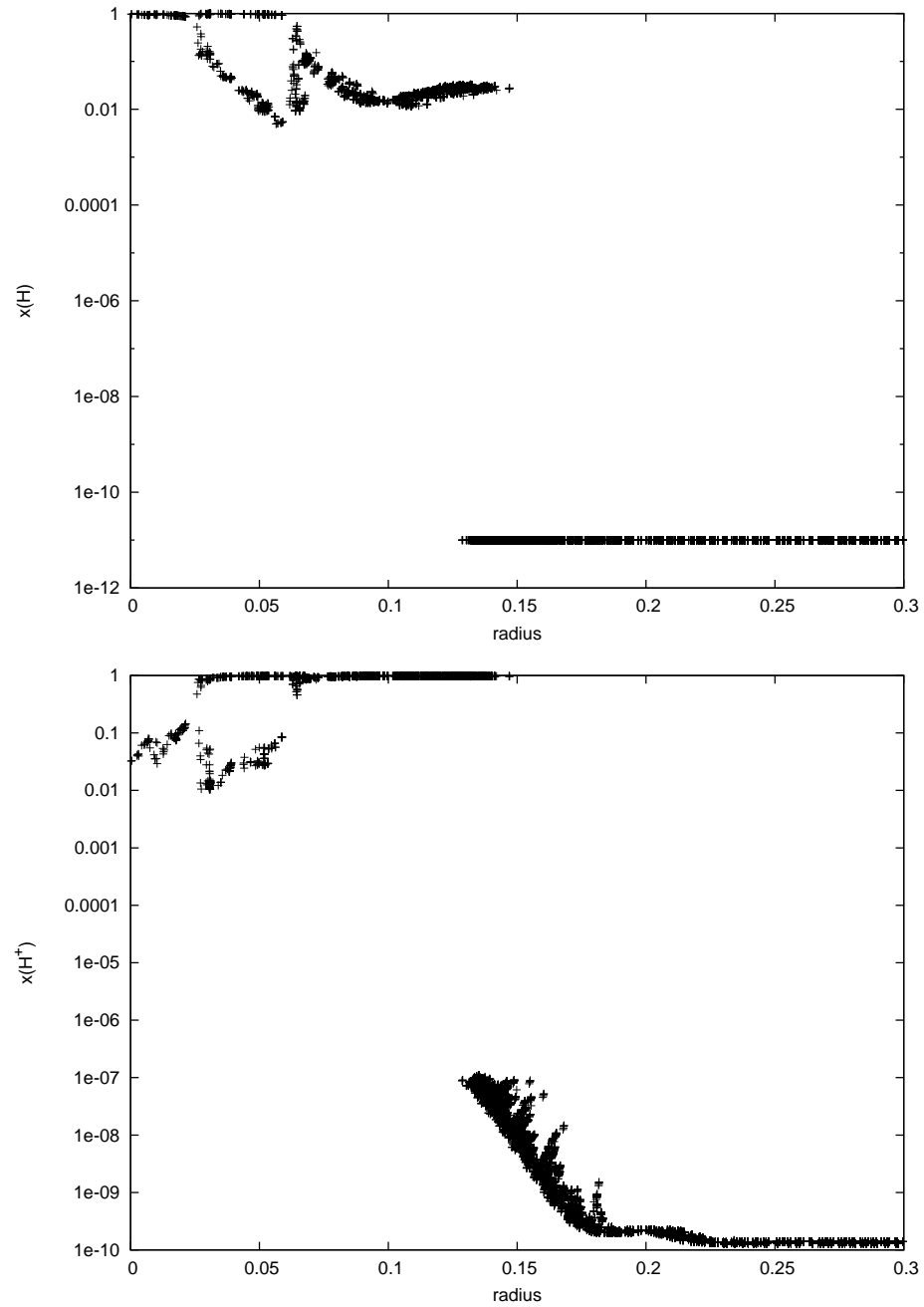


Figure 5.4: The result of the RFST. Top: hydrogen mass fraction. Bottom: ionized hydrogen mass fraction. The radius is arbitrary. Each point represents a gas particle in the NB-TSPH code.

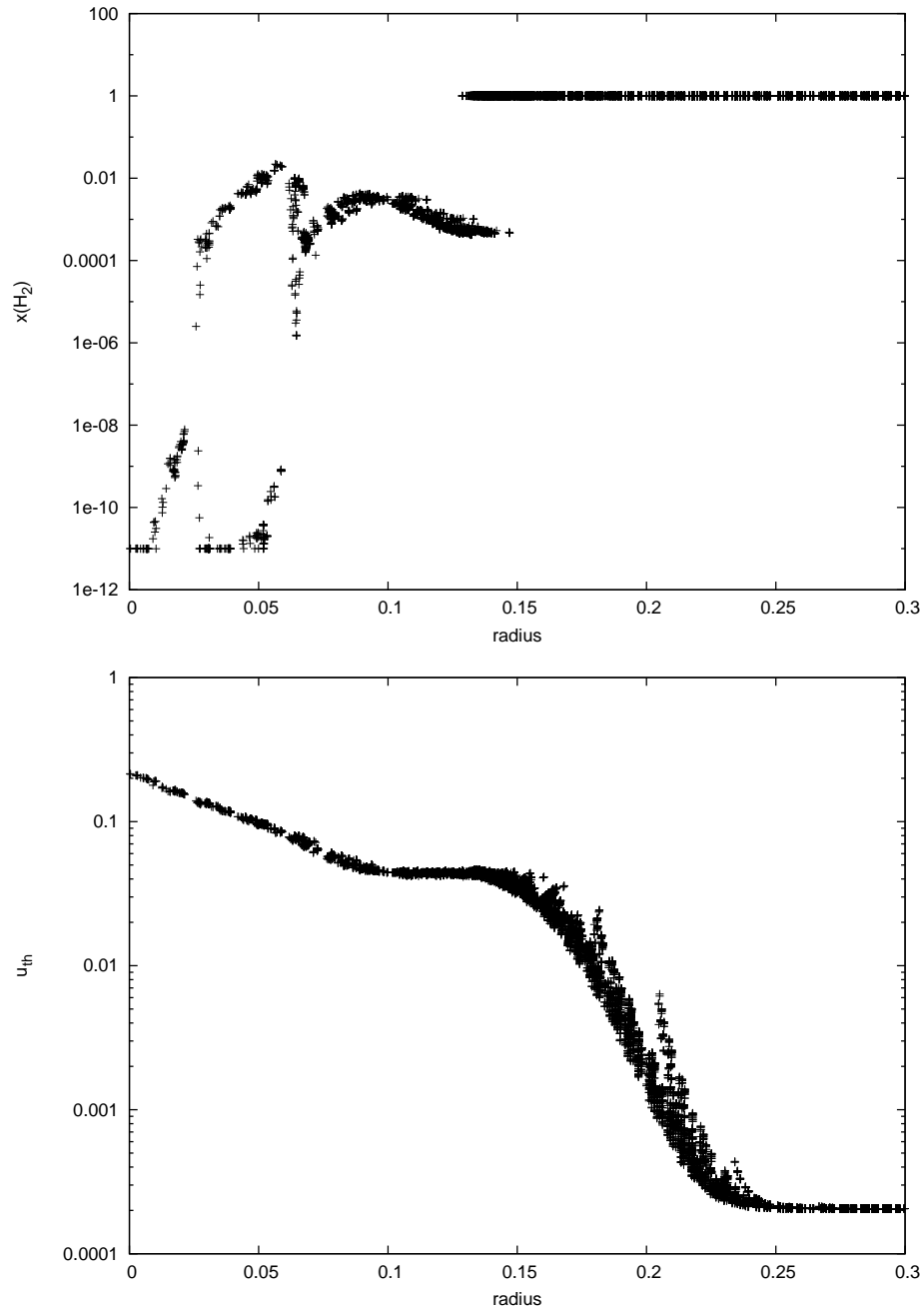


Figure 5.5: The result of the RFST. Top: molecular hydrogen mass fraction. Bottom: energy per unit of mass. The radius is arbitrary. Each point represents a gas particle in the NB-TSPH code.

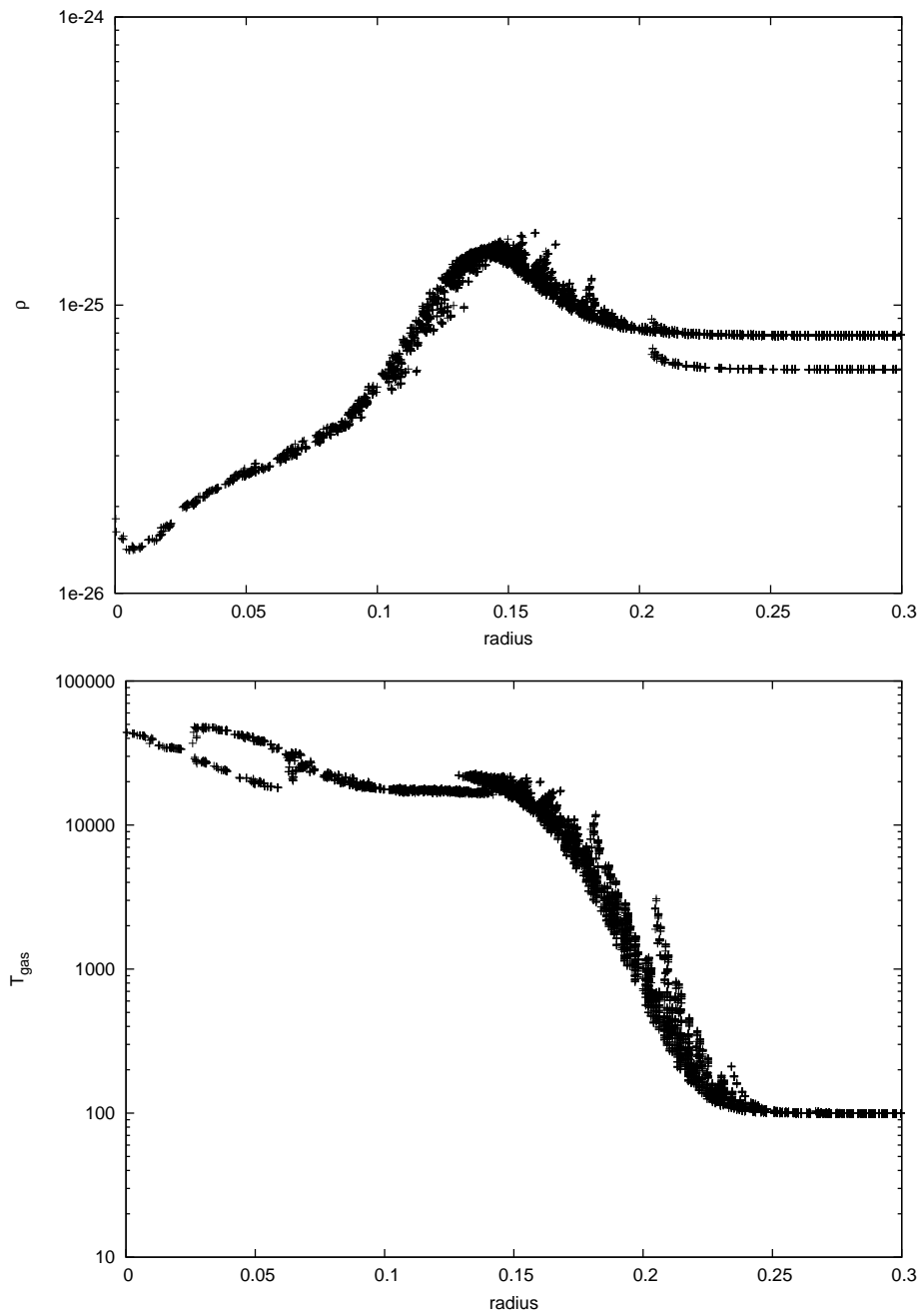


Figure 5.6: The result of the RFST. Top: gas density in g/cm^3 . Bottom: gas temperature in K. The radius is arbitrary. Each point represents a gas particle in the NB-TSPH code.

on the database created with ROBO. We refer to this test as RBST. The physics involved in this version of the code is summarized in the Section 5.2, but it is worth to notice that the database has been created with the CEN92 cooling disabled for $T < 10^4$ K in ROBO. This remark will be useful in the next lines. The learning stage shows a small error, and the test presents interesting results, including a smooth distribution of the chemical elements as shown for instance in the Fig. 5.1. We refer to the configuration (ROBO+MaNN without CEN92) as (A).

After this test we decide to improve the physics of the model including the CEN92 cooling at lower temperatures ($T < 10^4$ K). This new feature causes a large increasing of the error during the training stage. Probably it could be determined by a larger amount of cooling that increases the degeneracy of the database, but this last problem is still under analysis.

To cope with this unexpected behaviour we introduced the code modifications summarized in the Section 5.3, even if the large editing we made is the use of the SaNN architecture. All these choices have improved the learning of the ANN, but the test error was still greater than the first attempt (A). We refer to this implementation of the problem (ROFO+CEN92+SaNN) as (B).

The test shown in the Section 5.3.1 uses the best configuration obtained with (B). We have concluded at the end of the Section 5.3.1 that these results are not as good as the one obtained in the RBST with the configuration (A). These results suggest that the configuration (B) needs more work to be improved and to be embedded in the NB-TSPH code. Anyway, the results of the test (A) are encouraging, proving that ANNs are efficient tools, but when the problem becomes too much complex the tuning of the parameters of this method can be really tricky. Fortunately, ANNs permit some different configuration than the ones proposed in this Thesis. These configurations will be the subjects of our future analysis to use the ANNs efficiently in the NB-TSPH.

Chapter 6

Future developments

The future cannot be predicted, but futures can be invented.

Dennis Gabor¹

The model of ISM proposed in this Thesis needs several improvements. We have to include more species into the chemical network, such as the molecules that are involved in many significant reactions of the ISM (HCN, H₂O, HCO, OH, and their ions). We also need to increase the number of ionization levels of the atoms and include the nitrogen. Some of these species are important to trace the properties of the ISM in the galaxies, and to check the validity of the models produced by the NB-TSPH code, thus tracking these species plays a key role.

In this Thesis we have suggested some other improvements within the text, for example the inclusion of the PAHs, or the need for an accurate model to find the temperature of the grains from the impinging UV radiations. This Section is dedicated to three improvements that have not yet been discussed within this Thesis. (i) The first of them consists in embedding a Single Stellar Population (SSP) into the volume of gas considered. Stars are sources of the UV radiation. The SSP permits to model with accuracy the evolution of a set of stars, and in particular its spectral energy distribution. (ii) The second issue concerns the cooling by [122] adopted in this code for $T > 10^4$ K. This is a grid-based model with two free parameters, namely the metallicity and the temperature. This model considers only the global metallicity, but it neglects the mixture of metals into the gas. This aspect of the model could be improved considering another parameter that better characterize the content of metals of the ISM. (iii) To conclude this Chapter we introduce a strategy

¹Inventing the Future, Pelican Books, 1964, p. 161

to retrieve the properties of the ISM database produced with ROBO/ROFO. This technique uses the Markovian processes to analyze the evolution of the gas.

6.1 Including stellar feedback

A further step would be the inclusion in the model of some form of stellar feedback. We consider the action of a Single Stellar Population (SSP) as a source of radiation, in particular taking into account the UV photons from young, massive stars. The chemistry of the ISM is heavily affected by the radiation at these wavelengths. So, the first aim of this improvement is to investigate how the ISM is affected by a nearby SSP.

There are four main effects caused by the presence of an UV field:

(i) A first phenomenon is the influence on the chemical network through photon-based processes, that unbound the molecules (e.g. coolants) and ionize/excite the atoms - see Section 2.2.2.

(ii) A second effect is the heating of the ISM via the injection of high-energy electrons in the gas - Section 2.2.2.

(iii) Moreover, the dust can be heated by high-energy photons, thus it gets warmer and consequently changes its efficiency in enriching the ISM with molecules - see Section 2.5.6.

(iv) Finally, the dust loses electrons when is impinged by an UV field. These electrons have a large amount of kinetic energy and then they heat the gas - Section 2.5.3.

First we define the SSP as a set of stars born within a short burst of star formation activity. In this way they all have the same age and the same initial chemical composition. The masses of the new born stars is determined by the Initial Mass Function (IMF), $dN(M) \propto M^{-\alpha}dM$, with M the mass of the star, $N(M)$ the number of star for a given mass M , and $\alpha > 0$ the slope of the power-law. Hence, from the stellar evolution theory it is possible to follow the evolution of the SSP as a whole, since each star born with a given mass has a defined history determined by the stellar evolutionary tracks [55, 13, 45, 44, 43, 46]. An evolutionary track describes the path in the color-magnitude diagram of a star of given mass M during its life for a given metallicity Z . It can be parametrized as a function $\mathcal{T} : \mathbb{R}^3 \rightarrow \mathbb{R}^2$ where $\mathcal{T}(t, Z, M) = (L, T_{\text{eff}})$ with T_{eff} the effective temperature and L the luminosity of the star.

Once the evolution of a star is known, one can retrieve its Spectral Emission Distribution (SED) using a synthetic database (e.g. [16, 15, 123, 126, 126]). Alternatively we can use only the effective temperature of the star,

since for our purposes we are interested in the FUV part of the spectrum only. The effective temperature, provided by the evolutionary tracks, gives the black-body emission spectrum of a given star. Finally, for both methods the SED of the SSP is obtained summing all the contributions from all the stars that populate the SSP, considering that these stars follow the number distribution suggested by their IMF.

Moreover, embedding a SSP into the chemical code permits to add an important source of the UV into the NB-TSPH code *EvoL*. The amount of UV is particularly large when the SSP is young. The typical spectrum of an O-B star (massive and young) is characterized by a large fraction of photons in the UV wavelengths. These photons play a crucial role in the star formation history of a galactic system, since it can quench the star formation process, destroying the molecules and/or heating the ISM. The UV radiation from massive stars is therefore one of the most important sources of energy feedback in the galaxies formation models.

6.2 Metallicity dependent cooling - a more accurate version

In principle, the accurate value of the cooling function for metals depends on the temperature and on the detailed chemical composition.

In a cosmological simulation, one must deal with a huge number of gas particles with different metallicities. A full computation of the cooling function of each particle according to its detailed chemical composition would be very expensive in terms of computing time. To deal with the above difficulty, the most common approach consists of reducing the metal dependence of the cooling function into a much smaller number of parameters or, ideally, into just one parameter ξ .

$$\Lambda_Z = \Lambda_Z(T, \xi). \quad (6.1)$$

In this work the cooling by metals is divided into low-temperature cooling (inferred by direct calculation) and high-temperature cooling (interpolated from the tables of [122]). The latter presents the issue introduced in this Section, because it is metallicity dependent. The high-temperature cooling by [122] in fact satisfies the Eqn. (6.1) for $\xi = Z$. The value used for ξ in this case considers the mixture of metals used proportional to the solar one. In particular the $[\text{Fe}/\text{H}]$ is inferred with the classical definition of metallicity that consider only the iron, and assumes that the other metals have a ratio that is proportional to the solar ratios²: this assumption is not always true

²This definition forces for example the $[\text{O}/\text{H}]$ ratio of the gas to be proportional to the

(e.g. alpha-enhancement).

A full computation of the cooling function has been carried out for each particle by using MAPPINGS III³ and its individual chemical composition by [91]. The dots in Fig. 6.1 represent the individual values of the cooling function when the same temperature ($T = 10^{5.5}$ K) is assigned to all the gas particles in the sample. The solid line represents instead the cooling rate obtained from the [122] method. It can be seen from this figure that the latter approach gives a reasonable approximation of the cooling rate. However, the figure also shows an important dispersion on the cooling rate of gas particles with the same total metallicity but different metal mixtures. Such a dispersion could lead to errors in the estimate of cooling function of almost one order of magnitude for sub-solar metallicities. From these data the authors find a more accurate value for ξ that depends on the mixture of metals that are present in the gas (see [91] for further details and also for the tabulated new cooling function).

Finally, this methodology permits to have a more accurate cooling function, reducing the errors due to the assumption that the mixture of metals is always proportional to the solar one. We will introduce this new characteristic in the new version of ROBO/ROFO. The final effect on the chemical evolution is not quantifiable at the moment, since this feature has not yet been implemented. The effect on the evolution will be at temperature $T > 10^4$ K and it will could cause a faster or a slower decline toward the lower temperatures, in particular toward the 10^4 K barrier, where the cooling efficiency has a sudden variation.

6.3 Markovian-like ISM evolution

Astronomers like to classify things.

Duncan Forbes and Pavel Kroupa [50]

An approach based on the same predictive paradigm of the ANNs is the one we define here Markovian-like method. This method follows the same theoretical considerations of the Markov's chains. First consider a transformation from a state A to a state B of a given system \mathcal{S} . This transformation is a Markovian process if the conditional probability distribution of future states of the process, given the present state and the past states, depend only

[O/H]_⊙ ratio, as determined by the [Fe/H] ratio of the gas respect to [Fe/H]_⊙ ratio.

³MAPPING III is a photoionization code developed over two decades by Mike Dopita, Ralph Sutherland, Ian Evans, Luc Binette, Mark Allen, and Brent Groves. <http://www.ifa.hawaii.edu/~kewley/Mappings/>

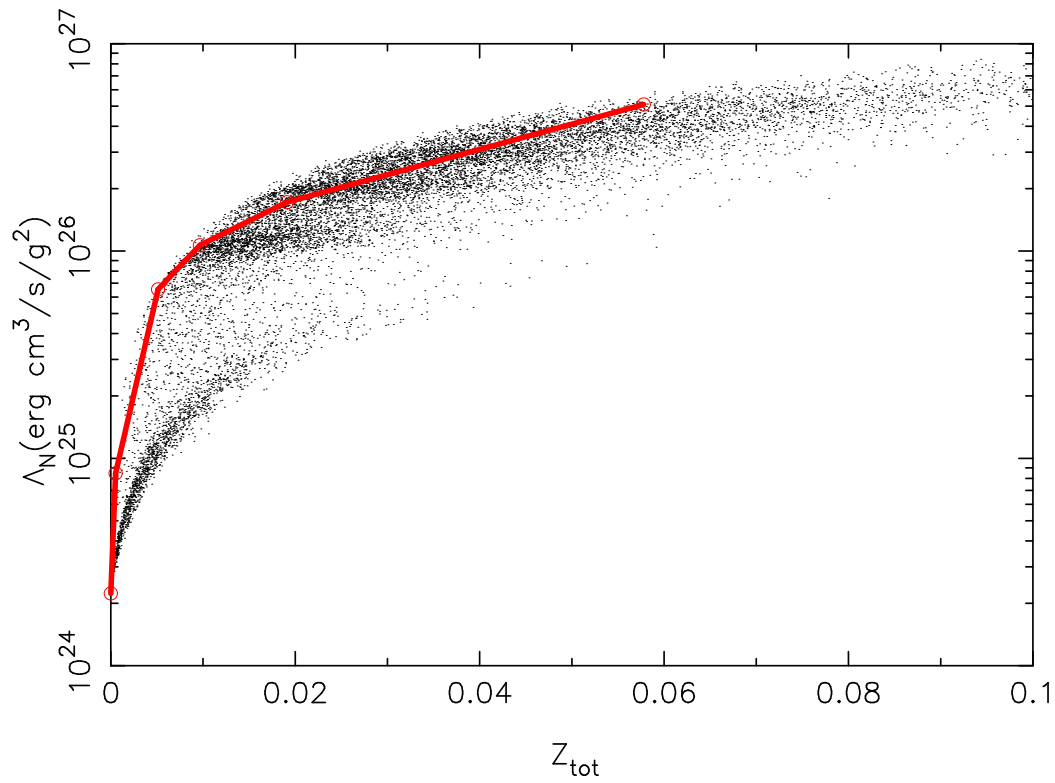


Figure 6.1: Cooling function dependence on the total metallicity Z for a given ($T = 10^{5.5}$ K) temperature for distribution of abundances present on a cosmological self-consistent simulation with metal enrichment. The solid line represents the cooling according to [122].

upon the present state. This can be modeled as a function $f : \mathbb{R}^N \rightarrow \mathbb{R}^N$, with N that depends on the number of the parameters used. In this case we have

$$\mathcal{S}_B = f(\mathcal{S}_A). \quad (6.2)$$

The state A represents the system at a given time t_A , while the state B represents the \mathcal{S} after an interval Δt , so we have $t_B = t_A + \Delta t$. It is worth to notice that for the observer the time interval is discrete, since we cannot have any information about the system at smaller intervals. In this way the system moves from state A to B and the observer cannot have any information about the intermediate states.

Following the definition of Markovian process we assume the system at the time t_B depends only on the system at time t_A even if the system is defined at a time $t_A - k\Delta t$, where k is a positive integer⁴. This approach permits to describe the evolution of a system applying the transformation (i.e. the function f) to the system in the initial state (\mathcal{S}_0) to obtain the system after a Δt (i.e. \mathcal{S}_1), and the complete evolution is calculated using this transformation recursively

$$\mathcal{S}_0 \xrightarrow{f} \mathcal{S}_1 \xrightarrow{f} \mathcal{S}_2 \xrightarrow{f} \dots \xrightarrow{f} \mathcal{S}_T, \quad (6.3)$$

where \mathcal{S}_j is the system at $t_j = t_0 + j\Delta t$.

It is now clear how this method could be applied to the evolution of the ISM. Analogously we choose a set of variables that are essential to describe the ISM (for example the fraction of H and H₂, the temperature and the ionization fraction), and we consider them discrete. In this sense the ISM is now “classified” with these discrete parameters.

Let’s consider for instance only the temperature and the ionization state. One can divide the temperature into $s_T = 3$ states like hot (H), warm (W) and cold (C), and something of analogous can be done for the ionization fraction, using $s_\chi = 3$ states, e.g. high (H), intermediate (M) and low (L). In this example we obtain $s_{\text{tot}} = \Pi_i s_i = s_T s_\chi = 9$ combinations labeled with XY where X is the temperature, and Y represents the ionization fraction (e.g. WM for warm-intermediate, CL for cold-low, HH for hot-high, ...). In this sense the ISM is described only by the properties XY. This classification⁵ clearly could be more accurate if using a more refined division of the space of the parameters. The nine combinations are summarized in Table 6.1.

⁴With this formalism the state B depends only on the state with $k = 0$ which is exactly the system at time t_A .

⁵Note that this is implicitly done when we describe the ISM as WIM or CNM and so on.

Table 6.1: The nine possible XY combination for a gas with two properties each one classified with three states. Temperature are hot (H), warm (W) and cold (C), while ionization are high (H), intermediate (M) and low (L).

	H	M	L
H	HH	HM	HL
W	WH	WM	WL
C	CH	CM	CL

The Markovian process is now defined as $(XY)_j \xrightarrow{f} (XY)_{j+1}$. At this point we don't know nothing about the function f except its domain and its co-domain. Thus, the two ingredients we need are (i) the shape of the transformation function f and (ii) the way to determine this function. If we follow the Markovian approach the function $\mathcal{S}_{j+1} = f(\mathcal{S}_j)$ could be represented by a matrix indicating for each state XY the probability of changing the current gas state to a newer state XY. So, each element M_{ij} of the matrix represents the $(XY)_i \xrightarrow{f} (XY)_j$ transition. This is the commonly-used way to define a Markovian matrix.

If we use this matrix-based approach we also need to know the values of the M_{ij} elements. To achieve this task we can use a chemical code like ROBO/ROFO. First we create a database of models as we have done for the ANN. Then we simply count the models that change their state from $(XY)_i$ to $(XY)_j$ obtaining the matrix N . To obtain M we normalize each line of the matrix N as $M_{ij} = N_{ij} / \sum_j N_{ij}$.

6.3.1 A simple application

We have applied this method to a metal-free ($Z = -20$) sample of gas. The model follows the assumption made for ROFO, except that in this case the free parameters are the temperature T in the range $10 \leq T \leq 10^4$ K, and the ionization fraction χ in the range $0 \leq \chi \leq 1$. The initial number density for the hydrogen is $n_{\text{H}} = n(1 - \chi)$, the ionized hydrogen is $n_{\text{H}^+} = n\chi$, the molecular hydrogen is $n_{\text{H}_2} = 10^{-1}n(1 - \chi)$ and its ion is $n_{\text{H}_2^+} = n_{\text{H}_2}\chi$. The other terms follows the same prescriptions made for ROFO.

The cooling processes enabled are [27], H_2 and metal (which is meaningless since the gas has metallicity $Z = -20$). The cosmic rays, the dust and the UV radiation are all turned off. The gas does not contain the deuterium-based species. It is let to evolve for $\Delta t = 10^3$ yr, for 3025 models dividing the grid in 50 temperatures (logarithmic) and 50 ionization states (linear). More-

over, the gas does not receive energy from the outside, so it has no chance to increase its temperature, but only to cool down, since the cooling is the only thermal process enabled. The same occurs for the ionization, since without external source of heating the gas becomes less and less ionized.

The classes are three for the temperature and three for the ionization. A gas class is then the composition of two classes (temperature and ionization) and is labeled as XY. In particular we have

$$X = \begin{cases} C & \text{if } 0 < T \leq 10^2 \text{ K} \\ W & \text{if } 10^2 < T \leq 10^3 \text{ K} \\ H & \text{if } 10^3 < T \leq 10^4 \text{ K} \end{cases} \quad Y = \begin{cases} L & \text{if } 0 \leq \chi \leq 0.3 \\ M & \text{if } 0.3 < \chi \leq 0.6 \\ H & \text{if } 0.6 < \chi \leq 1.0 \end{cases} \quad (6.4)$$

The nine combination are listed in Table 6.1

The matrix M is calculated from these models and the results are plotted in the Fig. 6.2. The classes are represented by the labels in the form XY inside the circles where the X represents the temperature classification (H=hot, W=warm, C=cold) and Y the ionization status (H=high, M=intermediate, L=low). The element M_{ij} of the matrix is the probability of the event $(XY)_i \rightarrow (XY)_j$ after a Δt . The probability is indicated as a percentage. The circular arrows represents a transformation $(XY)_i \rightarrow (XY)_i$, that is a volume of gas that remains in the same class. It is worth to notice that some elements of the matrix are equal to zero, and in the plot they are not indicated.

We analyze the main features of Fig. 6.2. (i) At first glance we notice that the gas always cools, as expected. This is indicated by the fact that the arrows always point to status with same temperature or lower. (ii) Moreover, for the same reason we notice the gas always decreases its ionization or remains in the same ionization state, but never increases. (iii) The ISM converges to the CL class which is a cold and neutral medium. It means that when $t \rightarrow \infty$ the ISM will always reach the state CL. Note that a gas in the CL state can go only in another CL state, since it cannot get hotter or more ionized (this fact is stressed by the circular arrow labeled with 100%). (iv) The hot gas never shows circular arrows except when the ionization is low. This is because the cooling is efficient when $T > 10^3$ K, and in $\Delta t = 10^3$ yr it goes always below 10^3 K. At low degrees of ionization they are not enough collision partners to have an efficient cooling. (v) This fact is supported by the lack of circular arrows in the WH class. In this case the gas is colder but the high degree of ionization makes the cooling more efficient. (vi) The class CM has the higher probability to be “crossed” and is the most connected. It is also the target of the arrows with a probability greater than the 40%.

Note that the classes with a small standard deviation between the values of their escaping arrows contain a small degree of information (for example

CM, that has two arrows of about 50%). This suggests that such classes must be refined increasing the detail of their parameters. The class CM for example has a chance of the 50% to remain CM, and the 50% to become less ionized. This means that maybe there is one (or more) intermediate class that better describe the phenomenon.

Is important to remark that we are not dealing with actual probabilities. The probability here arises because we are representing a problem with exact solutions (i.e. the evolution of the ISM) with some arbitrary classes. The chance to move from one class to another is represented like a probability because, introducing these classes, our problem becomes less defined, and the probability is exactly this “blur”. Nevertheless, we obtain some interesting results, such as an insightful representation of the evolution of the ISM. The simple example proposed in this Section gives us a clear representation of the behavior of a complex system like the ISM.

This method could be used for statistical models of the ISM, where a very detailed representation is not useful. Since this representation of the ISM is predictive, it could be ancillary to other method, for example in the NB-TSPH codes to save CPU-time, establishing what is the best numerical method to compute the evolution of a given gas particle. This is also a good method to study the properties of the ISM or to check the behavior of the various parameters that define the ISM.

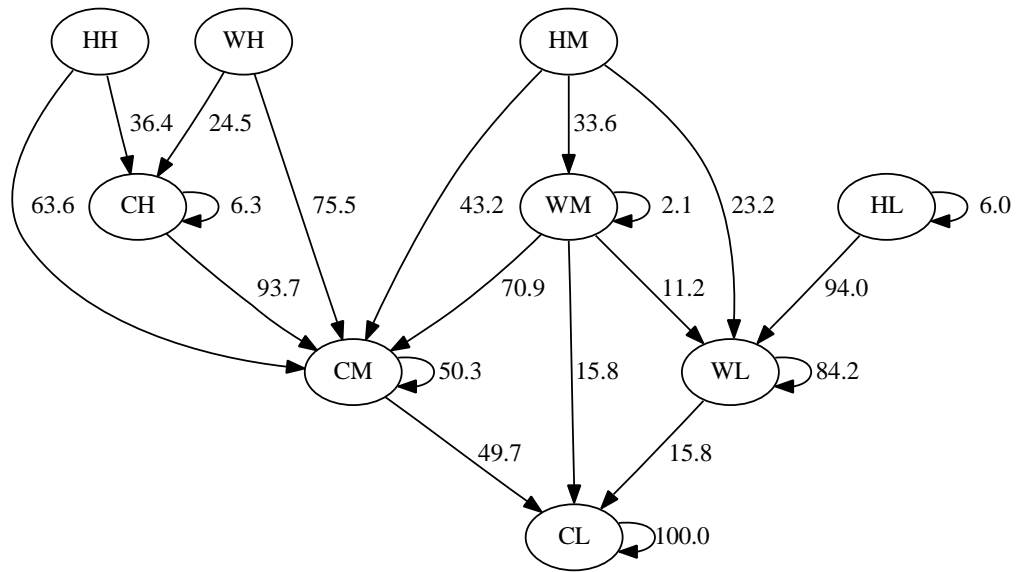


Figure 6.2: The map representing the Markovian matrix M (see text for details). The labels inside the circles are XY where X represents the temperature classification (H=hot, W=warm, C=cold) and Y the ionization status (H=high, M=intermediate, L=low), e.g. HM represents a hot gas with an intermediate degree of ionization. The labels near the arrows are the percent probability to move from one state to another following the direction of the arrow itself. e.g. $WH \rightarrow CM$ has a probability of 75.5% to happen. The circular arrows represent a status that remain the same. Transition with probability of 0% are omitted.

Chapter 7

Conclusions

A conclusion is the place where you get tired of thinking.

Arthur Bloch

In this Thesis we have discussed the ISM and its leading chemical processes. We have also presented a model to describe the ISM and a code ROBO that is based on the assumptions we made for the model.

In the first part of this work we summarize the main physical characteristics of the ISM. We review the many different structures belonging to the ISM, including their main features (HII regions, dark clouds, reflection nebulae and supernova remnants). We also describe the material components characterizing the interstellar gas, classifying them both in temperature and degree of ionization (HIM, WNM, WIM, CNM and molecular clouds). The energy sources, such as thermal processes, UV, cosmic rays, magnetic fields and kinetic energy coupled with turbulent phenomena have been described as well. This qualitative introduction to the ISM also includes a discussion on the interplay between the stars and the gas and a briefly description of the ISM in the Milky Way.

The first Chapter continues with a detailed description of the formalism needed to describe the chemistry-related phenomena, introducing the chemical reactions and their network, the photoionization processes and some considerations about the numerical issues due to the chemical reactions.

The radiative cooling process is the topic of the subsequent Section. We describe its behaviour considering both atomic and molecular species, the latter component giving both rotational and vibrational cooling. The counterpart of the cooling process is the heating process, which is essentially produced by cosmic rays and turbulence. The crucial heating by dust and photoelectric processes is described in two different Sections.

The last component of the ISM we have described is the interstellar dust. We analyze the distribution, the temperature, the formation and the destruction of dust grains by shocks and by thermal processes. We conclude the first Chapter discussing the formation of molecules in the dust-phase and with the cooling and the heating connected to the presence of the dust in the ISM.

The second Chapter is dedicated to our model of the ISM, and its companion code ROBO. First we discuss the chemical reactions we included in the model, then the CO network and the photochemistry. The modeled cooling processes are molecular cooling (H_2 , HD and CO), metal cooling (C, O, Fe, Si and relative ions), and the high-temperature cooling functions by [27] and [122]. The model also include dust physics, describing the formation and the destruction of grains by shocks (both at low and high speed) and by thermal sputtering through the collisions with the gas species. The last part of this Section is dedicated to the modeling of the heating due to photoelectric emission of electrons into the medium.

At the end of the Chapter we introduce the code ROBO and some tests to check the performance of the code.

The topic of the subsequent Chapter is the interplay between ROBO and the NB-TSPH code EvOL. We first discuss two typical approaches, namely the “classical” methods, that includes the direct integration, the fit and the grid interpolation, and the class of methods based on the Artificial Intelligence. These include the Support Vector Machines, the Radial Basis Functions and the Artificial Neural Networks (ANN). The ANNs are our choice to interface ROBO and EvOL.

We then describe the ANN in detail, including the descriptions of the back-propagation algorithm, and we show how the learning and the training stages work.

In the Chapter 5 we show some tests performed by EvOL with the ANN embedded. The Sedov blast wave test is discussed here with some differences as we introduce the chemistry in the NB-TSPH code with promising results. Finally, we present a new version of ROBO called ROFO, which only includes the chemical species followed in EvOL. Its aim is to have code which is at once easy to handle and less CPU-demanding than ROBO. We show a test also for this version of the code.

The last Chapter of the Thesis is dedicated to future developments. First we discuss the action of stellar feedback, and in particular the study of SSPs evolution in time as a source of UV flux for the ISM. We then suggest an

improvement to the [122] cooling, following [91]; the proposed cooling function keeps into account the mixture of metals of the ISM, instead of using the simple definition of metallicity. The Chapter ends with a Markovian-like analysis of the ISM and a simple application of this analysis to a small database produced with ROFO.

In this Thesis we have repeatedly pointed out the importance of cooling and related phenomena in the star formation process. We have developed a model to analyse the major key aspects of the physics of the ISM from the chemical point of view. This model has a numerical counterpart: we have tried to obtain a good compromise between the accuracy of the physics used and the work-load on the CPU. This problem has been explored also for the toughest task of our work: the interface between a complex code like ROBO and a complex N-body code like EVOL. To cope with this difficult task, we have introduced a new technique, the Artificial Neural Networks. This AI-based method allows to obtain results which are similar to the ones provided by the direct integration, but using a very small fraction of the work-load needed by the direct integration method. The test performed with this new technique are promising, and in the future we hope to successfully embed the Artificial Neural Network into the NB-TSPH code EVOL.

Appendix A

Complete matrices for metal cooling

In this Appendix we list the matrices for the metal cooling. They are necessary to define and solve the linear system $A_X \otimes n_X^* = B_X$, where A_X is a square matrix of size $L \times L$ where L is the number of fine structure levels of the given metal X. A_X contains the coefficients for the metal X, B_X is the vector of size L of the known terms which is defined as $B_X = (n_X, 0, 0, \dots)$. Finally, n_X^* is the vector of size L that contains the unknown number densities of the atoms at the various excitation levels, and \otimes indicates the matrix-vector multiplication.

The cooling matrix for two-levels atoms (0,1) like C^+ and Si^+ is

$$A_{C^+} = \begin{pmatrix} 1 & 1 \\ M_{01}^{C^+} & -M_{10}^{C^+} \end{pmatrix}$$

where

$$\begin{aligned} M_{01}^{C^+} &= {}^{(C^+)}\gamma_{01}^H n_H + {}^{(C^+)}\gamma_{01}^{e^-} n_{e^-} \\ M_{01}^{Si^+} &= {}^{(Si^+)}\gamma_{01}^H n_H + {}^{(Si^+)}\gamma_{01}^{e^-} n_{e^-} . \end{aligned}$$

In the previous Equations ${}^{(X)}\gamma_{ij}^Y$ is the reaction rate for the transition $i \rightarrow j$ (where i and j are two excitation levels) for the atom Y colliding with the species X.

We show here only the terms of the form M_{ij} for $i < j$. Their analogous M_{ji} are defined as

$$M_{ji}^X = \sum_k {}^{(X)}\gamma_{ji}^k + A_{ji}^X, \quad (A.1)$$

where the sum is over the colliders, X is the atom considered and A_{ji} is the Einstein coefficient.

The cooling matrix for three-levels atoms (0,1,2) like C, Si, O and O⁺ is

$$A_C = \begin{pmatrix} 1 & 1 & 1 \\ M_{01}^C + M_{02}^C & -M_{10}^C & M_{20}^C \\ -M_{01}^C & M_{10}^C + M_{12}^C & -M_{21}^C \end{pmatrix}$$

where C is for carbon, and M_{ij}^C is for carbon:

$$\begin{aligned} M_{01}^C &= {}^{(C)}\gamma_{01}^{\text{H}_2^{\text{O}}} n_{\text{H}_2} + {}^{(C)}\gamma_{01}^{\text{H}_2^{\text{P}}} n_{\text{H}_2^{\text{P}}} + {}^{(C)}\gamma_{01}^{\text{H}} n_{\text{H}} + {}^{(C)}\gamma_{01}^{\text{H}^+} n_{\text{H}^+} + {}^{(C)}\gamma_{01}^{e^-} n_{e^-} \\ M_{12}^C &= {}^{(C)}\gamma_{12}^{\text{H}_2^{\text{O}}} n_{\text{H}_2} + {}^{(C)}\gamma_{12}^{\text{H}_2^{\text{P}}} n_{\text{H}_2^{\text{P}}} + {}^{(C)}\gamma_{12}^{\text{H}} n_{\text{H}} + {}^{(C)}\gamma_{12}^{\text{H}^+} n_{\text{H}^+} + {}^{(C)}\gamma_{12}^{e^-} n_{e^-} \\ M_{02}^C &= {}^{(C)}\gamma_{02}^{\text{H}_2^{\text{O}}} n_{\text{H}_2} + {}^{(C)}\gamma_{02}^{\text{H}_2^{\text{P}}} n_{\text{H}_2^{\text{P}}} + {}^{(C)}\gamma_{02}^{\text{H}} n_{\text{H}} + {}^{(C)}\gamma_{02}^{\text{H}^+} n_{\text{H}^+} + {}^{(C)}\gamma_{02}^{e^-} n_{e^-} \end{aligned}$$

where H_2^{O} and H_2^{P} are the para and the ortho molecular hydrogen respectively. For Si we have

$$\begin{aligned} M_{01}^{\text{Si}} &= {}^{(\text{Si})}\gamma_{01}^{\text{H}} n_{\text{H}} + {}^{(\text{Si})}\gamma_{01}^{\text{H}^+} n_{\text{H}^+} \\ M_{12}^{\text{Si}} &= {}^{(\text{Si})}\gamma_{12}^{\text{H}} n_{\text{H}} + {}^{(\text{Si})}\gamma_{12}^{\text{H}^+} n_{\text{H}^+} \\ M_{02}^{\text{Si}} &= {}^{(\text{Si})}\gamma_{02}^{\text{H}} n_{\text{H}} + {}^{(\text{Si})}\gamma_{02}^{\text{H}^+} n_{\text{H}^+} . \end{aligned}$$

and for oxygen we have

$$\begin{aligned} M_{01}^{\text{O}} &= {}^{(\text{O})}\gamma_{01}^{\text{H}_2^{\text{O}}} n_{\text{H}_2} + {}^{(\text{O})}\gamma_{01}^{\text{H}_2^{\text{P}}} n_{\text{H}_2^{\text{P}}} + {}^{(\text{O})}\gamma_{01}^{\text{H}} n_{\text{H}} + {}^{(\text{O})}\gamma_{01}^{\text{H}^+} n_{\text{H}^+} + {}^{(\text{O})}\gamma_{01}^{e^-} n_{e^-} \\ M_{12}^{\text{O}} &= {}^{(\text{O})}\gamma_{12}^{\text{H}_2^{\text{O}}} n_{\text{H}_2} + {}^{(\text{O})}\gamma_{12}^{\text{H}_2^{\text{P}}} n_{\text{H}_2^{\text{P}}} + {}^{(\text{O})}\gamma_{12}^{\text{H}} n_{\text{H}} + {}^{(\text{O})}\gamma_{12}^{\text{H}^+} n_{\text{H}^+} + {}^{(\text{O})}\gamma_{12}^{e^-} n_{e^-} \\ M_{02}^{\text{O}} &= {}^{(\text{O})}\gamma_{02}^{\text{H}_2^{\text{O}}} n_{\text{H}_2} + {}^{(\text{O})}\gamma_{02}^{\text{H}_2^{\text{P}}} n_{\text{H}_2^{\text{P}}} + {}^{(\text{O})}\gamma_{02}^{\text{H}} n_{\text{H}} + {}^{(\text{O})}\gamma_{02}^{\text{H}^+} n_{\text{H}^+} + {}^{(\text{O})}\gamma_{02}^{e^-} n_{e^-} . \end{aligned}$$

If the atom has five levels (0, 1, 2, 3, 4) like Fe and Fe⁺ the matrix is then

$$A_{\text{Fe}} = \begin{pmatrix} 1 & 1 & 1 & 1 & 1 \\ \sum M_{0i}^{\text{Fe}} & -M_{10}^{\text{Fe}} & -M_{20}^{\text{Fe}} & -M_{30}^{\text{Fe}} & -M_{40}^{\text{Fe}} \\ -M_{01}^{\text{Fe}} & M_{10}^{\text{Fe}} + M_{20}^{\text{Fe}} & -M_{21}^{\text{Fe}} & 0 & 0 \\ -M_{02}^{\text{Fe}} & -M_{12}^{\text{Fe}} & M_{20}^{\text{Fe}} + M_{21}^{\text{Fe}} & 0 & 0 \\ -M_{03}^{\text{Fe}} & 0 & 0 & M_{30}^{\text{Fe}} + M_{34}^{\text{Fe}} & -M_{43}^{\text{Fe}} \end{pmatrix} ,$$

Table A.1: The number of the atomic levels considered in our model for different species.

specie	levels	specie	levels
C	3	C ⁺	2
Si	3	Si ⁺	2
O	3	O ⁺	3
Fe	5	Fe ⁺	5

where the sum is over $i \in [1, 4]$ and the coefficients are defined by

$$\begin{aligned}
 M_{01}^{\text{Fe}} &= {}^{(\text{Fe})}\gamma_{01}^{\text{H}} n_{\text{H}} + {}^{(\text{Fe})}\gamma_{01}^{\text{e}^-} n_{\text{e}^-} \\
 M_{12}^{\text{Fe}} &= {}^{(\text{Fe})}\gamma_{12}^{\text{H}} n_{\text{H}} + {}^{(\text{Fe})}\gamma_{12}^{\text{e}^-} n_{\text{e}^-} \\
 M_{02}^{\text{Fe}} &= {}^{(\text{Fe})}\gamma_{02}^{\text{H}} n_{\text{H}} + {}^{(\text{Fe})}\gamma_{02}^{\text{e}^-} n_{\text{e}^-} \\
 M_{03}^{\text{Fe}} &= {}^{(\text{Fe})}\gamma_{03}^{\text{e}^-} n_{\text{e}^-} \\
 M_{04}^{\text{Fe}} &= {}^{(\text{Fe})}\gamma_{04}^{\text{e}^-} n_{\text{e}^-} \\
 M_{34}^{\text{Fe}} &= {}^{(\text{Fe})}\gamma_{34}^{\text{e}^-} n_{\text{e}^-}
 \end{aligned}$$

and for Fe⁺ we have

$$\begin{aligned}
 M_{12}^{\text{Fe}^+} &= {}^{(\text{Fe}^+)}\gamma_{12}^{\text{H}} n_{\text{H}} + {}^{(\text{Fe}^+)}\gamma_{12}^{\text{e}^-} n_{\text{e}^-} \\
 M_{23}^{\text{Fe}^+} &= {}^{(\text{Fe}^+)}\gamma_{23}^{\text{H}} n_{\text{H}} + {}^{(\text{Fe}^+)}\gamma_{23}^{\text{e}^-} n_{\text{e}^-} \\
 M_{34}^{\text{Fe}^+} &= {}^{(\text{Fe}^+)}\gamma_{34}^{\text{H}} n_{\text{H}} + {}^{(\text{Fe}^+)}\gamma_{34}^{\text{e}^-} n_{\text{e}^-} \\
 M_{02}^{\text{Fe}^+} &= {}^{(\text{Fe}^+)}\gamma_{02}^{\text{H}} n_{\text{H}} + {}^{(\text{Fe}^+)}\gamma_{02}^{\text{e}^-} n_{\text{e}^-} \\
 M_{03}^{\text{Fe}^+} &= {}^{(\text{Fe}^+)}\gamma_{03}^{\text{H}} n_{\text{H}} + {}^{(\text{Fe}^+)}\gamma_{03}^{\text{e}^-} n_{\text{e}^-} \\
 M_{04}^{\text{Fe}^+} &= {}^{(\text{Fe}^+)}\gamma_{04}^{\text{H}} n_{\text{H}} + {}^{(\text{Fe}^+)}\gamma_{04}^{\text{e}^-} n_{\text{e}^-} \\
 M_{13}^{\text{Fe}^+} &= {}^{(\text{Fe}^+)}\gamma_{13}^{\text{H}} n_{\text{H}} + {}^{(\text{Fe}^+)}\gamma_{13}^{\text{e}^-} n_{\text{e}^-} \\
 M_{14}^{\text{Fe}^+} &= {}^{(\text{Fe}^+)}\gamma_{14}^{\text{H}} n_{\text{H}} + {}^{(\text{Fe}^+)}\gamma_{14}^{\text{e}^-} n_{\text{e}^-} \\
 M_{24}^{\text{Fe}^+} &= {}^{(\text{Fe}^+)}\gamma_{24}^{\text{H}} n_{\text{H}} + {}^{(\text{Fe}^+)}\gamma_{24}^{\text{e}^-} n_{\text{e}^-} .
 \end{aligned}$$

The definition of the coefficients ${}^{\text{X}}\gamma_{ji}^{\text{Y}}$ is analogous. See the text for more details.

Acknowledgments

I would like to thank my supervisor Prof. Cesare Chiosi, and also E. Merlin, L. Piovan, U. Buonomo, and J. Krivacic for the useful discussions and their help.

I'm grateful to the examiner Prof. Francesco Palla and also to Dr. F. Combes for the kind hospitality at the Observatoire de Paris - LERMA under EARA grants where part of the Thesis has been developed and the many stimulating discussions.

Bibliography

- [1] T. Abel, P. Anninos, Y. Zhang, and M. L. Norman. Modeling primordial gas in numerical cosmology. *New Astronomy*, 2:181–207, August 1997.
- [2] P. Alotto and M. A. Nervi. An efficient hybrid algorithm for the optimization of problems with several local minima. *Int. J. Numer. Meth. Engng.*, 50:847–868, 2001.
- [3] P. Anninos, Y. Zhang, T. Abel, and M. L. Norman. Cosmological hydrodynamics with multi-species chemistry and nonequilibrium ionization and cooling. *New Astronomy*, 2:209–224, August 1997.
- [4] U. M. Ascher and L. R. Petzold. *Computer methods for ordinary differential equations and differential-algebraic equations*. SIAM, Philadelphia, 1998.
- [5] E. L. O. Bakes and A. G. G. M. Tielens. The photoelectric heating mechanism for very small graphitic grains and polycyclic aromatic hydrocarbons. *ApJ*, 427:822–838, June 1994.
- [6] J. Barnes and P. Hut. A hierarchical $O(N \log N)$ force-calculation algorithm. *Nature*, 324:446–449, December 1986.
- [7] C. F. Barnett, H. T. Hunter, M. I. Fitzpatrick, I. Alvarez, C. Cisneros, and R. A. Phaneuf. Atomic data for fusion. Volume 1: Collisions of H, H₂, He and Li atoms and ions with atoms and molecules. *NASA STI/Recon Technical Report N*, 91:13238–+, July 1990.
- [8] W. Benz. Smooth Particle Hydrodynamics - a Review. In J. R. Buchler, editor, *Numerical Modelling of Nonlinear Stellar Pulsations Problems and Prospects*, pages 269–+, 1990.
- [9] A. M. Boesgaard and G. Steigman. Big bang nucleosynthesis - Theories and observations. *ARAA*, 23:319–378, 1985.

- [10] N. W. Boggess, J. C. Mather, R. Weiss, C. L. Bennett, E. S. Cheng, E. Dwek, S. Gulkis, M. G. Hauser, M. A. Janssen, T. Kelsall, S. S. Meyer, S. H. Moseley, T. L. Murdock, R. A. Shafer, R. F. Silverberg, G. F. Smoot, D. T. Wilkinson, and E. L. Wright. The COBE mission - Its design and performance two years after launch. *ApJ*, 397:420–429, October 1992.
- [11] A. C. Boley, T. W. Hartquist, R. H. Durisen, and S. Michael. Erratum: “The Internal Energy for Molecular Hydrogen in Gravitationally Unstable Protoplanetary Disks” ([jA href="/abs/2007ApJ...656L..89B"](/abs/2007ApJ...656L..89B)) *ApJ*, 656, L89 [2007]i/Aj). *ApJ*, 660:L175–L175, May 2007.
- [12] A. C. Boley, T. W. Hartquist, R. H. Durisen, and S. Michael. Erratum: “The Internal Energy for Molecular Hydrogen in Gravitationally Unstable Protoplanetary Disks” ([jA href="/abs/2007ApJ...656L..89B"](/abs/2007ApJ...656L..89B)) *ApJ*, 656, L89 [2007]i/Aj). *ApJ*, 660:L175–L175, May 2007.
- [13] A. Bressan, F. Fagotto, G. Bertelli, and C. Chiosi. Evolutionary sequences of stellar models with new radiative opacities. II - $Z = 0.02$. *AAPS*, 100:647–664, September 1993.
- [14] Peter N. Brown, G. D. Byrne, and A. C. Hindmarsh. Vode: a variable-coefficient ode solver. *SIAM J. Sci. Stat. Comput.*, 10:1038–1051, September 1989.
- [15] G. Bruzual and S. Charlot. Stellar population synthesis at the resolution of 2003. *MNRAS*, 344:1000–1028, October 2003.
- [16] G. Bruzual A. and S. Charlot. Spectral evolution of stellar populations using isochrone synthesis. *ApJ*, 405:538–553, March 1993.
- [17] Martin D. Buhmann and M. D. Buhmann. *Radial Basis Functions*. Cambridge University Press, New York, NY, USA, 2003.
- [18] F. Bulsara, M. A. Nervaro, and M. V. Shaney. Decentralized, signed theory for the influence of trainable archetypes. *Int. J. Tech. Neur. Endev.*, 32:372–377, 2004.
- [19] G. D. Byrne and A. C. Hindmarsh. A polyalgorithm for the numerical solution of ordinary differential equations. *ACM Trans. Math. Softw.*, 1:71–96, March 1975.

- [20] Gail A. Carpenter and Stephen Grossberg. A massively parallel architecture for a self-organizing neural pattern recognition machine. *Computer Vision, Graphics, and Image Processing*, 37(1):54–115, 1987.
- [21] Gail A. Carpenter and Stephen Grossberg. The art of adaptive pattern recognition by a self-organizing neural network. *IEEE Computer*, 21(3):77–88, 1988.
- [22] Gail A. Carpenter and Stephen Grossberg. Art 3: Hierarchical search using chemical transmitters in self-organizing pattern recognition architectures. *Neural Networks*, 3(2):129–152, 1990.
- [23] G. Carraro, C. Lia, and C. Chiosi. Galaxy formation and evolution - I. The Padua tree-sph code (pd-sph). *MNRAS*, 297:1021–1040, July 1998.
- [24] S. Cazaux, P. Caselli, V. Cobut, and J. Le Bourlot. The role of carbon grains in the deuteration of H₂. *AAP*, 483:495–508, May 2008.
- [25] S. Cazaux and M. Spaans. HD and H₂ formation in low-metallicity dusty gas clouds at high redshift. *AAP*, 496:365–374, March 2009.
- [26] S. Cazaux and A. G. G. M. Tielens. Molecular Hydrogen Formation in the Interstellar Medium. *ApJ*, 575:L29–L32, August 2002.
- [27] R. Cen. A hydrodynamic approach to cosmology - Methodology. *ApJS*, 78:341–364, February 1992.
- [28] F. Combes. Molecular gas in galaxies at all redshifts. *ArXiv e-prints*, January 2011.
- [29] Corinna Cortes and Vladimir Vapnik. Support-vector networks. In *Machine Learning*, pages 273–297, 1995.
- [30] H. M. P. Couchman, P. A. Thomas, and F. R. Pearce. Hydra: an Adaptive-Mesh Implementation of P 3M-SPH. *ApJ*, 452:797–+, October 1995.
- [31] H. Croft, A. S. Dickinson, and F. X. Gadea. Rate coefficients for the Li⁺/H⁻ and Li⁻/H⁺ mutual neutralization reactions. *MNRAS*, 304:327–329, April 1999.
- [32] A. Dalgarno and S. Lepp. Chemistry in the early universe. In M. S. Vardya and S. P. Tarafdar, editors, *Astrochemistry*, volume 120 of *IAU Symposium*, pages 109–118, 1987.

- [33] A. E. Depristo, S. D. Augustin, R. Ramaswamy, and H. Rabitz. Quantum number and energy scaling for nonreactive collisions. *JCP*, 71:850–865, July 1979.
- [34] B. T. Draine. Interstellar Dust Models and Evolutionary Implications. In T. Henning, E. Grün, & J. Steinacker, editor, *Astronomical Society of the Pacific Conference Series*, volume 414 of *Astronomical Society of the Pacific Conference Series*, pages 453–+, December 2009.
- [35] B. T. Draine and H. M. Lee. Optical properties of interstellar graphite and silicate grains. *ApJ*, 285:89–108, October 1984.
- [36] B. T. Draine and E. E. Salpeter. Time-dependent nucleation theory. *JCP*, 67:2230–2235, September 1977.
- [37] B. T. Draine and E. E. Salpeter. On the physics of dust grains in hot gas. *ApJ*, 231:77–94, July 1979.
- [38] E. Dwek. The Evolution of the Elemental Abundances in the Gas and Dust Phases of the Galaxy. *ApJ*, 501:643–+, July 1998.
- [39] E. Dwek. Interstellar dust: what is it, how does it evolve, and what are its observational consequences? In C. C. Popescu & R. J. Tuffs, editor, *The Spectral Energy Distributions of Gas-Rich Galaxies: Confronting Models with Data*, volume 761 of *American Institute of Physics Conference Series*, pages 103–122, April 2005.
- [40] E. Dwek. The Chemical Evolution of Interstellar Dust. In R. Szczerba, G. Stasińska, & S. K. Gorny, editor, *Planetary Nebulae as Astronomical Tools*, volume 804 of *American Institute of Physics Conference Series*, pages 197–203, November 2005.
- [41] E. Dwek, F. Galliano, and A. Jones. The Cycle of Dust in the Milky Way: Clues from the High-Redshift and Local Universe. In T. Henning, E. Grün, & J. Steinacker, editor, *Astronomical Society of the Pacific Conference Series*, volume 414 of *Astronomical Society of the Pacific Conference Series*, pages 183–+, December 2009.
- [42] G. Efstathiou. Suppressing the formation of dwarf galaxies via photoionization. *MNRAS*, 256:43P–47P, May 1992.
- [43] F. Fagotto, A. Bressan, G. Bertelli, and C. Chiosi. Evolutionary sequences of stellar models with new radiative opacities. III. $Z=0.0004$ and $Z=0.05$. *AAPS*, 104:365–376, April 1994.

- [44] F. Fagotto, A. Bressan, G. Bertelli, and C. Chiosi. Evolutionary sequences of stellar models with new radiative opacities. IV. $Z=0.004$ and $Z=0.008$. *AAPS*, 105:29–38, May 1994.
- [45] F. Fagotto, A. Bressan, G. Bertelli, and C. Chiosi. Evolutionary sequences of stellar models with very high metallicity. V. $Z=0.1$. *AAPS*, 105:39–45, May 1994.
- [46] F. Fagotto, A. Bressan, G. Bertelli, and C. Chiosi. Evolutionary sequences V. (Fagotto+ 1994). *VizieR Online Data Catalog*, 410:50039–+, January 1994.
- [47] G. J. Ferland, K. T. Korista, D. A. Verner, J. W. Ferguson, J. B. Kingdon, and E. M. Verner. CLOUDY 90: Numerical Simulation of Plasmas and Their Spectra. *PASP*, 110:761–778, July 1998.
- [48] J. Fischer, E. Sturm, E. González-Alfonso, J. Graciá-Carpio, S. Hailey-Dunsheath, A. Poglitsch, A. Contursi, D. Lutz, R. Genzel, A. Sternberg, A. Verma, and L. Tacconi. Herschel-PACS spectroscopic diagnostics of local ULIRGs: Conditions and kinematics in Markarian 231. *AAP*, 518:L41+, July 2010.
- [49] D. J. Fixsen. The Temperature of the Cosmic Microwave Background. *ApJ*, 707:916–920, December 2009.
- [50] D. Forbes and P. Kroupa. What is a Galaxy? Cast your vote here... *ArXiv e-prints*, January 2011.
- [51] B. Fryxell, K. Olson, P. Ricker, F. X. Timmes, M. Zingale, D. Q. Lamb, P. MacNeice, R. Rosner, J. W. Truran, and H. Tufo. FLASH: An Adaptive Mesh Hydrodynamics Code for Modeling Astrophysical Thermonuclear Flashes. *ApJS*, 131:273–334, November 2000.
- [52] D. Galli and F. Palla. The chemistry of the early Universe. *AAP*, 335:403–420, July 1998.
- [53] F. Galliano, E. Dwek, and P. Charnial. Stellar Evolutionary Effects on the Abundances of Polycyclic Aromatic Hydrocarbons and Supernova-Condensed Dust in Galaxies. *ApJ*, 672:214–243, January 2008.
- [54] M. W. Gealy and B. van Zyl. Cross sections for electron capture and loss. I - $H(+)$ and $H(-)$ impact on H and H_2 . *Phys. Rev. A*, 36:3091–3107, October 1987.

- [55] L. Girardi, A. Bressan, C. Chiosi, G. Bertelli, and E. Nasi. Evolutionary sequences of stellar models with new radiative opacities. VI. $Z=0.0001$. *AAPS*, 117:113–125, May 1996.
- [56] S. C. Glover, D. W. Savin, and A.-K. Jappsen. Cosmological Implications of the Uncertainty in $H(-)$ Destruction Rate Coefficients. *ApJ*, 640:553–568, April 2006.
- [57] S. C. O. Glover and T. Abel. Uncertainties in $H(2)$ and HD chemistry and cooling and their role in early structure formation. *MNRAS*, 388:1627–1651, August 2008.
- [58] S. C. O. Glover, C. Federrath, M.-M. Mac Low, and R. S. Klessen. Modelling CO formation in the turbulent interstellar medium. *MNRAS*, 404:2–29, May 2010.
- [59] S. C. O. Glover and A.-K. Jappsen. Star Formation at Very Low Metallicity. I. Chemistry and Cooling at Low Densities. *ApJ*, 666:1–19, September 2007.
- [60] S. C. O. Glover and D. W. Savin. Is H_3^+ cooling ever important in primordial gas? *MNRAS*, 393:911–948, March 2009.
- [61] R. Goldflam, D. J. Kouri, and S. Green. Infinite order sudden approximation for rotational energy transfer in gaseous mixtures. *JCP*, 67:4149–4161, November 1977.
- [62] T. Grassi, P. Krstic, E. Merlin, U. Buonomo, L. Piovan, and C. Chiosi. ROBO: a Model and a Code for the Study of the Interstellar Medium. *ArXiv e-prints*, December 2010.
- [63] Jacques Hadamard. Sur les problèmes aux dérivés partielles et leur signification physique. *Princeton University Bulletin*, 13:49–52, 1902.
- [64] D. Harris, C. J. C. Burges, L. Kaufman, A. J. Smola Smola, and V. Vapnik. Support vector regression machines. In *NIPS*, pages 155–161, 1996.
- [65] Donald O. Hebb. *The Organization of Behavior: A Neuropsychological Theory*. Wiley, New York, new edition edition, June 1949.
- [66] L. Hernquist and N. Katz. TREESPH - A unification of SPH with the hierarchical tree method. *ApJS*, 70:419–446, June 1989.

- [67] A. C. Hindmarsh. Odepack, a systematized collection of ode solvers , r. s. stepleman et al. (eds.), north-holland, amsterdam, (vol. 1 of), pp. 55-64. *IMACS Transactions on Scientific Computation*, 1:55–64, 1983.
- [68] H. Hirashita and H. Yan. Shattering and coagulation of dust grains in interstellar turbulence. *MNRAS*, 394:1061–1074, April 2009.
- [69] D. Hollenbach and C. F. McKee. Molecule formation and infrared emission in fast interstellar shocks. I Physical processes. *ApJS*, 41:555–592, November 1979.
- [70] D. Hollenbach and C. F. McKee. Molecule formation and infrared emission in fast interstellar shocks. III - Results for J shocks in molecular clouds. *ApJ*, 342:306–336, July 1989.
- [71] J. J. Hopfield. Neural Networks and Physical Systems with Emergent Collective Computational Abilities. *Proceedings of the National Academy of Science*, 79:2554–2558, April 1982.
- [72] J. J. Hopfield. Neurons with Graded Response Have Collective Computational Properties like Those of Two-State Neurons. *Proceedings of the National Academy of Science*, 81:3088–3092, May 1984.
- [73] K. R. Jackson and R. Sacks-Davis. An alternative implementation of variable step-size multistep formulas for stiff odes. *ACM Trans. Math. Softw.*, 6:295–318, September 1980.
- [74] R. K. Janev, W. D. Langer, D. E. Post, Jr., and K. J. Evans. Elementary processes in hydrogen-helium plasmas: Cross sections and reaction rate coefficients. *Shock and Vibration*, 4, 1987.
- [75] A. P. Jones. Dust Destruction Processes. In A. N. Witt, G. C. Clayton, & B. T. Draine, editor, *Astrophysics of Dust*, volume 309 of *Astronomical Society of the Pacific Conference Series*, pages 347–+, May 2004.
- [76] A. P. Jones and A. G. G. M. Tielens. in “*The Cold Universe*”, eds. Montmerle Th., Lada, Ch. J., Mirabel I. F., Trân Thanh Vân J. Éditions Frontières, Gif-sur-Yvette, 1994.
- [77] N. Katz, D. H. Weinberg, and L. Hernquist. Cosmological Simulations with TreeSPH. *ApJS*, 105:19–+, July 1996.
- [78] P. S. Krstić. Inelastic processes from vibrationally excited states in slow $H^+ + H_2$ and $H + H_2^+$ collisions: Excitations and charge transfer. *Phys. Rev. A*, 66(4):042717–+, October 2002.

- [79] T. Kusakabe, M. Kimura, L. Pichl, R. J. Buenker, and H. Tawara. Observation of significant differences in charge transfer between collisions of H^+ ions with H_2 and with D_2 molecules in the high-eV to low-keV range. *Phys. Rev. A*, 68(5):050701–+, November 2003.
- [80] A. Laor and B. T. Draine. Spectroscopic constraints on the properties of dust in active galactic nuclei. *ApJ*, 402:441–468, January 1993.
- [81] M. A. Leitch-Devlin and D. A. Williams. Sticking coefficients for atoms and molecules at the surfaces of interstellar dust grains. *MNRAS*, 213:295–306, March 1985.
- [82] A. K. Leroy, F. Walter, F. Bigiel, A. Usero, A. Weiss, E. Brinks, W. J. G. de Blok, R. C. Kennicutt, K.-F. Schuster, C. Kramer, H. W. Wiesemeyer, and H. Roussel. Heracles: The HERA CO Line Extragalactic Survey. *AJ*, 137:4670–4696, June 2009.
- [83] A. Li and B. T. Draine. Do the Infrared Emission Features Need UV Excitation? The PAH Model in UV-poor Reflection Nebulae. In *Bulletin of the American Astronomical Society*, volume 33 of *Bulletin of the American Astronomical Society*, pages 1451–+, December 2001.
- [84] A. Li and B. T. Draine. Infrared Emission from Interstellar Dust. II. The Diffuse Interstellar Medium. *ApJ*, 554:778–802, June 2001.
- [85] A. Li and B. T. Draine. On Ultrasmall Silicate Grains in the Diffuse Interstellar Medium. *ApJ*, 550:L213–L217, April 2001.
- [86] C. Lia, L. Portinari, and G. Carraro. Star formation and chemical evolution in smoothed particle hydrodynamics simulations: a statistical approach. *MNRAS*, 330:821–836, March 2002.
- [87] A. Lipovka, R. Núñez-López, and V. Avila-Reese. The cooling function of HD molecule revisited. *MNRAS*, 361:850–854, August 2005.
- [88] S. Lukaszuk. A new concept of probability metric and its applications in approximation of scattered data sets. *Computational Mechanics*, 33:299–304, 2004. 10.1007/s00466-003-0532-2.
- [89] U. Maio, K. Dolag, B. Ciardi, and L. Tornatore. Metal and molecule cooling in simulations of structure formation. *MNRAS*, 379:963–973, August 2007.

- [90] R. Maiolino, R. Schneider, E. Oliva, S. Bianchi, A. Ferrara, F. Mannucci, M. Pedani, and M. Roca Sogorb. A supernova origin for dust in a high-redshift quasar. *Nature*, 431:533–535, September 2004.
- [91] F. J. Martínez-Serrano, A. Serna, R. Domínguez-Tenreiro, and M. Mollá. Chemical evolution of galaxies - I. A composition-dependent SPH model for chemical evolution and cooling. *MNRAS*, 388:39–55, July 2008.
- [92] J. S. Mathis, P. G. Mezger, and N. Panagia. Interstellar radiation field and dust temperatures in the diffuse interstellar matter and in giant molecular clouds. *AAP*, 128:212–229, November 1983.
- [93] J. S. Mathis, W. Rumpl, and K. H. Nordsieck. The size distribution of interstellar grains. *ApJ*, 217:425–433, October 1977.
- [94] J. L. McClelland, D. E. Rumelhart, and the PDP Research Group. *Parallel Distributed Processing: Explorations in the Microstructure of Cognition: Psychological and Biological Models*, volume vol. II. MIT Press-Bradford Books, Cambridge, MA, 1986.
- [95] I. D. McGreer and G. L. Bryan. The Impact of HD Cooling on the Formation of the First Stars. *ApJ*, 685:8–20, September 2008.
- [96] C. McKee. Dust Destruction in the Interstellar Medium. In L. J. Allamandola & A. G. G. M. Tielens, editor, *Interstellar Dust*, volume 135 of *IAU Symposium*, pages 431–+, 1989.
- [97] C. F. McKee, J. W. V. Storey, D. M. Watson, and S. Green. Far-infrared rotational emission by carbon monoxide. *ApJ*, 259:647–656, August 1982.
- [98] E. Merlin, U. Buonomo, T. Grassi, L. Piovan, and C. Chiosi. EvoL: the new Padova Tree-SPH parallel code for cosmological simulations. I. Basic code: gravity and hydrodynamics. *AAP*, 513:A36+, April 2010.
- [99] E. Merlin and C. Chiosi. Simulating the formation and evolution of galaxies: multi-phase description of the interstellar medium, star formation, and energy feedback. *AAP*, 473:733–745, October 2007.
- [100] E. Merlin, C. Chiosi, T. Grassi, U. Buonomo, and S. Chinellato. Simulating the formation and evolution of galaxies with EvoL, the Padova N-body Tree-SPH Code. *Nuovo Cimento C Geophysics Space Physics C*, 32(2):020000–146, March 2009.

- [101] H. Mizusawa, K. Omukai, and R. Nishi. Primordial Molecular Emission in Population III Galaxies. *PASJ*, 57:951–967, December 2005.
- [102] J. T. Moseley, W. Aberth, and J. R. Peterson. Two-body mutual neutralization rates of $O_2^+ + \phi^-$, $NO^+ + O^-$, and $Na^+ + O^-$ obtained with merged beams. *J. Geophys. Res.*, 77:255–259, 1972.
- [103] J. F. Navarro and M. Steinmetz. The Effects of a Photoionizing Ultraviolet Background on the Formation of Disk Galaxies. *ApJ*, 478:13–+, March 1997.
- [104] R. P. Nelson and W. D. Langer. The Dynamics of Low-Mass Molecular Clouds in External Radiation Fields. *ApJ*, 482:796–+, June 1997.
- [105] M. L. Norman, G. L. Bryan, R. Harkness, J. Bordner, D. Reynolds, B. O’Shea, and R. Wagner. Simulating Cosmological Evolution with Enzo. *ArXiv e-prints*, May 2007.
- [106] P. Panuzzo, N. Rangwala, A. Rykala, K. G. Isaak, J. Glenn, C. D. Wilson, R. Auld, M. Baes, M. J. Barlow, G. J. Bendo, J. J. Bock, A. Boselli, M. Bradford, V. Buat, N. Castro-Rodríguez, P. Chaniel, S. Charlot, L. Ciesla, D. L. Clements, A. Cooray, D. Cormier, L. Cortese, J. I. Davies, E. Dwek, S. A. Eales, D. Elbaz, T. Fulton, M. Galametz, F. Galliano, W. K. Gear, H. L. Gomez, M. Griffin, S. Hony, L. R. Levenson, N. Lu, S. Madden, B. O’Halloran, K. Okumura, S. Oliver, M. J. Page, A. Papageorgiou, T. J. Parkin, I. Pérez-Fournon, M. Pohlen, E. T. Polehampton, E. E. Rigby, H. Roussel, N. Sacchi, M. Sauvage, B. Schulz, M. R. P. Schirm, M. W. L. Smith, L. Spinoglio, J. A. Stevens, S. Srinivasan, M. Symeonidis, B. Swinyard, M. Trichas, M. Vaccari, L. Vigroux, H. Wozniak, G. S. Wright, and W. W. Zeilinger. Probing the molecular interstellar medium of M82 with Herschel-SPIRE spectroscopy. *AAP*, 518:L37+, July 2010.
- [107] S. J. Petuchowski, E. Dwek, J. E. Allen, Jr., and J. A. Nuth, III. CO formation in the metal-rich ejecta of SN 1987A. *ApJ*, 342:406–415, July 1989.
- [108] Linda Petzold. Automatic selection of methods for solving stiff and nonstiff systems of ordinary differential equations. *SIAM Journal on Scientific and Statistical Computing*, 4(1):136–148, 1983.
- [109] J. P. Prieto, L. Infante, and R. Jimenez. Revisiting the effect of H₂, HD and LiH molecules in the cooling of primordial gas. *astroph/0809.2786*, September 2008.

- [110] Frank Rosenblatt. *Principles of neurodynamics*. Spartan Book, New York, spartan book edition, 1962.
- [111] D. P. Ruffle, J. G. L. Rae, M. J. Pilling, T. W. Hartquist, and E. Herbst. A network for interstellar CO - The first application of objective reduction techniques in astrochemistry. *AAP*, 381:L13–L16, January 2002.
- [112] D. E. Rumelhart, G. E. Hinton, and R. J. Williams. Learning representations by back-propagating errors. *Nature*, 323:533–536, October 1986.
- [113] F. Santoro and J. M. Shull. Critical Metallicity and Fine-Structure Emission of Primordial Gas Enriched by the First Stars. *ApJ*, 643:26–37, May 2006.
- [114] D. W. Savin, P. S. Krstić, Z. Haiman, and P. C. Stancil. Rate Coefficient for $\text{H}^+ + \text{H}_2(\text{X}^1\Sigma_g^+, \nu = 0, J = 0) \rightarrow \text{H}(1s) + \text{H}_2^+$ Charge Transfer and Some Cosmological Implications. *ApJ*, 606:L167–L170, May 2004.
- [115] R. Schinke, V. Engel, U. Buck, H. Meyer, and G. H. F. Diercksen. Rate constants for rotational transitions of CO scattered by para-hydrogen. *ApJ*, 299:939–946, December 1985.
- [116] C. G. Seab. Grain destruction, formation, and evolution. In D. J. Hollenbach & H. A. Thronson Jr., editor, *Interstellar Processes*, volume 134 of *Astrophysics and Space Science Library*, pages 491–512, 1987.
- [117] P. Sigmund. Theory of Sputtering. I. Sputtering Yield of Amorphous and Polycrystalline Targets. *Physical Review*, 187:768–768, November 1969.
- [118] B. Smith, S. Sigurdsson, and T. Abel. Metal cooling in simulations of cosmic structure formation. *MNRAS*, 385:1443–1454, April 2008.
- [119] V. Springel. The cosmological simulation code GADGET-2. *MNRAS*, 364:1105–1134, December 2005.
- [120] V. Springel, N. Yoshida, and S. D. M. White. GADGET: a code for collisionless and gasdynamical cosmological simulations. *NewA*, 6:79–117, April 2001.
- [121] G. Steigman. Primordial Nucleosynthesis: Successes and Challenges. *International Journal of Modern Physics E*, 15:1–35, 2006.

- [122] R. S. Sutherland and M. A. Dopita. Cooling functions for low-density astrophysical plasmas. *ApJS*, 88:253–327, September 1993.
- [123] R. Tantaló and C. Chiosi. Measuring age, metallicity and abundance ratios from absorption-line indices. *MNRAS*, 353:917–940, September 2004.
- [124] A. G. G. M. Tielens. *The Physics and Chemistry of the Interstellar Medium*. Cambridge University Press, September 2005.
- [125] A. G. G. M. Tielens, C. F. McKee, C. G. Seab, and D. J. Hollenbach. The physics of grain-grain collisions and gas-grain sputtering in interstellar shocks. *ApJ*, 431:321–340, August 1994.
- [126] A. Vazdekis, P. Sánchez-Blázquez, J. Falcón-Barroso, A. J. Cenarro, M. A. Beasley, N. Cardiel, J. Gorgas, and R. Peletier. MILES SSP Models. In G. Bruzual & S. Charlot, editor, *IAU Symposium*, volume 262 of *IAU Symposium*, pages 65–68, April 2010.
- [127] H. Vedel, U. Hellsten, and J. Sommer-Larsen. Formation of disc galaxies in the presence of a background UVX radiation field. *MNRAS*, 271:743–+, December 1994.
- [128] D. A. Verner and G. J. Ferland. Atomic Data for Astrophysics. I. Radiative Recombination Rates for H-like, He-like, Li-like, and Na-like Ions over a Broad Range of Temperature. *ApJS*, 103:467–+, April 1996.
- [129] G. S. Voronov. A Practical Fit Formula for Ionization Rate Coefficients of Atoms and Ions by Electron Impact: $Z = 1-28$. *Atomic Data and Nuclear Data Tables*, 65:1–+, 1997.
- [130] J. W. Wadsley, J. Stadel, and T. Quinn. Gasoline: a flexible, parallel implementation of TreeSPH. *NewA*, 9:137–158, February 2004.
- [131] R. V. Wagoner. Big-Bang Nucleosynthesis Revisited. *ApJ*, 179:343–360, January 1973.
- [132] V. Wakelam, I. W. M. Smith, E. Herbst, J. Troe, W. Geppert, H. Linnartz, K. Öberg, E. Roueff, M. Agúndez, P. Pernot, H. M. Cuppen, J. C. Loison, and D. Talbi. Reaction Networks for Interstellar Chemical Modelling: Improvements and Challenges. *Space Science Reviews*, pages 137–+, November 2010.
- [133] C. M. Walmsley, D. R. Flower, and G. Pineau des Forêts. Complete depletion in prestellar cores. *AAP*, 418:1035–1043, May 2004.

- [134] J. C. Weingartner and B. T. Draine. Dust Grain-Size Distributions and Extinction in the Milky Way, Large Magellanic Cloud, and Small Magellanic Cloud. *ApJ*, 548:296–309, February 2001.
- [135] J. C. Weingartner and B. T. Draine. Photoelectric Emission from Interstellar Dust: Grain Charging and Gas Heating. *ApJS*, 134:263–281, June 2001.
- [136] M. Wetzstein, A. F. Nelson, T. Naab, and A. Burkert. Vine-A Numerical Code for Simulating Astrophysical Systems Using Particles. I. Description of the Physics and the Numerical Methods. *ApJS*, 184:298–325, October 2009.
- [137] M. White. Anisotropy in the microwave background. In D. O. Caldwell, editor, *COSMO-98*, volume 478 of *American Institute of Physics Conference Series*, pages 157–163, July 1999.
- [138] J. Woodall, M. Agúndez, A. J. Markwick-Kemper, and T. J. Millar. The UMIST database for astrochemistry 2006. *AAP*, 466:1197–1204, May 2007.
- [139] E. L. Wright. Theoretical Overview of Cosmic Microwave Background Anisotropy. *Measuring and Modeling the Universe*, pages 291–+, 2004.
- [140] L. B. Zhao, P. C. Stancil, J. P. Gu, H.-P. Liebermann, Y. Li, P. Funke, R. J. Buenker, B. Zygelman, M. Kimura, and A. Dalgarno. Radiative Charge Transfer in Collisions of O with He⁺. *ApJ*, 615:1063–1072, November 2004.